Measurement of Nitrous Acid Production from Aerosol Surfaces using Photo-fragmentation Laser Induced Fluorescence

Graham Alexander Boustead

Submitted in accordance with the requirements for the degree of Doctor of Philosophy

The University of Leeds

School of Chemistry

September 2019

Acknowledgements

It has been a long 4 years and while it has been challenging it has always remained enjoyable and it was always interesting to find out which way the instrument will decide to break next.

I would like to thank all my supervisors; Lisa, Dwayne, Dan and Mark for their help and support throughout. In particular Lisa who was always available to help teach me how to run the equipment, talk through the data and run the atmospheric models. Trev and Mark for their technical assistance throughout helping teach me how to fix my temperamental equipment.

The B36 office for both their support with problems during my project but also for their friendship and providing plenty of distractions throughout the day.

Lastly I would like to thank my family and Rachel for their support throughout my PhD

Abstract

The hydroxyl radical (OH) is the primary oxidant in the atmosphere with its concentration determining the lifetime of many species and its reaction with volatile organic compounds leading to the production of secondary organic aerosols and tropospheric ozone. It is therefore important that its sources are well understood. Nitrous acid (HONO) is an important source of OH, building up overnight and is photolysed to form OH in the morning. HONO is also present during the day at much lower concentrations. Models however are currently under predicting these daytime concentrations, indicating a missing source of HONO. With HONO being a dominant source of OH in polluted environments it is important that its concentration is accurately modelled in order to predict a correct OH production rate.

In order to identify and study these missing sources and determine their atmospheric relevance, a photo-fragmentation laser induced fluorescence (PF-LIF) instrument has been built and coupled to an aerosol flow tube to provide a fast and sensitive measurement of HONO. Two aerosol types, previously proposed as possible HONO sources, have been investigated. Illuminated TiO_2, was found to generate HONO in the presence of NO_2 and the reactive uptake coefficient was calculated for a range of NO_2 concentrations, peaking at 2.5×10^{-4} for 30 ppb NO_2. Investigation of ammonium and sodium nitrate aerosols showed no measureable HONO production. Results from the TiO_2 experiment were included in a box model for Beijing where, assuming all the observed aerosol surface area was pure TiO_2, the HONO contribution from this aerosol source was modelled to be roughly 10% of the modelled concentration at midday. This model was not able to replicate the measured HONO data, however, indicating the need for other sources of HONO.

As part of the atmospheric chemistry of amines project measurements of OH and HO_2 were carried out at the EUPHORE chamber using LIF. The measured OH and OH calculated from the amine decay did not agree indicating either a possible interference from the amine oxidation products in the LIF system or in

homogeneous air at the LIF and amine sampling ports. The measured HO_2 in the dark was observed to have a lifetime exceeding 2 hours. This slow HO_2 decay could not be reproduced by a kinetic model which predicted a HO_2 lifetime of seconds suggesting an unknown a source of HO_2 in the dark.

Table of Contents

List of figures

List of tables

List of abbreviations

ACA	Atmospheric Chemistry of Amines
AMS	Aerosol Mass Spectrometer
APHH	Atmospheric Pollution & Human Health in a Chinese Megacity
BBO	Beta Barium Borate
BNC	Berkeley Nucleonics Corporation
BTCA	The British Technical Council for the petroleum and motor industries (calibration gases)
CH_4	Methane
CHARON	Chemical Analysis of Aerosol on-line
CIMS	Chemical Ionisation Mass Spectrometry
CO	Carbon Monoxide
CPC	Condensed Particle Counter
CPM	Channel Photo-Multiplier
CRDS	Cavity Ring-Down Spectroscopy
DMA	Differential Mobility Analyzer
DNPH-HPLC	2,4-Dinitrophenylhydrazine Derivatization and High-Performance Liquid Chromatographic Analysis.
DOAS	Differential Optical Absorption Spectroscopy
ER	Eley-Rideal
EUPHORE	European Photo Reactor
FAGE	Fluorescence Assay by Gas Expansion
FTIR	Fourier Transform Infra-Red
FWHM	Full Width at Half Maximum
GC	Gas Chromatography
GC-FID	Gas Chromatography – Flame Ionisation Detector
GC-TOF-MS	Gas Chromatography Time of Flight Mass Spectrometry
H_2SO_4	Sulphuric acid

H3O	Hydronium Ion
HCCT-2010	Hill Cap Cloud Thuringia – 2010
HCHO	Formaldehyde
HDPE	High Density Polyethylene
HEPA	High Efficiency Particulate Air
HIRAC	Highly instrumented reactor for atmospheric chemistry
HNO_3	Nitric acid
HNO_3	Nitric acid
HO_2	Hydroperoxyl radical
HONO	Nitrous acid
HO_x	$OH + HO_2$
HPLC	High-Performance Liquid Chromatography
HT-PTR-MS	High-Temperature Proton-Transfer-Reaction Mass Spectrometer
ID	Internal Diameter
IPCC	Intergovernmental Panel on Climate Change
IR	Infrared
IUPAC	International Union of Pure and Applied Chemistry
K	Kelvin
LBO	Lithium Triborate
LED	Light Emitting Diode
LH	Langmuir-Hinshelwood
LIF	Laser-Induced Fluorescence
LIFBASE	Spectral Simulation Software
LOD	Limit Of Detection
LOPAP	Long Path Absorption Photometer
LP-DOAS	Long-Path Differential Optical Absorption Spectroscopy
m	meter
MAX-DOAS	Multi-Axis Differential Optical Absorption Spectroscopy
MC/IC	Mist chamber/ Ion Chromatography.
MCM	Master Chemical Mechanism
MCP	Micro-Channel Plate

MFC	Mass Flow Controller
N_2	Nitrogen
N_2O	Nitrous oxide
N_2O_5	Dinitrogen pentoxide
NO	Nitric oxide
NO_2	Nitrogen dioxide
NO_3	Nitric acid
NO_x	NO + NO_2
O	Singlet oxygen
O2	Oxygen
O_3	Ozone
OC	Output coupler
OD	Outside Diameter
OH	Hydroxyl radical
OVOC	Oxidised Volatile Organic Compound
PF-LIF	Photo-fragmentation Laser Induced Fluorescence
PM	Particulate Matter
PMT	Photo-multiplier Tube
ppb	Parts per billion
ppm	Parts per million
ppt	Parts per trillion
PSL	Polystyrene Latex
PTR-ToF-MS	Proton-transfer-reaction Time of Flight Mass Spectrometry
RH	Relative Humidity
s	Seconds
SA	Surface Area
SAPHIR	Simulation of Atmospheric Photochemistry in a Large Reaction Chamber
sccm	Standard cubic centimetres per minute
SHG	Second harmonic generator
SLM	Standard litres per minute

SMPS	Scanning Mobility Particle Sizer
SNR	Signal-to-Noise Ratio
SO_2	Sulphur dioxide
SOA	Secondary Organic Aerosol
t_0	Time zero
Tg	Tera gram, 10^{12} grams
THG	Third harmonic generator
TiO_2	Titanium Dioxide
UK	United Kingdom
UV	Ultraviolet
UVA	Ultraviolet A (λ = 315 – 400 nm)
VOC	Volatile Organic Compound
W	Watts
WHO	World Health Organisation
WP	Wave plate

Chapter 1 Introduction

1.1 Air Quality

In recent years there has been a big focus on improving air quality and reducing the impacts of climate change in order to mitigate the damaging effects on public health, impacts to economies and damage to the environment. For government to implement policies that will improve air quality in a changing climate the policies need to be based on reliable science to ensure that they will be effective. Atmospheric models are used to assess the impacts of pollutants and greenhouse gases on local, regional and the global scales, however, for the models to be considered accurate they need to be validated against measurements made in the field. When there are discrepancies in between the model and measurement, research in a controlled laboratory experiment or environmental chamber can help to better understand individual processes. Atmospheric science relies on modelling, fieldwork and lab studies with results from each supporting and driving research in the other areas.

Two targets of the governments clean air strategy 2019 are nitrogen oxides (NO_x) and fine particulate matter ($PM_{2.5}$) with aims to reduce PM by 46% and NOx by 75% compared to their baseline averages[1]. Both species are regulated with WHO guidelines[2] recommending limits of 10µg m^3 annual mean and 25 µg m^3 daily mean for $PM_{2.5}$ (UK target[3] 25 µg m^3), and 40 µm^3 annual mean and 200 µg m^3 1 hour mean for NO_2 (UK target[3] identical). No official recommended guidelines for exposure to HONO are available however, a study investigating the correlations between lung function to measurements of HONO and NO_2 showed that a similar decline in lung function with increases in both species[4]. This indicates that limits for HONO should be similar to those set for NO_2. NO_x is primarily emitted from combustion sources and the public awareness of it as a harmful pollutant stemmed from the “diesel gate[5]” saga. NO_2 can cause damage to human health and leads to the generation of tropospheric ozone, another harmful secondary species.

Aerosol particles are a major contributor to the severe haze events (100 to 1000 μg m^{-3})[6] seen in many cities. The source of this haze varies depending of the city and often the season: for example in Beijing severe haze events are most prevalent in the wintertime[6] and are caused by both meteorological and topographic effects[6] and elevated emissions from power stations, black carbon, during the heating season. There is increasing evidence, however, that secondary aerosols[7] do contribute to PM even in the wintertime in Beijing. In the springtime haze events are dust events where dust is transported in from the Gobi desert leading an increase in metal ions present in the aerosols[8] (e.g. Ca^{2+} vs NH_4^+) while in the summer larger the formation of secondary organic aerosols is greater due to increased emissions of biogenic compounds[9]. This means that different approaches may be needed to reduce the occurrence of severe pollution events in different locations and at different times of the year. Inhalation of aerosols increases human mortality by causing damage to respiratory and cardiovascular functions[10].

These severe haze events are also important when considering heterogeneous processes. Reactions involving gas and aerosol interactions are often not included in models, yet within haze episodes, particles can provide a large reactive surface for the production or loss of atmospherically important species. There has been active research into the heterogeneous loss of HO_2 via aerosol uptake where studies have found an over prediction of modelled HO_2 concentration when uptake coefficients are not included. Measurements of HO_2 during the Hill Cap Cloud Thuringia campaign[11] in 2010 found that modelled HO_2 was over predicting the HO_2 concentrations compared to the measured values unless a loss term was included. While a global model[12], figure 1.1, comparing the change in species concentration if a uptake of HO_2 was included or not. The plots show the difference in concentration for the model with no HO_2 uptake and a model with an uptake of 1. This shows the decrease in the hydroxal radicals in the atmosphere as less recycling occurs between OH and HO_2. This decrease results in an increase in CO concentration because it is no longer removed through reaction with OH and there is an decrease in ozone which is a product of the recycling process when HO_2 reacts with NO. Understanding the product from the uptake is also important as HO_2 uptake is assumed to form H_2O_2 which can photolyse back to OH regenerating the gas phase HO_x radical

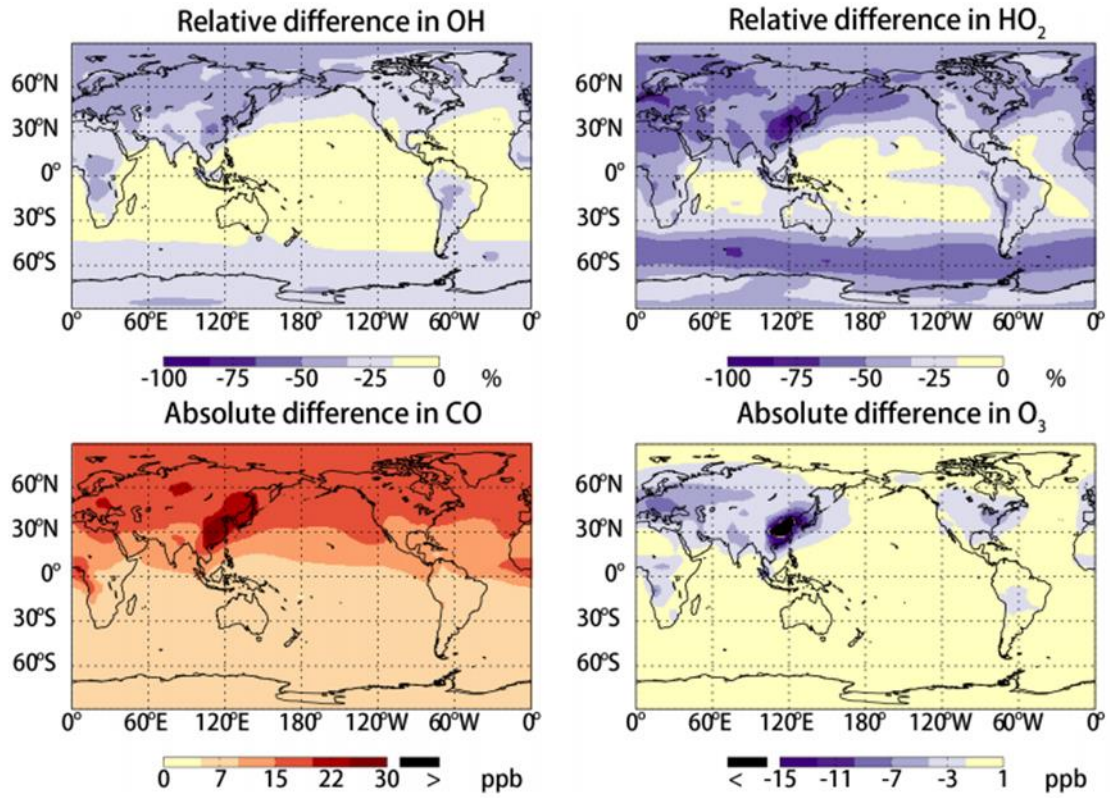

Figure 1.1. The effects of HO_2 uptake on aerosols (γ (HO_2)=1) on concentration of OH, HO_2, CO, and O_3 in the GEOS-CHEM model. The plot has been taken from Mao et. al. [12] and the data represent annual means for 2005. The difference was calculated by subtracting results from a model with no HO_2 uptake.

At Leeds research has continued the investigation of HO_2 uptake onto a range of species including Arizona test dust[13, 14], ammonium nitrate[14] and inorganic aerosols doped with transition metal ions[15]. Most recently both the uptake[16] and production[17] from TiO_2 aerosols.

The focus of the research presented in this thesis is on the role of atmospheric particles in the generation of daytime nitrous acid.

1.2 Aerosols in the troposphere

Atmospheric aerosol are solid or liquid particles suspended in the air with diameters between 0.002 and 100 μm[18]. Aerosols in the atmosphere have both a positive and negative radiative forcing effect on the atmosphere, either cooling[19] or warming[20] the atmosphere. This effect is caused by their ability to absorb and reflect solar radiation, they also act as cloud condensation nuclei[21]; the formation of clouds increases the albedo of the earth's surface. Aerosols also impact gas phase chemistry through heterogeneous loss or production. As figure 1.2 shows it is believed that the overall effect of aerosols in the atmosphere is a cooling affect however because processes that interact with aerosols are not well understood, the error bars are large so this impact has the possibility to change in the future

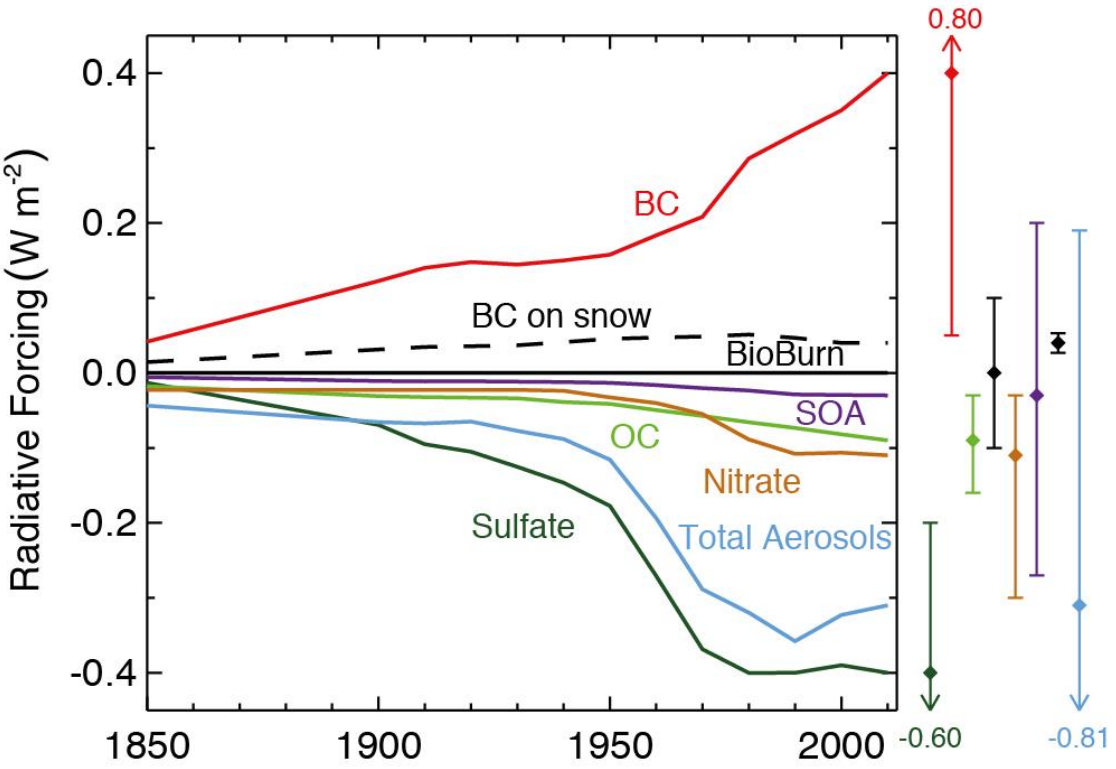

Figure 1.2. Plot showing the effect aerosols have on radiative forcing since 1850. Negative values represent a cooling effect while positives indicate a heating effect. Figure taken from the IPCC 2013 report.

Atmospheric aerosols, both natural and anthropogenic, are formed through two different routes either emissions of primary particulate matter or the formation of secondary particulates from gas phase species[22]. Examples of primary particulate production routes include incomplete combustion, suspension due to wind for example mineral dust from deserts or sea salt from sea spray. Secondary organic aerosols, are formed via the condensation of VOCs with low vapour pressures leading to the formation of new aerosols directly or by condensation onto the surface of existing aerosols; this mechanism can contribute to the growth of existing particles.

1.3 The Hydroxyl Radical

The hydroxyl radical (OH) is the primary daytime oxidant in the atmosphere. It is an important reactive species in the atmosphere and is highly reactive to many primary emissions such as carbon monoxide (CO), methane and volatile organic compounds (VOCs) [23]. Understanding the sources and reactivity of OH is critical for climate change as OH controls the lifetime of the greenhouse gas methane. It also controls the lifetime of toxic gases such as benzene and CO and so plays a central role in air quality too. Following reaction with OH, VOCs form either HO_2 or RO_2. These peroxy radicals react with NO leading to the generation of NO_2 that can photolyse to form ozone, a secondary pollutant that is harmful to both human and plant life. Oxidised VOCs can also form secondary organic aerosols (discussed above), which are important components of particulate matter (PM) in the atmosphere. These reactions, initiated by OH, are shown in figure 1.3 below, with the red reactions showing the recycling of the HO_x radicals, blue shows primary sources of OH.

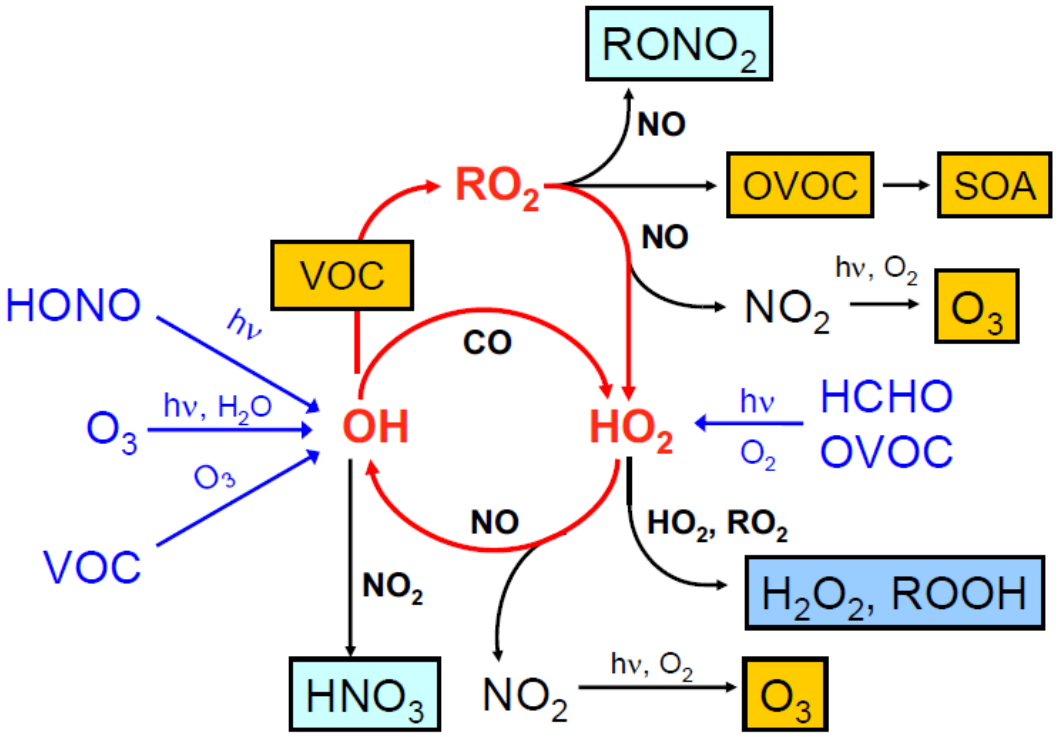

Figure 1.3. Reaction diagram showing the major reaction pathways in the troposphere, taken from reference [24].

The significant reactivity of OH means its lifetime is typically much less than 1 s. With such a short lifetime, the observed OH concentration is controlled by chemistry rather than transport. This makes OH an ideal tracer for atmospheric chemistry models because if a model is able to accurately simulate OH concentrations, then this suggests that the sources and loss pathways for OH are well represented in the model. The accuracy of a model chemistry scheme is important in determining the lifetime of longer lived species that are relevant to air quality and climate (e.g. CH_4 or CO), and also the production of secondary pollutants (e.g. O_3 or SOA).

In clean ,unpolluted environments the primary source of OH is the photolysis of ozone followed by a reaction with water (R1, R2, R3)[25].

$$O_3 + hv_{(\lambda<320nm)} \rightarrow O(\,^1D) + O_2 \text{ (R1)} \qquad \text{R(1)}$$

$$O(\,^1D) + H_2O \rightarrow 2OH \qquad \text{R(2)}$$

$$O(\,^1D) + H_2O \rightarrow 2OH \qquad \text{R(3)}$$

In more polluted atmospheres, OH is also produced, via the reaction of HO_2 with NO (R4) and following photolysis of HONO (R5). Ozonolysis reactions can also generate OH.

$$HO_2 + NO \rightarrow OH + NO_2 \qquad \text{R(4)}$$

$$HONO + hv_{(320nm<\lambda<400nm)} \rightarrow OH + NO \qquad \text{R(5)}$$

1.4 Nitrous Acid

HONO was first detected in the atmosphere in 1979 by Perner and Platt[26] using the DOAS technique, see section 3.1.1 . The group detected concentrations of ~0.8 ppb before sunrise in Jülich. In urban areas HONO is an early morning source of OH with the photolysis (R5)[27] of HONO. The concentration of HONO builds up overnight as the main loss pathways (photolysis and reaction with OH) switch off. The slow heterogeneous conversion of NO_2 to HONO on humid ground surfaces[28] contributes to HONO production overnight. HONO photolyses at longer wavelengths than O_3, meaning that it is photolysed earlier in the morning than ozone at higher solar zenith angles and can act as the dominant OH source at these times[29].

Atmospheric HONO can impact human health, HONO causes damage to the lungs and mucous membranes due to its acidity or it can combine with secondary amines either in the atmosphere or in-vivo producing nitrosamines which are carcinogenic[4].

High concentrations of HONO have been observed in urban locations throughout the day and current models are often unable predict these elevated concentrations[30, 31, 32, 33, 34] . A detailed chemistry box model based on the Master Chemical Mechanism v3.2 and constrained to data collected during the ClearfLo campaign in London[30], predicted a daytime HONO concentration close to 0 whilst the measured values reached ~0.4 ppbV. The base model only considered the gas-phase source of HONO from the reaction between OH and NO. The inclusion of additional HONO sources, including heterogeneous sources (discussed in section 1.5.3) (figure 1.4), improved the modelled to measured agreement for HONO.

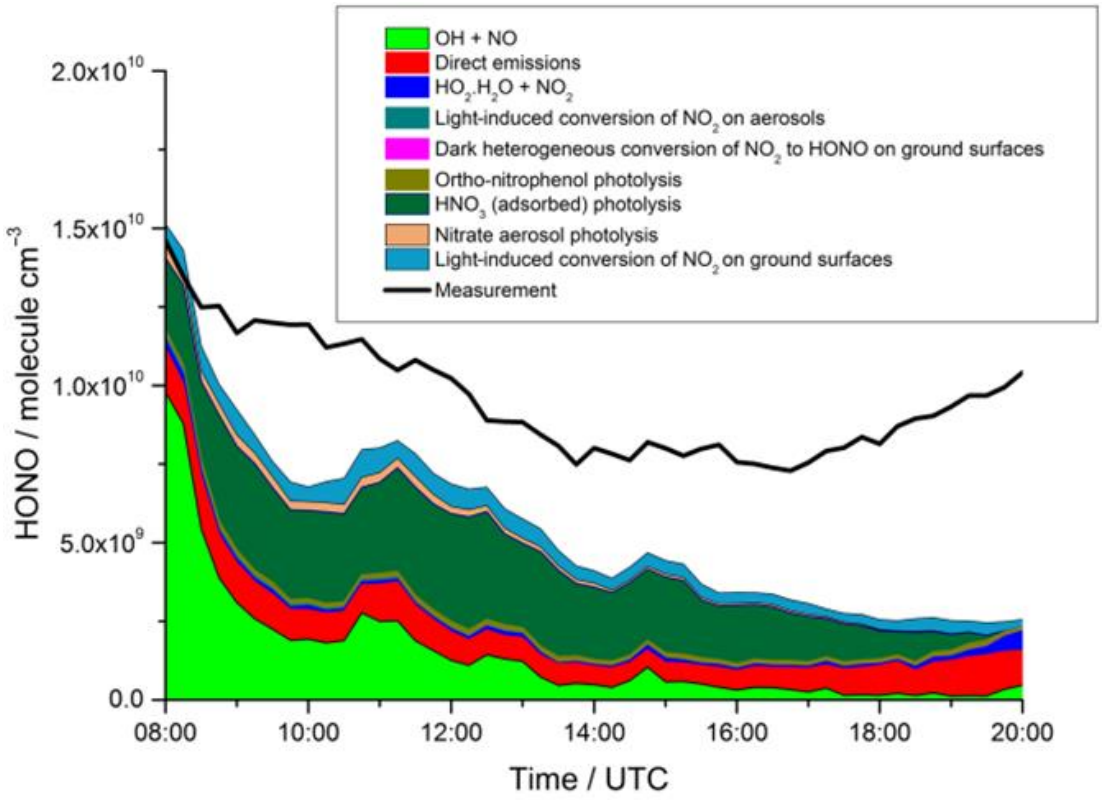

Figure 1.4. Modelled production rates of HONO from various sources compared to measured values (black line) showing the large gap in unknown sources of HONO during the day. This model was run using the master chemical mechanism (MCM). The proposed sources of HONO are discussed later in section 1.5.

HONO is primarily removed from the atmosphere during the day by photolysis. It can also be removed by reaction with OH[35] (R6).

$$OH + HONO \rightarrow H_2O + NO_2 \quad \text{R(6)}$$

During the day, HONO only has a lifetime of around 10 minutes at midday[35]. Daytime concentrations remain at around 100-300 parts per trillion (ppt) in urban areas and 10-200 ppt in rural areas[36] showing that there must be a source of HONO that is able to maintain these levels in balance with the removal of HONO[35].

Table 1.1 below gives a summary of HONO measurements across a range of different sites and the average day and night concentrations measured at each location. These results all show a similar trend, with HONO concentration peaking in the early morning before sunrise and reaching a minimum at solar noon. The only outlier are measurements made at Cape Verde were the HONO maximum was observed at solar noon[37]. This maxima was thought to relate to the photolysis of particulate nitrates acting as a source of HONO, discussed further in section 1.5.3. The NO produced from the photo dissociation of HONO is significant in clean environments where it will react with peroxy radicals to form NO_2[24] (R7). The NO_2 can then lead to the formation of ozone in the troposphere[38] (R8-9). This addition of NO_2 and O_3 to the remote atmosphere will contribute to the increase in their concentrations seen in background environments[39].

$$RO_2 + NO \rightarrow RO + NO_2 \quad \text{R(7)}$$

$$NO_2 + hv\ (\lambda < 420nm) \rightarrow NO + O \quad \text{R(8)}$$

$$O + O_2 + M \rightarrow O_3 + M \quad \text{R(9)}$$

Table 1.1. Field measurement data of HONO across and range of locations showing the average day and night concentrations

Site	*Date*	*Day (ppb)*	*Night (ppb)*	*Ref.*
IEECAS (Xi'an, China)	Jul.–Aug. 2015	0.51	1.57	Huanng et. al.[40]
ICCAS (Beijing, China) (Urban)	Dec 2016 (Haze)	4.6	1.4	Zhang et. al.[41]
ICCAS (Beijing, China) (Urban)	Dec 2016 (Severe Haze)	10.0	1.4	Zhang et. al.[41]
London, UK (Urban background)	Jul – Aug 2012	0.3-0.6	0.7-1.8	Lee et. al.[42]
Pearl River Delta, China (Rural)	July 2006	0.2	1.5	Li et. al.[33]
Jülich, Germany (Forest)	June-Aug 2003	0.04-0.3	0.5-2	Kleffmann et. al.[43]
Cape Verde Atmospheric Observatory (remote marine)	Nov – Dec 2015	0.0035	~0	Reed et. al.[37]

1.5 Sources of Nitrous Acid in the Troposphere

Various sources have been suggested for HONO involving both homogenous and heterogeneous (on surfaces and aerosols) reactions and also direct emissions.

1.5.1 Homogenous Reactions

The primary, well understood, homogenous source of HONO involves the reaction R10;

$$OH + NO + M \rightarrow HONO + M \qquad \text{R(10)}$$

This is primarily a daytime reaction, due to the requirement of OH[38] and occurs at a rate of approximately 9.7×10^{-12} cm^3 $molecule^{-1}$ s^{-1} (1 bar of N_2 at 300 K)[44]. If OH is present at night, for example through ozonolysis reactions or due to the oxidation of VOCs by NO_3[45] then reaction R10 could remain as a potential source of HONO during the night.

The photolysis of ortho-nitrophenols is a potential daytime gas-phase HONO source[46]. Ortho-nitrophenols form HONO by undergoing a proton transfer rearrangement to form a nitronic acid structure, and the dissociation of the nitro group, due to photolysis, will lead to the formation of HONO. Experimental estimations made by I. Bejan et. al. determined an atmospheric formation rate for HONO of 100 ppt h^{-1} from 1 ppb nitrophenol when $J(NO_2)$ is 10^{-2} s^{-1}.

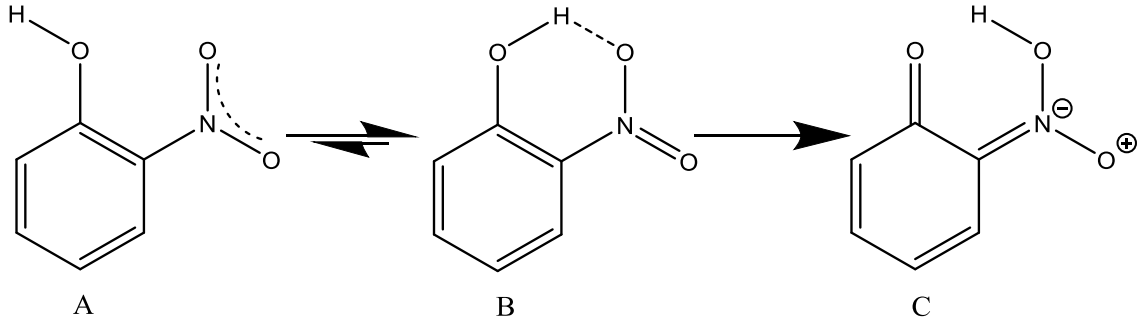

Figure 1.5. Reaction scheme showing the proton rearrangement of the nitrophenol (A) forming the nitronic acid (C). Scheme taken from reference [46].

Another recent formation mechanism involves the reaction between NO_2 and a $HO_2.(H_2O)$ complex[47] as a possible source of HONO with this complex reacting 3-4 times faster with NO_2 than HO_2 alone.

1.5.2 Direct Emissions

It has been found that HONO can be emitted directly into the atmosphere through a variety of combustion processes, for example, cars and power stations[48].

Measurements of car exhaust emissions have shown that older cars will generally emit higher concentrations of HONO than newer cars, with the presence of a catalytic converter significantly reducing the concentration to below detectable levels[49]. Tunnel studies have demonstrated that during periods of high traffic the concentration of HONO can increase to roughly 45 ppbv while decreasing to 10 ppbv during quiet periods[48]. This background level is still relatively high and they believed this to be caused by either NO_2 and water reacting on the tunnel walls, or the reduction of HNO_3 in the presence of VOCs emitted by the vehicles, either homogenously or heterogeneously as particles are co-emitted from motor vehicles[50]. Studies using a chassis dynamometer, rolling road, found that emissions had HONO/NO_x ratio of between 0.03-0.42 percent when simulating Beijing driving conditions[51].

1.5.3 Heterogeneous reactions

The heterogeneous formation of HONO involves the uptake of gas phase reactants, such as NO_2, onto either surfaces or aerosols.

The primary source for HONO at night involves the heterogeneous reaction of NO_2 with water on various surfaces which is why field campaigns observe a build-up of HONO through the night[35].

$$2NO_2 + H_2O_{(ads)} \xrightarrow{surface} HONO_{(g)} + HNO_{3(ads)} \quad \text{R(11)}$$

$$NO_2 + NO + H_2O \rightarrow 2HONO \quad \text{R(12)}$$

Of these two reactions the dominant pathway is R11, where HONO is released as a gas while HNO_3 remains adsorbed on the surface, while R12 has been shown to only be a significant source of HONO in areas of high pollution[52]. There have been several laboratory studies investigating light induced production of HONO following the uptake of NO_2 on to surfaces (coated-wall experiments) and on to aerosols of different composition in an attempt to explain the missing daytime HONO source. The study of heterogeneous production of HONO from aerosol surfaces remain relatively rare, however.

HONO production from humic acid particles and titanium dioxide (TiO_2) particles, which is a component of mineral dust have been reported in the literature. Various other studies have also shown that snow[53] and soot[54] surfaces enhance the production of HONO in the atmosphere under illuminated conditions.

1.5.3.1 Humic Acid

Humic acid is the most abundant group of organic compounds on the earth's surface, formed from the degradation of biological matter[55]. HONO production from surfaces of humic acid were discussed in a paper by Stemmler et al. (2006)[56]. By coating a wall in the flow tube with humic acid and flowing NO_2 across it they were able to estimate a light activated production of HONO. At 20ppb NO_2 and at solar irradiances between 300–700 nm of approximately 400 W m^{-2}, a HONO production rate of roughly 5×10^{10} molecule cm^{-2} s^{-1} and an uptake coefficient equal to 2×10^{-5} was reported. From this a HONO production rate of roughly 700 ppt hr^{-1} over the lowest 100 m of the atmosphere was calculated[57].

The pathways by which aerosols of humic acid are formed can be through either biomass burning or soil abrasion. In a later paper by Stemmler et al. (2007)[57] the production of HONO from humic acid aerosols was measured using an aerosol flow tube. From these experiments, an upper limit for the production of HONO of 1.2 ppt hr^{-1} (10 ppb NO_2) in rural environments and 17 ppt hr^{-1} (20 ppb NO_2) in urban environments (actinic flux= 17×10^{17} photons cm^{-2} s^{-1}, relative humidity between 20-60%, uptake coefficient of 3×10^{-6}) was calculated.

The suggested pathway through which HONO is formed on humic acid involves the photocatalytic production of a reductive species (A^{red}) which can then react with NO_2 to form HONO (R13-14).

$$HA \xrightarrow{hv} A^{red} + X^{ox} \qquad \text{R(13)}$$

$$A^{red} + NO_2 \rightarrow HONO \qquad \text{R(14)}$$

The photo-oxidant (X^{ox}) which also forms, was suggested as a side product (HA') that forms resulting in the competition reaction (R15) in order to explain why they observed a decrease in HONO production at higher light intensities.

$$A^{red} + X^{ox} \rightarrow HA' \qquad \text{R(15)}$$

1.5.3.2 Mineral Dust

Atmospheric mineral dust, fine particles of crustal origin carried from arid and semi-arid regions, is an important component in the troposphere[52] with 1000 to 3000 Tg being released into the atmosphere every year[58]. One component of mineral dust is TiO_2 which is known to act as a photo-catalyst for the degradation of organic molecules into carbon dioxide and water[52]. The photo-catalytic nature of TiO_2 has motivated a number of studies investigating TiO_2 aerosol as a potential source of HONO following the uptake of NO_2. Dupart et al.[58] identified HONO as a product from the reaction between TiO_2 aerosol and NO_2 when exposed to light. They proposed that this reaction is activated by the formation of electron-hole pairs (e_{cb}^- and h_{vb}^+) with an electron in the conduction band, which initiates reduction, and a valence band hole, which will initiate oxidation[59]. This can then cause the following set of surface reactions[58], leading to the formation of HONO;

$$Dust(TiO_2) + hv \rightarrow h_{vb}^+ + e_{cb}^- \quad \text{R(16)}$$

$$h_{vb}^+ + H_2O \rightarrow OH + H^+ \quad \text{R(17)}$$

$$NO_2 + OH \rightarrow HNO_3 \quad \text{R(18)}$$

$$e_{cb}^- + O_2 \rightarrow O_2^- \quad \text{R(19)}$$

$$NO_2 + O_2^-(or\ e_{cb}^-) \rightarrow NO_2^- + O_2 \quad \text{R(20)}$$

$$NO_2^- + H^+ \rightarrow HONO \quad \text{R(21)}$$

1.5.3.3 Particulate Nitrate

Nitric acid, HNO_3, is formed in the atmosphere primarily through the oxidation of NO_2 by OH, R22, with other formation routes also including N_2O_5 hydrolysis, and the NO_3 reactions with dimethylsulfide or hydrocarbons. Global yields for these routes are 76%, 18% and 4% respectively[60].

$$NO_2 + OH \rightarrow HNO_3 \qquad \text{R(22)}$$

The formation of nitrate aerosols from N_2O_5 involves the reaction of N_2O_5 with water on surfaces via reactions 23-25[61]

$$N_2O_{5(g)} + H_2O_{(l)} \rightarrow 2HNO_{3(aq)} \qquad \text{R(23)}$$

$$NO_2 + O_3 \rightarrow NO_3 + O_2 \qquad \text{R(24)}$$

$$NO_3 + NO_2 \rightleftharpoons N_2O_5 \qquad \text{R(25)}$$

N_2O_5 is formed via the reaction of NO_2, first with O_3 and then the NO_3 product from this reaction. N_2O_5 is thermally unstable, reforming NO_2 and NO_3 so the formation of N_2O_5 primarily occurs at night when temperatures are low and photolysis of NO_2 and O_3 does not occur.

Figure 1.6 shows the global distribution of nitrate aerosols at two times of the year. Nitrate aerosols peak in winter where the fine mode nitrate, diameters smaller than 1.25 µm, is form primarily through the hydrolysis of N_2O_5 on surfaces as there is less thermal and photolytic decomposition of N_2O_5 in the winter months. The formation of coarse mode nitrate, diameters greater than 1.25 µm, in Africa has been attributed to biomass burning. While in the summer there is a minimum due to the generation of sulphate aerosols, via the oxidation of SO_2, which ammonia preferentially reacts with reducing the nitrate aerosol concentration[62].

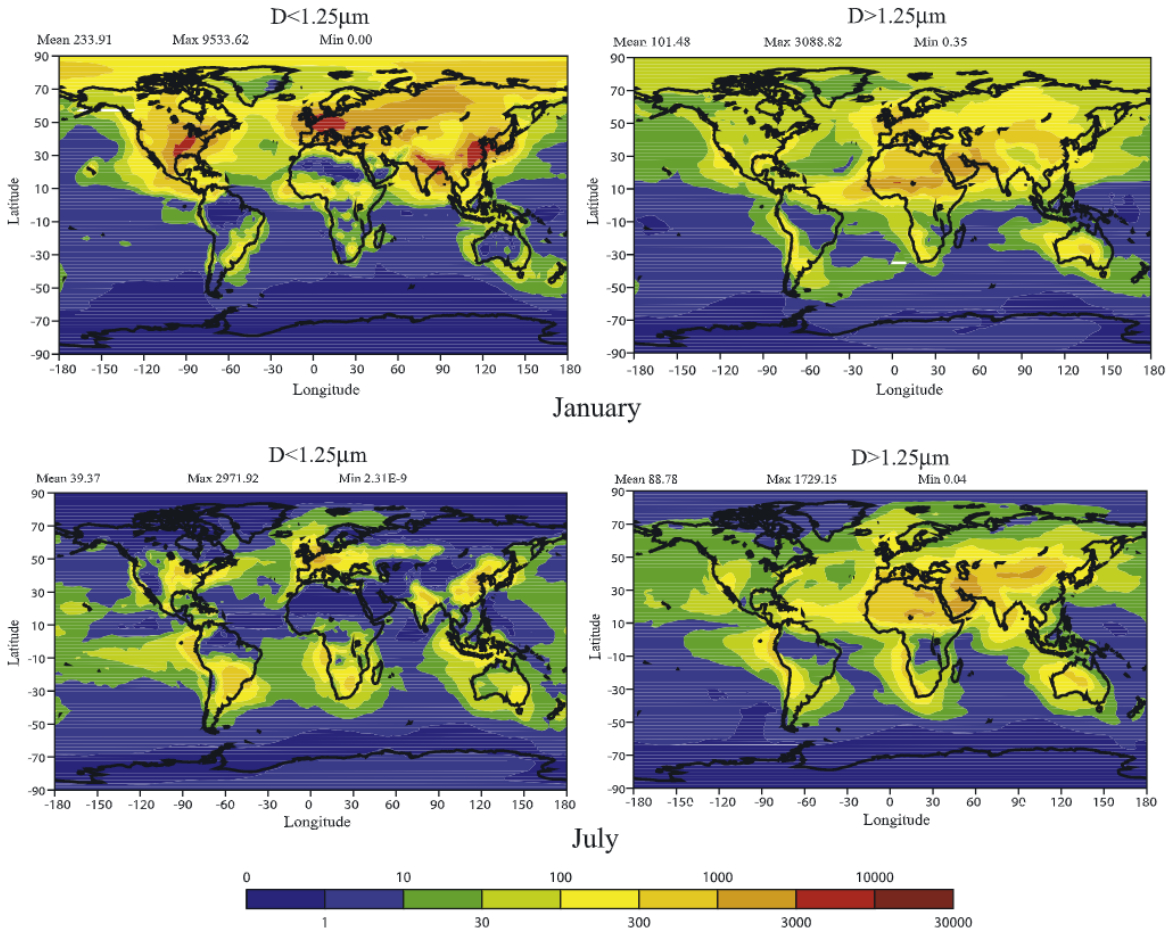

Figure 1.6. Monthly predicted mixing nitrate aerosols near the surface for January (top) and July (bottom)[62]. Broken down into fine (diameter <1.25µm, left) and coarse (diameter >1.25µm, right) aerosol modes.

Nitrate formation in the atmosphere is generally considered a sink for reactive nitrogen as HNO_3 only photolyses slowly at a rate of 7×10^{-7} s^{-1} in the gas phase[63]. Reactions with water droplets and aerosols leads to the formation of particulate nitrate in the atmosphere, this wet deposition is considered the primary loss route of HNO_3 from the atmosphere[64]. Studies by C. Ye et. al.[63] of particulate nitrate aerosols collected on filter samples demonstrated HONO and NO_2 production when exposed to UV, as shown in figure 1.7, with production rates increasing with nitrate loading. The production rate was variable depending on the location where the aerosols were collected with a rate of 6.2×10^{-6} s^{-1} for a winter urban environment and 5.0×10^{-7} s^{-1} for a summer rural environment.

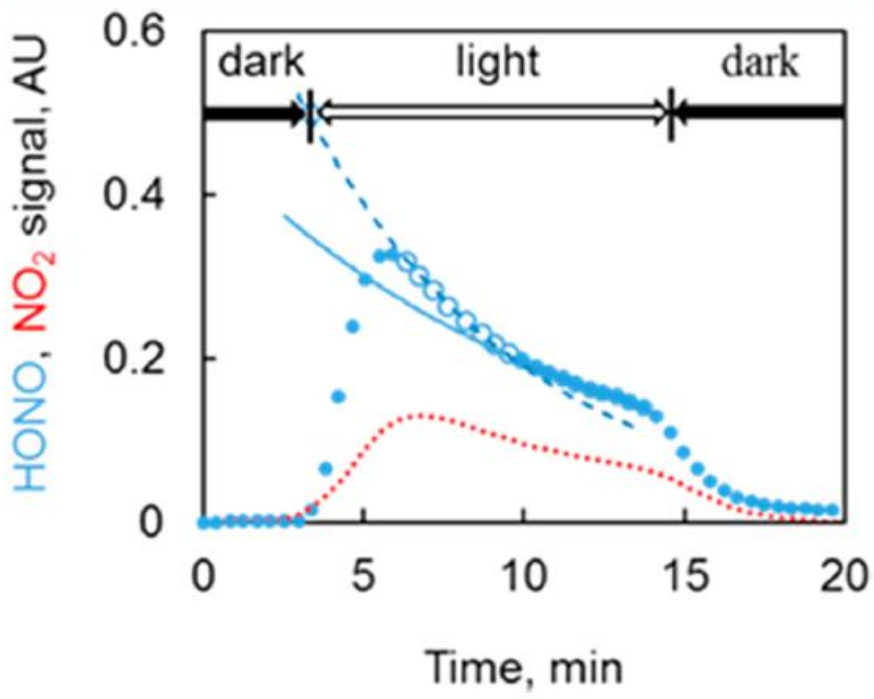

Figure 1.7. HONO and NO_2 production from filter samples containing nitrates. Plot taken from reference [63].

Measurements of HONO in Cape Verde, a remote marine boundary layer location, showed a daytime peak of 3.5 pptV hinting at a potential photolytic source. A box modelling studies by C. Ye et. al.[65] and C. Reed et. al.[37] using a photolysis rate for particulate nitrate that is 10× higher than gas phase nitrate, was able to replicate these measured HONO concentrations[37]. This generation of HONO from a nitrates is significant as it is a renoxification route in remote environments where NO_x concentrations are small.

1.5.4 Experimental parameters affecting HONO production rates

Relative humidity and aerosol acidity have been identified in both the TiO_2 and the humic acid aerosol experiments as experimental parameters which can affect the rate of HONO production.

1.5.4.1 Impact of RH

The relative humidity can impact the production of HONO from both aerosol and coated wall surfaces. For TiO_2, peak HONO production was observed at humidity's around 20% with production dropping as the humidity was systematically increased or decreased from 20%[52, 66]. This trend is likely due to TiO_2 being hydrophilic so it attracts the water readily, yet when the water content is high it will compete with NO_2 for the sites on the aerosol surface[52]. At lower RHs the reaction is limited by the availability of water, which is required in the production of HONO (R17 and R21) where it is oxidised to generate H^+ ions which reacted with the reduced NO_2^-.

In experiments conducted on humic acid surfaces, of the production of HONO was insensitive to RH until high humidities were reached (>60%). At high RH humic acid aerosol may have dissolved into the water[57], removing the reactive surface. The effect on the NO_2 uptake onto the humic acid aerosols as a function of RH in shown below in figures 1.8 and 1.9.

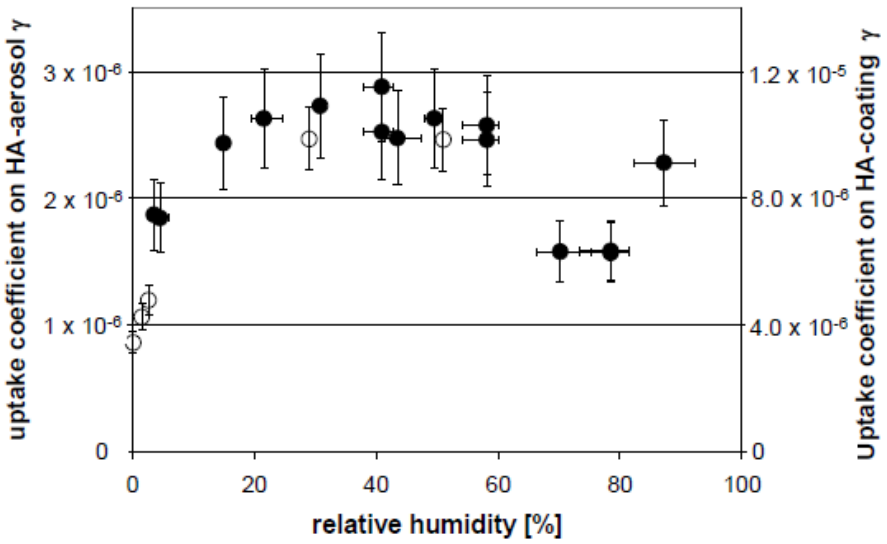

Figure 1.8. The effect of increasing humidity on the uptake of NO_2 onto humic acid aerosols (filled circles) and surfaces (empty circles), taken from reference [57].

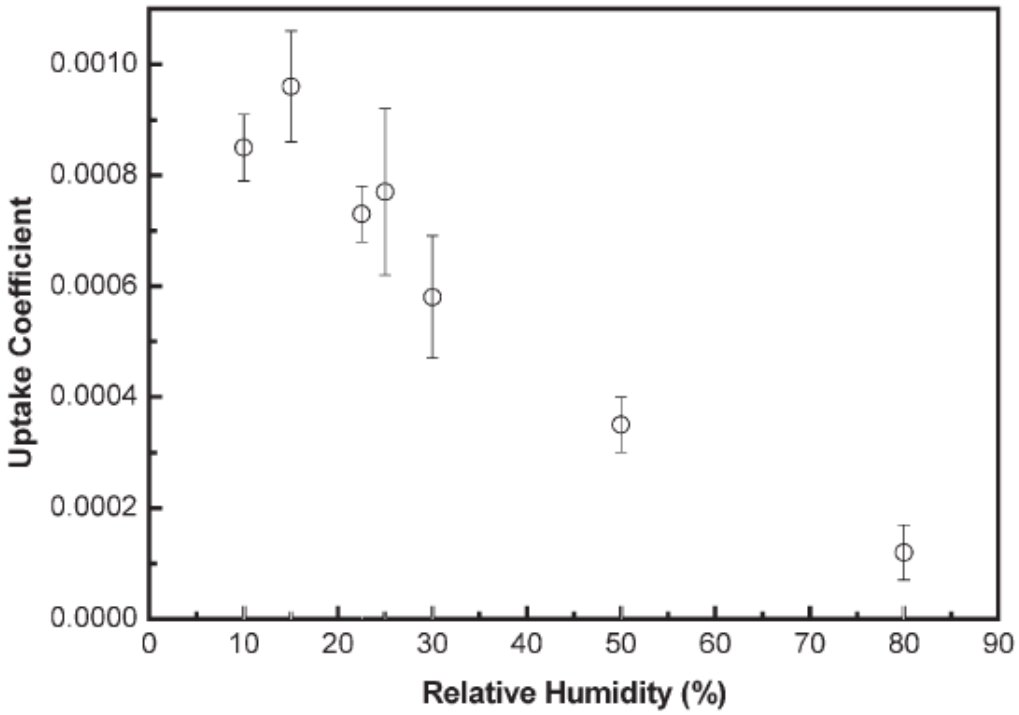

Figure 1.9. The effect of increasing humidity on the uptake of NO_2 onto TiO_2 aerosols, taken from reference 33.

1.5.4.2 Impact of pH

For humic acid aerosols, increasing the pH was found to reduce the amount of HONO produced withhout significantly effecting the removal of NO_2 from the system, under illuminated conditions[57]. The more basic aerosols appeared to show a greater uptake of the NO_2 in the dark with an enhancement of dark HONO production at pH 7.5. This can be seen in figure 1.10 below where the black points, representing HONO production, decreases as the aerosols becomes more basic while the empty circles represent the amount of NO_2 removed from the air.

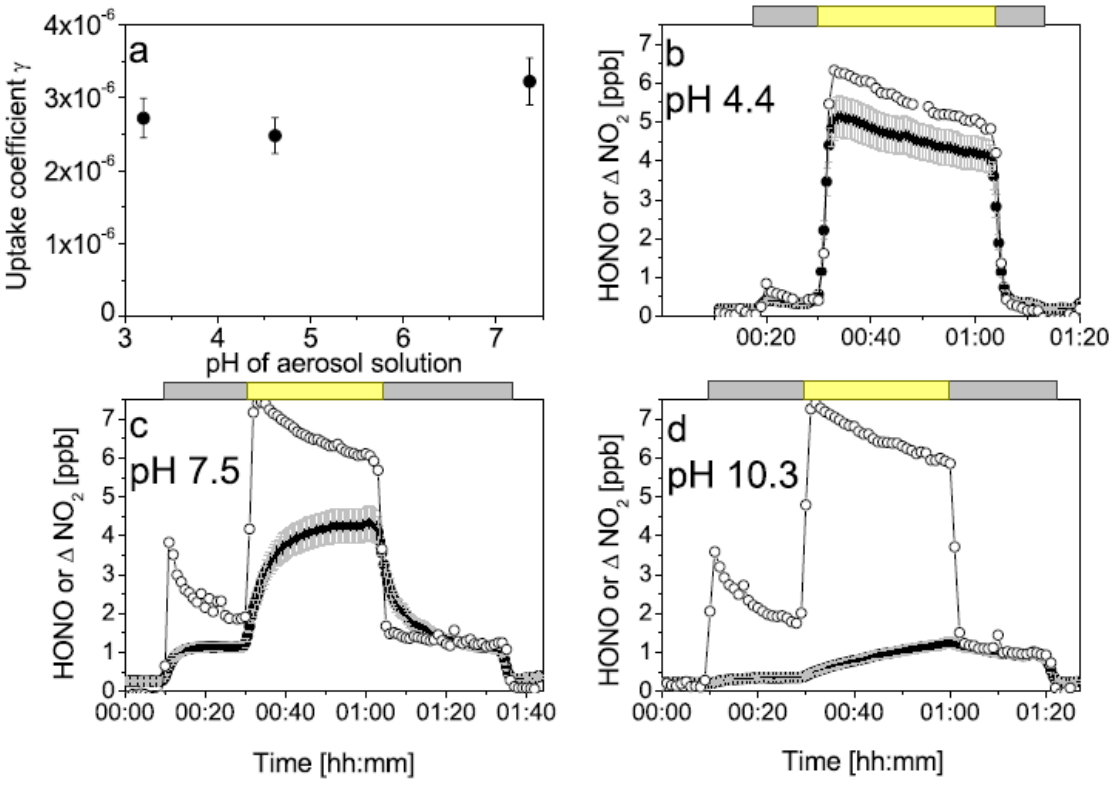

Figure 1.10. The formation of HONO (filled circles) and removal of NO_2 (empty circles) on humic acid coatings and various pH and the NO_2 uptake coefficients at various pH values. The bar above plots b, c and d represent when the coatings were exposed to light (yellow) and were in the dark (grey). Figure taken from reference [57]**.**

The effect of pH on the reactions on TiO_2 can be seen by comparing the experiments invovling the mineral dust by Y. Dupart et al.[58] to a second project investigating the conversion of nitrogen oxides on photocatalytic dispersion paints[59] (S. Laufs et al.). HONO production was reported from the mineral dust, yet no gas phase HONO production was observed from the paint surfaces (pH 8-8.5). S. Laufs et al. proposed that this may be due to the surface reaction below (R 26) which under acidic conditions will be shifted towards the left but under basic conditions will favour the right[59], after which the NO_2^- will be oxidised by the electron hole to form NO_3^- (R 27). This will also explain why a reduced HONO production is observed at higher humidity's as the larger water concentration will also push the reaction to the right.

$$HONO + H_2O \rightleftharpoons NO_2^- + H_3O^+ \qquad \text{R(26)}$$

$$NO_2^- + 2h^+ + H_2O \rightarrow NO_3^- + 2H^+ \qquad \text{R(27)}$$

1.5.5 Aerosol Chemistry

1.5.5.1 Liquid Aerosols

Aqueous aerosols are important for heterogeneous chemistry as they generally result in higher uptake rates than dry aerosols. The overall volume of aerosols in the aqueous phase is small, however the collision rate of gas phase species with condensed phase aerosols is relatively rapid. In polluted atmospheres a gas phase molecule will undergoes a collision with an aqueous phase aerosol every few minutes[67].

The resistor model, described by equation 1 is used to describe reaction involving uptake onto liquid aerosols. The model is compared to the principle of operation of an electrical circuit with the movement of species within the liquid bulk in terms of their conductance (Γ) and normalised to the rate of gas-surface collisions [68]. The steps considered in this model are;

1. Gas phase transport to the aerosol surface.
2. Accommodation at the aerosol surface.
3. Diffusion in and out of the aerosol.
4. Chemical reaction.
5. Desorption from the surface.

$$\frac{1}{\gamma} = \frac{1}{\Gamma_{gas\ diff}} + \frac{1}{\alpha} + \frac{1}{\Gamma_{sol} + \Gamma_{rxn}} \qquad \text{Eq(1)}$$

$\Gamma_{gas\ diff}$ is the conductance associated with gas-phase diffusion to the surface of the aerosol, Γ_{sol} is the conductance associated with solubility, Γ_{rxn} is the conductance associated with the reaction in the aqueous bulk, γ is the uptake coefficient and α is the mass accommodation coefficient.

The first step of the process of heterogeneous uptake involves diffusion of the gas phase molecule to the surface of the aerosol this is dependent on the gas phase diffusion and gas-surface collision frequency. This is process is characterised in the Resistance Model by $\Gamma_{gas\ diff}$.

Once a collision occurs the gas phase molecule will either “bounce” off the surface or be accommodated into the interface of aerosol. The fraction of gas phase molecules that are accommodated is a function of the viscosity of the

aerosol. The character of the interface of the aerosol is between the gas and bulk liquid phases and is only a few monolayers in thick. The fraction of gas phase molecules that are accommodated into the interface against the number of collisions with the surface, is defined by the mass accommodation coefficient (α).

From here most molecules diffuse into the bulk of the aerosol however surfactant type molecules preferentially adsorb to the interface rather than undergo diffusion into the bulk. The hydrophilic heads and hydrophobic tails of the surfactants make it less energetically favourable for these molecules to diffuse in the bulk where they would cause disruption to the hydrogen bond networks. Diffusion in the liquid bulk of the aerosol is characterised in the Resistance Model by Γ_{sol}.

Uptake of the gas-phase molecule by the aerosol can either lead to desorption back into the atmosphere, a non-reactive uptake, or a reaction within the bulk of the aerosol which leads to its destruction, a reactive uptake. Reactive uptake occurs when the rate of the reaction between the adsorbed species and bulk aerosol is faster than rate of uptake and diffusion. The conductance of reaction in the bulk, Γ_{rxn}. A non-reactive uptake occurs if the rate of reaction is slower than the rate of uptake and diffusion in the liquid, this process is expressed by equation …without Γ_{rxn} term.

1.5.5.2 Solid Aerosols

Two possible mechanisms have been developed to describe heterogeneous reactions on solid aerosol surfaces; the Eley-Reid (ER) and Langmuir-Hinshelwood (LH). The ER mechanism involves the adsorption of one gas phase molecule to the surface and a second molecule, still in the gas phase reacting with it. The LH involves the adsorption of both molecule to the surface where once they diffuse across the surface until they are in close enough proximity to react. The two reaction can be distinguished experimentally as the LH mechanism will reach a maximum rate as the concentration of the reactants is increased due to competition for binding sites at the surface, which is not observed in the ER mechanism. Figure 1.11 below shows how these two processes differ for a simplified reaction between two species.

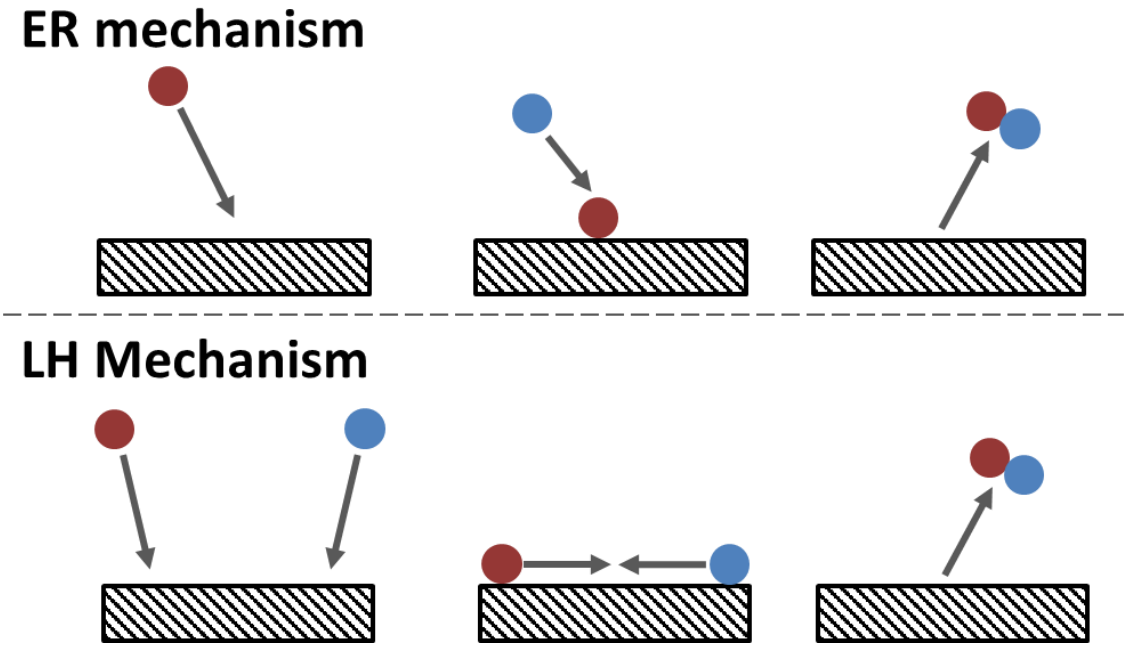

Figure 1.11. Diagram showing two possible reaction mechanisms for reaction between two molecules on a solid surface.

1.6 Project Aims

The aim of this project was to investigate missing heterogeneous sources of HONO in the atmosphere focussing on light-induced HONO production on the surfaces of aerosols. Initial work involved developing a photo-fragmentation laser induced fluorescence (PF-LIF) instrument to detect HONO. The instrument measures the resulting hydroxyl radical (OH) photo fragment produced following the photolysis of HONO using 355 nm laser light. To accomplish this the following steps were carried out;

1. A base FAGE cell was built as the basis of the HONO instrument.
2. Testing of two photolysis light sources, LED or laser, to determine the best choice.
3. Optimisation of experiment conditions to enhance the detection of HONO.
4. Develop a suitable gas phase calibration technique.

The FAGE method used as the basis of the HONO instrument is described in chapter 2, detailing the measurement technique and the calibration process currently used at the University of Leeds. Chapter 3 details the final HONO instrument and the optimisation steps investigated in its development.

Chapter 4 details the application of the newly developed HONO instrument in order to study heterogeneous production from aerosols. The chapter describes the following;

1. The coupling of the instrument to an aerosol flow tube.
2. Measurement of HONO production from illuminated TiO_2.
3. Measurement of HONO production from sodium and ammonium nitrate.
4. Use of experimental results in an atmospheric box model to assess the impact on daytime chemistry in Beijing.

The TiO_2 aerosol was chosen as it has been previously investigated for its ability to convert NO_2 to HONO under illuminated conditions. This allows the instrument to be tested using a system that is known to generate HONO and allow for comparison to previous results. Nitrate aerosols were investigated as they are a proposed source of HONO in the atmosphere and there are minimal studies investigating the potential contribution.

The final chapter covers the measurement of OH and HO_2 data collected during a chamber study at EUPHORE, Spain as part of the atmospheric chemistry project investigating the oxidation of carbon capture related amines. Chapter 2 details the experimental for this field work.

Chapter 2 The FAGE Technique

This section will describe how the hydroxyl radical (OH) is measured and will detail the method used at the University of Leeds to measure OH in both laboratory and field scenarios. This chapter serves as an introduction to chapter 3 (PF-LIF experimental chapter) because the development of the PF-LIF instrument for the measurement of HONO utilises the Fluorescence Assay by Gas Expansion (FAGE) technique for the measurement of the OH photo-fragment and is the basis for the PF-LIF instrument. This chapter also serves as the experimental section chapter 5 where the aircraft FAGE instrument[69] was used to measure OH and HO_2 during a chamber study at the EUPHORE chamber in Valencia.

Measurements of the OH radical in the atmosphere provide a good tracer for understanding the oxidation chemistry in the atmosphere. This is because as a radical the lifetime of OH is very short, less than 1 s, so its concentration is primarily dependent on the local chemistry rather than via transport effects. Hence, it is possible to use the agreement between measured OH and modelled OH, a good agreement shows that the chemistry is well understood while disagreements suggest a problem with the chemistry. Due to the short lifetime of OH, its concentration in the atmosphere is very low (10^6-10^7 maxima), therefore in order to detect it highly sensitive instruments are needed.

FAGE is currently the most common[70] method used to directly measure atmospheric OH both in the field and in atmospheric simulation chambers. Other methods used to measure OH include chemical ionisation mass spectrometry (CIMS) and differential optical absorption spectroscopy (DOAS, chamber only). A summary of all techniques and their sensitivity for detection, is shown in table 2.1. CIMS is an indirect method for OH detection where the OH is first chemically converted, by reaction with $^{34}SO_2$, to form sulphuric acid (H_2SO_4). The H_2SO_4 is converted to a HSO_4^- ion by reaction with NO_3^- (chemical ionisation), and the HSO_4^- ion is detected in the mass spectrum[71]. The DOAS technique is the only measurement of OH where a calibration is not required because it is an absorption technique. The DOAS technique uses a broadband laser, centred at

~308 nm wavelength that covers a range of OH rotational lines. OH is detected by measuring the absorption of light at these wavelengths, with the concentration calculated using the Beer-Lambert law. Currently the only DOAS instrument still used to measure OH is housed in the SAPHIR chamber in Julich, Germany[72]. An inter-comparison between this DOAS system and the Julich FAGE instrument in SAPHIR demonstrated good agreement between both techniques for a range of atmospheric conditions[73].

Table 2.1. Summary of atmospheric concentrations of OH and HO_2 measurement techniques.

Technique	Summary	Sensitivities	Reference
DOAS **Differential Optical Absorption Spectroscopy**	Utilises a laser light source at ~308 nm. Measures the absorption over a long path length. Currently not used in the field but used in the SAPHIR chamber (path length 2.24 km). Requires no calibration, however the long path lengths required requires a complex mirror setup.	**OH**: detection limit = 7.3×10^5 molecule cm^{-3} 100 s integration time. uncertainty = 6.5%	[73,74]
CIMS **Chemical Ionisation Mass Spectrometry**	Air is sampled into a reaction chamber where OH is converted to H_2SO_4 by reaction with $^{34}SO_2$. The H_2SO_4 is then converted to HSO_4^- ions, through reaction with NO_3^-, and detected via quadrupole mass spectrometry. HO_2 detection by conversion to OH through the reaction with NO.	**OH**: detection limit = 2×10^5 molecule cm^{-3} uncertainty = 25% **HO_2:** detection limit = 1×10^5 molecule cm^{-3} uncertainty = 30% 10 min integration time.	[71]
FAGE **Fluorescence assay by gas expansion**	A laser induced fluorescence technique. The OH molecule is selectively excited using a 308 nm laser with the resulting fluorescence being proportional to the [OH]. Possible to measure HO_2 through conversion to OH after reaction with NO. Non-absolute technique so requires calibration.	**OH**: detection limit = 7.1×10^5 molecule cm^{-3} 1 min integration time. uncertainty = 25% **HO_2:** detection limit = 7.5×10^5 molecule cm^{-3} 1 min integration time. uncertainty = 26%	[69, 75]

2.1 Principle of Operation

Measurement of OH in the atmosphere is challenging because of the low concentration of OH, with a daytime range[73] of 10^5 - 10^7 molecules cm^{-3}. Because of this, a sensitive and selective method is needed for an accurate detection. Fluorescence assay by gas expansion (FAGE) is one method that is used to detect OH in both the laboratory, atmospheric simulation chambers and in the atmosphere. The process involves using a laser, whose wavelength is tuned to a specific OH transition, to electronically excite ($X^2\pi\ \nu''=0 \leftarrow A^2\sum\ \nu'=0$) the OH molecule. The resulting fluorescence, that is emitted as OH relaxes back to the ground state via the same transition, is detected using a sensitive detector such as a photo-multiplier tube (PMT).

Using laser induced fluorescence (LIF) to measure atmospheric OH was first suggested in 1972[76]. This initial method used a wavelength of 282 nm as the excitation wavelength, however, it was soon found that by using this method introduced an interference to the technique, caused by the generation of OH from O_3 photolysis within the detection cell, and the wavelength was changed to use a wavelength of 308 nm wavelength. By utilising low pressure detection cells it is possible to further reduce the effect of interferences as the concentrations of O_3 and H_2O are reduced, this decreases the production of laser generated OH and secondary chemistry within the cell[77], while also reducing the quenching rate of OH. A high pulse repetition frequency laser is also used to further reduce the laser generated interference as there is less energy per pulse reducing the possibility of photolysis occurring[78]. By using these techniques to reduce the background it cancels out the loss of signal due to the reduction of the concentration of OH in the detection cell.

As shown below in figure 2.1, LIF operates by exciting the OH molecule from its ground state to an excited electronic state, with specific transitions occurring due to the transition to and from different rotation energy levels during this excitation. By using a laser it is possible to target a specific transition due to the laser's narrow spectral line width. The excited OH molecule will return to its ground state via several pathways[79]. It can be quenched back to its ground state, with no emission, due to transfer of energy through collisions with other molecules, such

as N_2 and O_2; this is reduced by decreasing the pressure in the detection cell.

The final transition that OH will undergo is fluorescence where the molecule returns to the ground state emitting the energy as a photon, which can be measured.

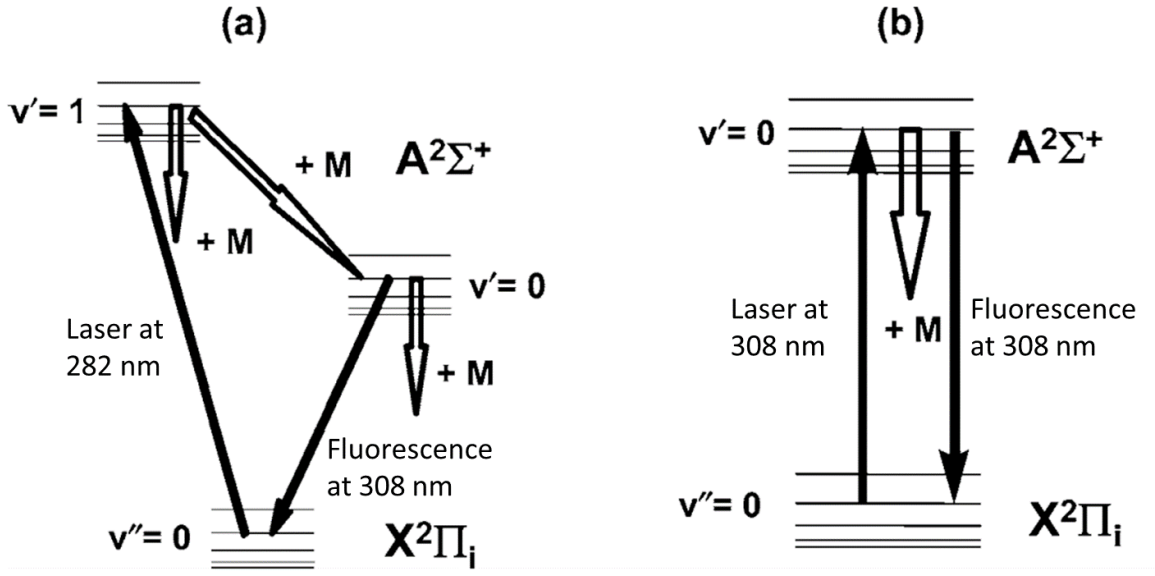

Figure 2.1. OH transitions which occur for both the on resonance (a) measurement using 282nm laser and the off resonance (b) measurements using the 308nm laser. Figure taken from reference [80]**.**

Two laser wavelengths have been used for the measurement of OH, one at 282 nm and the other at 308 nm. Using a 282 nm laser, involves exciting the OH molecule to an excited electronic state ($A^2\sum\ \nu'=1 \leftarrow X^2\pi\ \nu''=0$), OH then will then relax to a lower vibrational energy state ($A^2\sum\ \nu'=0 \leftarrow A^2\sum\ \nu'=1$) before it relaxes back to its ground state during which it fluoresces at 308nm ($X^2\pi\ \nu''=0 \leftarrow A^2\sum\ \nu'=0$). The advantage of the off resonance method is because it is easily possible to distinguish the laser scatter from the fluorescence signal using optical filters. The O_3 interference (R28, R29) this method suffers from limits its use to areas of very low humidity (e.g. stratosphere, Antarctica, laboratory studies).

$$O_3 + hv\,(282nm) \rightarrow O(\,^1D) + O_2 \qquad \text{R(28)}$$

$$O\,(\,^1D) + H_2O \rightarrow 2OH \qquad \text{R(29)}$$

Measurement of OH at 308 nm simply involves exciting the OH ($A^2\sum v'=0 \leftarrow X^2\pi v''=0$) after which it will relax with the fluorescence occurring at the same wavelength. This on resonance measurement requires a low pressure detection cell (~2 Torr or less) to extend the fluorescence lifetime of the OH molecule beyond the laser pulse separating the small fluorescence signal from the much larger laser scatter[80]. The absorption cross section of O_3 is also smaller at the 308 nm wavelength compared to 282 nm, so this interference has a negligible effect on the measured OH when using the on resonance method[80]. The on resonance method is predominantly used currently in the field.

2.2 The FAGE Instrument

The equipment used for the measurement of OH in the experiments described in chapters 3 and 5 is described below. It consists of the laser system, used to generate the 308 nm probe light, a detection cell, containing the detector used to measure the fluorescent signal, a reference cell, which provides an environment of high OH concentrations to allow the scanning of a reference spectrum. Lastly the data collection system, in which is a fast photon counters are used to monitor the fluorescent signal. Laser light is delivered to the cell via a fibre optic cable and data was collected using a PMS-400a counting card.

2.2.1 Laser System

Two laser systems were used in this project for the excitation of OH. The first is an Nd:YAG pumped Ti:Sapphire laser (Photonics Industries Inc), which was used in the detection of OH during the ACA campaign (chapter 5), and the second was a SIRAH dye laser system, which was used in the PF-LIF experiment described in chapters 3 and 4.

2.2.1.1 Laser system 1 - Nd:YAG pumped Ti:Sapphire laser

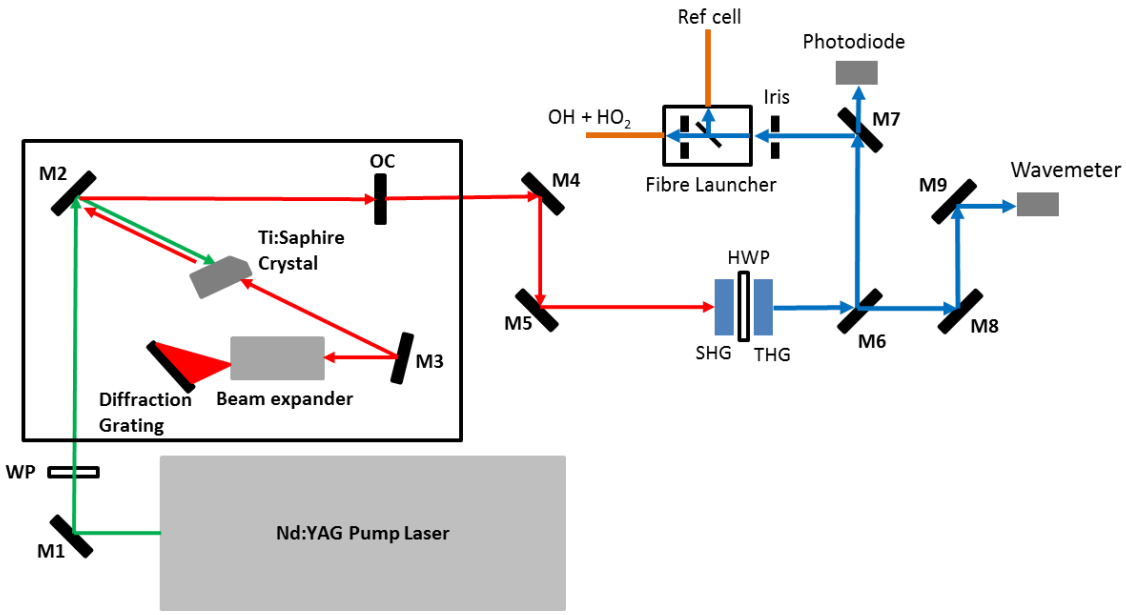

Figure 2.2. Diagram showing the laser system for the Leeds aircraft FAGE. M = mirror, WP = waveplate, OC = output coupler, SHG = second harmonic generator, THG = third harmonic generator. Green lines represent laser light at 532 nm, red lines represents light at 924 nm, blue lines represents light at 308 nm. The average power of each wavelength is approximately 10 W, 1 W and 20-40 mW respectfully.

The laser, which is shown in figure 2.2 above, is the Nd:YAG Ti:Sapphire system used to generate the pulsed 308 nm light (5 kHz pulse frequency) needed to measure OH during the ACA campaign, described in chapter 5. In this system laser light (532 nm) from the Nd:YAG is focused onto a Ti:Sapphire crystal. The crystal generates a broad range of light (700 nm to 1000 nm) which is passed through a prism and onto a diffraction grating. The incident angle of the light hitting the grating is controlled by rotating the grating with a stepper motor allowing for a precise selection of ~924 nm wavelength. The 924 nm light is then passed through a second harmonic generation crystal (SHG), LBO (Lithium

triborate), to generate light at 462 nm. This light then passes through a third harmonic generation crystal (THG), BBO (β-barium borate), which generates the 308 nm light by mixing the fundamental and second harmonic frequencies. Two small fractions (~1%) of the second harmonic blue light are focused onto a wavemeter, in order to monitor the wavelength, and a photodiode, to track the timing of the laser pulse. It is necessary to track the laser pulse timing because the exact laser trigger time varies slightly for each pulse, due to changes to the internal optics of the Nd:YAG (e.g. alignment or burns). By tracking the timing of the laser pulse relative to the initial trigger, factors dependent on the position, such as the collection of fluorescence, of the laser pulse can be time corrected. The 308 nm light is delivered to the detection cell and reference cell via a series of beam splitters, fibre launchers, and fibre optics (Oz optics). The 308 nm light is generated at a pulse repetition frequency of 5000 Hz and typical power of 5-10 mW (1-2 µJ per pulse).

2.2.1.2 Laser system 2 - SIRAH dye laser

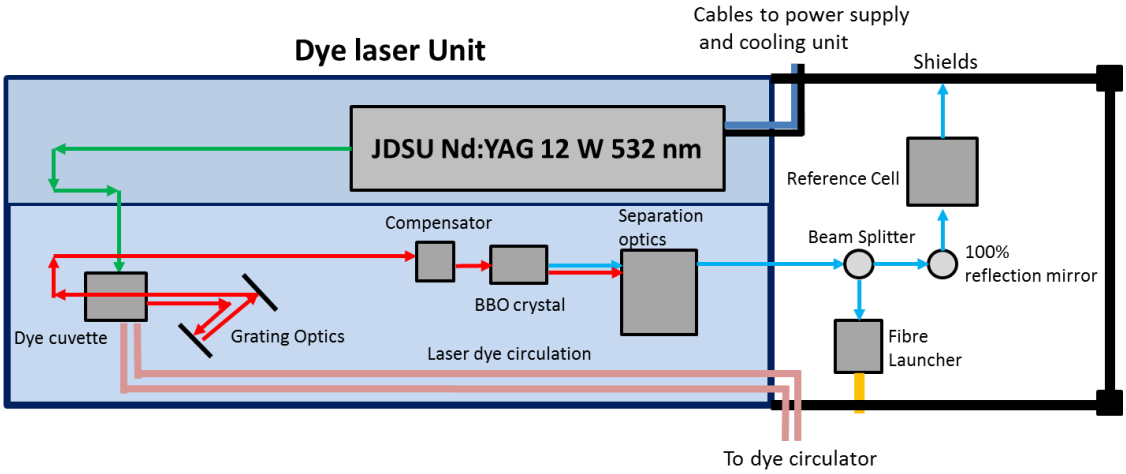

Figure 2.3. Dye laser system used in the PF-LIF setup.

For the measurement of OH using the PF-LIF instrument a SIRAH dye laser was used to generate the 308 nm light, figure 2.3. The system used in a JDSU Q201-HD Q-series Nd:YAG and a SIRAH Cobra Stretch dye laser. Laser light is generated by pumping a dye mix of Rhodamine B and Rhodamine 640 (0.15 g L^{-1} and 0.0375 g L^{-1} in methanol) using 532 nm light generated from the Nd:YAG laser.

The peak maximum power for the red shifted output is centred at ~616 nm with a single wavelength being enhanced by specific reflection from a grating that forms part of a laser cavity. The 616 nm light is then passed through a non-linear barium borate (BBO) crystal that frequency doubles the light to 308 nm. A Pellin Broca optic set is used to separate the 308 nm light from the remaining 616 nm light. After exiting the main laser system 90% of the 308 nm light is directed into a fibre launcher while the remaining light is passed through a reference cell. The 308 nm light is generated at a pulse frequency of 5000 Hz and typical power of 3 -10 mW.

2.2.2 Detection Cell

The detection cells used in the PF-LIF experiments and the ACA campaign both follow the same design as those used in the Leeds aircraft FAGE [69] instrument. This section will cover the design used during the ACA campaign with the design of the PF-LIF cell being described later in chapter 3, however the principle behind the measurement of OH remains the same for both instruments.

Air is sampled through a flat pinhole (0.7 mm diameter), 10 cm from the detection region. This *insitu* sampling is needed for the detection of OH as the radical will quickly be lost by collisions to the walls if a sampling line is used. The cell is evacuated to a pressure of ~2 Torr using a rotary pump (Edwards, model E1M80), super charger combination (Edwards, model EH1200). The low pressure is needed to allow the temporal separation of the fluorescent signal from the laser scatter. The pressure is monitored using a pressure gauge (MKS, 10 Torr baratron pressure transducer).

The gas that passes through the pinhole is accelerated by the pressure differential between atmospheric pressure and the pressure in the detection cell. The gas velocity after the pinhole will be close to the speed of sound and will form a rotationally cold jet. The gas in the jet is under expanded and so begins to rapidly expand to reach the background pressure of the detection cell, causing the jet to break down. The lifetime of the jet is determined using equation 2 that is dependent on the pressure differential and the pinhole diameter.

$$\left(\frac{x_m}{d}\right) = 0.67\left(\frac{P_0}{P_b}\right)^{1/2} \qquad \text{Eq(2)}$$

For the FAGE cell used in the HONO instrument and during the ACA campaign distance of the jet is approximately 2 mm. This is before the measurement region, HONO instrument = 60 mm and ACA instrument = 150 mm. This means that the laser in both instruments are sampling a region where the jet has broken down and the gas can now be considered well mixed across the cell. The temperature in this region is no longer rotationally cooled as it would be in the jet with experiments carried out by Creasey et. al.[81] showing that the gas has returned to approximately room temperature.

Figure 2.4 shows a cross section through the detection region. Laser light is delivered to the cell via a fibre optic cable connected to a fibre coupler connected to the cell entrance arm via a collimating unit. The light is delivered perpendicular to the air flow across the detection region and exits the cell through a 308 nm anti-reflective coated window on the opposite side. The detector is mounted perpendicular to both the laser beam and gas flow axes. A window coated for the transmission for 308 nm light separates the detector barrel from the low pressure cell. Any fluorescence that passes through the window will pass through an optics barrel which focuses the light onto the detector. The optics barrel also contains a Barr Associates filter that only allows the transmission of light at 308 nm (± 8 nm with approx. 50% transmission) in order to prevent room light reaching the detector. The light is focused onto a multi-channel plate (MCP) detector which outputs an electronic pulse when a photon makes contact with the detection plate. Opposite the detector barrel, a retro reflector mirror is positioned to increase the amount of fluorescence signal captured.

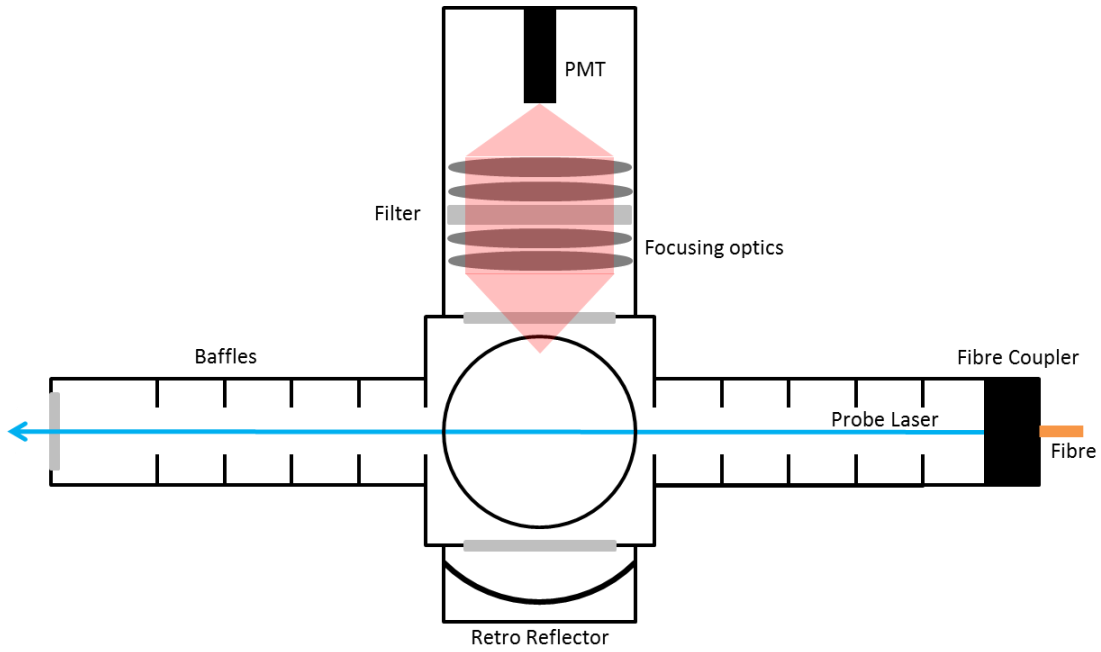

Figure 2.4. Cross section of the detection region in the FAGE cell. The air flow travels through the central region.

2.2.3 Reference Cell

In order to ensure that the laser wavelength is tuned to the peak of the OH transition a reference cell is used. The reference cell provides an environment with a constant amount of OH by flowing humidified air over a hot filament (0.2 mm diameter 80:20 NiChrome wire) and the thermolysis of the water generates the OH. By directing 5% of the laser light through the reference cell and measuring the fluorescence, using an ungated CPM with a 308 nm filter, allows the laser software to scan the online peak, the Q_1 (2) rotational peak is targeted (figure 2.5), so that on a second scan it can accurately find the point when the wavelength peak is at its maximum.

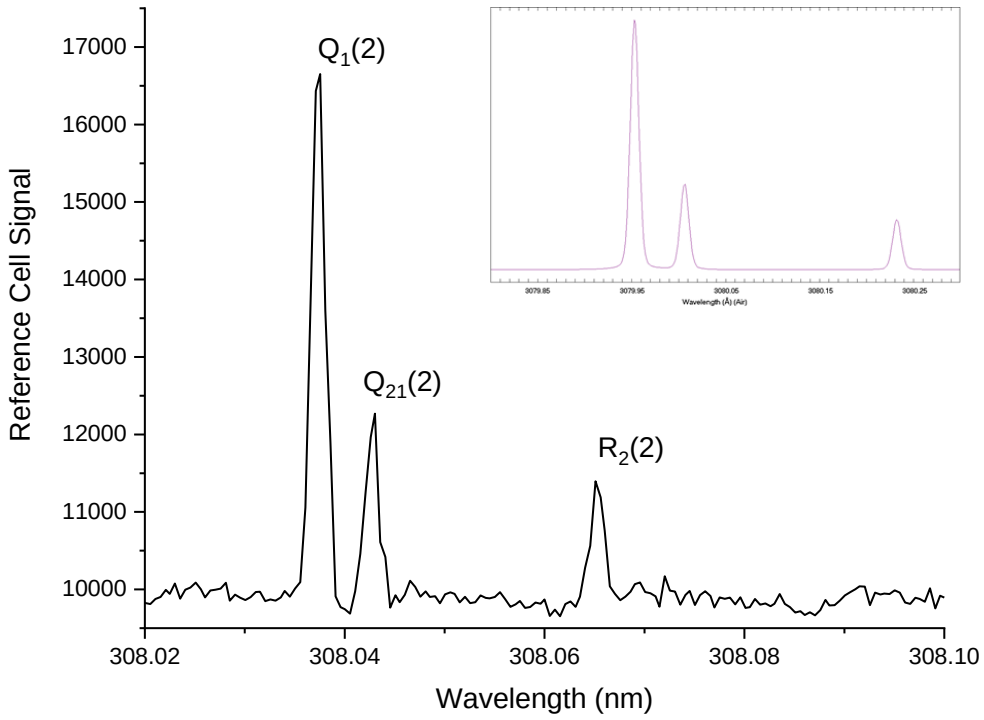

Figure 2.5. Measured OH fluorescence spectrum around the 308 nm wavelength showing three rotational lines with a spectrum simulated using LIFBASE inserted. The Q_1 (2) line is the transition targeted during measurements of OH in subsequent experiments.

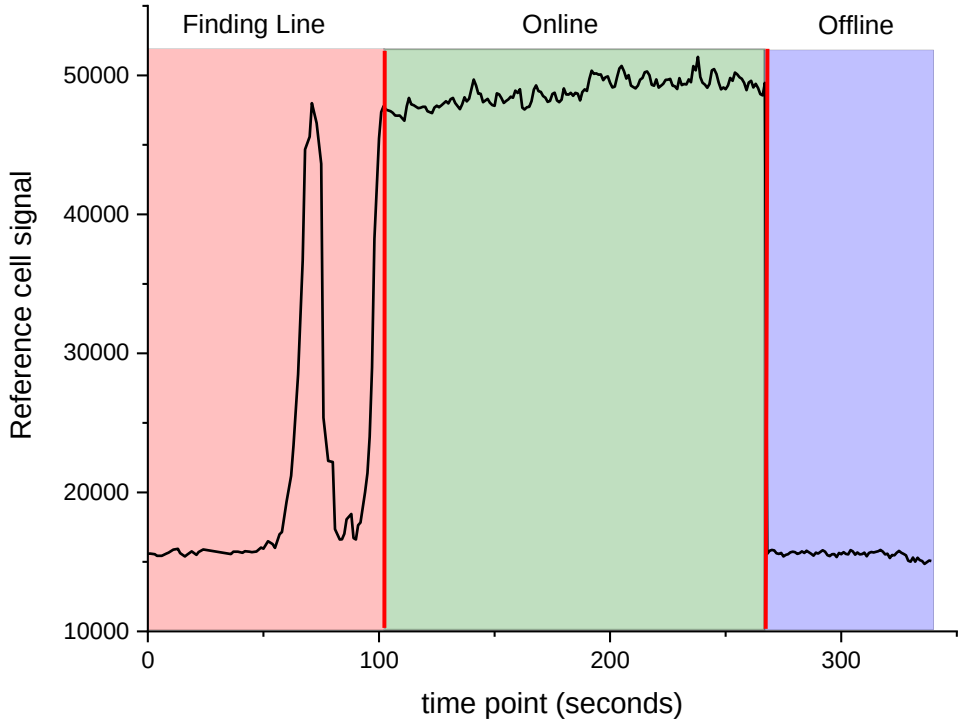

Figure 2.6. An example scan of a reference cell showing the initial scan across the peak Q_1 (2) (red), the online measurement (green) and the offline measurement (blue).

Figure 2.6 shows a single scan of the reference cell: the first section of the plot, 'finding the line', involves the software scanning the laser wavelength over a range that encompasses the transition to find the maximum. Figure 2.5 shows the OH absorption peaks around the 308 nm wavelength. The $Q_1(2)$ peak used represents a transition from the 2nd rotational energy level in the ground state to the same rotation level in the electronic excited state. The software return to a starting wavelength and rescans, stopping at the wavelength where the peak height is similar (within 95%) to the first scan. The laser will then stay on this wavelength, 'online', for a defined length of time to measure the OH signal. The laser will then move to 308.004 nm where OH does not absorb to measure the offline signal, this consists of signal generated by laser scatter.

2.2.4 Data Acquisition

This measurement method uses the on resonance method, where the laser and resulting fluorescence are both at a wavelength of 308 nm, gating of the MCP detector is required to minimise collection of the laser pulse and the resulting laser scatter signal from the fluorescence signal. Gating involves switching the detector to a low gain state during the laser pulse using a Photek gating box (GM10-50B), to prevent oversaturation of the detector, and it is then rapidly turned back to a high gain state to capture the fluorescence signal. The width of this low gain state is changed so that any residual laser scatter is minimised to an acceptable level, 1-2 counts s^{-1}, before it returns to a high gain state.

Figure 2.7 shows the relation between the laser pulse, fluorescence, and gating and data collection. The photon counters used are PMS-400A counting cards (Becker & Hickl GmbH), these count the output pulses from the MCP detector. The photon counter is turned on after the laser pulse in order to count the fluorescence signal, it is then turned off after 500 ns and then turned on again for 5 µs, 50 µs after the laser pulse, in order to collect a dark count signal, which represents the solar/room counts and detector dark counts. These background counts are divided by 10 (to correct for the different counting widths) and subtracted from the fluorescence signal in order to remove any signal due to room light that enter the cell through the pinhole. Electronic noise is minimised by disregarding any signal below a set voltage, a discriminator level.

The trigger for both the gate and the photon counting card is controlled by a BNC 555 delay generator which also define the t_0 position and trigger the laser.

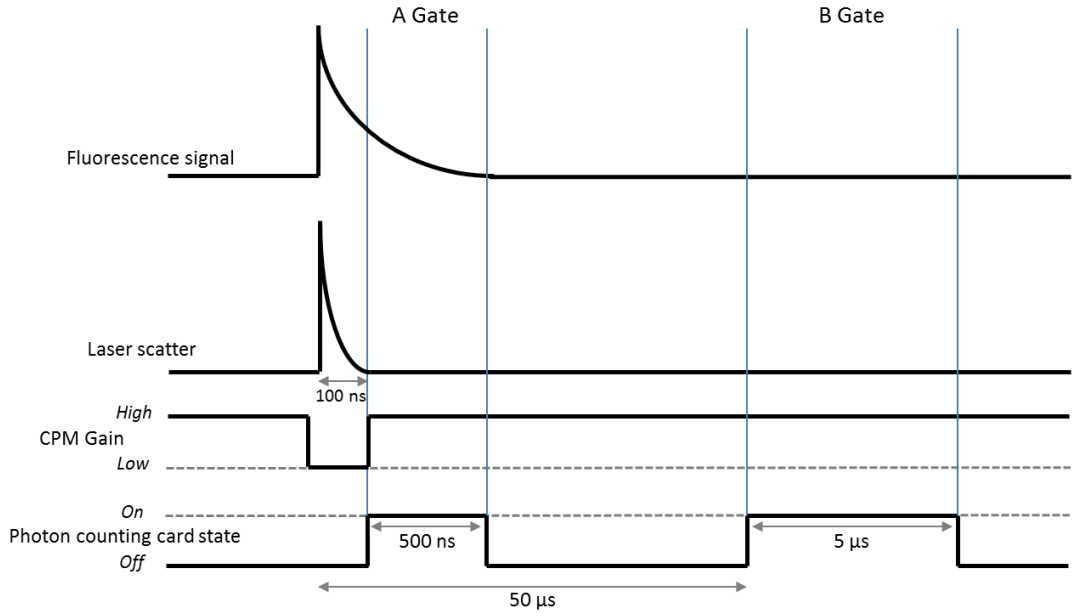

Figure 2.7. Timing diagram representation of the fluorescence and laser scatter signal and the CPM and counting card switching pulses.

Data collected, is integrated over a one second period, which will consist of 5000 laser pulses. The OH signal is determined using the following equation:

$$OH\ signal = OH_{sigA} - \frac{OH_{sigB}}{x} \qquad \text{Eq(3)}$$

where OH_{sigA} and OH_{sigB} are the accumulated counts in the A and B gates respectively, x (= 10) is the difference in width between the A and B gates and OH signal is the fluorescence signal and laser scatter signal. During a standard measurement, the instrument will initially scan the OH transition to find the maximum signal. Once online, the instrument will remain at that wavelength for the time set for that experiment. Once the allotted online time has been reached the software will scan the laser to a wavelength position where OH does not absorb, 'offline', to provide a background measurement of the 308 laser scatter that is present during the A gate – this is then subtracted from the OH signal determined in Eq 3. As the amount of fluorescence is linearly dependent on the amount of laser light absorbed, i.e. a higher OH signal will be observed when the laser power is higher. To correct for changes in laser power, the signal is divided by the laser power at that time to normalise the signal.

To convert this signal to a concentration the following equation is used;

$$OH_{conc} = \left(\frac{OH_{on}}{LP_{on}} - \frac{OH_{off}}{LP_{off}}\right)/C_{OH} \quad \text{Eq(4)}$$

where OH_{conc} is the concentration of OH in molecule cm^{-3}, OH_{on} and OH_{off} (counts s^{-1}) are the online and offline signals respectively, LP_{on} and LP_{off} are the UV power of the online and offline signal (mW). C_{OH} is the sensitivity of the instrument (cts^{-1} mW^{-1} $molecule^{-1}$ cm^3) which is determined by calibration as explained in the following section.

2.3 Calibration

As the FAGE technique does not provide an absolute measurement, a calibration is required in order to relate the amount of fluorescence measured to a concentration. At Leeds this is done using a "Calibration wand" which produces OH and HO_2 in equal concentrations (R30 and 31) from the photolysis of water (in the presence of O_2) using light at 185 nm.

$$H_2O \xrightarrow{h\nu} OH + H \quad \text{R(30)}$$

$$H + O_2 + M \rightarrow HO_2 + M \quad \text{R(31)}$$

A diagram of the wand is shown in figure 2.8. A mercury pen ray lamp (LOT Oriel) is used to generate the 185 nm light, this is then collimated using multiple small tubes before it passes through a glass window to irradiate the gas flowing down the wand.

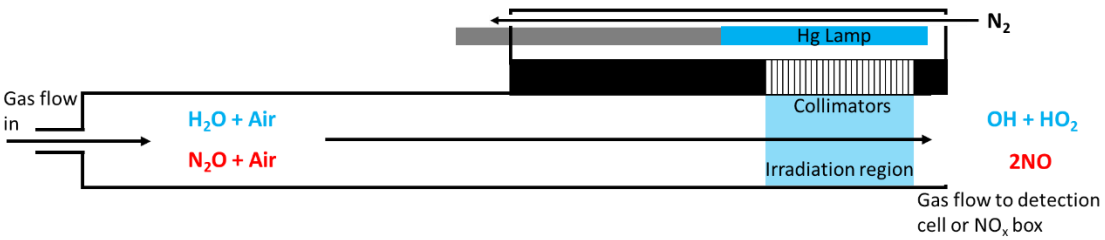

Figure 2.8. Cross section of the calibration wand used for the calibration of the FAGE cells for OH. The species in blue are for the calibration for OH/HO_2 and the species in red are for the N_2O actinometry experiments, see next section. The flow of nitrogen over the lamp is to both help cool the lamp and prevent the formation of ozone.

The amount of HO_x produced in the wand is calculated using equation 5;

$$[OH] = [HO_2] = [H_2O]\,\sigma_{H2O}\,\emptyset_{OH}\,F\,t \qquad \text{Eq(5)}$$

where $[H_2O]$ is the concentration of water in the gas flow, σ_{H2O} is the absorption cross section of H_2O at 185 nm (7.14×10^{-20} cm^2 molecule^{-1}), $\emptyset_{OH}$ (= 1) is the quantum yield of OH (and HO_2) for the photodissociation of H_2O at 185nm. *F* is the lamp flux, which can be changed by altering the lamp current, and *t* is the irradiation time. The product, F.t are calculated experimentally using N_2O actinometry, the process of which is discussed below in section 2.3.1.

The flow rate in the wand is held at 40 L min^{-1} so the air flow down the tube is turbulent. This ensures that the flow rate will be equal across the cross section of the wand, otherwise under laminar flow conditions it would be necessary to take into account that the air in the centre of the wand will flow faster that the air near the walls which would mean that each region would experience different irradiation times.

To calibrate, 40 SLM of zero air (BOC, BTCA 178) is humidified by flowing it through a water bubbler. The air is then flowed down the calibration wand, with a small flow (1 L min^{-1}) going to a chilled mirror hygrometer (Buck Research Instruments, CR-4) to measure the concentration of water vapour in the flow. The wand is positioned so that the air flow exiting overflows the pinhole at an angle of 45 degrees. The flow rate exiting the wand is significantly higher than the sampling rate of the instrument, this ensures that only the air from the wand is sampled and not the surrounding lab air. The gradient of a plot of the observed signal, normalised for laser power, (cts^{-1} mW^{-1}) against OH concentration (molecule cm^{-3}), determined by equation 3, provides the sensitivity. The sensitivity achieved for the detection cell used during the Valencia campaign was C_{OH} = 1.09 x 10^{-7} counts s^{-1} molecule-1 cm^3 mW^{-1}, see figure 2.9, and the sensitivity for the HONO cell was C_{OH} = 9.36 × 10^{-8} counts s^{-1} mW^{-1} molecule^{-1} cm^3 (MCP detector) and 5.79 × 10^{-9} counts s^{-1} mW^{-1} molecule^{-1} cm^3 (CPM detector), figure 2.10. Typical sensitivities achieved for other FAGE instruments in Leeds are ~1.7 x 10^{-7} counts s^{-1} mW^{-1} molecule^{-1} cm^3 for the container FAGE cell and 3.95 x 10^{-7} counts s^{-1} mW^{-1} molecule^{-1} cm^3 for the HO_2 uptake flow tube cell. This shows that the current set up for the HONO instrument is not as sensitive towards OH as the other FAGE instruments currently in use. The main

reason for the low sensitivity seen in the HONO cell is due to the pinhole design being optimised for the detection of HONO rather than OH.

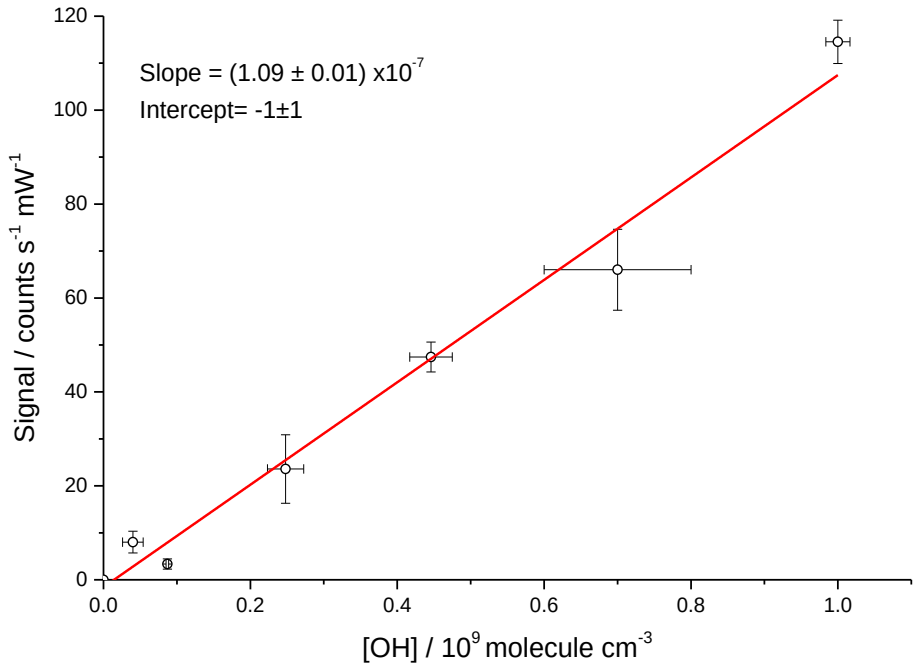

Figure 2.9. Results showing the OH sensitivity of the aircraft detection cell used during the Valencia campaign, allowing the calculation of the measured OH concentration from an observed number of counts per mW of laser power. MCP detector used. 2 % water.

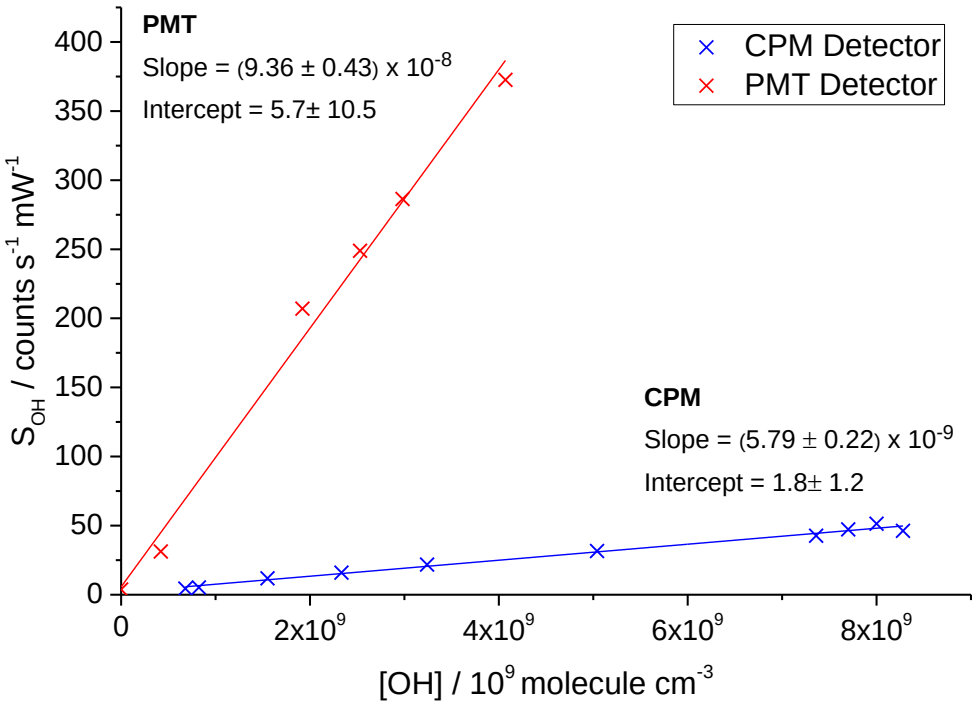

Figure 2.10. Results showing the difference in OH sensitivity for two different detectors used on the HONO detection cell (CPM and MCP). The significant increase in sensitivity is due to the MCP being a newer more efficient detector.

2.3.1 N_2O Actinometry

The product of the lamp flux (*F*) and the irradiation time (*t*) from equation 4 is determined using N_2O actinometry. N_2O and air are turbulently flowed through the calibration wand where the N_2O is photolysed to produce NO and $O(^1D)$ (R 32). The (O^1D) reacts with N_2O (and other species R 33, 34, 35) to form NO (R 36) which is measured using a NO_x analyser.

$$N_2O + h\nu \rightarrow N_2 + O(^1D) \quad \text{R(32)}$$

$$O(^1D) + O_2 \xrightarrow{k6} O(^3P) + O_2 \quad \text{R(33)}$$

$$O(^1D) + N_2 \xrightarrow{k7} O(^3P) + N_2 \quad \text{R(34)}$$

$$O(^1D) + N_2O \xrightarrow{k8} N_2 + O_2 \quad \text{R(35)}$$

$$O(^1D) + N_2O \xrightarrow{k9} 2NO \quad \text{R(36)}$$

Table 2.2. Rate constants for the quenching a reactions of $O(_1D)$ in the N_2O actinometry experiments.

Rate Constant	***Value at 298 K/ cm³ molecule⁻¹ s⁻¹***
k_6	3.95×10^{-11}
k_7	3.1×10^{-11}
k_8	4.95×10^{-11}
k_9	7.75×10^{-11}

The NO_x analyser (Thermo Electron Corp. 42C) is a chemiluminescence instrument and measures NO by measuring the light produced when NO is reacted with ozone to produce electronically excited NO_2 and oxygen. As the NO_2* decays to lower energy states it emits visible and near IR light which is detected by a PMT and a NO concentration determined. The NO_x box is first calibrated using known amounts of NO, from an NO standard. However, it is also necessary to do these calibrations at various concentrations of N_2O as the NO_2* can be collisionally quenched by the N_2O. This is done by mixing a flow of air and NO in various ratios to give different concentrations of NO which the NO_x analyser

samples directly from a sample line. 3 runs are done; one with no N_2O present and two with N_2O at 7 % and 14 %. The results from this are shown in figure 2.11. A decrease in the instrument sensitivity as the percentage of N_2O increases is observed demonstrating that the N_2O is an interference in the NO measurement.

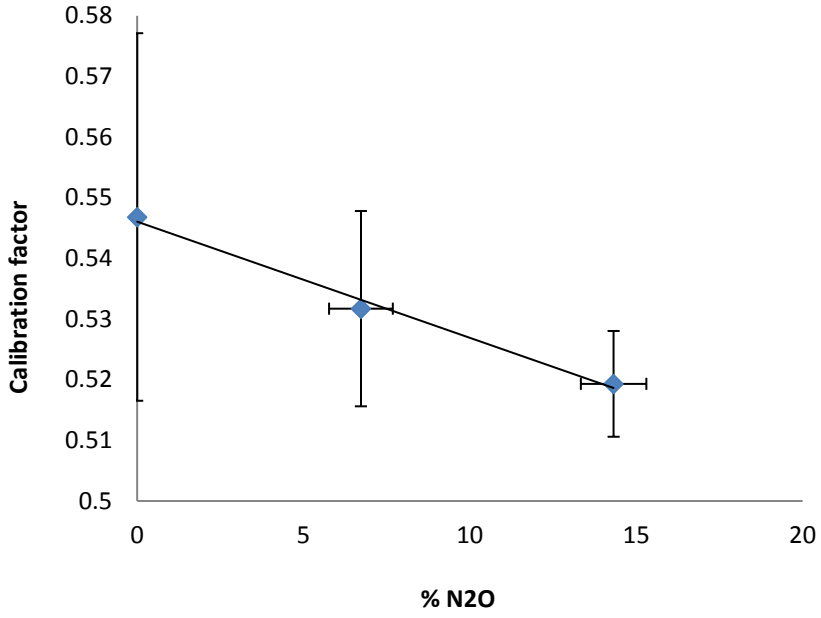

Figure 2.11. Plot showing results from the NO_x analyser showing the impact on the NO signal with increasing N_2O.

The actinometry experiment is then done by flowing a mixture of synthetic air (40 SLM) and N_2O (5 SLM) through the calibration wand. The output from the wand is sampled using the NO_x analyser with a sampling line placed in front of the exit of the wand. By altering the lamp current the amount of NO produced will change and by substituting the measured concentrations of NO using equation 6 it is possible to calculate the product *F* and *t*. See appendix A for how equation has been derived.

$$F\,t = \frac{[NO]\,(k_1\,[O_2] + k_2\,[N_2] + \,(k_3 + \,k_4)\,[N_2O])}{2k_4\,\sigma_{N2O}\,\emptyset_{NO}[N_2O]^2} \qquad \text{Eq(6)}$$

The value for *t* can then be calculated using the gas flow rates and the dimensions of the wand, which will remain constant throughout the experiment as only the lamp current is changed. The graph below shows the resulting plot of lamp flux against current. The gradient in this example is similar to previous actinometry experiments, using the same wand and lamp which were 7.53 x 10^{12} and 5 x 10^{12} photons cm^{-2} s^{-1} mA^{-1}, suggesting the lamp output has remained similar.

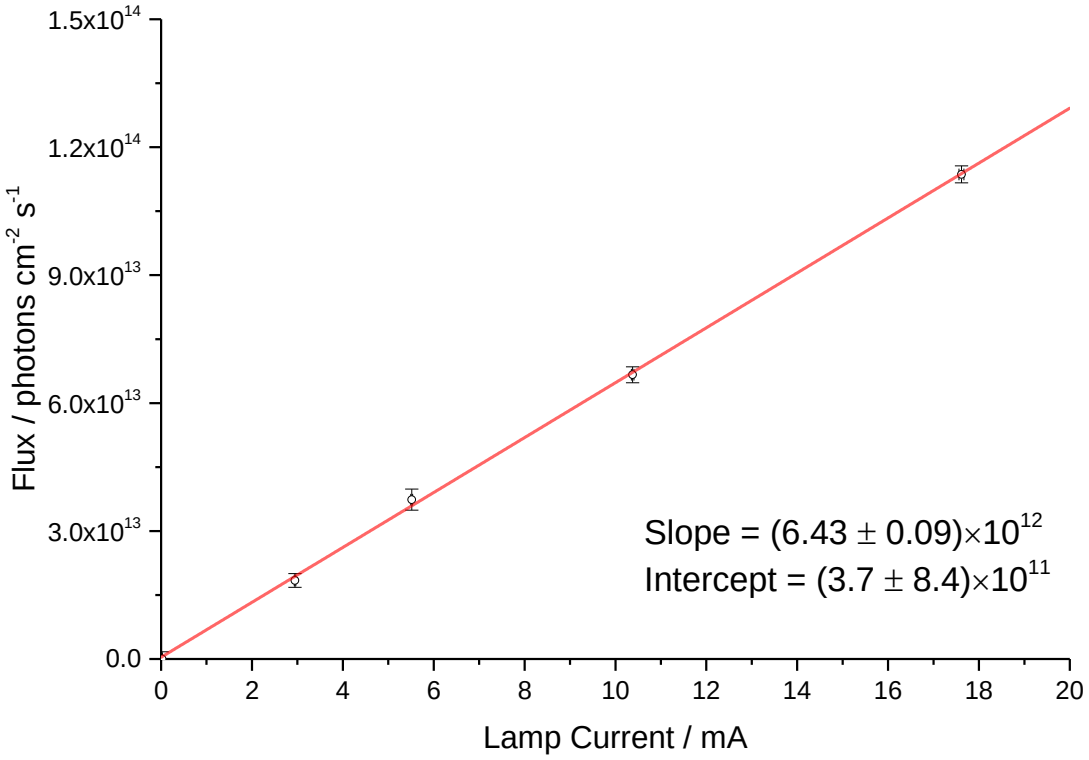

Figure 2.12. Actinometry plot of lamp flux vs lamp current. The gradient, (6.45±0.01) × 10^{12} photons cm^{-2} s^{-1} mA^{-1} can be used to calculate the lamp flux for a given lamp current to be used in equation 4.

2.3.2 Determination of calibration and measurement uncertainties

The uncertainty in the [OH] measurements is determined using the sum in quadrature of the fractional uncertainty in C_{OH}, the standard deviation of the online and offline OH signals, and the standard deviation of the laser power measurement in the OH cell. The uncertainty in the OH calibration coefficient is given by the standard error of the slope of the linear fit to the calibration data, figure2.9

The uncertainty in each point in the calibration plot is given by the sum in quadrature of the fractional uncertainties for each element in equation 5 For the calculated concentration, while the error in the fluorescence signal is determined from the standard deviation in the raw signal and laser power. Approximate uncertainty for these values is shown in table 2.3.

Table 2.3. Summary of the uncertainties that contribute to the accuracy of the OH calibration factor.

Term	***Value or range of values***	***Uncertainty***
$[H_2O]$	0.29–2.5 × 10^{17} molecule cm^{-3}	1 %
σ_{H2O}	7.14 × 10^{-20} cm^2 $molecule^{-1}$	2.8 %
ϕ_{OH}	1	negligible
F	0.0–1.5 × 10^{13} photon cm^{-2} s^{-1}	13 %
t	7.5 × 10^{-3}	1.3 %
Online wavelength position	~ 308 nm	5 %
OH LP	20–30 mW	8 %
Accuracy	16 %	
Precision	4 %	
Final Uncertainty	17 %	

The uncertainty in *t* stems from uncertainty in total flow rate and gas temperature. The uncertainty in laser power (OH LP) is determined from the calibration of the OH photodiodes across a range of laser powers. The uncertainty in the position of the online wavelength stems from procedure for finding the online wavelength, where the laser wavelength is scanned until the reference cell signal reaches 95 % of the maximum signal obtained when initially scanning over the OH rotational line (see section 2.4.2).

The largest uncertainty in the FAGE calibration comes from the determination of the lamp flux. This uncertainty is smaller than the true uncertainty when calculated for an individual lamp current, as it is determined using the standard error in the slope and intercept of the NO actinometry plot, shown in figure 2.12 Uncertainty in the NO actinometry points are determined in the following manner. The x error bars are the standard deviations of the lamp current during measurement period. The y error bars are calculated by propagating the uncertainties in each of the terms on the right hand side of equation 6, details of which are given in Table 2.4.

Table 2.4. Summary of uncertainties in the calculation of the lamp flux during the N2O actinometry experiments.

Parameter	*Uncertainty calculation*	*Uncertainty*	*References*
Flow rate	0.007 × flow rate + 0.002 × full range	1 %	Brooks Smart 5850S Manual
Temperature		1 %	
Pressure		1 %	
k_1	$1.1 \times exp\left\|10\left(\frac{1}{T}-\frac{1}{298}\right)\right\|$	10 %	Sander *et al.* (2011)
k_2	$1.1 \times exp\left\|10\left(\frac{1}{T}-\frac{1}{298}\right)\right\|$	10 %	Sander *et al.* (2011)
k_4	$1.1 \times exp\left\|10\left(\frac{1}{T}-\frac{1}{298}\right)\right\|$	10 %	Sander *et al.* (2011)
k_5	$1.1 \times exp\left\|10\left(\frac{1}{T}-\frac{1}{298}\right)\right\|$	10 %	Sander *et al.* (2011)
F		25 %	

2.3.3 Calculating a Limit of Detection

The FAGE limit of detection (LOD) for OH and HO_2 is commonly defined as the lowest concentration that can be reliably distinguished from the background noise for a given averaging period. It is determined from the instrument sensitivity and the variability (standard deviation) of the background signal using the following equation:

$$[OH]_{min} = \frac{SNR}{C_{OH} \times OHP_{on}} \sigma_{off} \sqrt{\frac{1}{m}+\frac{1}{n}} \qquad \text{Eq(7)}$$

where $[OH]_{min}$ is the minimum concentration of OH that can be detected, the limit of detection. SNR is the signal to noise ratio above which OH can be detected, C_{OH} is the calibration coefficient for OH, OHP_{on} is the online laser power, σ_{off} is the standard deviation of the background signal (laser scatter, room light and dark counts), *m* and *n* are the number of points measured both online and offline respectively. This equation, with substitution of C_{OH} for C_{HO2}, is also used for calculating the LOD for HO_2.

During the ACA campaign the average LOD was 1.01×10^7 molecule cm^{-3} for OH and 6.14×10^6 molecule cm^{-3} for HO_2 for 3 minute averages and a SNR of 1.

2.4 Summary

This chapter has described the fundamental principles behind the detection of OH and HO_2 radicals using laser induced fluorescence at low pressures, FAGE. The method operates by sampling gas into a low pressure cell and electronically exciting the OH molecule using a laser at the 308 nm wavelength. As the molecule of OH returns to its ground state it emits a photon of light, fluorescence, which can be detected. This fluorescence is proportional to the amount of OH and with calibration can be converted to a concentration. The technique described was used to measure the HO_x radicals during the ACA campaign at the EUPHORE chamber, which will be described in more detail in chapter 5. The instrument design also forms the basis for the development of the PF-LIF instrument used for the detection of HONO, which will now be described in the following chapter.

Chapter 3 Detection of HONO via PF-LIF

This chapter describes the nitrous acid (HONO) instrumentation used for measurement of HONO in the aerosol flow tube experiments that are described in chapter 4. The optimisation of the instrument to improve its sensitivity to HONO is described in section 3.5. In order to better explain the choice of instrument, a summary is given of previous detection methods that have been used to measure HONO both in the field and the lab.

3.1 Previous HONO instrumentation

This section will describe the different instrumentation used to measure HONO. The three most common methods used to detect HONO either in the field and/or in laboratory studies investigating the heterogeneous production of HONO will be described, with other methods summarised in table 3.1.

3.1.1 DOAS

Two types of differential optical absorption spectroscopy (DOAS) instruments have been used in the measurement of HONO; the long path DOAS (LP-DOAS) and the multi axis DOAS (MAX-DOAS) instruments. Both operate on the same principle, where the absorption by different species is measured between a broadband light source and a detector. For LP-DOAS the absorption area covers a distance between an artificial light source and a detector. The path length of the light will generally be several km in length and this can be achieved either by placing the light source and detector a set distance apart or through the use of mirrors to achieve multiple passes over a shorter distance. The light source will be a high powered lamp or laser that is able to generate a wide range of wavelengths. The light is then collimated into a parallel light beam and directed towards the detector. A spectrometer will generate an absorption spectrum and by using the known output from the lamp it is possible to determine concentrations of a range of species over the lights path after correcting for atmospheric effects[82].

MAX-DOAS uses scattered sunlight as the light source and is able to scan different angles from the vertical to determine concentrations at different altitudes[83]. The instruments consist of a light collector that focuses the light into a fibre optic that is connected to a spectrometer that is able to measure the intensity of light at different wavelengths. The absorption spectrum is converted to an integrated trace gas concentration along the path length of the light in the atmosphere by fitting a range of reference spectra to the initial measured spectra[84].

As an absorption technique DOAS does not require any calibration for individual species, but reference spectra are needed for interpretation of data. The main disadvantage in DOAS measurements is that the measured concentration is averaged over the entire path length making it difficult to identify local sources.

3.1.2 LOPAP

The long path absorption photometer, LOPAP, is a wet chemical technique used in the measurement of HONO that was developed in 2001 at the University of Wuppertal[85]. The instrument operates by collecting gas phase HONO into a liquid sample where it reacts to form a dye which can be analysed using an optical absorption method. The standard instrument consists of 3 stages, the first is the stripping coil where the HONO gas is collected into the liquid phase; a sulphanilamide in HCl solution. The liquid then enters the azo dye unit where n-(1-naphthyl) ethylenediamine-dihydrochloride solution is injected, this reacts with the sample to form an azo dye. The final stage is the detection unit where the azo dye is detected by measuring the absorption of visible light by the solution. This technique does suffer from interferences both known, such as NO_2, and unknown. To remove the interference, LOPAP instruments use two stripping coils in sequence. The first coil removes virtually all the HONO from the sampled gas along with a small percentage of the interfering species, the second coil will only sample the interfering species. It is then possible to subtract the interference signal leaving just the HONO signal. This method operate assuming only small fractions of the interfering sample is adsorbed by each coil, however if a species is absorbed efficiently or is present in small concentrations all the sample may be removed by the first coil causing an underestimation of the interference by the second coil.

Reaction in the liquid stage may also generate in interference with the reaction between oxidised hydrocarbons and NO_2[86]. Calibrations for the instrument are carried out using liquid nitrite standard.

The LOPAP instrument has been compared against a DOAS instrument in the EUPHORE chamber in Valencia[86] under a range of conditions. These experiments showed good agreements between the 2 instruments in the chamber, with the slope of 0.9987 for plots of LOPAP HONO vs DOAS HONO. During the FORMAT-1 field campaign in Milan in 2002, the data was more spread out from the chamber experiment, this was predicted to be caused by the greater heterogeneity seen in the atmosphere compared to a simulation chamber.

3.1.3 Detection using a NO_x analysers

It has been shown that both NO_2 and HONO are efficiently converted to NO by a molybdenum catalyst used in the NO_2 channel of NO_x chemiluminescent analysers. Owing to this, modifications have been made to standard NO_x analysers (e.g. TECO NOx boxes) to quantify HONO. The NO_x analysers are operated by sequentially removing HONO from the gas flow by passing or bypassing the flow through Na_2CO_3 denuders[52]. By comparing the concentrations when the sample flow is either bypassing the converter or passing through the denuder it is possible to calculate the HONO concentration.

Another NO_2 conversion method that can be employed for HONO detection is a differential photolysis technique where two UV LEDs of different wavelengths (385 nm and 395 nm) are used to illuminate a reaction chamber[87]. The wavelengths of the LED's are chosen so that one wavelength more efficiently photolyses HONO to NO than the other wavelength. Using the production ratios of NO by each lamp the ambient HONO concentration can be calculated.

Table 3.1 Summary of techniques used for the measurement of HONO.

Technique	Description	Detection Limit	Advantages	Disadvantages	Ref.
DOAS ***Differential optical absorption spectroscopy.***	Measures total absorption along a fixed path length, using and artificial light source.	84 ppt per 5 min	No calibration required. Allows measurement of many different species at once. Well developed	Difficult to site due to size of equipment and need for a long absorption path. Poor spatial resolution. Poor performance when visibility is poor.	[88], [89]
Denuder	HONO sampled on humid alkaline Na_2CO_3 surfaces as nitrite (NO_2^-), which is determined by ion chromatography after washing the denuder with pure water.	5 ppt per 30 min	High sensitivity possible	Low time resolution Time consuming off line analysis Interferences	[88], [90], [91]
PF-LIF ***Photo- fragmentation laser induce fluorescence.***	Section 3.2	15 ppt per min	Is highly selective and sensitive. Has very good time resolution. Has a background measurement close to zero.	Requires calibration using a known concentration.	[88]

MC/IC ***Mist chamber/ Ion Chromatography.***	A dense mist of ultra-pure water scavenges any soluble gas from the air. The droplets are then collected and analysed.	1 ppt per 30 min	High sensitivity.	Long integration time. Interferences from pernitric acid	[88], [92]
DNPH-HPLC ***2,4-dinitrophenylhydrazine derivatization and high-performance liquid chromatographic analysis.***	Derivatization nitrite with DNPH to form DNPA. DNPA is then separated from DNPH on a HPLC column and detected using a UV detector.	1-5 ppt per 5 min	High sensitivity.	Interferences from other nitrogen species. Interferences from carbonyl compounds, however these can be separated in the HPLC.	[88], [93]
LOPAP ***Long Path Absorption Photometer.***	HONO sampled by a fast, selective chemical reaction in a stripping coil, converted into an azo dye, which is detected in long path absorption spectrometer.	1 ppt per 5 min	Comparison with DOAS instrument shows good agreement.	Interferences need to be corrected for using a two channel design.	[88], [85, 86, 94, 95]
IBBCEAS ***Incoherent broadband cavity-enhanced absorption spectrometer***	Time integrated light intensity measurement of light leaking from a cavity between two highly reflective mirrors.	~100 ppt per 30 sec	No calibration required as it is an absorption technique. Single instrument can target multiple species	Overlap of other absorption cross sections. Difficulty detecting low concentrations	[96], [97]

3.2 Description of the PF-LIF instrument

The PF-LIF technique for the measurement of HONO operates by photolysing the HONO molecule to OH and NO after which either species (OH or NO) can be measured using, for example, laser induced fluorescence (LIF). Two examples of previous PF-LIF instruments that have been developed for the detection of HONO in the field have been reported in the literature. The Georgia Institute of Technology instrument[88] achieved a detection limit of 15 ppt for a 1 min integration time, while a more recent example has been developed by a group at Indiana University who have achieved a limit of detection (LOD) for HONO of 18 ppt for a 30 min average. These LODs demonstrate that this instrument type is able to achieve the desired sensitivity necessary for the experiments discussed in chapter 4, and, as demonstrated by the Georgia Tech instrument, a short (1 min) time resolution. Both instruments use a 355 nm laser to photolyse HONO and then measure the OH photo-fragment with a probe laser at 282 nm (Georgia Tech institute), or 308 nm (Indiana University). The two instruments use 5 kHz photolysis and probe lasers that are aligned collinearly across the cell. This differs from the Leeds design (see section 3.2.4) where the probe laser is run at 5 kHz but the photolysis laser runs at 10 Hz. The two lasers in the Leeds design are aligned perpendicular to each other.

3.2.1 Fragmenting HONO

The photolysis of HONO has been shown to have a near unity quantum yield (Φ_A=0.95) to form OH, for dissociation at 355 nm[98], figure3.1 shows the absorption cross section showing the strong absorption peak at 355 nm. The photolysis process occurs due to movement of a non-bonding electron on the terminal O to the lowest π* orbital on the N=O bond[88]. This causes an extension in the N=O bond length with the vibration causing a recoil along the O-N bond which leads to the breaking of the bond as the bond length increases, generating OH and NO in the ground electronic state[99].

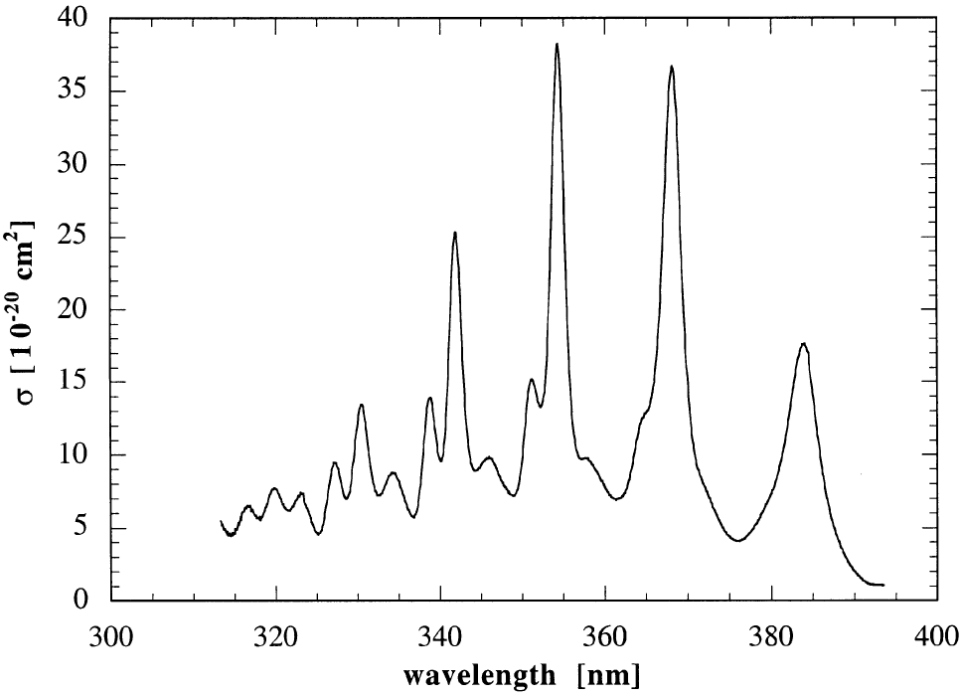

Figure 3.1. UV absorption spectrum of HONO showing the strong peak at 355nm, taken from reference [100].

In the development of the Leeds PF-LIF instrument, a 355 nm laser was used to photolyse HONO. Although it is possible to measure both the OH and the NO photo-fragments that result, this research has only detected the OH fragment. The challenge with detecting the NO fragment is that NO_2, a planned aerosol experiment reactant, will also photolyse to NO at the 355 nm wavelength[88]. This is significant because the amount of NO_2 that is added is in the range of 10-200 ppb, while the expected HONO will be ~100 ppt which will make differentiating the NO from HONO photolysis very difficult. OH, however, is not expected to form from any of the reagents or reaction products that have been used during the flow tube experiments. The detection of OH is also a much more sensitive technique compared to the detection of NO with OH LIF measurements achieving sensitivities of 0.018 ppt for a 7 min average[101] and NO chemiluminesence methods achieving 1.8 ppt for a 1 hour average[102].By measuring the OH fragment the higher sensitivity will allow detection of smaller changes in HONO concentration. The OH fragment was also chosen as the technique of measuring OH using LIF is well developed in the Heard group at Leeds.

3.2.2 Measurement of the OH Fragment

Detection of the OH fragment involves using the on-resonance FAGE technique introduced in chapter 2. In summary FAGE, fluorescence assay by gas expansion, is a low pressure laser induced fluorescence method, commonly used for the measurement of OH (and HO_2 indirectly) both in the lab and in the field[70]. The process involves using a laser to excite from specific rovibrational energy levels to an electronically excited state and then measure the resulting fluorescence as the electrons relax back to a ground vibrational state. Detection of ambient OH employs 308 nm laser light, which excites the OH molecule ($A^2\sum v'=0 \leftarrow X^2\pi\ v''=0$), after which it relaxes and fluoresces at 308 nm[80].

This on resonance OH detection method is utilised in the Indiana University PF-LIF HONO instrument for detection of the OH fragment. In contrast, the Georgia Tech Institute PF-LIF instrument utilised an off-resonant (OH excitation at 282 nm, detection at 308 nm) method for HONO detection. In the experiments discussed in this thesis, on-resonance excitation and detection was employed to minimise/prevent probe-induced signals (e.g. background signals generated from OH formed from ozone photolysis in humidified flows). If a 282 nm laser was used, the OH background (from probe-induced OH) can be subtracted by measuring without the photolysis laser, however when trying to achieve a low limit of detection (LOD) it is best to remove the majority of the background in order to maximise the signal-to-noise ratio.

3.2.3 Laser Systems

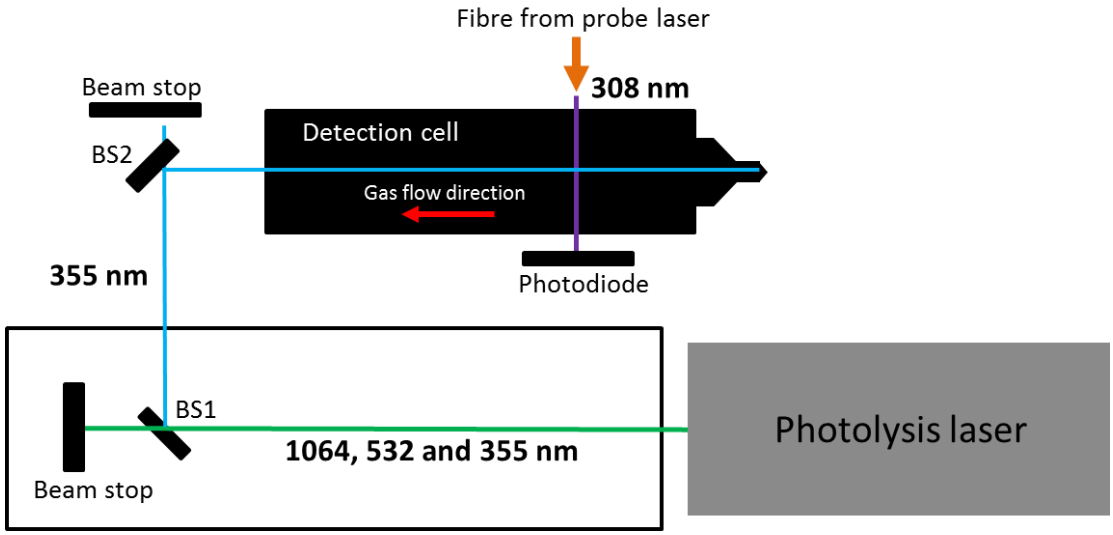

Figure 3.2. Top down diagram showing delivery of laser light to the detection cell**.**

As described in the previous section two laser wavelengths (and, hence laser systems) are used in the PF-LIF instrument (355 nm to photolyse HONO and 282 nm or 308 nm to detect the OH fragment). Figure 3.2 shows a plan of the layout of the Leeds PF-LIF instrument. The layout has the photolysis laser and the probe laser orientated perpendicular to each other on the same horizontal axis.

3.2.3.1 355 nm Light Generation

The 355 nm photolysis laser was generated by several different lasers over the course of this research, however, they each generate the 355 nm light using the same method. The lasers used were a Continuum Surelite I-10, Spectra-Physics GCR-130 and Spectron Nd:YAG laser; all lasers were operated at a pulse repetition frequency of 10 Hz. These three laser systems initially generate 1064 nm light from a flash lamp pumped Nd:YAG crystal. This light is then converted first to 532 nm light and then the 1064 and 532 are mixed to generate the 355 nm light. Upon exiting the laser, the 355 nm light is separated from the remaining 1064 and 532 nm light using two dichroic beam splitters before being delivered directly to the detection cell. The light entering the cell has a beam width of 0.5 cm and a power 200 mW (20 mJ per pulse).

3.2.3.2 308 nm Light Generation - SIRAH dye laser

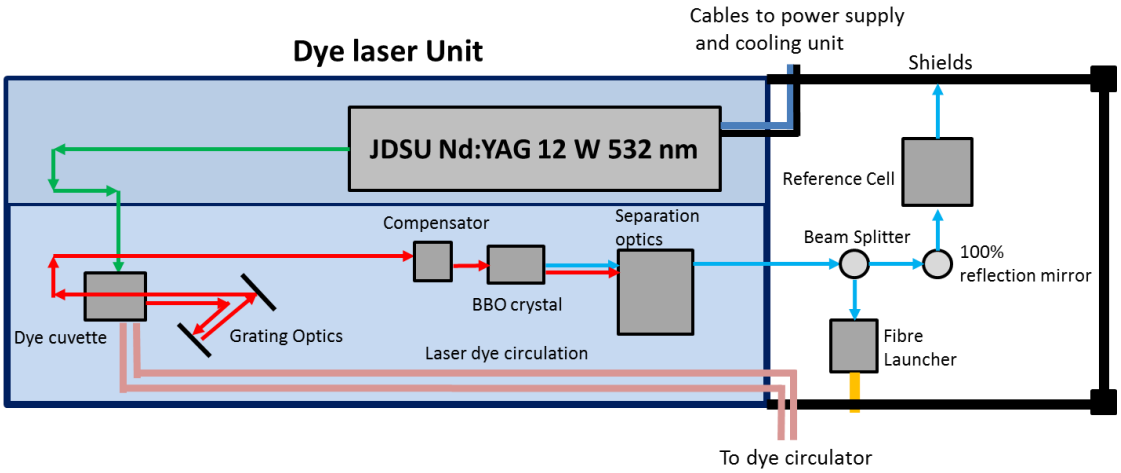

Figure 3.3. Dye laser system used in the PF-LIF setup.

The SIRAH dye laser system described in chapter 2 was used to generate the 308 nm probe light for this experiment. The laser operates by using the green light from a JDSU Nd:YAG to pump a dye cell to generate 616 nm light which is then doubled to generate the 308 nm light. See section 2.2.1 for a detailed description of the light generation. The power of 308 nm light generated ranged between 10-30 mW at 5 kHz. After exiting the main laser system 90% of the 308 nm light is directed into a fibre launcher while the remaining 10% of the light passed through a reference cell.

3.2.4 Detection Cell

Figure 3.4 shows a simplified cross section schematic of the PF-LIF instrument. The cell is constructed of several black anodised aluminium cylinders, 50 mm internal diameter, following the same design as the Leeds aircraft FAGE instrument[69].

Air is sampled through an off centre, angled pinhole (1 mm diameter), the design of this pinhole will be discussed further in section 3.4.4.1, at a typical flow rate of ~5 SLM, 5 cm from the detection region. The short distance between sampling and detection is required to reduce the loss of species (HONO and OH) to the inner walls of the cell. The cell is continuously pumped to a pressure of ~2 Torr using a rotary pump (*Edwards, model E1M80*), roots blower combination (*Edwards, model EH1200*). The pressure is monitored using a pressure gauge (Tylan General, CDC 11) mounted after the detection region.

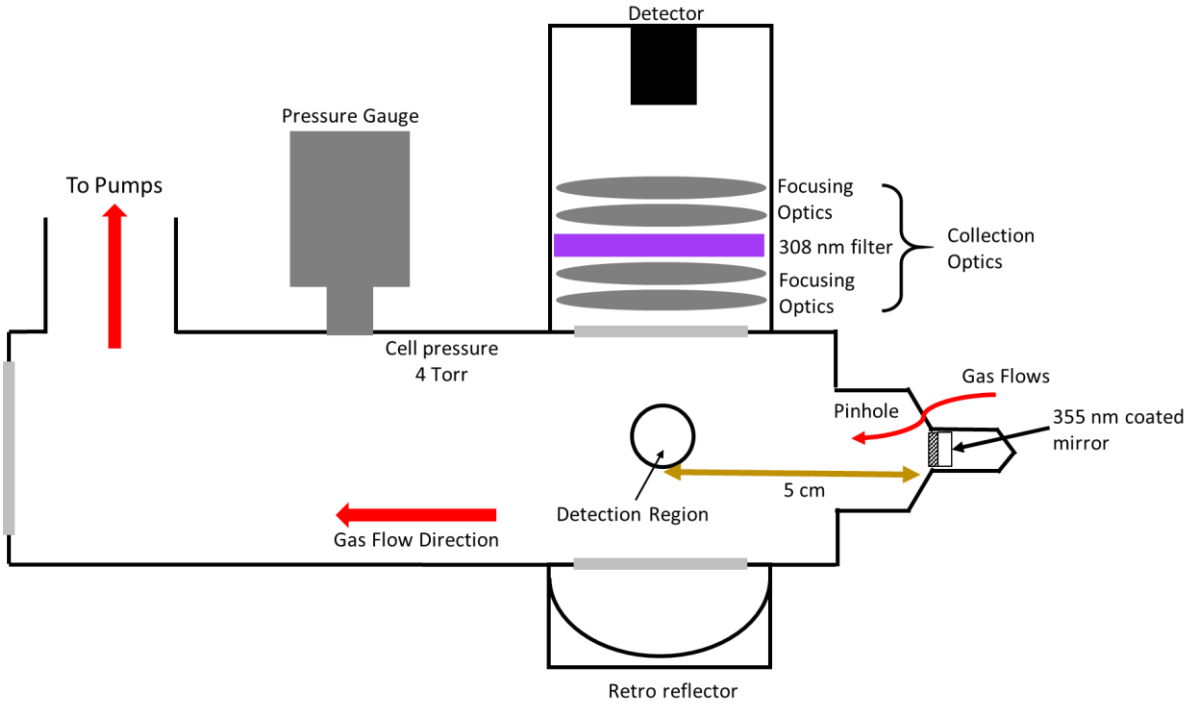

Figure 3.4. Vertical cross-section schematic of the PF-LIF detection cell.

The 308 nm probe light is delivered to the cell via a fibre optic cable connected to the cell entrance arm via a collimating unit. The light is delivered perpendicular to the air flow across the detection region and exits the cell through a 308 nm anti-reflective coated window on the opposite side. Both cell arms contain baffles to reduce scattered light by selectively blocking light that does not travel along the central axis. After the laser light exits the cell the relative laser power is measured using a UV sensitive photodiode (New Focus 2032) to monitor fluctuations in laser power and allow normalisation of the signal. The 355 nm photolysis laser light enters the detection cell through a quartz window opposite the pinhole. The 355 nm travels along the same axis as the gas flow but in the opposite direction. The light then strikes a 355 nm coated mirror at the top of the cell, directing the light back along the same path. This is to both enhance the percentage of HONO that is photolysed and removes the random scatter of the 355 nm light that would be generated by the laser reflecting off the metal surface.

A detector is mounted perpendicular to both the laser axis and gas flow. A window coated for the transmission for 308 nm light separates the detector barrel from the low pressure cell. Any fluorescence that passes through the window will pass through an optics barrel which focuses the light onto the detector. The optics barrel also contains a Barr associates interference filter that only allows the transmission of light at 308 nm (± 8 nm with approx. 50% transmission, FWHM = 5 nm) in order to prevent room light and scatter from the photolysis laser reaching the detector. The light is focused onto a detector; both a channel photomultiplier (Perkin Elmer 993P, CPM) and a multi-channel plate (Photek, MCP 325) were used in these experiments. The detector monitors the fluorescence signal by converting photons hitting the active area of the photocathode into electrical pulses. To avoid saturation by laser light, the detector is gated (switched off) during the laser pulses, using a Leeds home-built gating unit for the CPM detector and a Photek gating unit for the MCP detectors. Opposite the detector barrel a retroreflector mirror is positioned to increase the amount a fluorescence signal captured by reflecting any light traveling downwards back towards the detector.

Timing in the instrument is controlled by a delay generator (BNC, model 555) which acts as the master clock for the system. It is run with an internal trigger a 5 kHz. A direct output at this rate is used to trigger the OH probe laser and the gating of the detectors and counting card. A pulse divided output at 10 Hz is used to trigger the HONO photolysis laser and to initiate the counting cards. Using this shared triggered source for both lasers ensures that, although they are run at different rates, the triggering of each laser is the identical in each run.

3.2.5 Data Acquisition

A photon counting card (Becker and Hickl, PMS-400a) is used for data acquisition. Unlike the data collection for the OH instrument (chapter 2) which uses 2 distinct bins after the laser pulse (bin one = signal and scatter, bin two = dark counts), the software for the HONO instrument uses a continuous sequence of 2 µs wide bins. The detection of OH is carried out in the same way as in the standard FAGE cell described in chapter 2, with the MCP detector responding to photons when in a high gain mode and sending the electronic signal to the counting card. Here, for HONO data acquisition, the counting card is run at 10 Hz covering 500 probe pulses and a single photolysis pulse each time the counting card is triggered. The internal clock the BNC pulse generator was used to generate the triggers required at each stage of the instrument for laser operation and data collection. Figure 3.5 shows the pulses generated and their relation to each other.

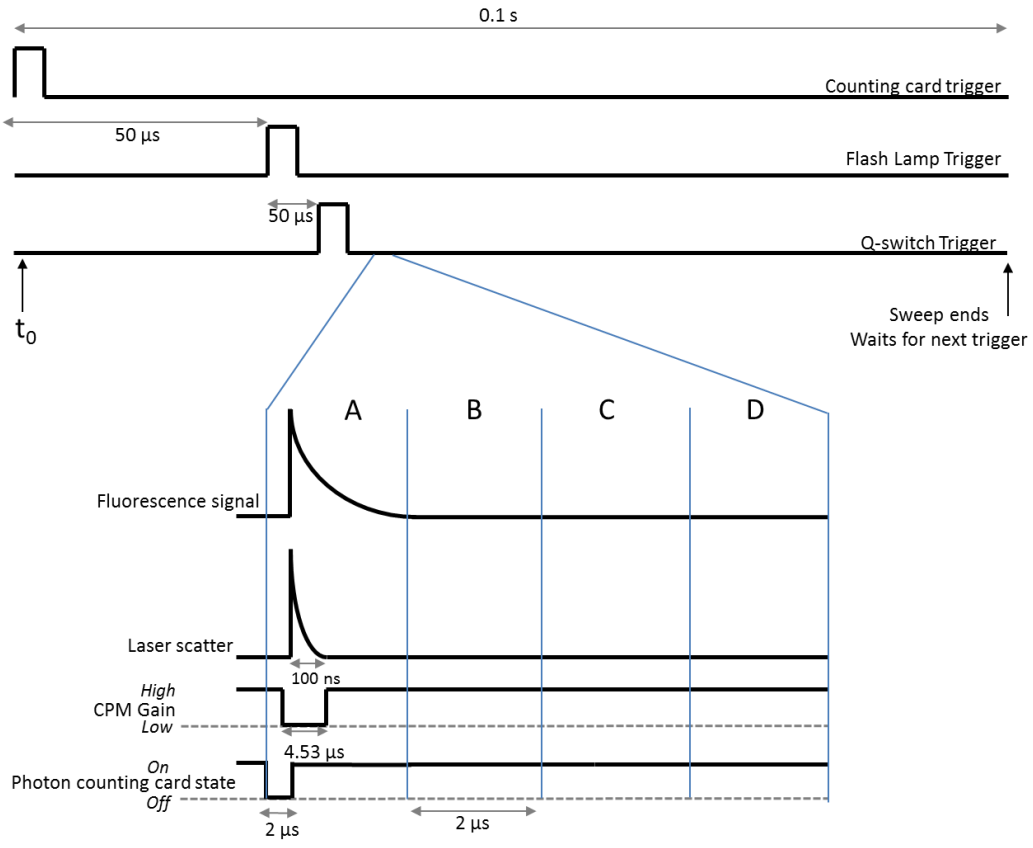

Figure 3.5. Representation of the pulses in a single measurement sweep with the top three panels repeating at a rate of 10 Hz and the bottom 4 panels at 5000 Hz. The flash lamp and Q-switch triggers control the photolysis laser with the time difference between them controlling the photolysis laser power. A-D are the different 2 µs measurements bins that the software counts the total fluorescence signal in.

After triggering the counting card (t_0), an initial OH signal is measured for 0.01 seconds, to provide a background measurement of the OH and 308 nm scattered light, present in the system, before HONO is photolysed. After this period the photolysis laser is triggered; the position of the 355 nm laser pulse in time is set so that it pulses 800 ns before a 308 nm probe pulse and, hence, occurs whilst the detector is in a low gain state, ensuring that detection of the initial scatter from the photolysis laser is minimised. The maximum fluorescence signal from the OH generated from the photolysis of HONO is observed immediately after the photolysis pulse as the OH detected at this time has been generated close to the probe region and has not diluted. The OH generated from photolysis in the cell is then measured for a further 0.01 seconds. A sweep refers to the period from the initial triggering of the counting card to the end of the OH measurement (0.01 sec later). Multiple sweeps are collected per run with the signal in each bin being added to the corresponding bin in the previous run. This accumulation helps increase the observed signal bringing any measured OH signal above the background noise. The number of sweeps can be adjusted for different experiments as increasing the number of sweeps will make it possible to detect smaller concentrations, however this will also increase the length of the measurement time for each run reducing the time resolution.

Typically the number of sweeps used in experiments discussed in chapter 4 were either 500 or 1000. Figure 3.5 above shows a representation of how all the triggers are set up.

Figure 3.6 shows a signal plot in which HONO was homogeneously generated by reaction of OH, generated by flowing humidified N_2 past a Hg lamp, in the presence of excess NO. Each point in figure 3.6, represents an OH signal that has been accumulated over 1000 sweeps. The photolysis laser pulse is indicated by the red line. Following photolysis, there is a large increase in the measured OH signal due to the generation from HONO via photolysis. The decay occurs primarily due to diffusion away from the central measurement axis as the recombination between the generated OH and NO is slow enough that it doesn't have a significant impact on this decay.

This was proven to be the case by a modelling exercise using the Kintecus integrator[103] where no HONO formation was seen during the time between photolysis at the pinhole and the detection of OH (~5 ms). For the aerosol experiments only the first OH point following the photolysis laser was used in the determination of HONO production due to interferences beginning to contribute to the signal in the later points; this interference signal is discussed further in section 3.4.4. To calculate the signal due to HONO the following equation is used;

$$HONO_{sig} = \frac{(bin_n - OH_{back})}{LP} \qquad \text{Eq(8)}$$

where $HONO_{sig}$ is the signal due to HONO, bin_n is a particular measurement bin, OH_{back} is the averaged value from all OH background bins (which occur pre-photolysis laser pulse) and LP is the average laser power for all sweeps in the run. This is repeated for both OH online and offline wavelengths, when the probe laser is tuned to (online) and away from (offline) the OH Q1(2) transition. The $HONO_{sig}$ for the offline wavelength is then subtracted from the online $HONO_{sig}$ to remove the signal due to laser scatter (355 nm and 308 nm), room light and detector dark counts.

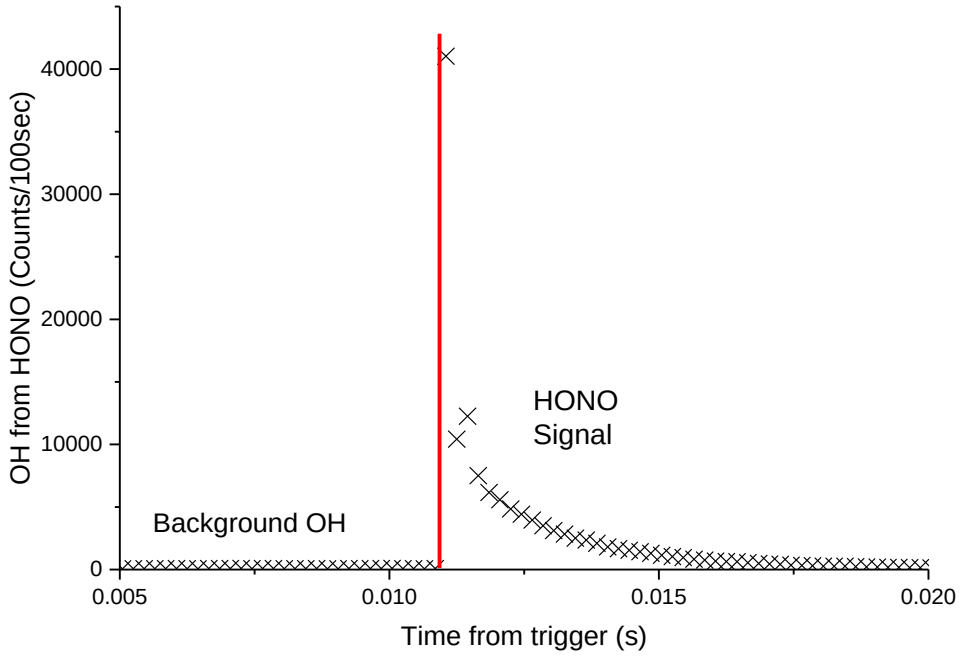

Figure 3.6. Data generated from the PF-LIF instrument when sampling HONO generated from the glass wand, section 3.3. Each cross is the OH fluorescence signal measured following each 308nm laser pulse (500 points per sweep). The red line shows when the photolysis laser is triggered. This plot was generated after 1000 sweeps which takes 100 seconds to collect.

3.3 Calibration

HONO used during the initial setup experiments (see section 3.4), where a constant concentration was needed in order to validate the design and optimise the sensitivity of the instrument, was generated via the reaction of OH and NO. The OH was generated within a glass flow tube with a mercury pen ray lamp housed inside (figure 3.7). Humidified N_2 was flowed past the lamp, generating OH through the photolysis of water vapour. By adding an excess of NO (10^{16} molecule cm^{-3}) to the flow, HONO is generated. The NO and HONO will not be affected by the 185 nm light that the lamp outputs as neither have strong absorption cross sections (HONO = 9×10^{-19} cm^2 $molecule^{-1}$, NO = 1.4×10^{-20} cm^2 $molecule^{-1}$) at this wavelength. This design generated large concentrations of HONO (10^{11} molecule cm^{-3}) that was readily detectable.

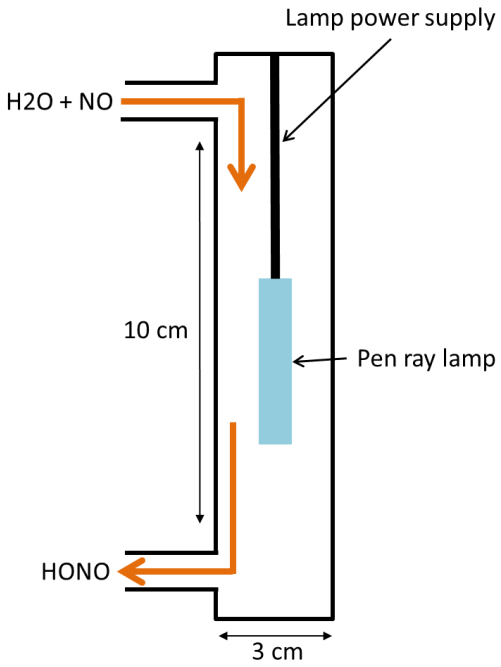

Figure 3.7. Cross section of the glass flow tube used to produce the HONO.

The flow rates used through the glass flow tube were 5 SLM N_2 and 5 SCCM of NO to give a 0.1 % mix of the NO. The HONO exiting the flow tube was measured, using UV/vis spectroscopy[104] (4.5 meter path length, Laser Driven Light Source, NIR to the UV) to determine the concentration of HONO generated. The absorption spectrum of HONO generated using the glass flow tube is presented below (figure 3.8) and closely resembles the published HONO spectrum (figure 3.1).

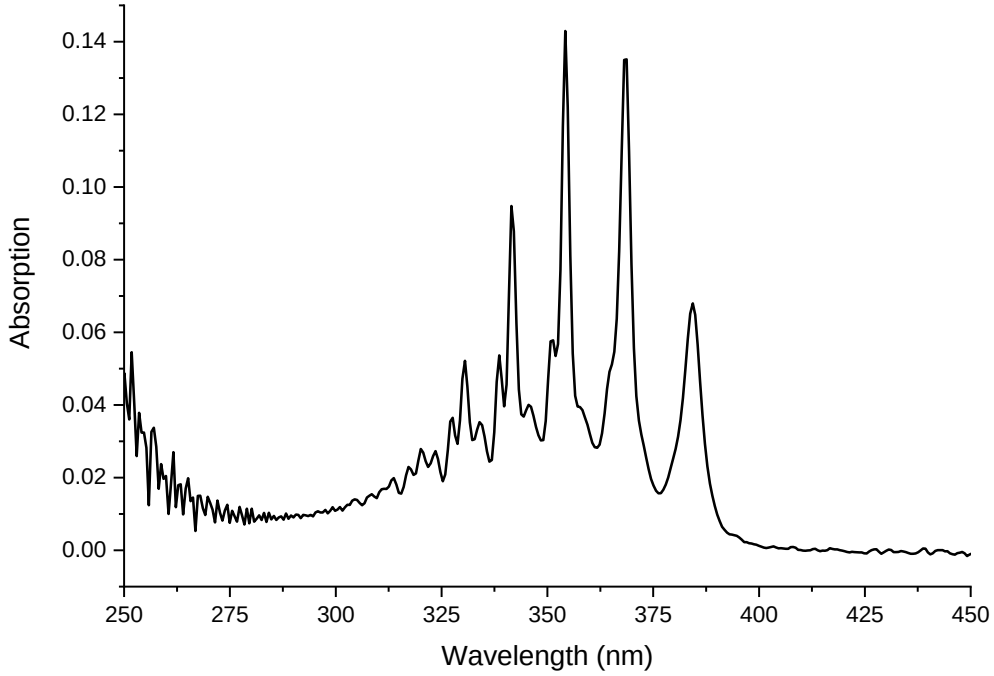

Figure 3.8. Measured spectrum of HONO produced in the glass flow tube. A background of NO_2 was observed however a measurement of the outflow from the wand with the lamp off, no HONO production, showed the same background of NO_2 allowing its subtraction from the lamp on spectrum. The absorption at lower wavelengths <280 nm is and instrument artefact.

Using the Beer lambert law equation;

$$A = \varepsilon\, l\, c \qquad \text{Eq(9)}$$

where A is absorbance, ε is the absorption cross section of HONO, *l* is the path length and c is the concentration it is possible to determine a concentration of HONO. Using the major peak at 355 nm in figure 3.8 a HONO concentration of 3.5 x 10^{14} molecule cm^{-3} was calculated (path length = 443 cm).

A method to generate a calibrated amount of HONO to allow for the calculation of a detection limit for the instrument is necessary. Methods used to calibrate HONO instruments that have been reported in the literature previously often rely on a second instrument to validate the concentration of HONO produced, for example an absorption technique that does not require calibration, or a LOPAP instrument that has been calibrated using liquid standards. A method used in the literature to generate flows of HONO involves flowing HCl gas over a bed of $NaNO_2$ generating HONO in the gas phase[90].

$$HCl_{(g)} + NaNO_{2(s)} \xrightarrow{H_2O} HONO_{(g)} + NaCl_{(s)} \qquad \text{R(37)}$$

The method chosen to calibrate the Leeds instrument involved adapting the methodology for the OH calibration (discussed in chapter 2, section 2.3) by adding NO to a humidified nitrogen flow (figure 3.10). The NO reacts with the known amount of OH generated (and also any HO_2, which forms from the small amount of O_2 present in the N_2) to form a known amount of HONO. The absolute amount of HONO generated was calculated using a kinetics model run using Kintecus[103] and the inputs listed in table 3.2. The literature rate constants have been taken from the IUPAC website, while the loss of OH and HONO were estimated by measuring the decrease in signal as the distance between the calibration wand and the pinhole was increased.

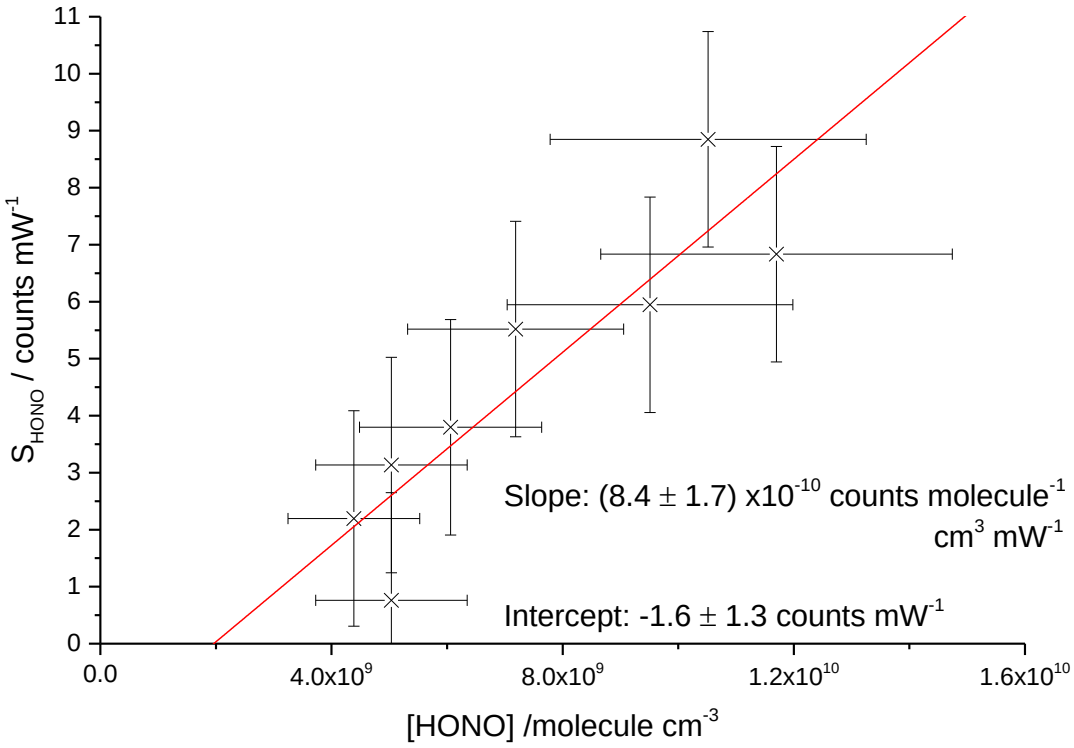

Figure 3.9. Results from a HONO calibration experiment using the CPM detector, with the normalised signal versus the calculated HONO concentration. Each point is an average of multiple runs, the y error bars represent the standard deviation for the averaged normalised signal at a set concentration. The x errors are calculated using the same method discussed in section 2.3.2 for the calibration of OH, this was because the HONO concentration is determined assuming conversion of all OH to HONO.

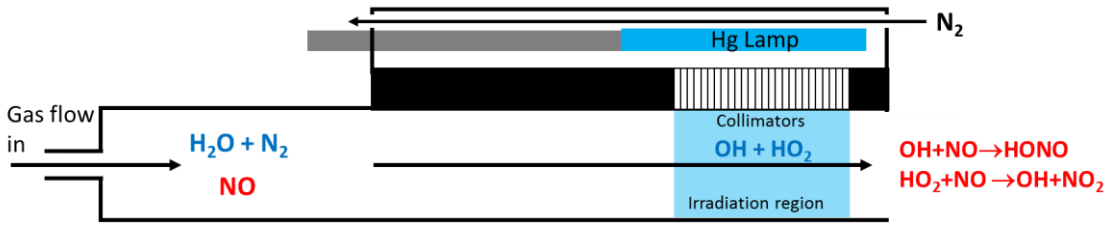

Figure 3.10. Calibration wand showing the reactions used to generate HONO.

Table 3.2. Reactions used in the Kintecus model to predict the amount of HONO produced in the calibration wand. Rate constant were taken from the IUPAC website (http://iupac.pole-ether.fr/).

Reaction	*Rate constant (T=298 K)*
$HO_2 + HO_2 = H_2O_2 + O_2$	2.90×10^{-12} *molecule*$^{-1}$ *cm*^{3} *s*$^{-1}$
$OH + H_2O_2 = H_2O + HO_2$	1.70×10^{-12} *molecule* $^{-1}$ *cm*^{3} *s*$^{-1}$
$OH + OH = H_2O_2$	2.26×10^{-11} *molecule* $^{-1}$ *cm*^{3} *s*$^{-1}$
$HO_2 + NO = NO_2 + OH$	8.54×10^{-12} *molecule* $^{-1}$ *cm*^{3} *s*$^{-1}$
$NO + NO_2 = N_2O_3$	8.03×10^{-15} *molecule*$^{-1}$ *cm*^{3} *s*$^{-1}$
$HO_2 + NO_2 = HO_2NO_2$	3.52×10^{-12} *molecule*$^{-1}$ *cm*^{3} *s*$^{-1}$
$OH + NO_2 = HONO_2$	8.11×10^{-11} *molecule*$^{-1}$ *cm*^{3} *s*$^{-1}$
$OH + NO_2 = HOONO$	2.54×10^{-12} *molecule*$^{-1}$ *cm*^{3} *s*$^{-1}$
$NO_2 + NO_2 = N_2O_4$	3.53×10^{-14} *molecule*$^{-1}$ *cm*^{3} *s*$^{-1}$
$N_2O_3 = NO + NO_2$	3.83×10^{5} *s*$^{-1}$
$N_2O_4 = NO_2 + NO_2$	1.54×10^{5} *s*$^{-1}$
$OH + HONO_2 = H_2O + NO_3$	1.50×10^{-13} *molecule*$^{-1}$ *cm*^{3} *s*$^{-1}$
$OH + NO_3 = HO_2 + NO_2$	2.00×10^{-11} *molecule*$^{-1}$ *cm*^{3} *s*$^{-1}$
$HO_2 + NO_3 = O_2 + HNO_3$	4.00×10^{-12} *molecule*$^{-1}$ *cm*^{3} *s*$^{-1}$
$NO + NO_3 = 2NO_2$	2.60×10^{-11} *molecule*$^{-1}$ *cm*^{3} *s*$^{-1}$
$NO_2 + NO_3 = N_2O_5$	9.10×10^{-11} *molecule*$^{-1}$ *cm*^{3} *s*$^{-1}$
HONO = Loss	1.00×10^{-3} *s*$^{-1}$
OH = Loss	1.00 *s*$^{-1}$
$HO_2 + NO_2 = PNA$	1.38×10^{-12} *molecule*$^{-1}$ *cm*^{3} *s*$^{-1}$
$PNA = HO_2 + NO_2$	8.30×10^{-2} *s*$^{-1}$
$NO_2 + NO_2 = HONO$	9.18×10^{-6} *molecule*$^{-1}$ *cm*^{3} *s*$^{-1}$
$HONO = OH + NO$	4.47×10^{-12} *s*$^{-1}$

For these experiments 40 SLM of humidified N_2 and 5 sccm of a 5% mix of NO in N_2 was used. The NO was added into the main N_2 flow, before entering the wand to allow it to mix into the bulk flow completely prior to reaching the irradiation region. Variable amounts of HONO were generated by varying the Hg lamp current. The NO used was found to have a large, variable HONO background (observed when the Hg lamp was switched off), that needed to be subtracted from each HONO signal measured. In order to reduce this background the NO concentration was kept as low as possible (but still in excess to ensure rapid conversion of OH to HONO) and it was passed through an Ascarite filter, which removes acidic compounds, and so removed HONO present in the NO cylinder without effecting the NO. Despite these clean-up steps, a HONO background, likely from HONO forming along the gas lines was still observed.

A multi-point calibration of HONO concentration vs HONO signal is shown in fig 3.9. From this calibration, a detection limit of 50 ppt, 2 min average, was determined. This compares well with the Georgia Tech institute instrument that has a detection limit of 15 ppt for a 1 min average. The use of the OH calibration system (which generates a maximum of 10^{11} molecule cm^{-3} OH) to determine the sensitivity of the PF-LIF instrument to HONO was challenging owing to the variability in the HONO background signal. The variability was often larger than the changes in the HONO signal generated by varying the Hg lamp current.

To overcome this limitation, a glass wand with the Hg lamp located within the gas flow, was used to calibrate the instrument. The glass wand generates a much larger OH concentration (> ~10^{12} molecule cm^{-3}) and, therefore, a larger HONO concentrations (~1 x 10^{14} molecule cm^{-3}). The lamp flux was calculated using ozone actinometry, this technique was carried out in a similar method to what is described in section 2.3.1 for N_2O actinometry. The difference is simply that a humidified air flow is passed over the lamp, this generates ozone in the flow, which is measured using an ozone box (Thermo environmental Instruments 49C).

$$[O_3] = [O_2]\,\sigma_{O2}\,\emptyset_{O3}\,F\,t \qquad \text{Eq(10)}$$

$$[OH] = [HO_2] = \frac{[O_3][H_2O]\sigma_{O2}\,\emptyset_{O3}}{[O_2]\sigma_{O2}\emptyset_{O3}} \qquad \text{Eq(11)}$$

Calibrations performed using the glass wand were run using a 20 SLM flow of N_2 and a 5 sccm flow of NO; a typical multi-point calibration is shown in, figure 3.11. The large y intercept is due to the presence of HONO in the NO gas. Varying the NO concentration in different calibrations results in a variable intercept, however, the gradient remains the same highlighting that the NO remained in excess and all OH was rapidly converted to HONO.

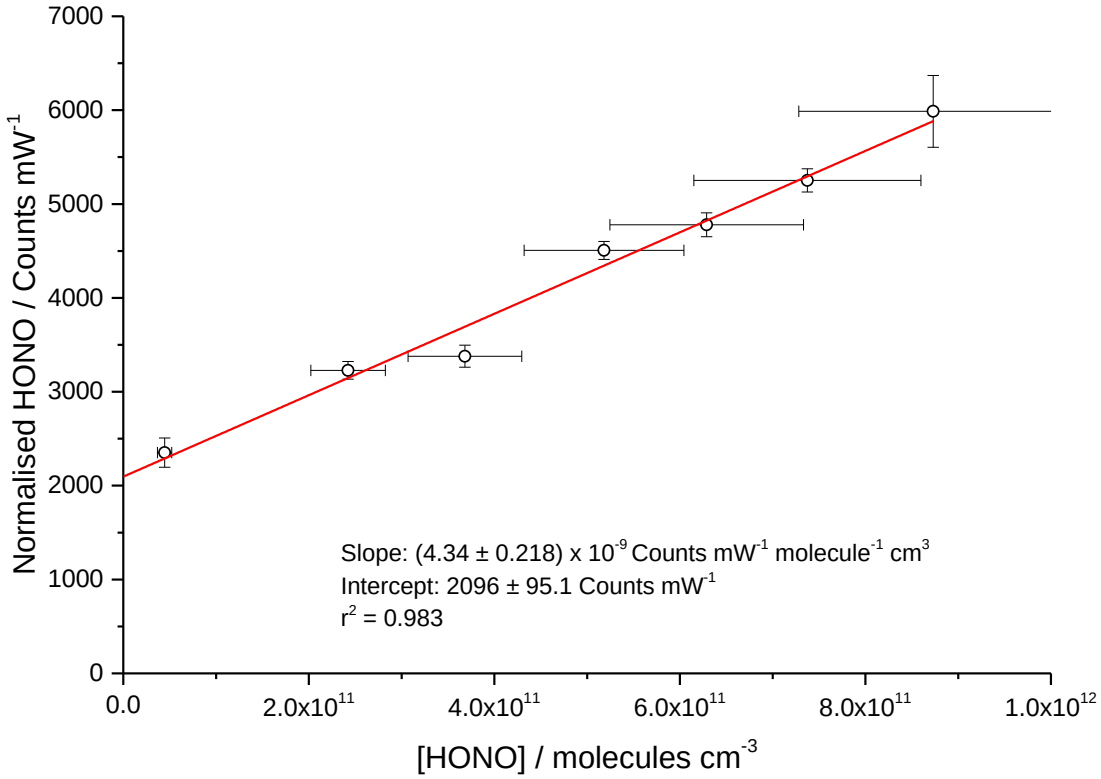

Figure 3.11. Calibration plot for the PF-LIF instruments sensitivity to HONO using the glass flow tube. The MCP detector was connected to the cell for this calibration. Calibration carried out using N_2, 0.025% NO, 3% water vapour.

This chapter so far has described the optimised PF-LIF instrument that was used in the heterogeneous HONO production experiments that are detailed in chapter 4. However, many iterations of the instrument were assessed before the development of the final apparatus. The following sections detail the major instrument developments that have occurred over the course of this research.

3.4 PF-LIF instrument Optimisation

3.4.1 Initial Experimental design

The initial design, figure 3.12, for the HONO cell was based on the Leeds aircraft FAGE cell, see chapters 2 or 5. The main design features of the instrument that were characterised and optimised were the detection cell inlet (or pinhole) and the radiation source used to photolyse HONO. In the initial cell design a flat and on the central axis pinhole was used, similar to other detection cells used for the measurement of OH.

Two photolysis methods were tested for their efficiency to photolyse HONO. These were an LED, centred around the 385 nm wavelength, and the 355 nm laser discussed above. Both light sources were also tested in two orientations: down the length of the cell, left to right in figure 3.12, and across the cell axis, via the quartz window.

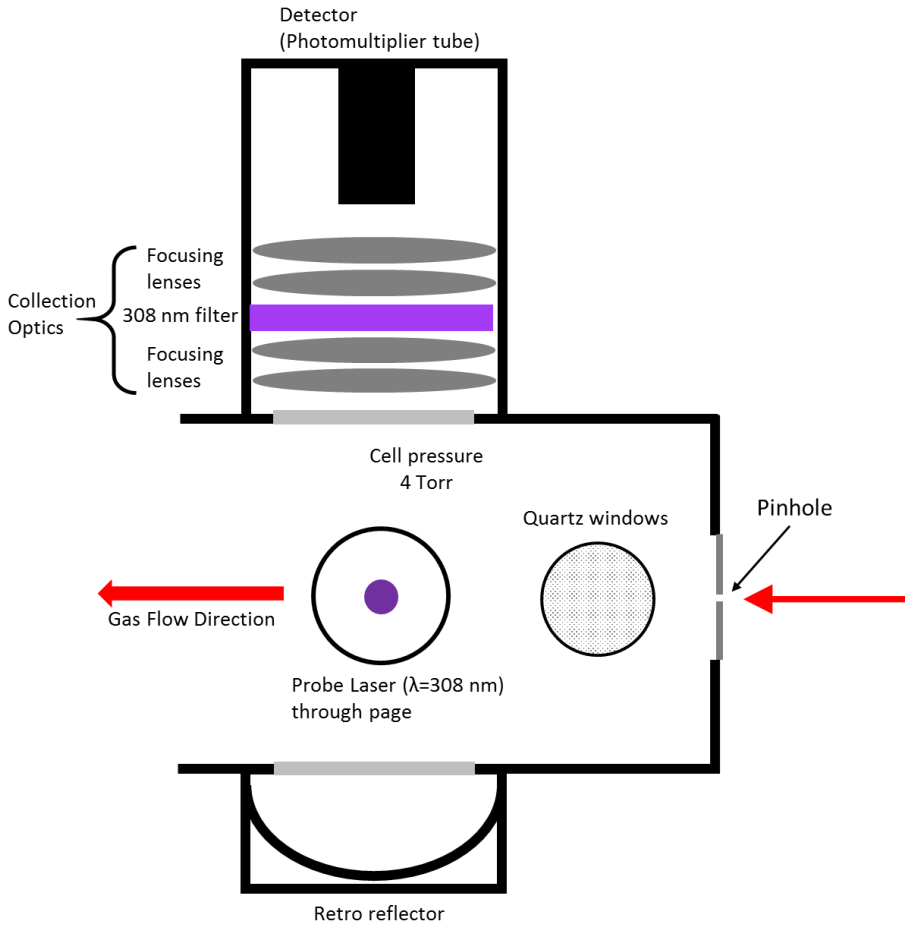

Figure 3.12. Starting cell design in the development of the photo fragmentation laser induced fluorescence instrument for the measurement of HONO.

3.4.2 LED Photolysis Source

The LED offers a cheaper and more compact alternative to using a laser for HONO photolysis. The LED also had the advantage of being able to provide a continuous light source (as opposed to a pulsed 355 nm laser) so it would be possible to measure the OH produced through photolysis during every 308 nm laser pulse (5000 shots per sec) and simply turning off the LED would give the background OH signal.

Figure 3.13. LED used initially to photolyse HONO. The lens is visible in the centre with the LED mounted beneath.

Initially a LED (Air Quality Design, Inc) centred on 385 nm, as seen in figure 3.13 above, was tested to see if it was able to provide enough energy to photolysis HONO. This LED had been successfully used in a differential photolysis HONO detector instrument[87]. The LED was housed with a lens in front in order to maximise the spread of the light over a short distance. This, however, was a disadvantage for any experiments using the FAGE cell as it was not possible to mount the LED within the detection cell, so it needed to be placed outside the cell with the light directed through one of the two windows on the cell figure 3.12. The spread of the light meant that the majority of the light was lost before it entered the cell, even with the addition of a focusing lens. The power of the LED was around 100 mW when measured directly in front of the lens but once moved 10 cm away the power dropped by roughly 70%. Compared to the photolysis laser which had 200mW of power it is both lower overall and because the LED is continuous the amount of energy is released over a broader time period while the laser is concentrating the energy in short pulses.

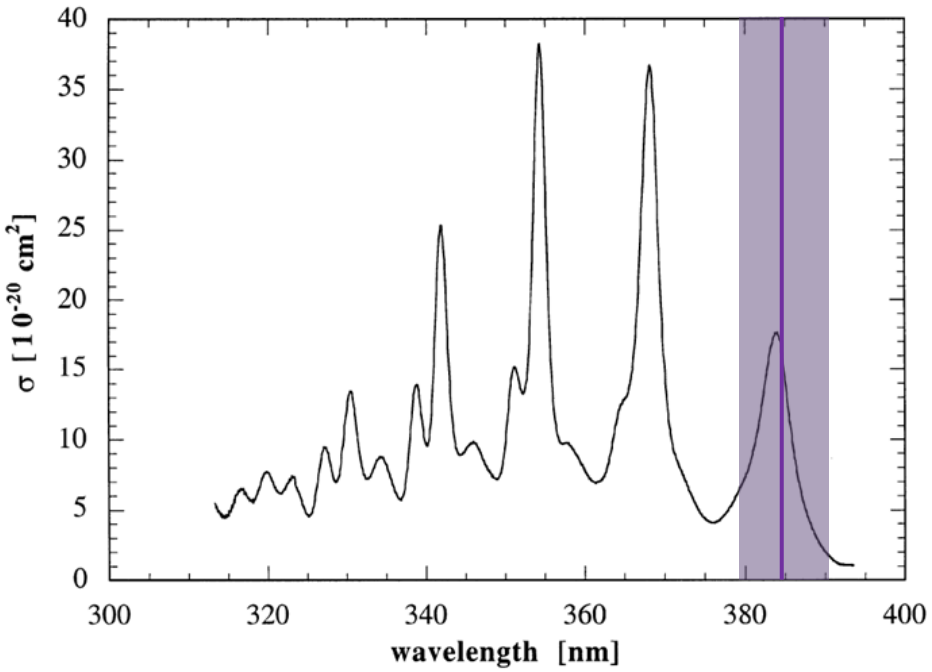

Figure 3.14. The absorption spectrum of HONO with the area in grey showing the range of light emitted by the 385 nm LED [100].

3.4.2.1 Orientation of the LED

Two orientations of LED light delivery were tested to see which would provide the greatest HONO sensitivity. These orientations are shown below in figures 3.15 and 3.26. For the cross axis orientation the LED was placed outside a window before the probe laser so that any HONO present in the sampled air flow would be photolysed as it passed. For the down axis orientation the LED was placed outside a window at the end of the cell, but because of the distance of this window from the measurement region and due to the divergence of the light it was necessary to use a focusing lens to focus the light to a point near the pinhole. This orientation allowed for a longer photolysis time as any HONO present will see the light as it moves down the cell immediately after entering the cell.

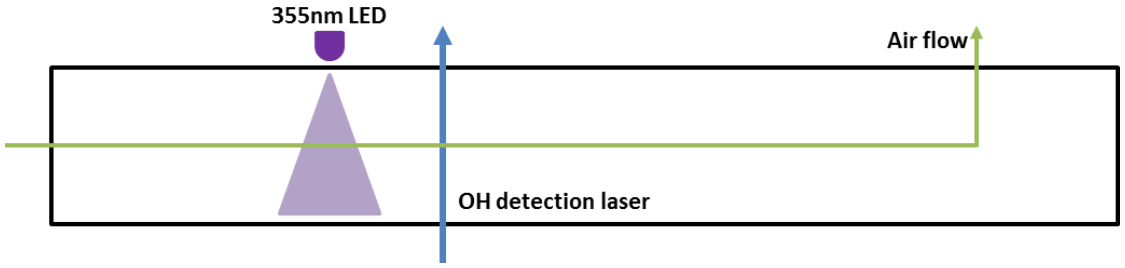

Figure 3.15. Representation of the detection cell with the LED placed in the cross axis orientation with the LED mounted outside a side window before the air flow reaches the probe laser.

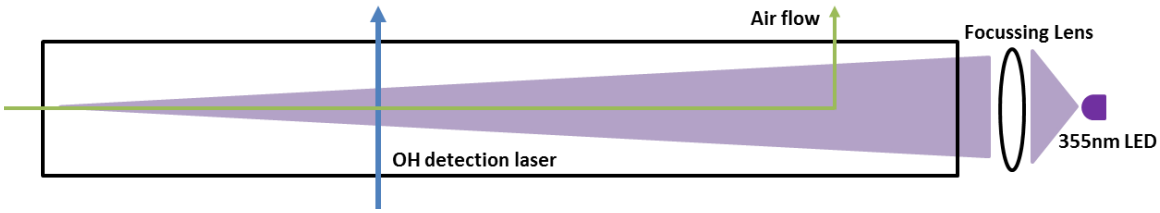

Figure 3.16. Down axis orientation, a focusing lens was used to focus as much light as possible onto the centre of the pinhole.

The results from both orientations are shown below in figures 3.17 and 3.18. The first notable feature is that the background signal is increased in each run when the LED is turned on. It is not completely understood why this occurs as the Barr filter in the fluorescence collection optics barrel should only allow 308 nm light through and the output spectrum of the LED, measured using a spectroradiometer (Ocean Optics), showed no emission around this wavelength. It is possible that due to the intensity of light generated by the LED the optical filter was unable to remove all light as it passed through to the detector. From experiments carried out using both orientations it was found that there was no significant increase in OH signal observed when comparing results with the LED turned off or on. The increase seen on both plots is removed when the background signal is subtracted. The smaller HONO signal (online – offline) observed in figure 4.18 (cross axis experiments) vs figure 4.19 (down axis experiments) are due to the use of a lower NO concentration which left some unreacted OH in the flow. The NO concentration was reduced to assess if the excess NO present was reacting with the OH formed from HONO photolysis. This test was not repeated for the cross axis orientation as it was thought that it was unlikely to be the reason for the lack of an increase in the measured OH.

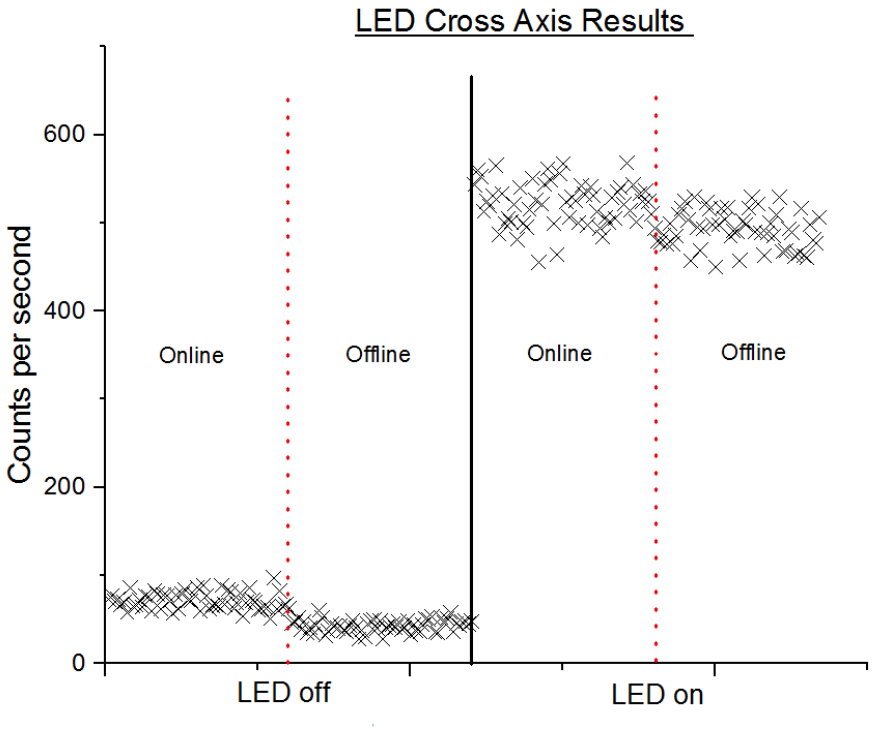

Figure 3.17. Example results from the cross axis LED experiments showing the increase in background counts when the LED was switched on. Each point represents a 1 second average. The counts have not been normalised in these plots as the laser power at the cell was not monitored throughout these runs so the difference between online and offline may be due to a change in the 308 nm laser power.

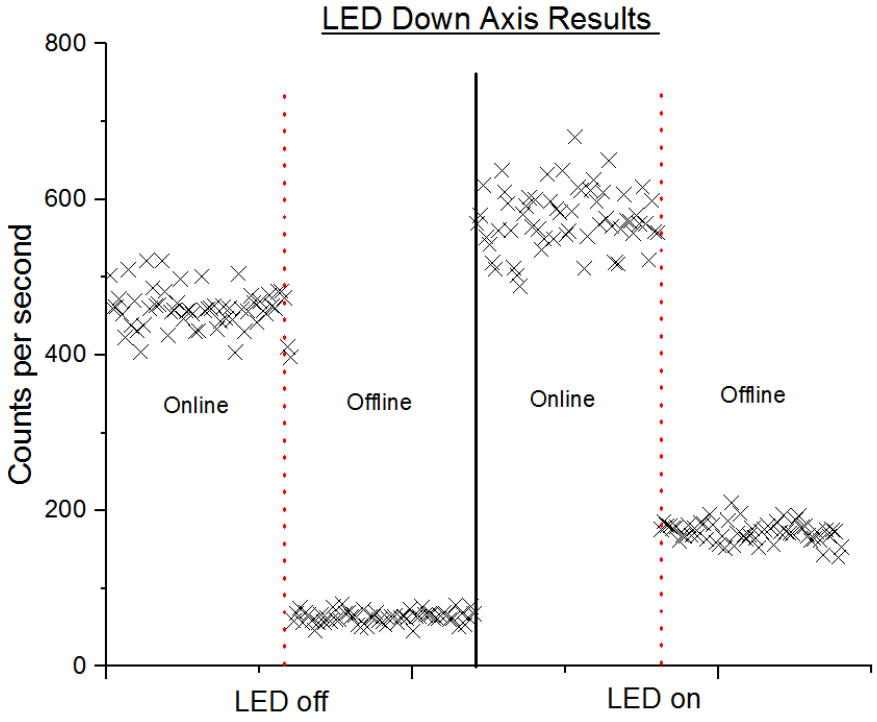

Figure 3.18. Example results from the cross axis LED experiments showing the increase in background counts when the LED was switched on. Each point represents a 1 second average.

Results from these experiments showed that using the LED in these ways will not provide an adequate photolysis source for measuring HONO sensitively in this instrument. Utilising the LED as a light source will result in a much higher detection limit of HONO this is because with no response to HONO generated using the glass wand it can be assumed that the detection limit is above the concentration generated by the wand. In this case that detection limit would be ~10ppm for a 2 min collection While for the laser instrument in the optimal setup the detection limit is 50 ppt for a 2 min collection, which is considerably less.. However, due to their low cost reinvestigating different designs using the LEDs as a photolysis source with the LEDs mounted inside the detection cell to take advantage of as much of the LEDs power as possible would be worthwhile. The LEDs could also be arranged in an array which would increase the area which is being irradiated. Alternatively, an attachment to the current FAGE cell before the pinhole, where HONO could be photolysed at atmospheric pressure, meaning HONO would be at a higher density, may increase the overall sensitivity. However, it should be noted that OH would be preferentially lost to the pinhole surface (relative to HONO) so it will be a balance between the extra OH production and the OH loss during sampling.

3.4.3 Photolysis Laser

The description of the photolysis laser method is found in section 3.2. This section will describe the effects of changing the orientation of the photolysis laser. Two different orientations were used for the experiments using the laser photolysis source, a down axis and an across axis, this can be seen in the layout diagram (figure 3.19). By moving the beam splitter 1 (BS1) between either of its two positions it was possible to direct the laser light along each axis.

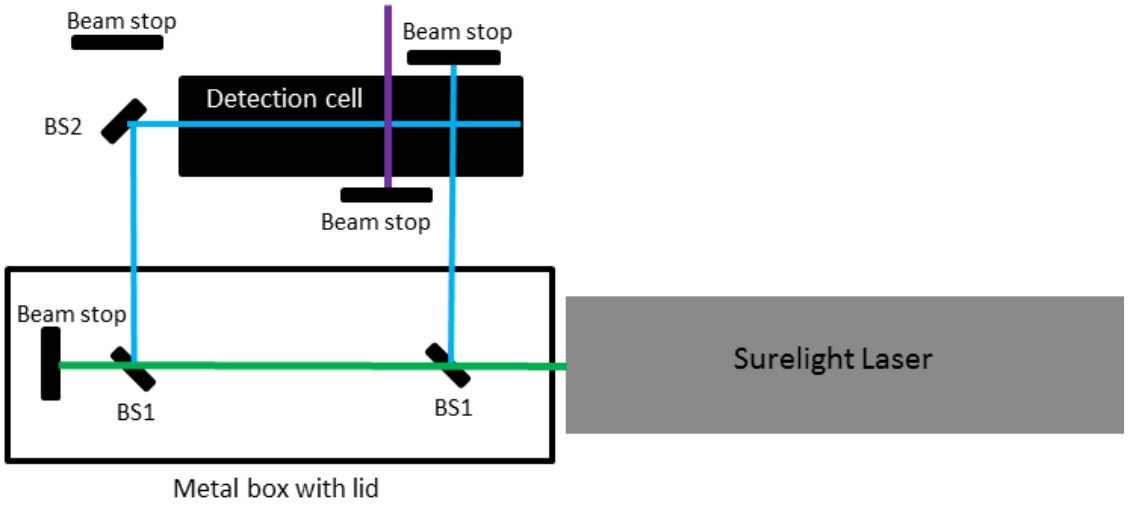

Figure 3.19. Diagram showing layout for the photolysis laser system. The green light represents the mixture of 1064 nm, 534 nm and 355 laser light. The blue lines represent the 355 nm light and the purple line represents the 308 nm light. BS represents the beam splitter/coated dichroic mirror.

The figures, 3.20 and 3.22, below show the results from the cross axis orientation. In the presence of HONO this produced a large signal compared to the background (figure 3.22). The shape of the curve is likely caused by the flow profile down the cell, with the steeper leading edge due to the faster moving air in the centre, while the longer trailing edge is due to the dilution within the cell and slower moving air near the walls of the cells. In this set up the photolysis laser is roughly 4 cm upstream of the probe laser, this leads to the OH generated diffusing away from the horizontal axis that the probe laser measures across so not all of the OH generated following HONO photolysis will be measured. This effect could be reduced by moving the photolysis and the probe laser closer together so that they almost overlap. This will reduce the amount of diffusion, maximising the amount of measured OH. The reason that this method has yet to be tested is due to the fact that we are delivering the OH probe laser via a fibre. This means that both the photolysis and probe laser are unable to enter the cell from the same side as previous groups have done by free-beaming their probe laser. And by introducing the photolysis laser opposite to the probe laser there is a chance that the fibre may be damaged due to the higher energy of the photolysis laser if it is hit.

Results from the down axis orientation (3.21 and 3.23) showed a large signal in the background scan, as seen in figure 3.23 , due to laser scatter caused by the photolysis laser. It is unknown why the scatter from the 355 nm light is seen by the detector when a 308 nm barr filter is present between the main cell body and the CPM, however it is assumed that it is due to the intensity of the 355 nm light being high enough that not all of it will be removed as it passes throught the filter, blocking intensity at 355 nm 10^6. In the background scan a second peak is seen, figure 3.23, and this is caused by OH being generated at the pinhole when the photolysis laser impacts it generating a plasma which is generating OH. This signal was determined to be caused by OH fluoresence as when the probe laser was blocked only the laser scatter peak was visible. Although compared to the actual signal seen in figure 3.21 this plasma signal is relatively small, it will become more of an issue when measuring ppt levels of HONO.

From these two orientations it was thought that the across axis set-up would provide the more reliable results due to the lower background.

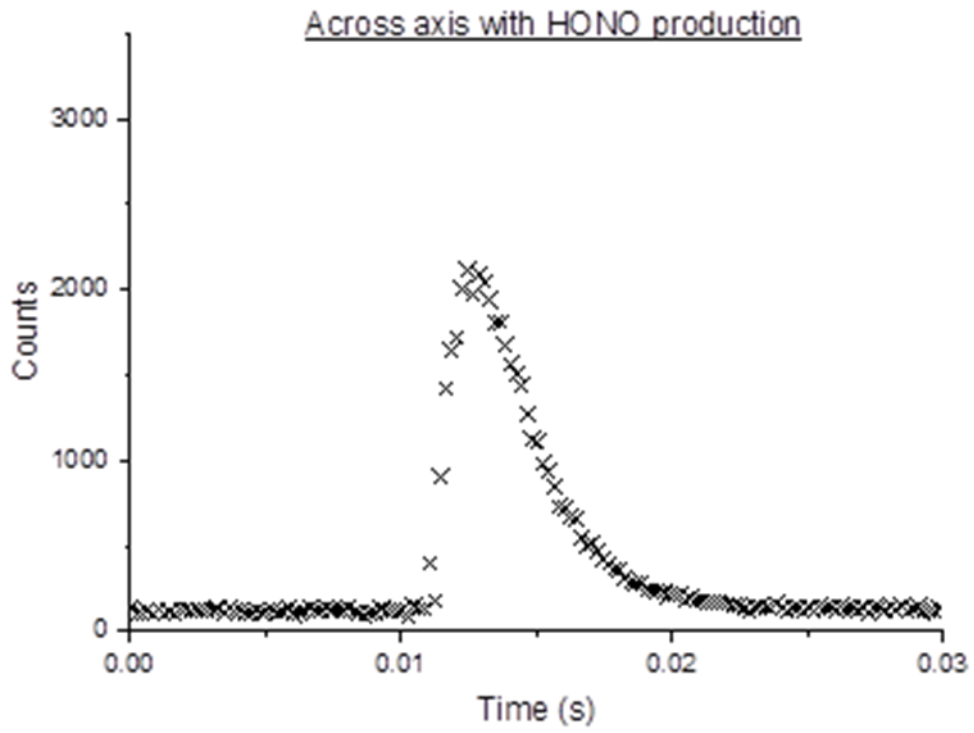

Figure 3.20. Measurement plot with HONO being introduced to the detection cell.

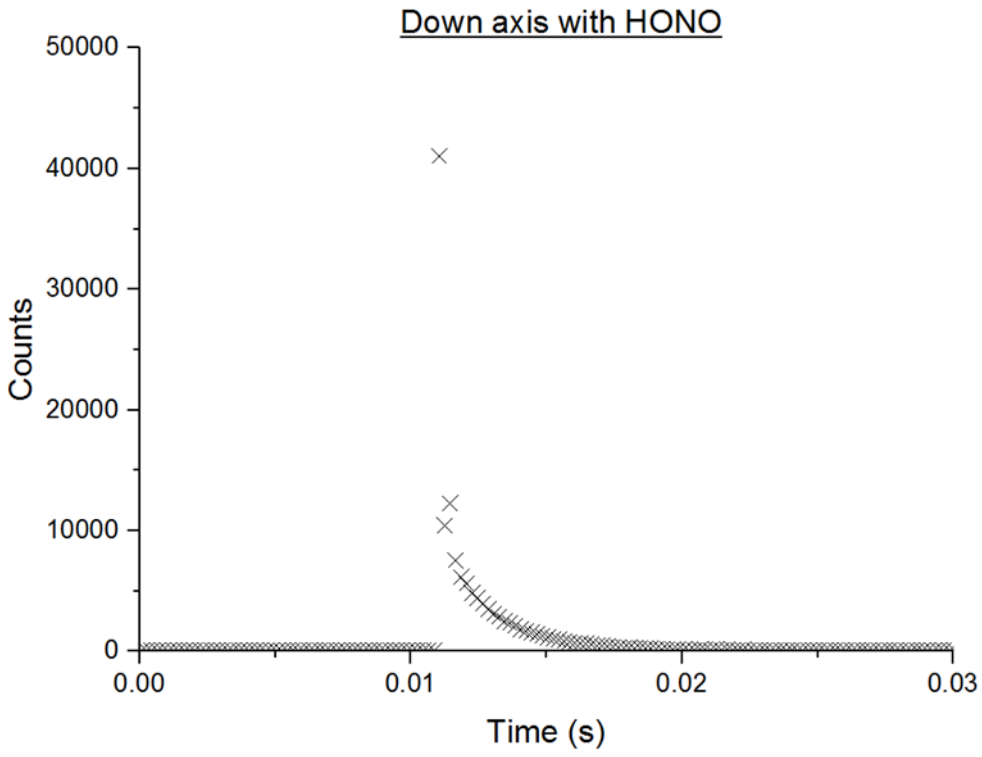

Figure 3.21. Measurement of HONO using the down axis orientation showing the curve generated.

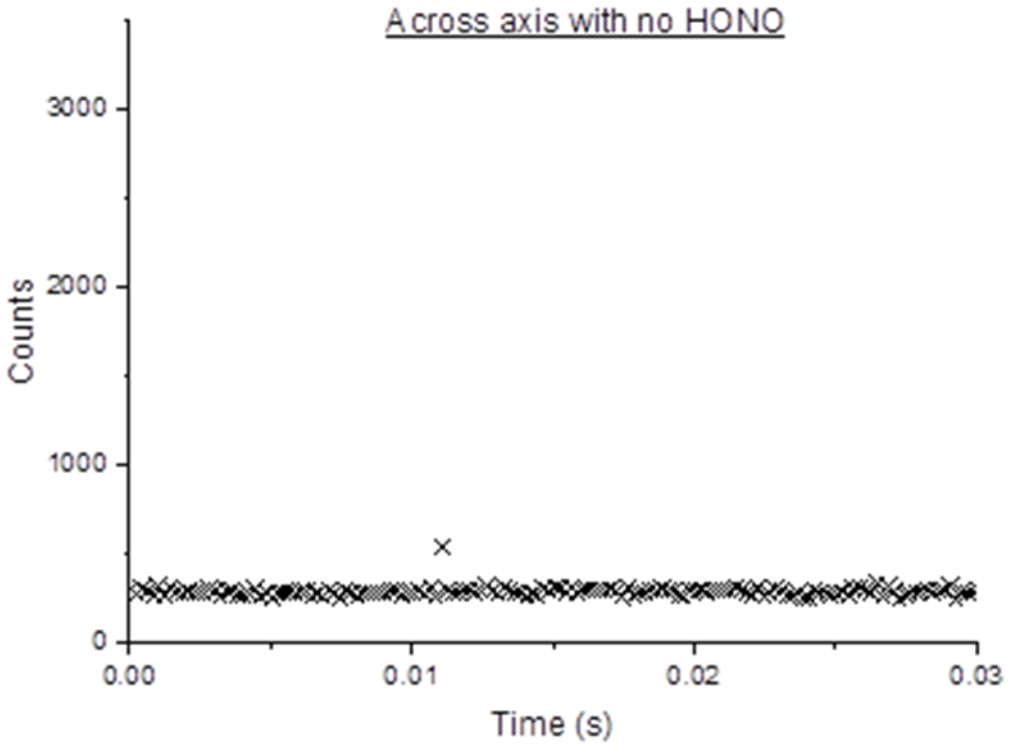

Figure 3.22. Background measurement with only H_2O and N_2 entering the cell. The higher baseline signal is due to the production of OH in the wand which is removed when NO is added to produce HONO.

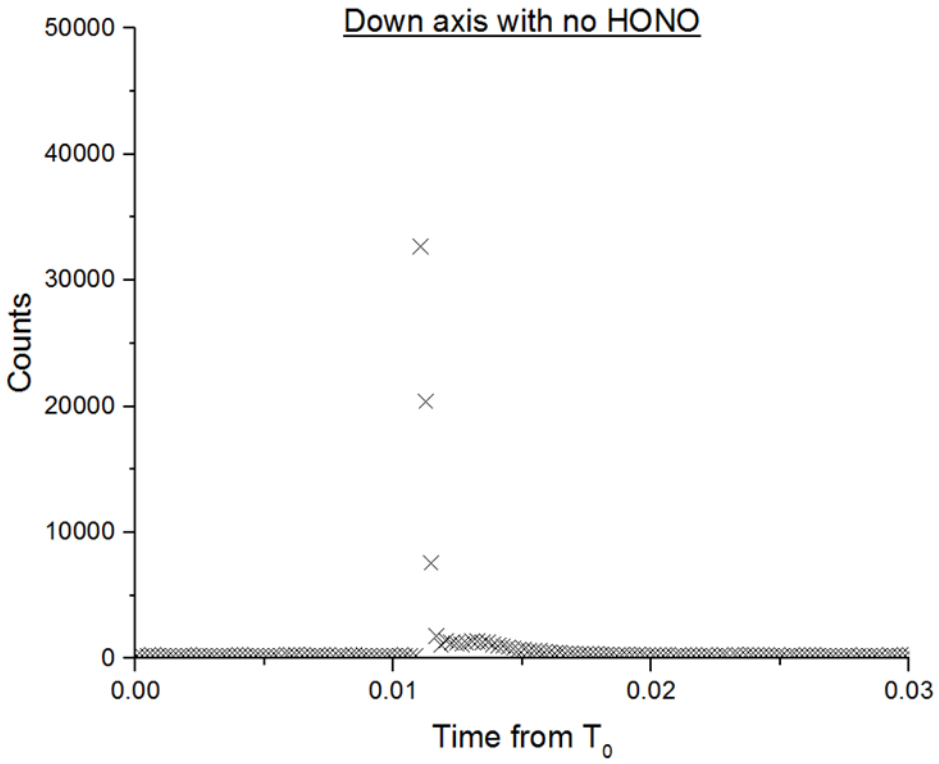

Figure 3.23. Background measurement for the down axis orientation showing the large peak caused by laser scatter from the photolysis laser.

3.4.4 Background Signal

In the earliest instrument configurations, the majority of the observed signal was not linked to the presence of HONO in the system. Decreasing this background signal observed has been the biggest challenge so far in the development of the PF-LIF instrument. The background signal is shown in figures 3.24 shows the laser scatter and plasma peak discussed above. Peak A remains when the probe laser is either tuned away from the OH transition (offline) or when the probe laser is blocked and, therefore, is not related to OH. By removing the pinhole, this allowed the laser to pass straight through the cell (these measurements were carried out at atmospheric pressure) peak A disappeared, indicating that it is generated by scatter of the photolysis laser off the pinhole surface.

Peak B is an OH signal. However, this is OH generated by the photolysis laser hitting the metal surface of the inlet generating a plasma which in turn generates a high concentration of OH. Peak B was determined to be OH as the signal disappeared when the probe laser was tuned away from the OH transition.

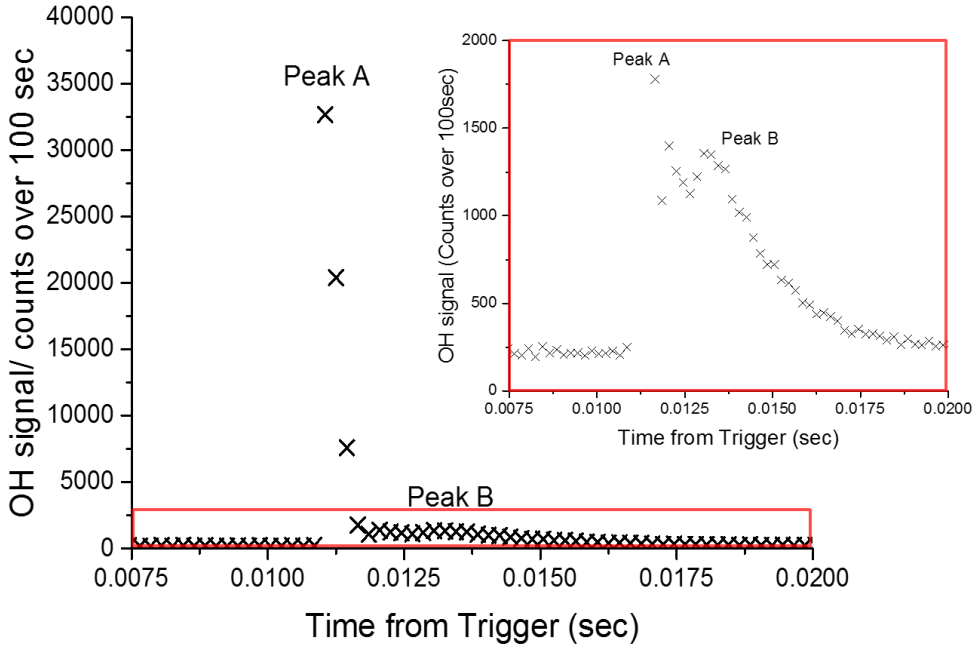

Figure 3.24. Figure showing the initial background signal observed when sampling a nitrogen flow. This shows the large peak A generated by laser scatter and peak B which is a plasma generated OH signal. The insert shows an expanded view of the lower half of data.

3.4.4.1 Plasma Background

The plasma generated OH background can be observed in several probe pulses and was found to vary in size meaning that it couldn't easily be subtracted from an overlying HONO signal.

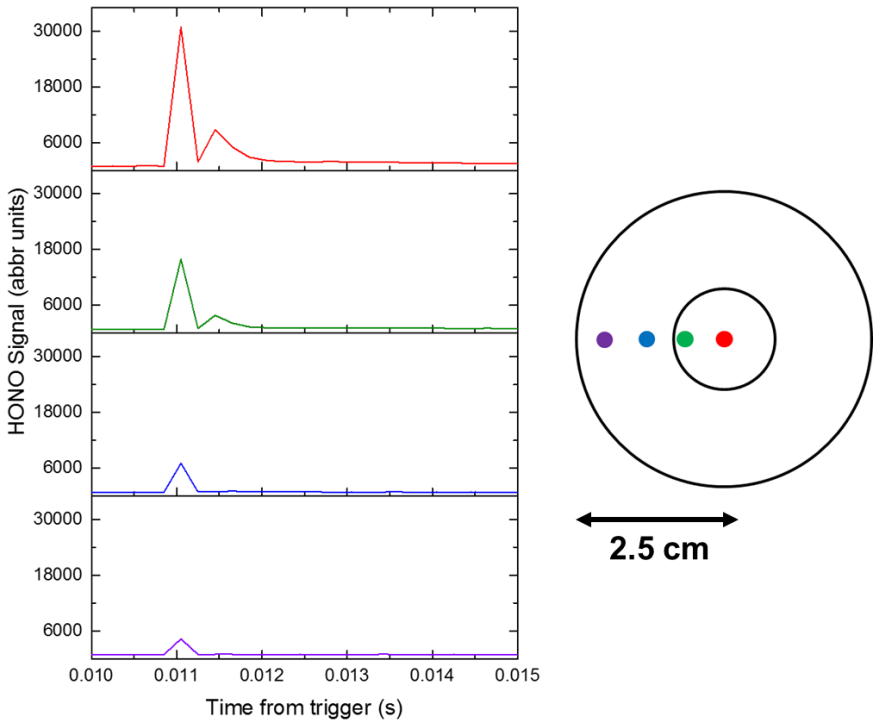

Figure 3.25. Plots showing the change to the background signal when the alignment of the laser down the axis of the detection cell is changed. The circular diagram shows where on the pinhole surface the laser hits. The inner circle is stainless steel and the outer part is black anodised metal.

It was found, however, that this plasma OH peak disappeared as the photolysis laser was walked away from the centre of pinhole. Figure 3.25 highlights that by adjusting the angle of beam splitter 2, fig 3.2, (and walking the photolysis laser away from the central axis – red to purple), the magnitude of the plasma peak (peak B) decreased. This suggests that it is necessary for the jet of sampled air, high density air immediately after the pinhole, to pass through the plasma to either provide the species/density needed to generate OH or to provide the gas flow to carry the OH away from the plasma at the surface to the detection region. Based on this hypothesis and experimental results, a new inlet was designed to allow for the photolysis laser to remain along the central axis, so that the OH generated is less likely to be lost to walls, but separates the pinhole from the plasma. Figure 3.26 below shows the new inlet design that uses an off centre pinhole and a turreted beam dump.

The turreted section creates a dead zone of air in the cell preventing any species generated by the plasma from being pulled into the cell. The off centre pinhole should have little impact on HONO loss as, unlike OH, HONO is a stable gas and so is not lost as quickly to walls. The effect on the flow inside the cell is not known, however, it is assumed that the jet quickly breaks up into a uniform flow away from the pinhole.

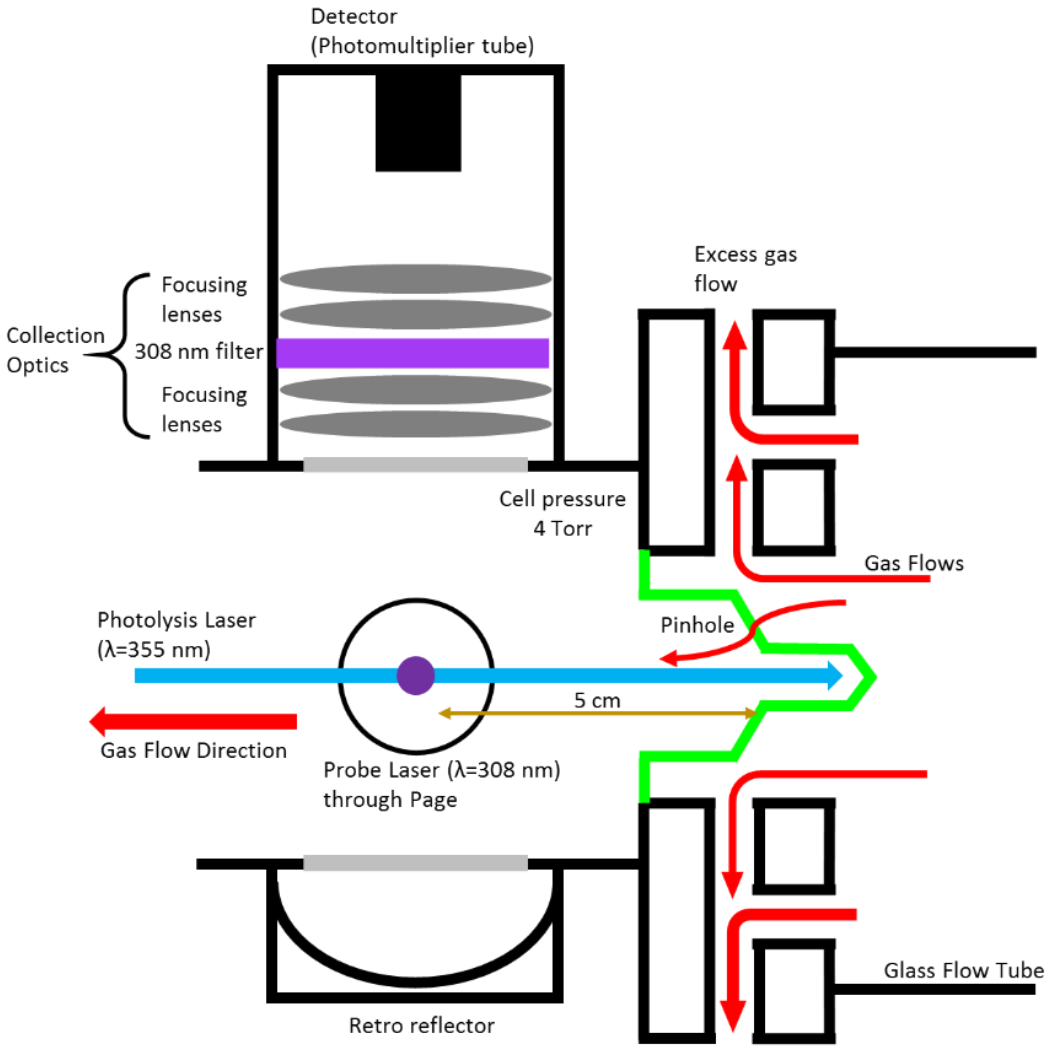

Figure 3.26. Cross section of the detection cell. The new inlet is highlighted in green. The current pinhole has been designed to be coupled with a flange that connects to an aerosol flow tube which will be discussed in chapter 4.

The results from a measurement using the off-axis pinhole when sampling ambient air is shown below (figure 3.27). These results clearly show the complete removal of the plasma OH peak simply leaving the laser scatter peak and this peak can be easily subtracted using the offline signal, compared to the original flat pinhole (figure 3.28).

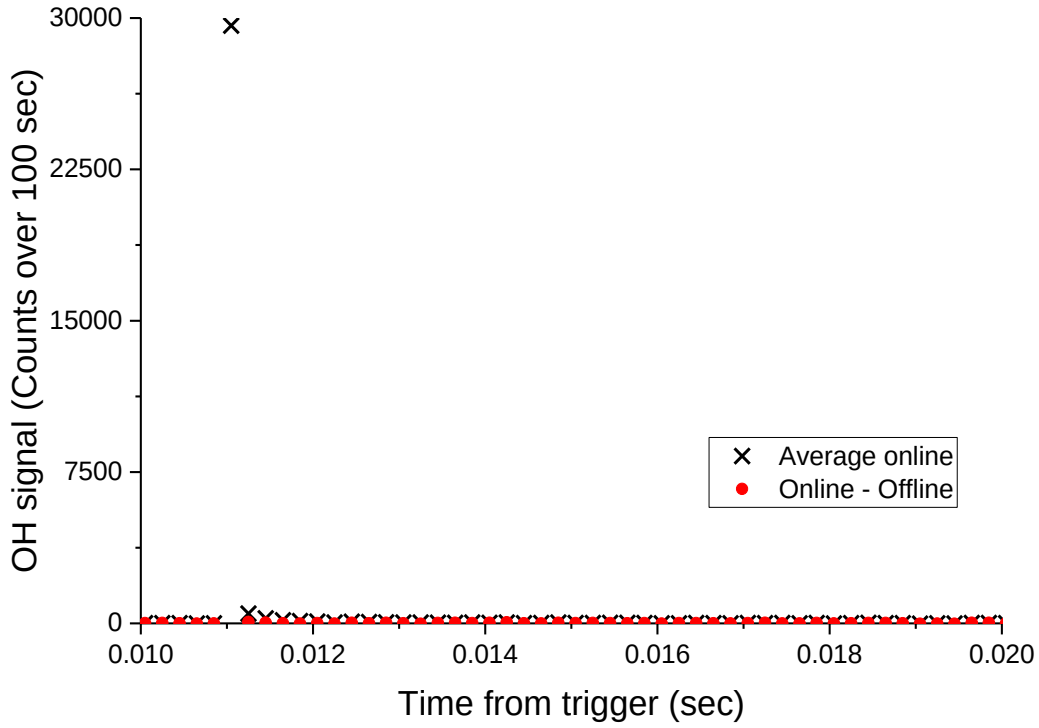

Figure 3.27. Plot showing the results using the redesigned turreted pinhole. The black points shows the online signal while the red points show the remain signal after the OH offline has been subtracted from the online signal.

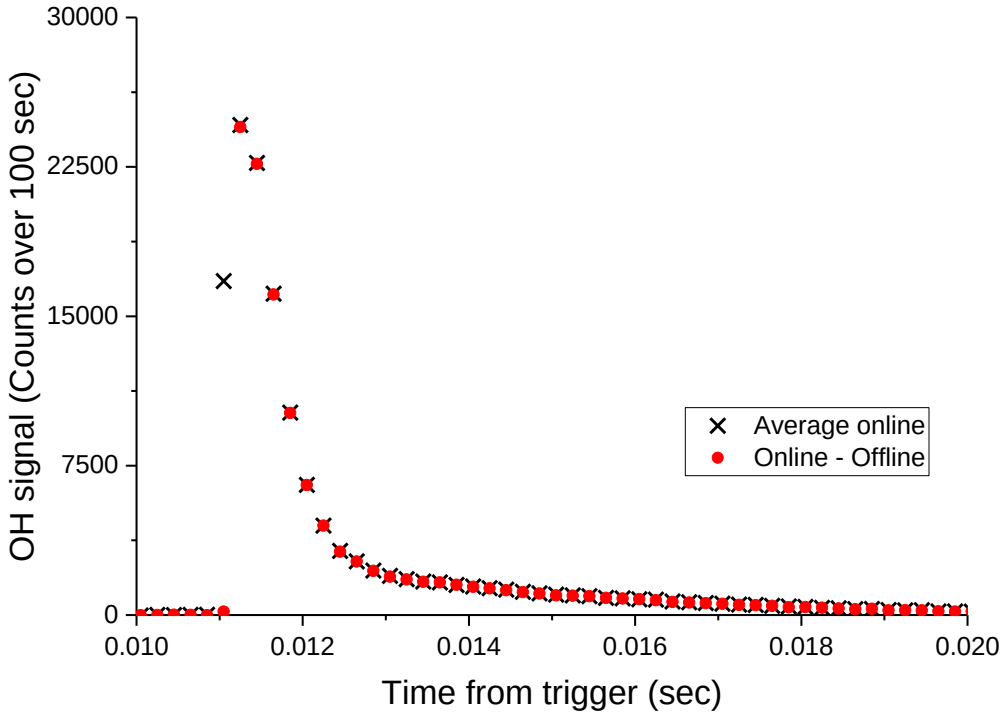

Figure 3.28. Plot showing the results using the original flat pinhole. The black points shows the online signal while the red points show the remain signal after the OH offline has been subtracted from the online signal. This shows that although the laser scatter peak is subtracted the plasma OH peak is not.

3.4.5 Decreasing Laser Scatter

Decreasing the laser scatter peak was important as the first few points after the photolysis laser (where the laser scatter peak is observed) are considered to be the most reliable as there is less time for secondary reactions to occur. Furthermore, the OH signal is at its maximum due to minimal diffusion away from the central detection axis.

3.4.5.1 Gating

The first method that was tried was to set the timings of the photolysis laser so that the 355 nm laser pulse occurred during the period when the detector was gated off during the probe laser pulse so it is not detected, see figure 3.5. In order to do this a fast photodiode was used to determine the delay between the trigger sent to the photolysis laser and when the laser pulse fired. When measuring the signal using the CPM detector it was found that the peak was close to 50000 counts when the laser pulse was positioned before and after the gating period but dropped to 3000 when positioned under the gate. This is a significant improvement with the remaining signal being due to some remaining scattered light that is not completely covered by the gate.

3.4.5.2 Counting card bin width

It is possible to adjust the bin width on the photon counting card. A bin is a time period over which the counting card will count pulses sent by the detector in response to the detection of a photon. A longer bin will result in a larger signal as it will integrate more counts into a single bin value. However, when measuring the fluorescence from OH, the majority of the signal is gone within the first 1 μs following the probe laser due to the short fluorescence lifetime of OH. By decreasing the bin width from 50 μs to 1 μs helps to decrease the laser scatter signal without decreasing the OH fluorescence signal. Figure 3.29 shows a zoomed in measurement of the laser scatter peak including all bins. For this experiment the probe laser was turned off so that the signal is solely from the photolysis laser scatter. By decreasing the bin width both the magnitude and the lifetime of laser scatter peak decreases as the signal from the laser scatter becomes spread over multiple bins, many of which can be ignored as fluorescence from OH will not be present in them. For the experiments described in chapter 5, the bin width was set to 2 μs.

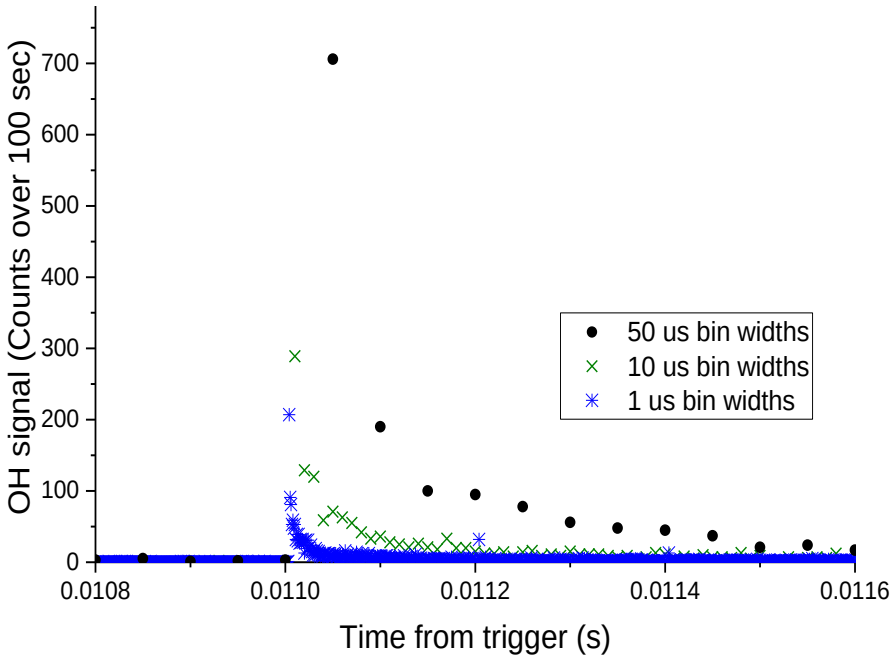

Figure 3.29. The decrease in counts as the bin width is decreased. Data from this plot also has the mirror in place, details of which are discussed below.

3.4.5.3 Addition of an internal mirror

A mirror was mounted inside the turreted section of the new pinhole with the aim of decreasing the scattered light further. The mirror prevents the 355 nm photolysis laser from hitting the bare metal surface of the pinhole and scattering randomly. Furthermore, with the mirror in place, the laser light is reflected back along the same axis with minimal scatter and so can potentially enhance HONO photolysis. In order to avoid any problems caused by the photolysis laser light following a path back to the laser, the laser light was directed along a slight angle in the cell so that its return path from the cell would miss the beam-splitter. Figure 3.30, has two overlaid OH offline background scans and highlights that the background has been reduced significantly from the original background with only a single peak of 100 counts remaining. This reduction in the laser scatter (from 30000 counts) results from a combination of mirror installation and changes to the bin width; using a bin width of 50 μs results in ~700 background counts from laser scatter.

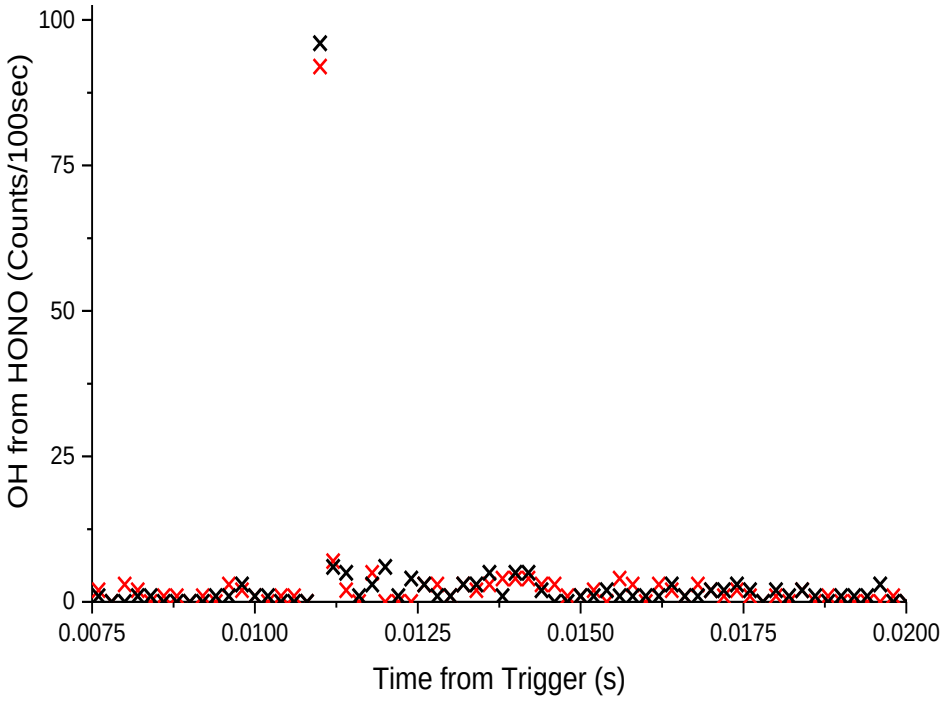

Figure 3.30. Two overlaid background scans, OH offline, after the bin width was reduced to 1 us and mirror put in place.

3.4.6 Run Repeatability

It was thought that the non-zero points after the main laser scatter peak could have been caused by a timing problem where the photolysis laser firing time might drift so that some of the scattered light might be seen in the adjacent bins. In order to ensure that any signal seen was not due to a variation in the laser pulse time that may change for each sweep, a repeatability test was done, by running 30 single sweep runs, ten 30 sweep runs and one 300 sweep run. Results from this showed very little variability between the same length runs indicating that there is no drift in the photolysis laser timing. The comparison between the sum of the ten runs with 30 sweeps and the 300 sweep run showed that when the shorter runs combined there is very little difference to the longer run indicating that the non-zero points after the laser scatter peak are not caused by a random drift in the timing of the laser pulses.

3.4.7 Addition of a Second 308 nm Filter

The aim for this experiment was to improve the removal of wavelengths other than 308 nm. To do this a second 308 nm coated Barr Associates filter was added after the standard optic set to improve the filtering efficiency. The background signal, shown in figure 3.31, shows that the laser scatter point is completely removed when two filters are used. However this reduction of the background is less beneficial as there is also a reduction of the online signal (figure 3.32). This is because although the Barr filter is coated for the 308 nm wavelength, only 50% of light at this wavelength is transmitted, this is demonstrated by the ~50 % drop in signal, seen in the online plot, when the second filter is present. From this it has been decided that a single filter will be used as the losses seen in the online signal where not regained by the reduction in the background.

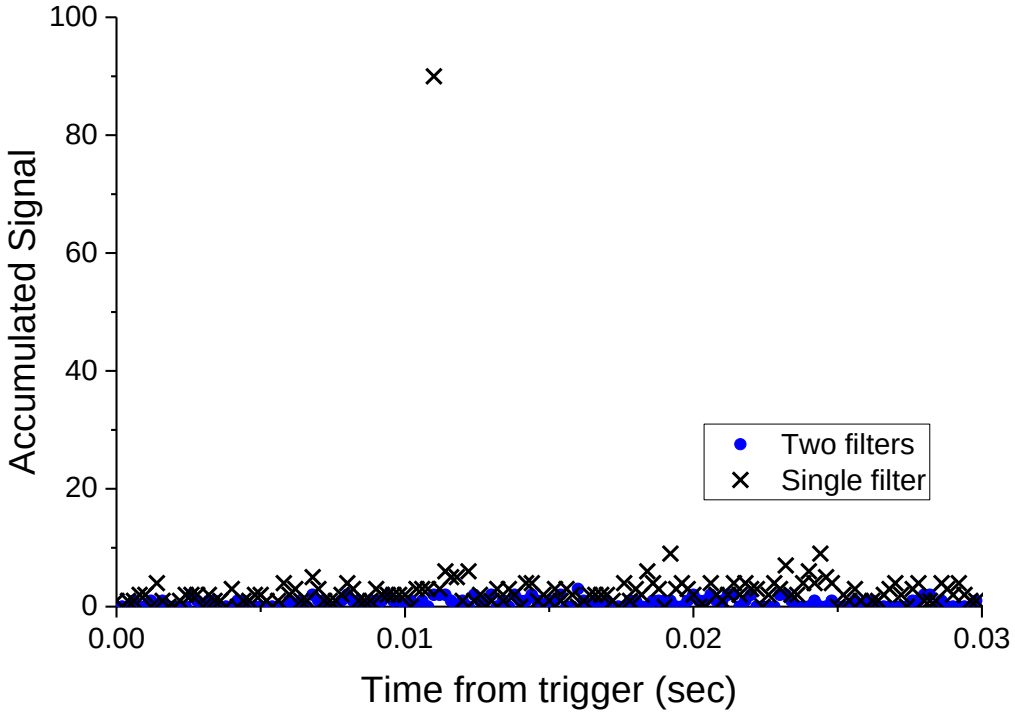

Figure 3.31. Offline signal. Comparing the results using a single Barr filter (black) and two Barr filters (blue).

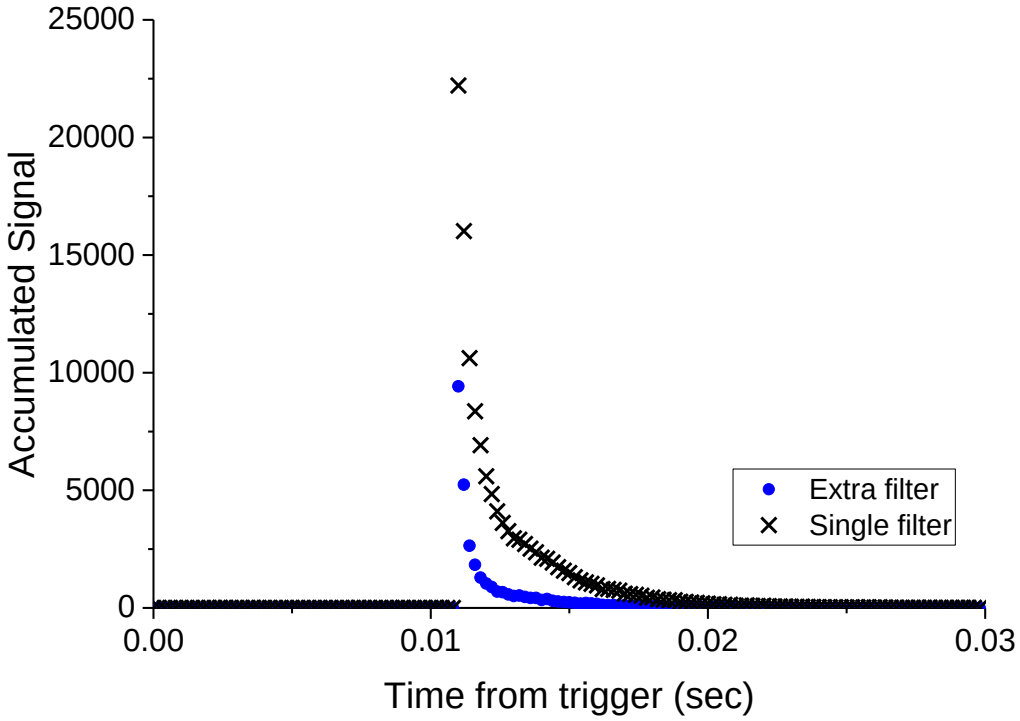

Figure 3.32. Online signal. Comparing the results using a single Barr filter (black) and two Barr filters (blue).

3.4.8 Dependence of HONO Signal on Detection Cell Pressure

A change in the cell pressure has two effects in the detection cell. At higher pressures the density of the gas in the cell will be higher which will result in a higher concentration of HONO that will be photolysed and therefore a larger OH signal. However, the fluorescence lifetime of molecules decreases as pressure increases due to increased quenching rates caused by the higher frequency in collisions. In the FAGE measurements of OH, low pressure is required to extend the fluorescence lifetime beyond the lifetime of the laser scatter at the same wavelength. Figure 3.33 shows the effect of pressure on the HONO signal, with the plot showing the balance between these two effects where, as pressure increases the increased number density increases the signal. However, above 4.5 Torr the gains in number density are lost due to a decreasing fluorescence lifetime. It may be possible to increase the pressure further with faster gating and a shorter probe laser pulse as this will allow measurements closer to the probe laser where the OH fluorescence is at a maximum.

This pressure dependence can be compared to the theoretical pressure dependence calculated for the fluorescence signal measured in FAGE cell at increasing pressure. Figure 3.33 shows how the fluorescent signal is dependent on the OH density in the cell, which increases with pressure and the fraction of OH that returns to the ground state via fluorescence, quantum yield, which decreases as pressure increases due to the increased rate of collisions that quench the excited OH[105]. The difference in the experimental to the literature are likely to be due to a combination of the results not following the ideal conditions the literature values depend on. The conversion of HONO to OH is also not considered in the model as the conversion efficiency for the photolysis process will also depend on pressure.

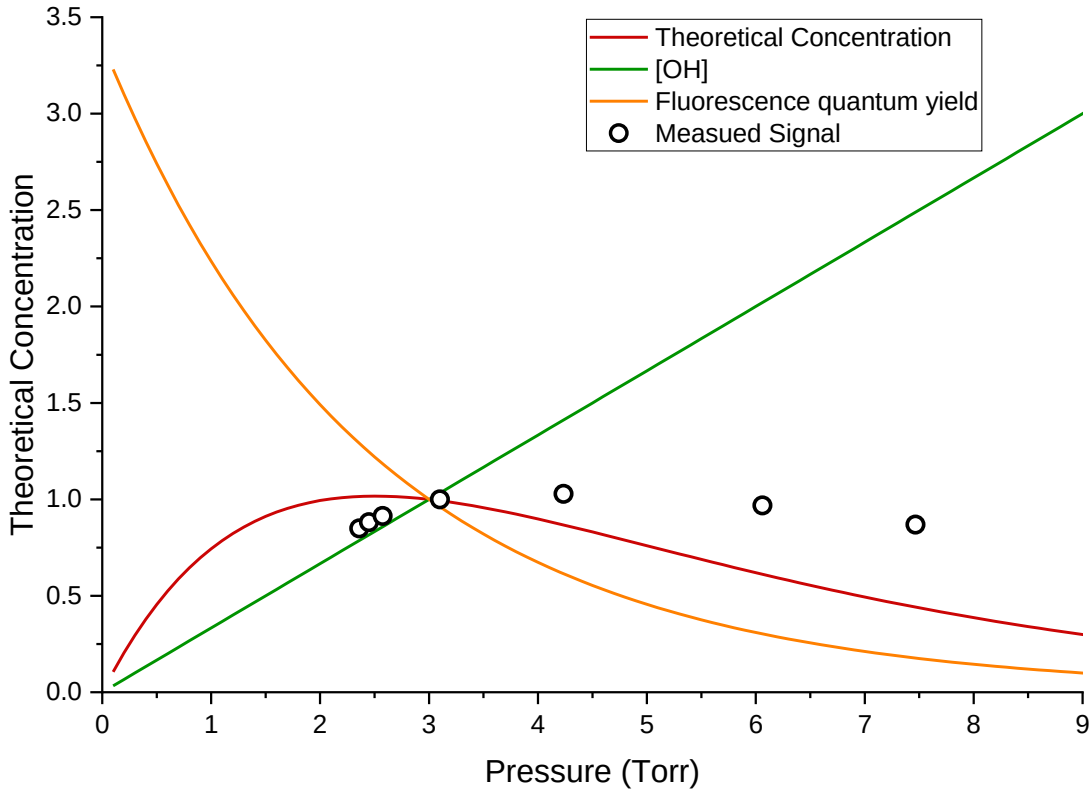

Figure 3.33. HONO pressure dependence normalised to the signal at 3 torr (black circles) compared to the theoretical sensitivity pressure dependence (red). The theoretical pressure dependence is defined by the OH concentration (green) and the fluorescence quantum yield (orange).

3.5 Summary

In this chapter the photo-fragmentation laser induced fluorescence instrument (PF-LIF) that has been developed has been discussed along with a comparison of previous techniques. A suitable gas phase calibration technique has been developed that allows for the generation of known concentrations of gas phase HONO. The calibration technique could be improved, however, by minimising the HONO background in the gas standards used. The optimisation of the instrument has also been described. This work demonstrated that a pulsed laser source was the most effective method for HONO photolysis in a FAGE cell. Overlapping the photolysis laser with the probe laser and, thereby, facilitating immediate detection of the OH product following the photolysis of HONO maximises the sensitivity of the technique. In the Leeds design this overlap has been achieved by aligning the two lasers perpendicular to one another. This laser orientation, resulted in with the requirement to move the pinhole away from the central cell axis to minimise the effects of laser-induced plasma OH at the pinhole surface. Chapter 4 will discuss the coupling of the PF-LIF instrument to an aerosol flow tube to allow the measurement of heterogeneous HONO production from illuminated aerosol surfaces.

Chapter 4 Production of HONO from Aerosols

This chapter will describe the experimental setup used for the measurement of production rates of HONO from aerosols. The results from experiments carried out using titanium dioxide and two nitrates, ammonium and sodium, are also shown. These laboratory experiments are being carried out to provide heterogeneous production data for atmospheric models in order to explain the missing HONO source discussed in chapter 1. The use of an aerosol experiment was chosen over a coated wall experiment as the reactive surface in a coated wall experiment will change over time while the aerosols are constantly "fresh" allowing a more accurate study of a particular surface type. It is also easier to define the total surface area in an aerosol experiment, utilising a size and mobility particle analyser, over the coated wall which depends on assumptions of a flat surface. Previous studies of HONO production from aerosol studies are shown in table 4.1 below showing the instrument used and the calculated reactive uptake.

Table 4.1. Previous illuminated aerosol experiments investigating the production of HONO.

Aerosol Type	*HONO measurement*	*Reactive uptake*	*Reference*
α-pinene/O_3	LOPAP	$< 1 \times 10^{-7}$	R. Bröske et. al.[106]
limonene/O_3	LOPAP	$< 8.5 \times 10^{-8}$	R. Bröske et. al.[106]
catechol/O_3	LOPAP	$< 8.5 \times 10^{-8}$	R. Bröske et. al.[106]
limonene/OH	LOPAP	$< 8.5 \times 10^{-8}$	R. Bröske et. al.[106]
tolouene/OH	LOPAP	$< 8.5 \times 10^{-8}$	R. Bröske et. al.[106]
Humic acid	LOPAP	$2.6\times10^{-6} – 3.7\times10^{-6}$	K. Stemmler et. al.[57]
TiO_2	Chemiluminescence NO_x analyser	$1.2\times10^{-4} – 9.6\times10^{-4}$	R. Gustafsson et. al.[52]

In order to show any atmospheric impact that these aerosol will have they will be included in a 1D box model using the chemistry data from Beijing collected during the APHH measurement campaign carried out during the summer of 2017.

4.1 HONO production experimental setup

For these experiments the PF-LIF cell described in chapter 3 was coupled to a quartz glass flow tube in order to investigate the production of nitrous acid from aerosol surfaces when illuminated by UV light. A PF-LIF instrument was chosen over other HONO measurement techniques as it does not have an NO_2 interference. This is important as NO_2 is used in many of the HONO production experiments. No changes were necessary to the detection cell other than coupling the cell to a flow tube.

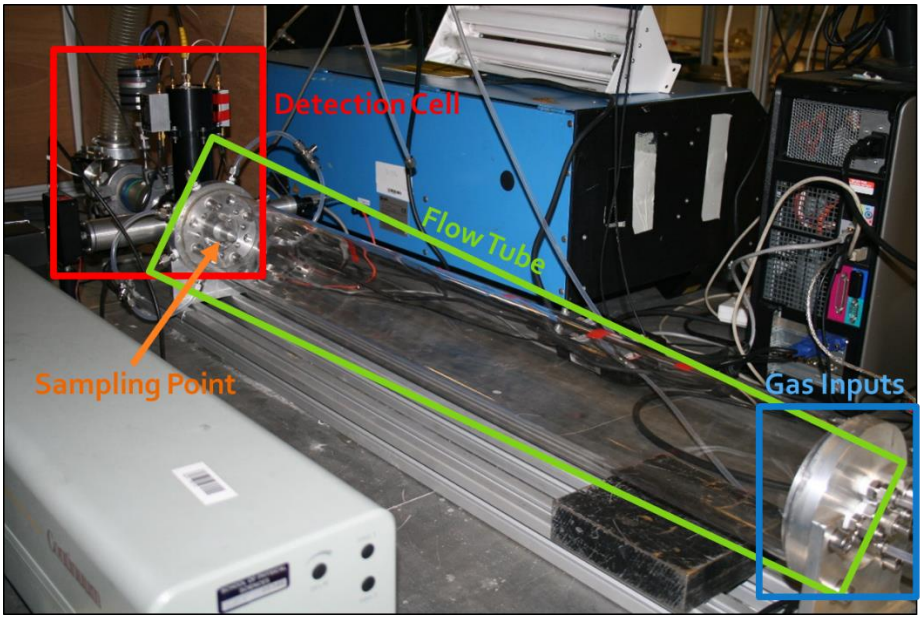

Figure 4.1. Image showing the experimental setup of the Leeds PF-LIF detection cell coupled to an aerosol flow tube.

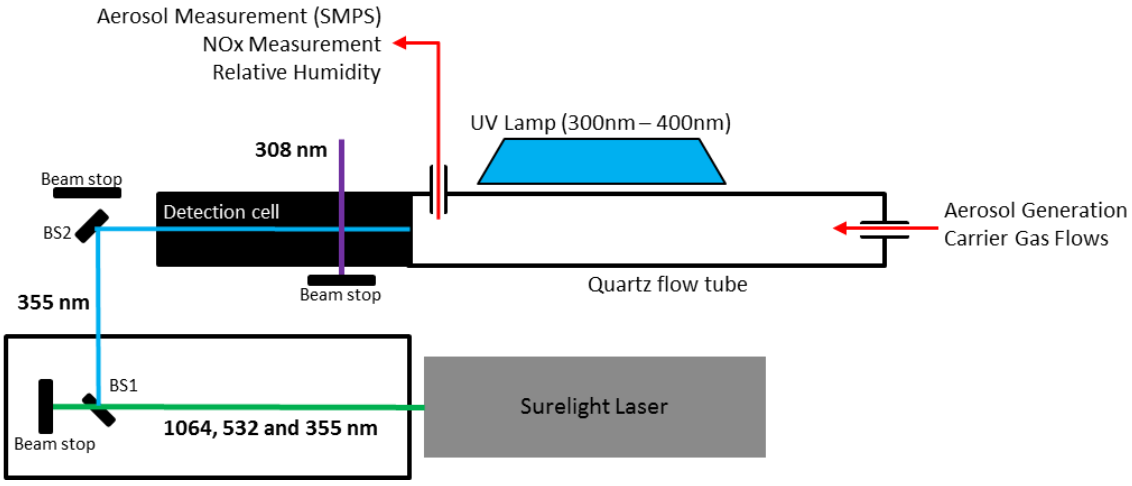

Figure 4.2. Top down simplified schematic of the Leeds PF-LIF setup for the measurement of HONO from illuminated aerosols, this shows the flow tube, detection cell and the orientation of the two lasers.

4.1.1 Cell coupling

Figure 3.27 shows the coupling used to attach the flow tube to the cell. The flow tube used in all the following experiments is 120 mm in diameter and made of quartz glass, to allow transmission of UV light. The tube was sealed to the detection cell by compression of an O-ring on the inner diameter of the tube at either end. There is also the possibility of connecting a 60 mm diameter flow tube to the cell with the fitting to allow measurements of faster reactions.

4.1.2 UV lamp

A UV lamp (UVproducts, XX-15LW Bench Lamp, 365nm) is placed outside the flow tube to illuminate the aerosol flow. This is used to investigate light induced heterogeneous reactions in the flow tube. The lamp used in the aerosol experiments described in this thesis is a 40 W lamp positioned on one side of the flow tube. Reactions that are photocatalytic will be affected by the amount of light the reactants are exposed to. In order to provide a comparison between the experiments and the solar spectrum the flux of the light inside the flow tube was calculated. Two methods where used; the first used a fibre optic cable connected to a spectrometer, and the second measured the concentration of NO produced from the photolysis of NO_2.

The spectrometer measurements show the wavelengths generated by the lamp and magnitude of light at each wavelength. This is the method used during field campaigns, with a 2-Pi actinic receiver optic to collect light equally across all angles, to measure the solar flux[107]. In the HONO experiment it is not possible to calculate an accurate total flux using this method as the measured output varied with the position of the fibre optic in the flow tube. Combining this with the second method where the photolysis of NO_2 was used to provide a value for the total flux across the entire flow tube. To do this NO_2 was added to the flow tube in increasing concentrations and the amount of NO produced, measured using a NO_x analyser (see section 2.3.1) from photolysis is proportional to the flux.

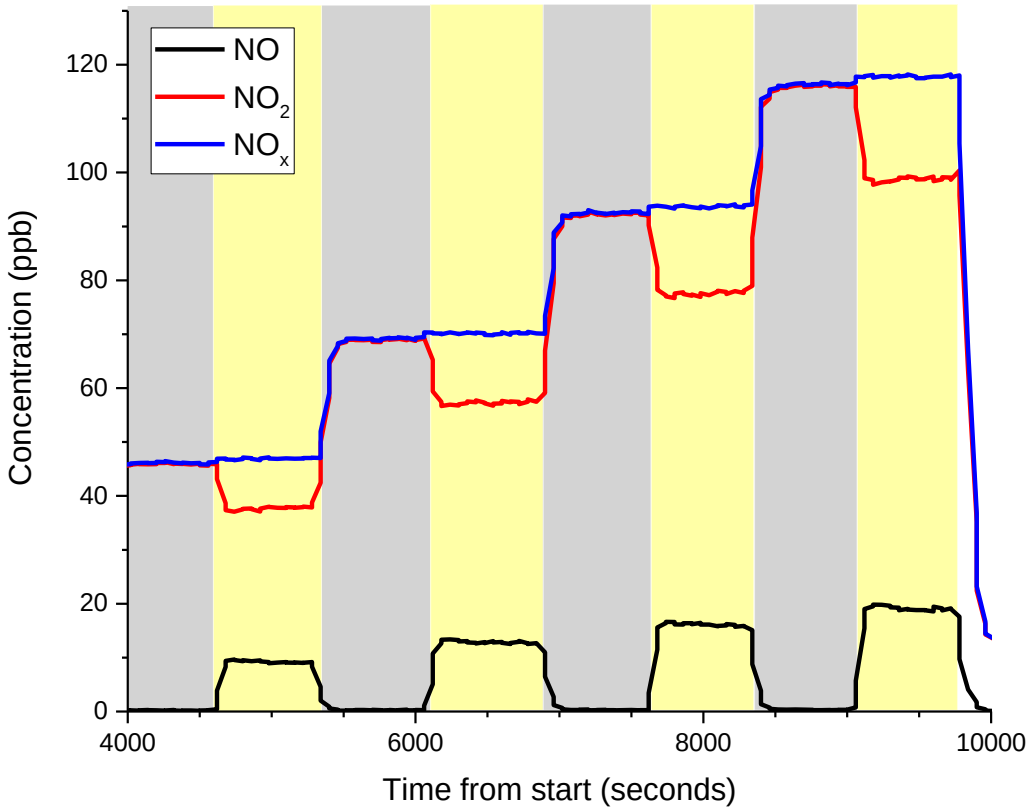

Figure 4.3. This plot shows the results from the NO_2 photolysis experiment. The coloured bars show the lamp state; grey = lamp off and yellow = lamp on. The blue line shows the total NOx concentration, the red line shows the NO_2 and the black shows the NO. This shows that when the lamp is on NO_2 concentration decreases while the NO concentration increases.

When NO_2 is photolysed NO and O is produced, the oxygen can either be in a triplet state or singlet state however due to the wavelength range of the lamp output only triplet state oxygen is produced[108]. The production of singlet oxygen only occurs below 244 nm where the lamp has no output, see figure 4.5. The rate of NO production is equal to the product of the [NO_2] and its photolysis rate;

$$\frac{d[NO]}{dt} = J[NO_2] \qquad \text{Eq(12)}$$

Converting this to the integrated rate equation and plotting the change in NO concentration versus the product of the initial NO_2 concentration and the reaction time allows calculation of the photolysis rate constant J from the gradient on the line, figure 4.4.

$$d[NO] = J[NO_2]dt \qquad \text{Eq(13)}$$

$$\Delta[NO] = J[NO_2]\Delta t \qquad \text{Eq(14)}$$

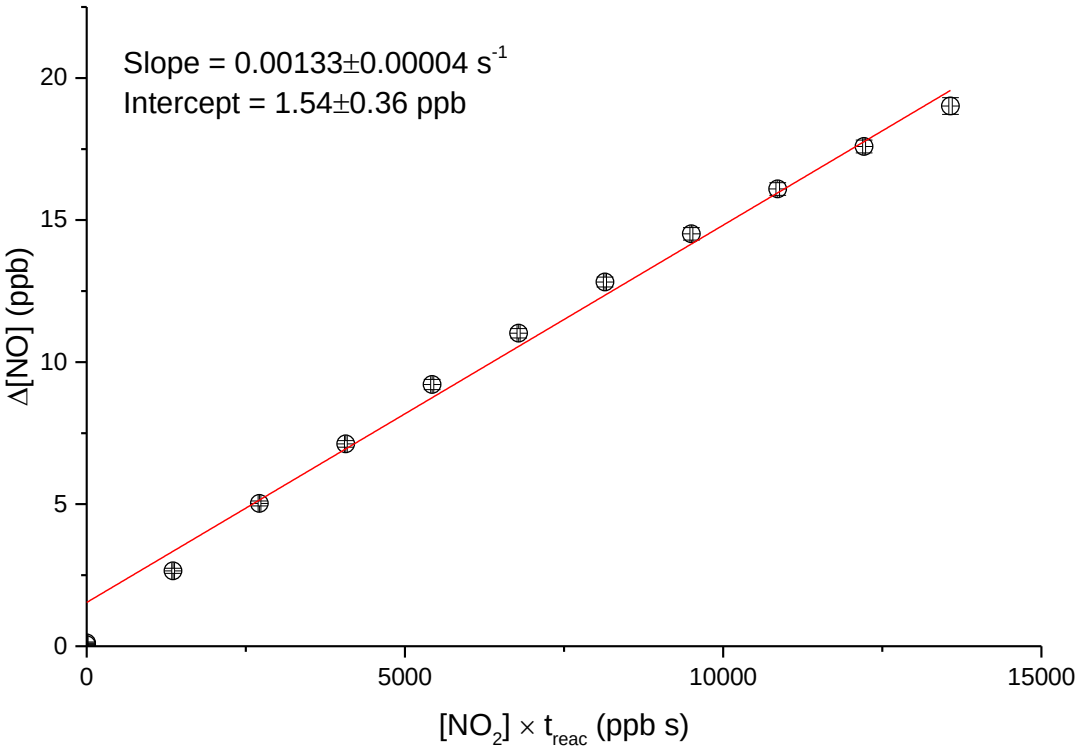

Figure 4.4. Plot showing concentrations of NO versus (NO_2 × t) where the slope of the line is equal to the photolysis rate constant, *J* (s^{-1}).

The value for *J* then allows the lamp flux to be determined using the following equation;

$$J = \int \Phi(\lambda,T)\sigma(\lambda,T)F(\theta,\lambda)d\lambda \qquad \text{Eq(15)}$$

Where *J* is the photolysis rate across all wavelengths and is the product of the quantum yield (*λ*, T), the absorption cross section (*λ*, T) and the total actinic flux (*λ*, T); the latter being the light source intensity. This flux value must be determined to allow comparison between experiments when lamps are changed and will allow the calculation of photolysis rate constants for other species i.e. *j*HONO present in the flow tube. For the photolysis rate of NO_2, the quantum yield is 1, the absorption cross section is taken from ref. [109] found on the "The MPI-Mainz UV/VIS Spectral Atlas" and integrated between 250 and 398 nm, figure 4.6. 250 nm is selected as it ensures that the full range of the lamp output is covered as there are some none zero values present below 300 nm. 398 nm is selected as an upper limit as photolysis of NO_2 does not occur above this value.

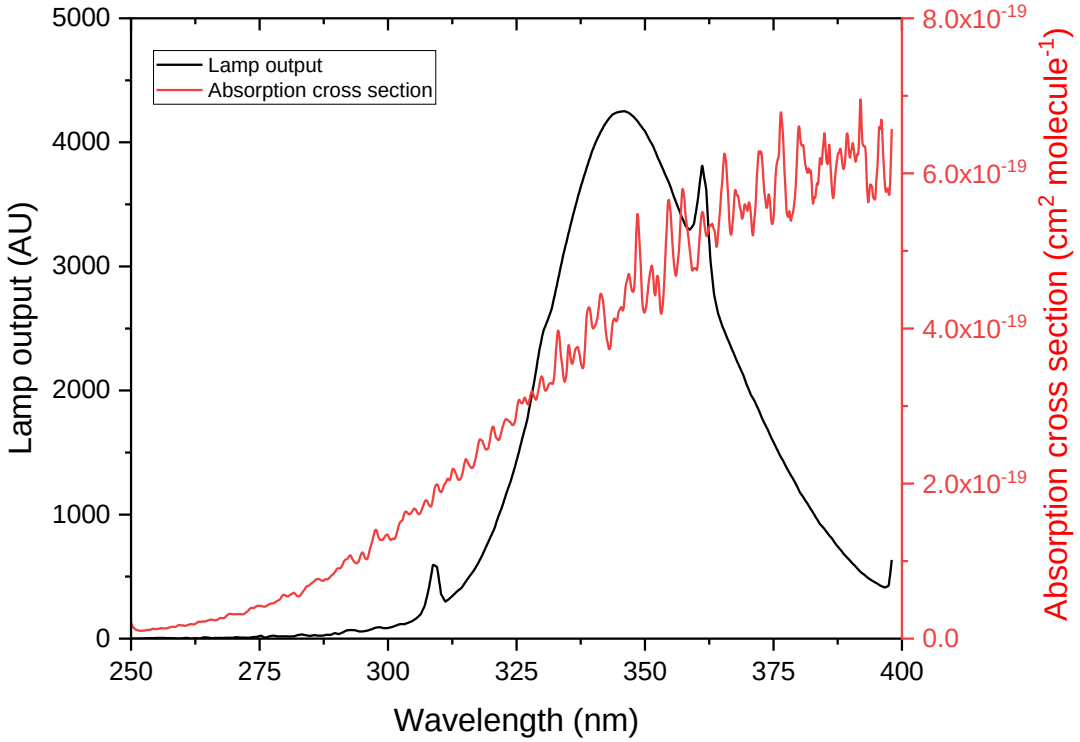

Figure 4.5. Overlap of the output of the UV lamp and the NO_2 absorption cross section for the region used in the calculation of the total flux inside the aerosol flow tube. The lamp output spectrum was measured using an ocean optics spectrometer. The NO_2 spectrum is taken from ref. [109] found on the MPI-Mainz UV/VIS Spectral Atlas. The intergrated cross section under the NO_2 spectrum is 4.46×10^{-17} cm^2 $molecule^{-1}$

It is then possible to use the integrated area under the NO_2 cross section as the absorption cross section σ, in equation 15 the quantum yield, Φ, is 1 and the value for J_{NO2} is 0.00133 s^{-1} taken from figure 4.4. Rearranging equation 2 it is possible to extract the total flux, 2.98×10^{13} molecule cm^{-2} s^{-1}. Using this in combination with the output spectrum of the lamp it is possible to determine the flux at the wavelengths that photolyse NO_2. The area under the curve for the lamp output where the NO_2 flux was measured is 189896.28417 AU, by making this equal to the total flux measured it will be possible to scale the flux depending on lamp output in the area of interest. For HONO, at the 354 nm wavelength, a photolysis rate constant, j_{HONO}, was calculated to be 3.87×10^{-7} s^{-1} ($\sigma = 5.81 \times 10^{-19}$ cm^2 $molecule^{-1}$, Φ = 1, $F = 6.66 \times 10^{11}$ molecule cm^{-2} s^{-1}). During the APHH campaign the maximum JHONO observed was 1.78×10^{-3} s^{-1}. This shows that

the current setup is below an atmospherically relevant flux. To increase the flux in the flow tube multiple lamps will be used to surround the flow tube.

Using a single lamp to illuminate the aerosol flow tube does have several drawbacks. The lamp output does not illuminate the full length of the flow tube and so it reduces the irradiation time experience by the aerosols. Secondly, the lamp is only positioned on one side of the flow tube and so the light field will not be constant across the flow-tube. These limitations could be solved by surrounding the flow tube with multiple lamps. A final drawback is that the current lamp primarily outputs in the UV meaning that reactions initiated at longer wavelengths, present in the solar spectrum, cannot yet be studied. Previous work by Stemmler et. al.[56, 57] found that HONO production showed a wavelength dependence, measured at 300–420 nm, 400–700 nm and 500–700 nm. Their results showed that at UV wavelengths the production of HONO from humic acid surfaces was greater than at the visible wavelengths. In the Leeds setup in the future studies of wavelength dependence are planned using either different lamp types or optical filters.

4.1.3 NO_2 Background

The aerosol experiments that have been conducted include studies into the production of HONO from aerosols when they are exposed to NO_2. In order to determine if there is a HONO background from the NO_2 gas generating HONO through wall reactions or the NO + OH reactions as NO is a product of NO_2 photolysis or from a HONO impurity in the cylinder, measurements were made of the HONO signal over a range of NO_2 concentrations. For this experiment a flow of NO_2 was diluted from a 2 ppm cylinder into a flow of humidified nitrogen to give concentrations similar to what are used in the aerosol experiments. The total flow through the flow tube was kept at 6 SLM and the full length of the flow tube was used, giving a residence time close to 2 min. At each concentration the HONO signal was measured under both room light conditions and when illuminated by a UVA lamp (300-400nm) and after each change the flow tube was given several minutes to equilibrate. The results from this experiment, shown below in figure 4.6, showed a small increase in HONO signal after the addition of NO_2. There was a slight increase in signal when the flow tube was exposed to UV light. The HONO signal gradually increased across the range of NO_2 concentrations. These results show that in the eventual aerosol experiments measurements of the background HONO signal without aerosols present will be required to account for the signal from the NO_2.

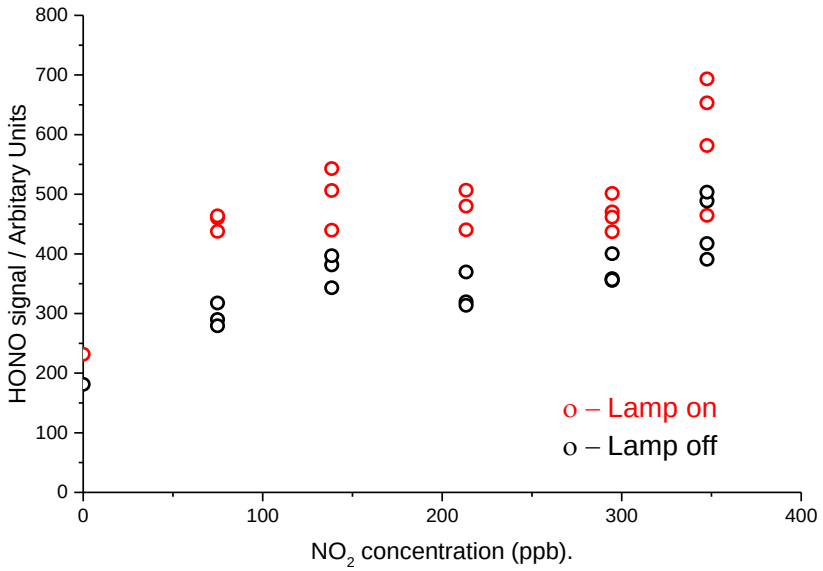

Figure 4.6. The effect of increasing NO_2 concentration on the HONO signal in the absence of aerosols. Each point uses the total OH signal across the measured curve.

4.1.4 Aerosol generation

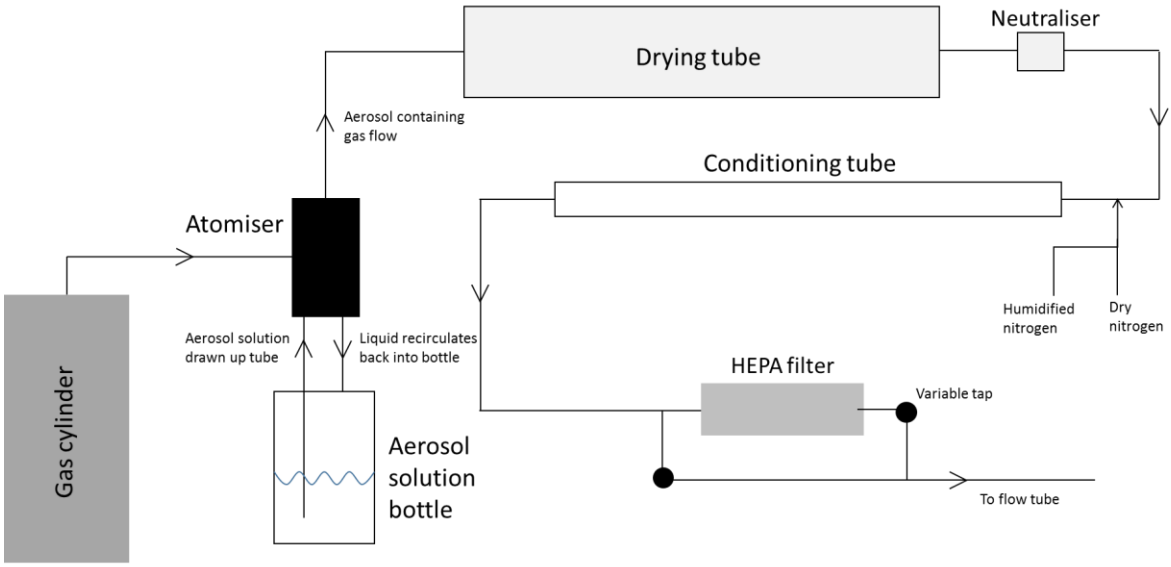

Figure 4.7. Schematic diagram of the aerosol generation system.

Figure 4.7 shows the complete setup for the delivery of the aerosols used in the heterogeneous HONO production experiments. To generate the titanium dioxide and nitrate aerosols a commercial constant output atomiser (TSI 3076) was used; a cross-section schematic of the atomiser is shown below in figure 4.8. The atomiser operates by passing a high pressure gas supply (N_2 or air) through a pinhole. This forms a high velocity jet. Liquid is drawn up from a reservoir and as the liquid steam enters the jet the liquid it is atomised. Larger droplets will impact on the wall of the atomiser and will return to the reservoir while small droplets become entrained in the gas flow and are carried out of the atomiser. The aerosol/gas flow exiting the atomiser is passed through a diffusion drying tube (TSI 3062) to reduce the relative humidity of the flow to below 15%. This reduces loss of aerosols to the walls but also allows RH to be controlled later on in the aerosol generation process.

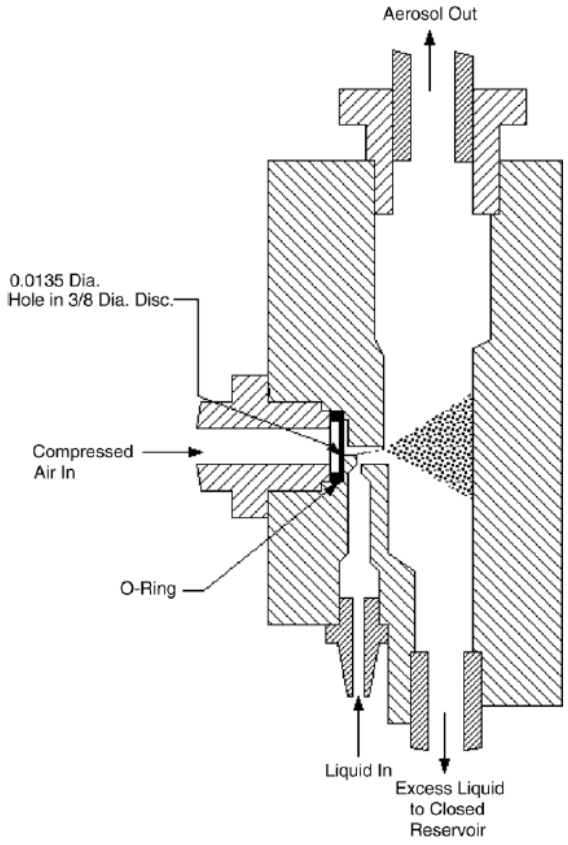

Figure 4.8. Cross section of the constant output analyser from TSI (model 3076)[110].

4.1.5 Neutraliser

The aerosols generated by the atomiser are highly charged due to a high frequency of collisions that occur[111]. This increases the loss of aerosols to the walls throughout the experimental setup due to coulombic forces. Aerosols that are highly charged are also more difficult to characterise using the Differential Mobility analyser (TSI 3080), described in section 4.1.8. After aerosols exit the atomiser they enter a neutraliser, reducing the overall charge of the aerosols. The neutraliser contains a radioactive source, Krypton-85, that ionises the aerosol flow into a balanced state of positive and negative charges. The radioactive source generates ions that the particles collide with, causing highly charged particles to lose some of their charge and low charge particles to gain some charge. To further reduce wall losses anti-static tubing (TSI, Conductive Silicon Tubing 0.19 inch ID) was used wherever possible to further reduce the loss of aerosols.

4.1.6 Control of relative humidity

After exiting the neutraliser, the flow from the atomiser is mixed with a humidified flow of nitrogen to adjust the RH in the experiment. The humidity of this flow is controlled by using two mass flow controllers, one is a dry nitrogen flow and the second is a flow humidified by passing nitrogen through a water bubbler. The ratio of the flows from these MFCs is altered to vary the resulting RH. After mixing with the humidified flow, the aerosols pass through a conditioning tube (~6 s residence time) allowing time for the aerosols to equilibrate with the surrounding environment, allowing absorption of water onto the aerosols and stabilised growth. The RH of the flow was measured using a humidity probe (Rotronics HygroClip2, accuracy $\pm$ 0.8 % RH) positioned in the exhaust flow after the flow tube.

4.1.7 Control of Aerosol Concentration

To determine an aerosol uptake number, the aerosol surface area must be varied. To vary the surface area of the aerosols the total number of aerosols are varied. The number of aerosols being delivered to the experiment are controlled by using a high-efficiency particulate (HEPA, PALL Life Science) filter with a bypass flow. By passing the total flow through the filter, 100 % of the aerosols are removed, while 100 % are delivered when the filter is fully bypassed by controlling the two fractions it is possible to vary the number of aerosols present in the flow tube, this can be seen in figure 4.7.

4.1.8 Monitoring Aerosol Surface area

As the aerosols generated by the atomiser are poly-dispersed in size it is necessary to characterise the size distribution in order to determine the total surface area. For this a scanning mobility particle sizer (SMPS) and a condensation particle counter (CPC) are used in combination and are connected to the apparatus after the aerosol flow tube. The SMPS extracts a known size fraction from the aerosol flow and the CPC counts the total aerosol number. Tests have been conducted where the SMPS and CPC were coupled to the experiment before the aerosol flow tube to assess losses on the aerosols to the flow tube walls. The surface area determined before and after the flow tube agreed within 10 %

4.1.8.1 SMPS

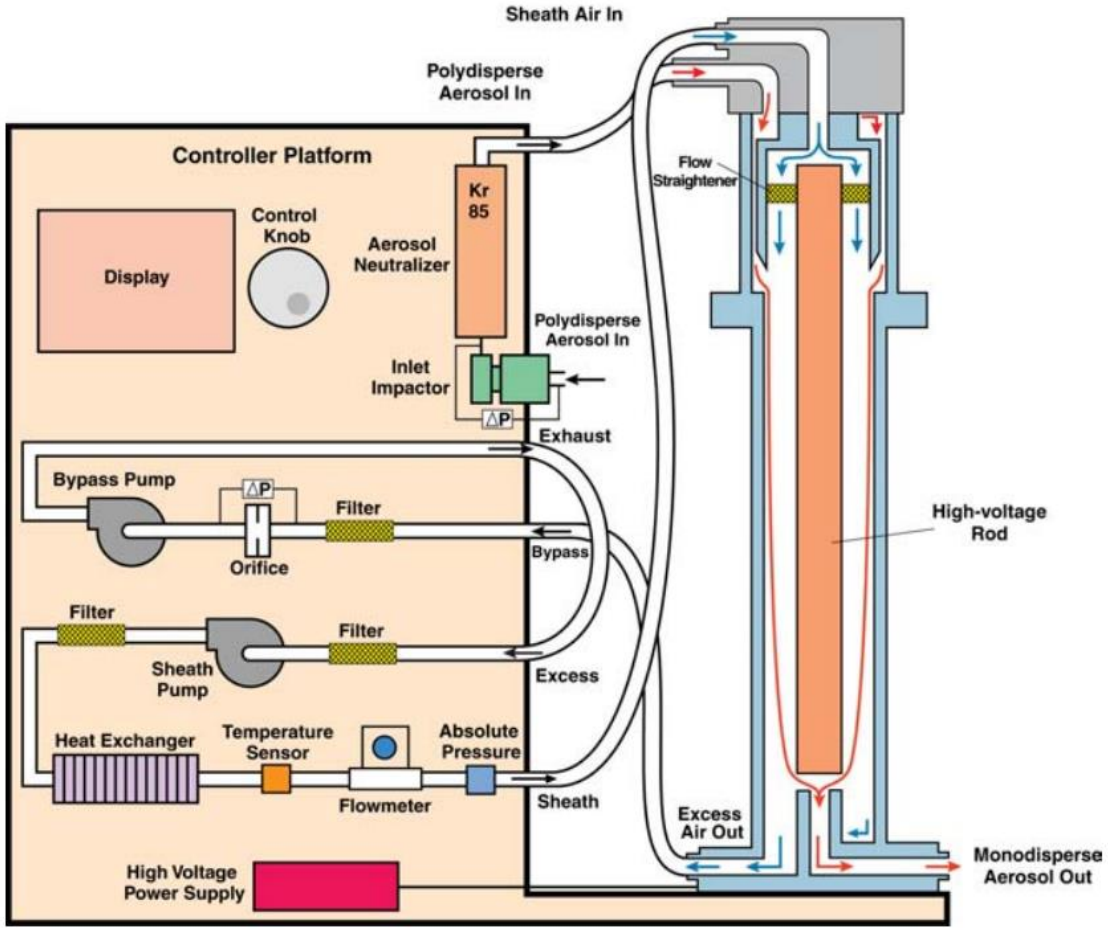

Figure 4.9. Schematic of the 3080 series SMPS model used in these experiments[112].

The SMPS is connected to the exhaust of the flow tube and samples at a rate of 0.3 L min^{-1}. Figure 4.9 shows a schematic of the instrument. As the schematic shows, prior to entering the SMPS, the flow first passes through an impactor (D50=1024 nm) that prevents large particles, that could block the instrument line, entering the instrument and then passes through a Kr-85 neutraliser that is needed to maintain the Boltzmann charge distribution, as described in section 4.1.5. The flow then enters the differential mobility analyser (DMA) which is responsible for the size separation of the aerosols. The DMA consists of a metal cylinder with a rod in the centre. The aerosol flow enters at the top of the DMA into a laminar sheath flow. The central rod has a high negative charge, while the outer cylinder is grounded.

This creates an electric field between them. Positively charged aerosols are attracted towards the central rod and will move though the sheath flow. The ability of these particle to move through the flow is described as the particles electrical mobility (Z_p) and as shown in equation 16, is dependent on the midpoint diameter of the particle, where n is the number of elementary charges on the particle, e is the elementary charge, C is the Cunningham slip correction and u is the gas viscosity[112].

$$Z_p = \frac{neC}{3\pi\mu D_p} \quad \text{Eq(16)}$$

Particles with a specific value of Z_p will flow out of the monodisperse aerosol outlet while the remaining aerosols flow through the excess air outlet.

$$Z_p = \frac{q_{sh}}{2\pi VL}\ln(\frac{r_2}{r_1}) \quad \text{Eq(17)}$$

Z_p can also be defined in terms of the parameters of the DMA tube, shown in equation 17[112], where q_{sh} is the sheath flow rate, V is the average voltage of the central rod, L is the length between the aerosol inlet and exit slit, r_1 and r_2 are the radii of the inner edge of the cylinder and the rod respectively. By combining equations 3 and 4 it is possible to determine the instrumental parameters required to select a particular aerosol diameter that will exit the SMPS, equation 5[112]. In this experiment the sheath flow was set at ten times the sampling flow at 3 L min^{-1}.

$$\frac{D_p}{C} = \frac{2neVL}{3\mu q_{sh}\ln(\frac{r_2}{r_1})} \quad \text{Eq(18)}$$

4.1.8.2 CPC

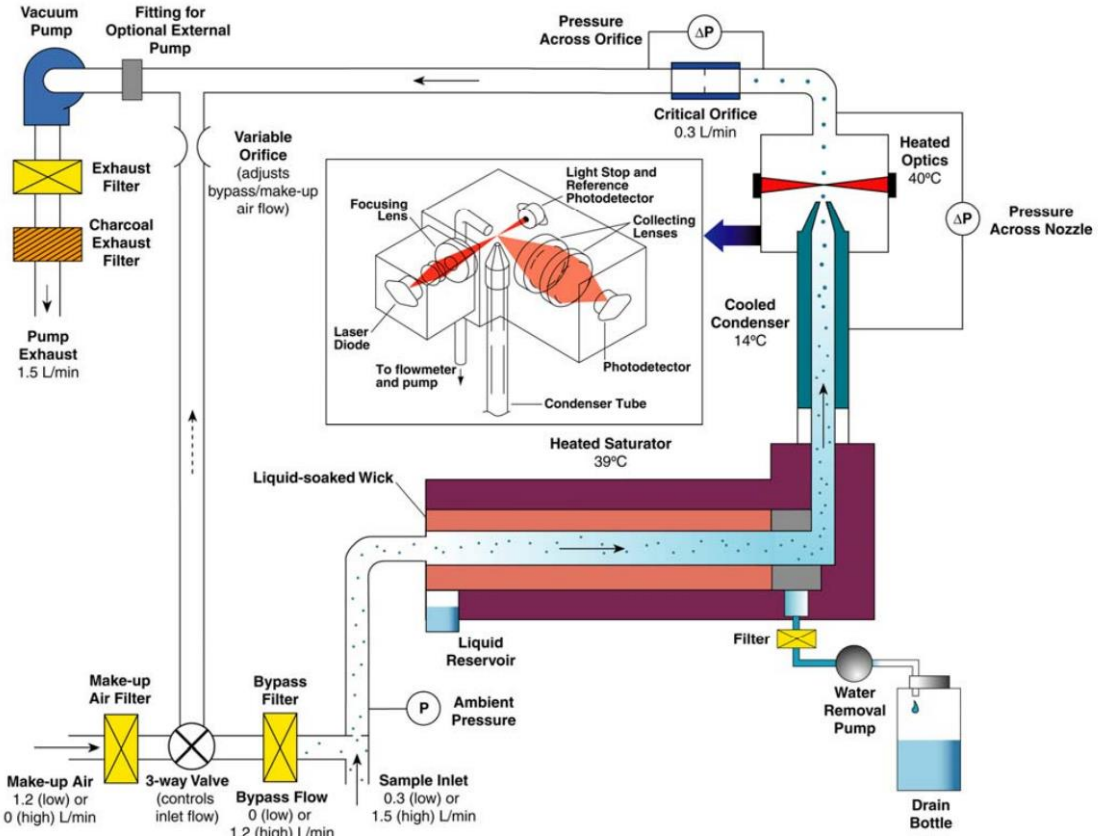

Figure 4.10. Schematic of the Model 3775 CPC schematic taken from reference [113].

The monodisperse aerosol flow then enters a CPC where the number of particles are counted. A schematic of the CPC instrument is shown in figure 4.10. Aerosols that enter the CPC pass through a cooled condenser containing butanol vapour. The butanol condenses on to the aerosols, growing them to larger diameters. This growth then allows each particle to be counted using an optical detector, consisting of a laser diode and a detector to measure the scattered light. When particle concentrations are below 5×10^4 particles cm^{-3} the instrument is able to detect individual particles. However, above this number multiple particles will pass through the beam at the same time resulting in an undercounting error. The instrument is able to correct for this by measuring the amount of scattered light[113].

Data is collected using the Aerosol Instrument Manager software (AIM v8.1.0.0). Each size distribution measurement takes 2 min 15 sec to run and is repeated every 3 minutes.

4.2 HONO Production from Aerosol Surfaces

Three aerosols were investigated for their potential to generate HONO under illuminated conditions. These were titanium dioxide (TiO_2) and two nitrates; ammonium and sodium nitrate. TiO_2 was chosen as it has been studied previously both in surface reactions and as an aerosol[52] for its ability to convert NO_2 to HONO under illuminated conditions. Comparing to these previous studies allows for confirmation that the experimental method is working as expected before moving on to new targets that have not yet been studied. TiO_2 is atmospherically relevant as it is a component of mineral dust (5 %) which is the dominant aerosol in the atmosphere. TiO_2 has also been used on various constructed surfaces, such as paint or glass, with the aim of "cleaning" the atmosphere by removing NO_x[114, 115]. The two nitrate aerosols were chosen because it has been proposed that nitrates, normally considered a loss route for NO_x in the atmosphere, may generate HONO under illuminated conditions recycling NO_x back into the atmosphere[37, 65]. This process is likely to be most significant in remote clean environments where atmospheric NO_x concentrations from other sources are low. A study[116] on sodium nitrate in a liquid reactor demonstrated gas phase HONO production when the system was illuminated. The primary work that will be discussed here covers the TiO_2 studies as no production was observed from the nitrate aerosols during initial studies.

4.2.1 Titanium Dioxide

The TiO_2 experiments were carried out using 5 g of TiO_2 (Aldrich Chemistry 718467, 99.5 % Degussa) suspended in 500 ml of water. A supply of 3 bar of nitrogen (BOC) was supplied to the atomiser to generate the aerosols. RH was set to 15 % as a previous aerosol study[52] reported peak HONO production at this RH. The total aerosol flow entering the flow tube was ~3.5 SLM. The NO_2 flow consisted of a flow of 1-20 sccm NO_2 (0.1 % mix in N_2) diluted in a 1.5 SLM flow of nitrogen. The aerosol and NO_2 flow were introduced through separate ports at one end of the flow tube. Each experiment was run at a constant NO_2 concentration and RH, while the aerosol surface area was varied.

After the addition of the NO_2 gas a 2 hour stabilisation period occurred, this was due to an increase in measured HONO after the first addition of NO_2, which would decay back to a stable background level. This initial increase in HONO signal is due to HONO formation in the NO_2 sample lines when not in use, that required time to flush out. Once stable, measurements began with the UV lamp being turned on and off for ~ 5-10 min periods, repeated for 5-10 runs (500 sweeps each), for each aerosol SA. After measuring a lamp on and off for a set SA an OH offline was measured (giving the signal due to laser scatter and room light). The aerosol surface area was then changed and allowed to stabilise before the measurement process was repeated.

Figure 4.11 shows the results from an experiment where each point is a single run; the point colours illustrates the lamp status. The error bars represent the variability of counts from the individual sweeps in each run. There is a gradual decrease in the lamp off points over time, possibly due to either the gas lines slowly clearing of background HONO or a deactivation of HONO production sites on the walls of the flow tube. To correct for this, a line of best fit was fitted through these point and subtracted from the lamp-on points. The calibration factor is applied and the concentration points plotted against the aerosol SA, producing the plot shown in figure 4.12 The figure shows that under illuminated conditions the concentration of HONO measured increases as the SA of TiO_2 increases, indicating that the aerosols are acting as a HONO source in the flow tube.

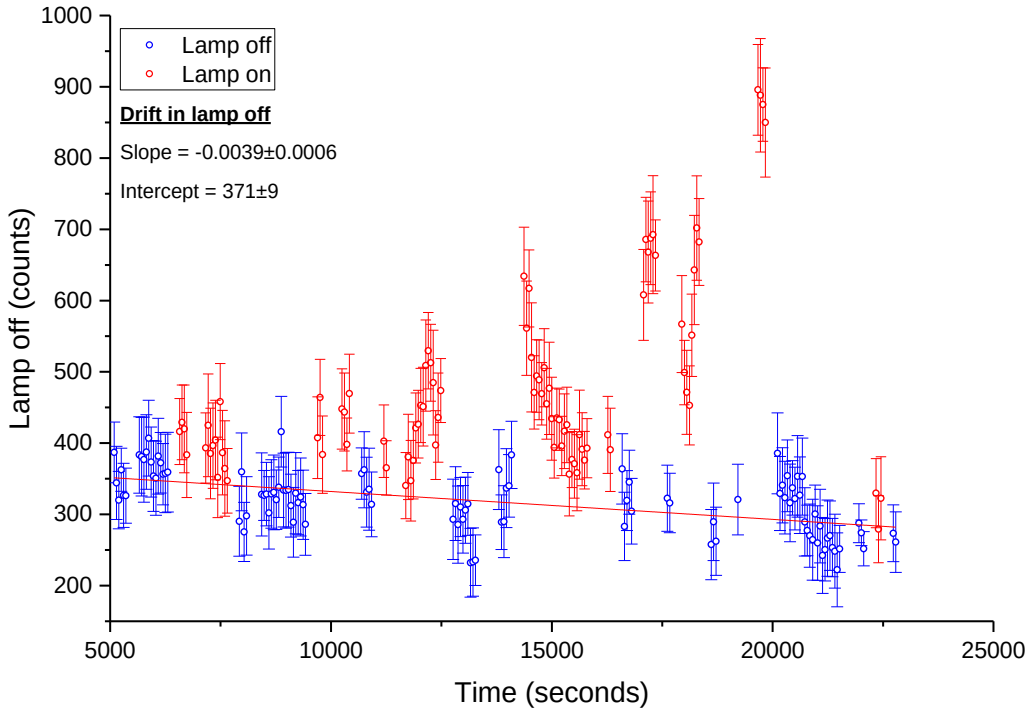

Figure 4.11. Plot of HONO signal during the experiment ([NO_2] = 400 ppb, Aerosol surface area = 0 – 0.035 m^2/m^3). The red points were measured while the lamp was turned on and the blue are when the lamp is off. The line fitted through the lamp off points allows subtraction of the drift in background signal.

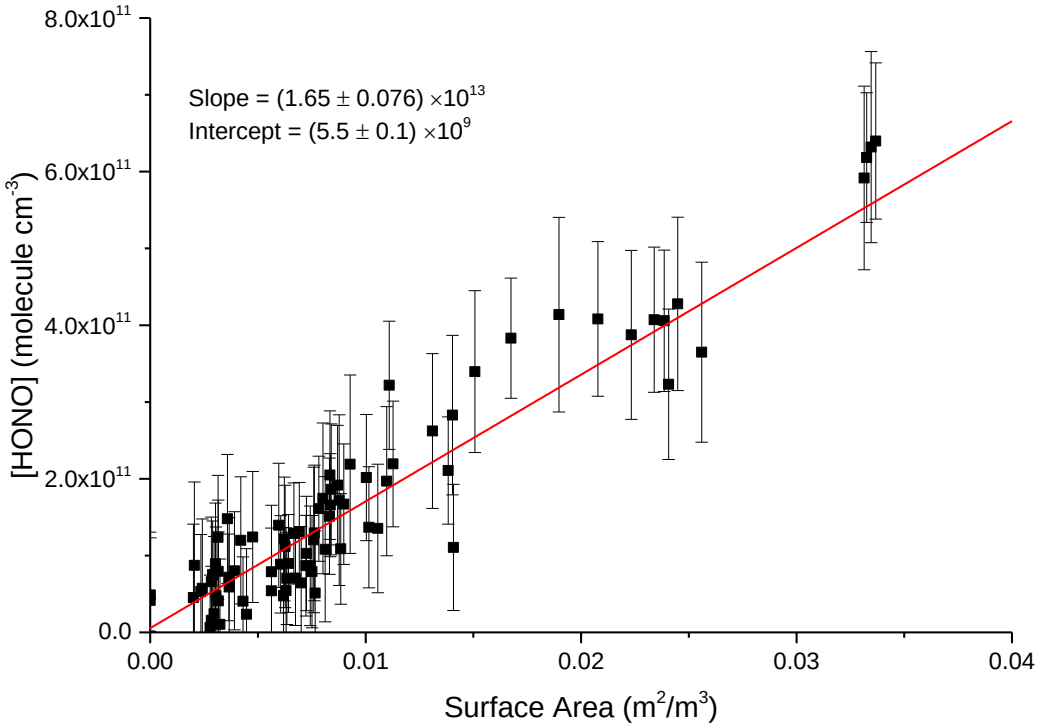

Figure 4.12. Plot of HONO concentration against the aerosol surface area using the data from figure 4.12 after subtraction of the lamp off points and the calibration factor has been applied.

4.2.1.1 Uptake coefficient calculation

A reactive uptake coefficient was then calculated using the results to allow a production rate to be calculated for models. The reactive uptake coefficient is a parameter that represents the probability that a collision of NO_2 with the aerosol surface will result in a reaction that generates HONO. This does not represent the total loss of NO_2 as it is possible that not all NO_2 taken up on the surface will react to form HONO. As the NO_2 concentration was not measured during these experiments it is not possible to state the unreacted NO_2 uptake, however, this factor will be investigated in the future. To calculate the reactive uptake coefficient the following formulas are used. Equations 19-22 show the rate equation for the loss of NO_2 and the integrated rate equation. $[NO_2]_t$ can be calculated from the initial NO_2 concentration with the fraction converted to HONO subtracted;

$$-\frac{d[NO_2]}{dt} = k\,[NO_2] \qquad \text{Eq(19)}$$

$$-\int_{[NO_2]_0}^{[NO_2]_t} \frac{d[NO_2]}{[NO_2]} = \int_{t_0}^{t} k\,dt \qquad \text{Eq(20)}$$

$$\ln[NO_2]_t - \ln[NO_2]_0 = kt \qquad \text{Eq(21)}$$

$$[NO_2]_t = [NO_2]_0 - [HONO] \qquad \text{Eq(22)}$$

Substituting equation 22 into equation 21 and rearranging to equation 24, allows the rate constant, k, for the heterogeneous reaction of NO_2 to HONO to be determined.

$$\ln([NO_2] - [HONO]) - \ln[NO_2]_0 = kt \qquad \text{Eq(23)}$$

$$\mathrm{k} = -\frac{ln\left(\frac{[NO_2]_0 - [HONO]}{[NO_2]_0}\right)}{t} \qquad \text{Eq(24)}$$

The rate constant for an aerosol reaction can also be calculated using equation 25, which contains the reactive uptake coefficient, γ_r, the aerosol surface area, SA, and ω (calculated using equation 14), which is the mean velocity of NO_2. Rearranging equation 25 to equation 26 and taking the gradient of k vs SA allows the determination of the reactive uptake coefficient.

$$\mathrm{k} = \frac{\gamma_r \times SA \times \omega}{4} \quad \text{Eq(25)}$$

$$\frac{\mathrm{k}}{SA} = \frac{\gamma_{rxn} \times \omega}{4} \quad \text{Eq(26)}$$

$$\gamma_{rxn} = \frac{\omega}{4 \times \frac{\mathrm{k}}{SA}} \quad \text{Eq(27)}$$

$$\omega = \sqrt{\frac{8RT}{\pi M}} \quad \text{Eq(28)}$$

Figure 4.13 shows the calculated uptake coefficient calculated at different concentrations of NO_2. The figure shows data collected by two users at Leeds using the most recent PF-LIF setup, one point collected during an early design and one point from a publish aerosol result by Gusstafasson et. al.[52]. The most recent Leeds measurements are considerably smaller than the value calculated by Gusstafasson and co-workers, potentially due to different experimental setup, such as the lamp output, which has not yet been parametrised for in the results. The point measured at the early stage of design may be higher due to higher UV output from the flow tube lamp; NO_2 actinometry experiments are underway to assess if the UV output has decreased since the initial actinometry experiments described in section 4.1.2. Photodiodes have now been added to the experimental set-up to monitor changes in the total lamp output over time. Periodic measurements of the lamp output using a spectral radiometer to monitor changes at different wavelengths will be conducted as part of the experimental protocol.

With the majority of experiments being carried out in nitrogen an experiment was done using air. This was to ensure that nitrogen experimental results are atmospherically relevant. Previous measurements[17] by the Leeds group investigating HO_2 production from TiO_2 aerosols found a production dependence on the oxygen content in the system, with HO_2 production increasing with oxygen concentration. The reactive uptake for HONO calculated in this experiment, at 1440 ppb NO_2, overlapped well with an experiment in nitrogen. However further repeats need to be carried out at lower NO_2 concentrations.

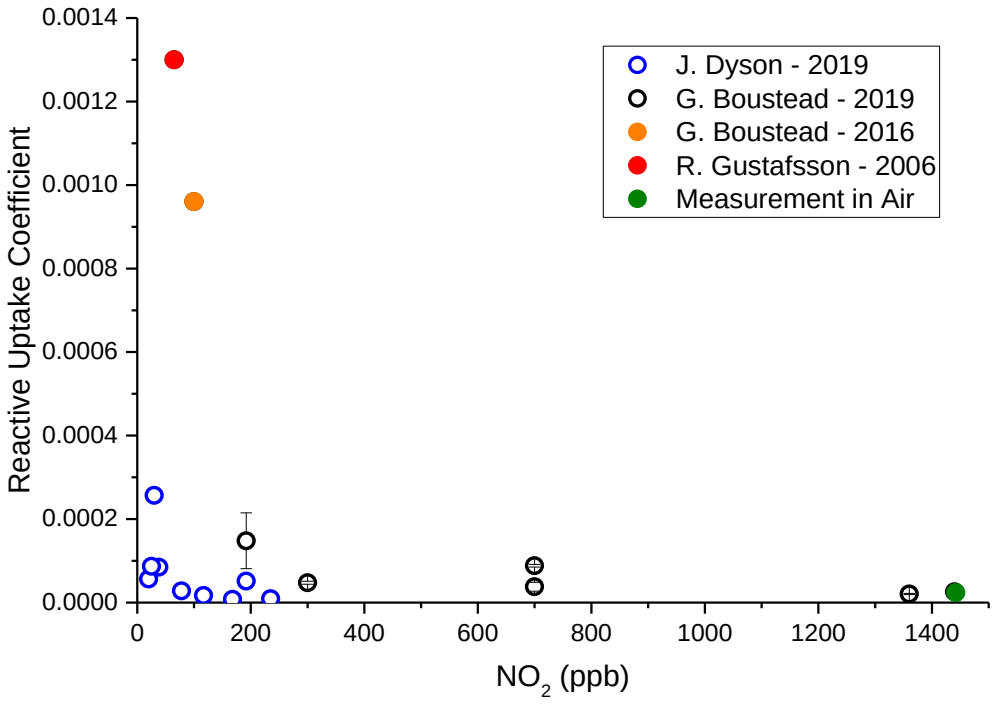

Figure 4.13. Reactive uptake values calculated using the Leeds PF-LIF instrument for a range of NO_2 concentrations. The Green point at 1440 ppb NO_2 is the experiment carried out in air, while the remaining points were all carried out in nitrogen. The red point shows the value calculated by Gusstafsson et. al[52].

The data shows that the reactive uptake of HONO decreases at high NO_2 concentrations. This trend could be explained by assuming that the reaction proceeds via the Lindemann-Hinshelwood mechanism, which describes a process where both reactive species (NO_2 and H_2O) bind to a catalyst surface and react when they are in proximity to each other (see section 1.5.5). This mechanism explains the decrease in HONO production as both species compete for binding sites and as the NO_2 concentration increases, the binding sites become saturated with NO_2, decreasing available sites for water to bind to and thereby slowing the reaction. This trend has also been observed in other studies investigating HONO production from TiO_2[58] and humic acid[57].

The Eley-Rideal mechanism, which is also used to describe reactions on solid surfaces, is not considered here due to the decrease in the reactive uptake with increasing NO2 concentration. This decrease is unlikely to be observed if this mechanism was followed as this mechanism considers only one species binding to the surface whilst the second species remains in the gas phase during the reaction. This mechanism results in no competition for reactive sites on the aerosol surface when a concentration of one reactant is increased.

Han et. al[117]. derived the following equation (eq. 29) from their measurements of reactive NO_2 uptake on humic acid in a coated wall experiment (34 cm length, 1.6 cm ID, 30-160 ppb NO2, 0.9 SLM, chemiluminescence NOx analyser) which they used to fit to their data with good accuracy and from this were able to calculate the Langmuir adsorption constant of NO_2 (K_{NO2}) on humic acid and the maximum reaction rate ($k[S]_T$). The results of fitting equation 29 to the experimental data from 2019 and allowing '$k[S]_T$' and 'K_{NO2}' to float is presented in figure 4.14. From this fit, Langmuir adsorption constant and the maximum rate are determined to be 2.62×10^5 cm^3 and 0.297 s^{-1}. Han et. al calculated values of 7.85×10^{-13} cm^3 and 12.3 s^{-1} respectively.

$$\gamma_{HONO} = \frac{a}{1 + K_{NO2}\,[NO_2]} \qquad \text{Eq(29)}$$

$$a = \left(\frac{4}{\omega \times SA}\right) k\,[S]_t K_{NO2} \qquad \text{Eq(30)}$$

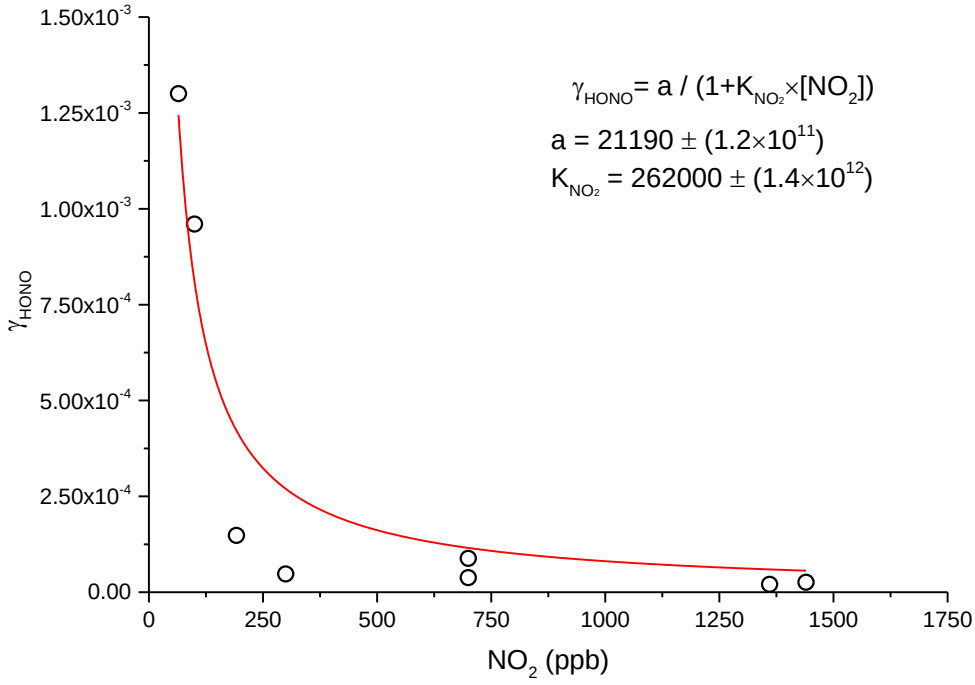

Figure 4.14. Reactive uptake versus NO_2 concentration where equation 27 has been used to fit a line allowing calculation of the Langmuir adsorption constant (K_{NO2}) and the maximum rate ($k[S]_T$).

This equation, however, does not best describe the mechanism as shown by the significant different values for both K_{NO2} and $k[S]_T$ and their large errors, as it does not include the uptake of water to the surface which is also required in the HONO reaction. The following equations have been derived that will allow the rate constant for the reaction to be calculated. For this the following reactions are used;

$$[NO_2] + [S] \overset{K_{[NO2]}}{\longleftrightarrow} [NO_2]_{ads} \quad \text{R(38)}$$

$$[H_2O] + [S] \overset{K_{[H2O]}}{\longleftrightarrow} [H_2O]_{ads} \quad \text{R(39)}$$

$$[H_2O]_{ads} + [NO_2]_{ads} \overset{k}{\rightarrow} [HONO] \quad \text{R(40)}$$

By assuming that the formation of HONO is the rate limiting step, the rate of the reaction will be;

$$\frac{d_{HONO}}{dt} = k_{17}.[H_2O]_{ads}.[NO_2]_{ads} \quad \text{Eq(31)}$$

here the concentrations of the adsorbed water and NO_2 are both described by the following, where $[S]_T$ is the number of surface sites and θ is the fraction adsorbed on the surface calculated using equation 33.

$$[NO_2]_{ads} = [S]_T \theta_{NO2} \quad \text{Eq(32)}$$

$$\theta_{NO2} = \frac{K_{NO2}[NO_2]_g}{1 + K_{NO2}[NO_2]_g} \quad \text{Eq(33)}$$

This can be substituted back into equation 31 to give equation 34 giving the rate of HONO formation.

$$\frac{d_{HONO}}{dt} = \frac{k_{17}[S]_T K_{NO2}[NO_2]_g K_{H2O}[H_2O]_g}{(1 + K_{NO2}[NO_2]_g + K_{H2O}[H_2O]_g)^2} \quad \text{Eq(34)}$$

However this equation requires further experiments at multiple RHs and concentrations of NO_2, to solve as both the values of K_{NO2} and K_{H2O}, the Langmuir adsorption constants, are unknown and so would require reactive uptake curves to be measured at different RH. The reaction would also likely have a temperature dependence which would affect the adsorption to the surface, however this currently cannot be studied using the current setup due to the difficulty in controlling the temperature evenly across the whole system.

For modelling purposes the data collect by J. Dyson was fitted using the LORENTZ fitting option in the origin pro software. This function was chosen as the fit followed the data trend well, allowing calculation of the reactive uptake coefficient across a range of NO_2 concentrations. These calculated uptake coefficients as a function of NO_2 have been used in the models described later in section 4.3, where proposed sources of HONO have been added to an atmospheric box model for Beijing, China, using data collected during a field campaign in the summer of 2017, in order to assess their atmospheric impact. The most recent experimental data provided by J. Dyson is used as the NO_2 concentration in these experiments were primarily below 100 ppb and so overlapped directly with the ambient NO_2 concentrations observed in Beijing.

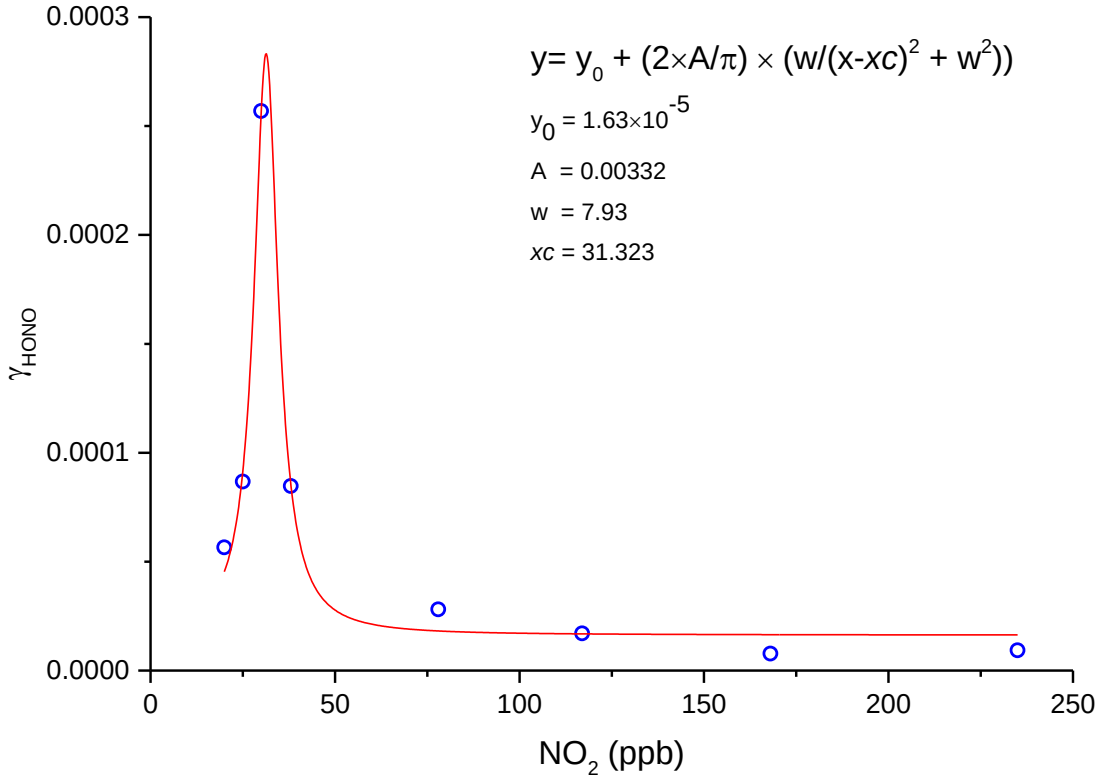

Figure 4.15. Reactive uptake data used to calculate values to be used in the atmospheric box model described in section 4.3.

4.2.1.2 Production dependence on Relative Humidity

The production of HONO was also measured a different relative humidities for a fixed aerosol concentration to compare with previous experiments that reported dependence on RH[52, 58]. Figure 4.16 shows the results for this experiment. These results show a peak in HONO production at 20 % RH which is similar to what other groups have shown[52, 58]. This peak is due to a requirement of water on the surface of the aerosol for the reaction, which is why the HONO concentration increases as RH increases. However there is a tail off at high humidities due to a blocking of active sites at the surface, due to water binding on the surface. This trend is linked to the competition covered by the Linderman-Hishertialwood mechanism with the increased water competing with the NO_2. This could be further investigated in the future by running experiments at higher RH and also to investigate how the peak in HONO production for different RHs is altered as NO_2 concentration is increased.

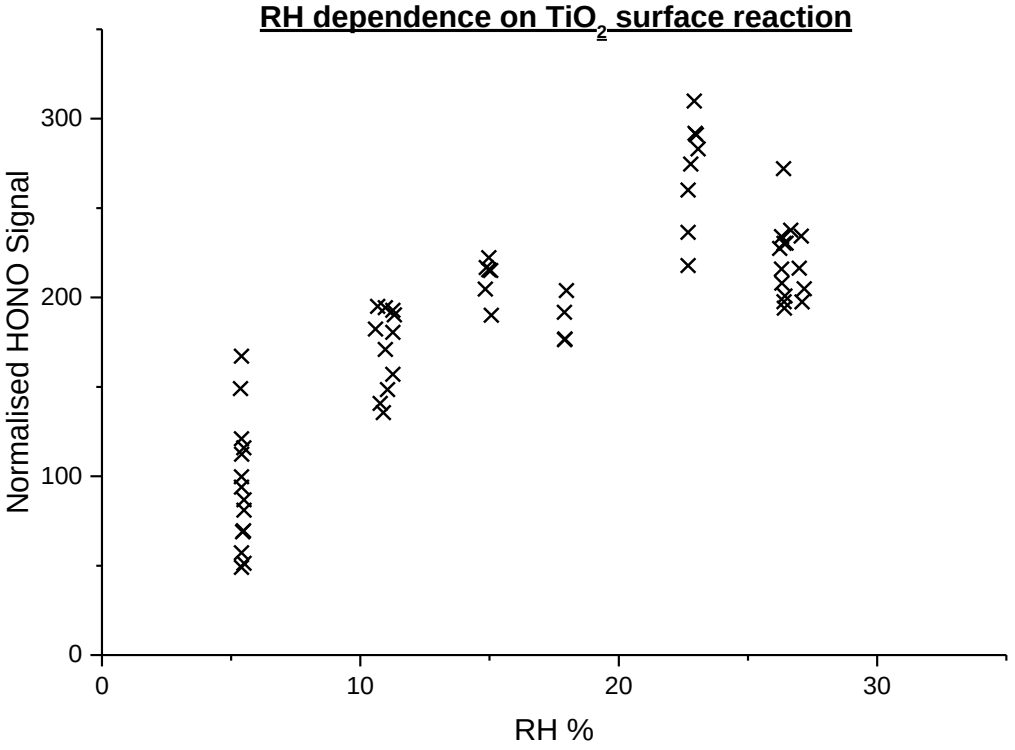

Figure 4.16. The effect of RH on the HONO production from TiO_2. Graph shows a maximum in HONO signal at 22% RH.

4.2.1.3 Error analysis

The following values in table 4.2 were used in the calculations of errors for the reactive uptake coefficient. These errors were propagated through the calculations using the standard error propagation formulas.

Error in the NO_2 concentration in the flow tube are determined as a combination of the error in the initial concentration of the NO_2 before mixing in the flow tube which comes from the 1% error for the pressure readings used during preparation of the cylinder. Further error is introduced due to errors in the flow values set on the MFCs used to deliver gasses to the flow tube (1 % of set flow). Errors in reaction time are taken from the errors of the flow rate the error to the volume is not used in this calculation as it is negligible and remains constant for all experiments. The standard deviation of the points averaged together normalised for laser power. The error for the line of best fit used to calculate the calibration coefficient (figures 3.9 and 3.11) is used when converting a HONO concentration. No error is considered for the aerosol surface as it is small compared to the contribution from the variation in the HONO signal. These errors are propagated through the equations used to calculate the reactive uptake coefficient using the sum in quadrature.

Table 4.2. Errors used in the calculation of the reactive uptake coefficient.

Parameter	***Error***
Gas flow	1 % of set flow
$[NO_2]_{cylinder}$	3 %
Temperature	0.5 ˚C
Relative Humidity	0.5 %
Signal	Variation in individual sweeps
Laser Power	Std. deviation during run
Calibration Factor	Fit error on calibration plot
k	Fit error on plot
Aerosol Surface Area	Not included

4.2.1.4 HONO production mechanism

The results from the experiments discuss highlight that TiO_2 will generate gas phase HONO when exposed to NO_2, water and UV light. This is shown by the positive gradient observed in figure 4.12 where the concentration of HONO, when the system is exposed to UV light, is plotted against the surface area of the TiO_2 aerosols. To explain this production the following mechanism has been proposed by previous groups who have studied the reaction on surfaces[52,58,115,118]

As a semiconductor, is considered both a conductor and an insulator, TiO_2, has a small energy gap between its conduction and valence band allowing irradiation to excite an electron from the valence band to the conduction band, creating an electron and hole pair. The electron (e^-_{CB}) in the conduction band acts as an electron donor and is able to oxidise different species, while the valence band hole(h^+_{VB}) will reduce species[119]. Figure 4.17 shows the pathways that may oxidise and reduce NO_2 and water to form the reactive species that will form HONO.

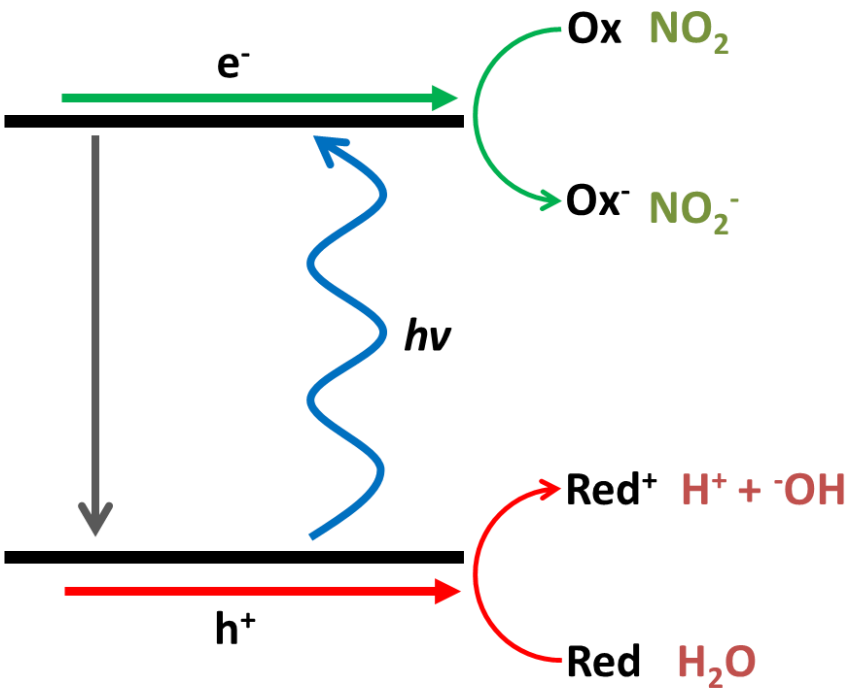

Figure 4.17. Figure showing the formation of electron and hole pairs after irradiation by UV light[120].

The proposed mechanism for this reaction has been discussed in previous papers and is shown in reaction 41 to 47.

$$TiO_2 + hv_{(\lambda<388\,nm)} \longrightarrow h^+_{VB} + e^-_{CB} \quad \text{R(41)}$$

$$h^+_{VB} + H_2O_{(ads)} \longrightarrow {}^{\cdot}OH_{(ads)} + H^+ \quad \text{R(42)}$$

$$NO_{2(ads)} + e^-_{CB} \longrightarrow NO^-_{2(ads)} \quad \text{R(43)}$$

$$NO^-_{2(ads)} + H^+ \rightleftharpoons HONO_{(ads)} \quad \text{R(44)}$$

$$NO_{2(ads)} + O^{\cdot-}_{2(ads)} \longrightarrow NO^-_{2(ads)} + O_2 \quad \text{R(45)}$$

$$NO^-_{2(ads)} + 2{}^{\cdot}OH_{(ads)} \rightleftharpoons NO^-_{3(ads)} + H_2O_{(ads)} \quad \text{R(46)}$$

$$NO^-_{2(ads)} + {}^{\cdot}OH_{(ads)} \rightleftharpoons NO^-_{3(ads)} + H_2O_{(ads)} \quad \text{R(47)}$$

A more visual mechanism is shown in figure 4.18. This mechanism has been adapted from a proposed mechanism for the conversion of NO_x to N_2 and water in a TiO_2 based photo-catalyst for a vehicle engine[121].

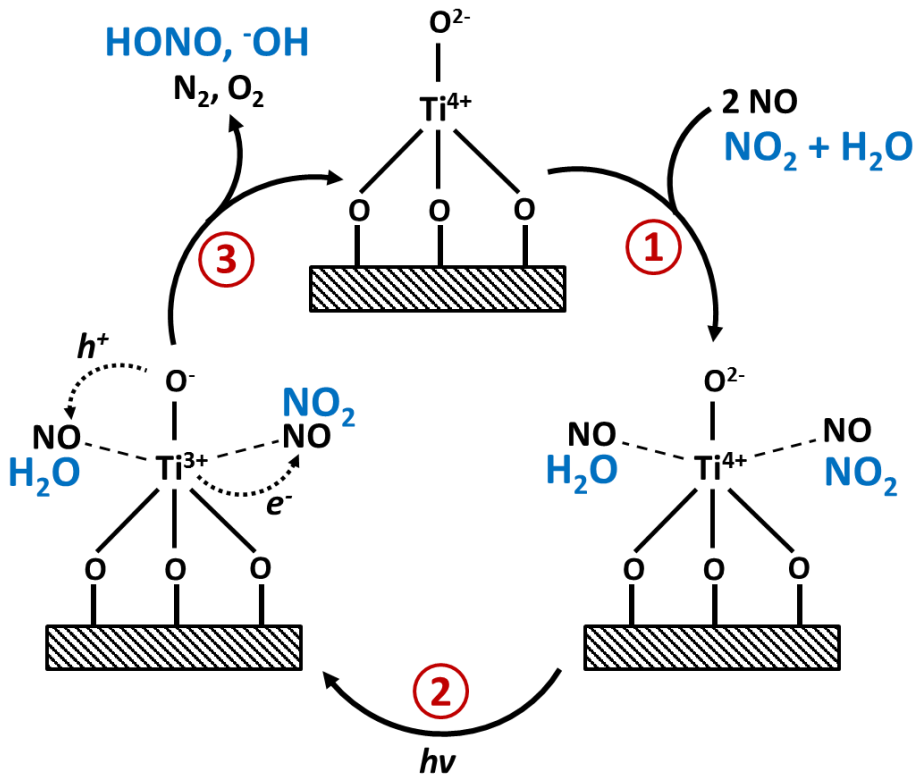

Figure 4.18. Mechanism for the conversion of NO_2 to HONO on TiO_2 surfaces. (1) Absorption to surface, (2) irradiation, (3) desorption. Proposed mechanism adapted from Schneider et.al. [121] to describe the conversion of NO to N_2 and H_2O seen in their experiment. The blue species represent how the mechanism could be adapted for the conversion of NO_2.

Results from these experiments do not permit for a detailed study of the reactive pathway mechanism, however, the results seen so far can be explained by the mechanism outlined in figure 4.18. Nonetheless, from the experimental results, a reactive uptake coefficient, dependent on the concentration of NO_2, has been determined. The impact of this experimentally determined reactive uptake coefficient on ambient HONO and OH concentrations in central Beijing is investigated in section 4.3.

4.2.2 Nitrate Aerosols

As discussed in the introduction (section 1.5.3.3), nitrates have been proposed as a possible source of HONO in the atmosphere. These sources are likely to be significant across a range of environments however the main interest are in low NO_x environments where the formation of nitrate aerosols was considered to be a removal pathway for NO_x in the atmosphere. However various modelling studies[37, 65] and lab studies[116,63] have found that there may be a recycling route back to gaseous NO_x via the production of HONO under sunlit conditions.

Two nitrate aerosols have been investigated in Leeds; ammonium nitrate and sodium nitrate. These were generated by dissolving 1 g of the respective nitrate in water. These aerosols were introduced into the aerosol flow tube as described for the TiO2 experiments and experiments were conducted over a range of relative humidity's. The initial aerosol solutions and the humidified flow in the aerosol generation stage, were also acidified using pH buffers as Scharko et. al. found a pH dependence on HONO production with increased HONO at lower pH values[116].

The studies of both nitrates showed no observable HONO production when the aerosol flow tube was illuminated under all conditions tested. Since HONO has been observed in previous experiments by other groups, a possible explanation for this is that the HONO concentration generated is below the instruments detection limit. Possibilities for the below detection limit concentrations include; too short a residence time in flow tube, problems with the 355 nm laser beam diameter (see comment below) or potentially insufficient aerosol surface area.

The residence time controls the amount of time the aerosols are exposed to the UV light and time for the HONO to escape from the aerosol surface. In the current setup it is not possible to reduce the gas flow due to the current flow being set very close to the sampling rate of the HONO detection cell.

During the nitrate experiments, due to a laser failure, it was necessary to change the photolysis laser used. The laser employed for the nitrate experiments had a larger beam diameter (1 cm vs 0.4 cm), this results in the photons being less focused along the central axis where there is overlap with the probe laser resulting in fewer HONO molecules being detected due to reduced photolysis.

Using the results achieved however a possible upper limit in production can be calculated using the instruments limit of detection as maximum amount of HONO that can be produced at the maximum aerosol surface area observed in the flow tube. Assuming the production of HONO involves the photolysis of the nitrate surface the reaction can be defined in terms of a photolysis rate constant ($J_{nitrate}$) and the surface area (SA) in equation 35 which rearranges to equation 36.

$$\frac{d[HONO]}{dt} = J_{nitrate} \times SA \quad \text{Eq(35)}$$

$$[HONO]_t = J_{nitrate} \times SA \times t \quad \text{Eq(36)}$$

Using the detection limit of 50 ppt, a surface area of 1 × 10^{-4} cm^2 cm^{-3}, and a reaction time of 120 s a rate constant of 1 × 10^{-4} molecule cm^2 s^{-1} can be calculated. This is in terms of the aerosol surface area. This is difficult to compare to literature values as previous studies have used the nitrate content of the samples to calculate the photolysis rate constant ($J_{nitrate}$ /s^{-1}). This is currently difficult to back out of the Leeds experiments as although a volume measurement is available from the SMPS the aerosols are they have deliquesced at the humidity the experiment is run at. This means that the volume measurement will not be representative of the pure nitrate content. Measurement of this could be achieved in the future using either an atmospheric mass spectrometer (AMS) or by collecting aerosol samples after the flow tube.

The experiments reported in the literature where HONO production has been observed used a coated surface[63] or liquid flow reactor[116] rather than aerosols. These will have a much larger surface areas for reaction compared to an aerosol experiment. Here it will be difficult to increase the total number of aerosols due to upper limits on what the aerosol generation equipment produce and because the reliability of results from the Leeds SMPS will decrease as particle numbers increase. However the advantage of the aerosol experiment is that the nitrate surface is always “fresh” while with a coated surface experiment the surface will be changing through the experiment. This may introduce alternative production pathways that do not rely on the initial surface nitrate.A final change that may increase the possibility of generating an observable HONO signal would be to increase the amount of light the aerosols are exposed to by adding multiple lamps

around the flow tube. Studies by Stemmler et. al.[57] showed a linear increase in HONO signal from humic acid surfaces as the number of lamps were increased.

4.3 Missing HONO in Beijing

In order to evaluate the effects of the reactive uptake values calculated for TiO_2 they have been included into a box model using measurements from a site in Beijing, China during the APHH campaign in 2017. A range of HONO sources are included in the model and the contribution from each to the modelled HONO concentration is assessed compared to the concentrations of HONO measured at the field site. An initial comparison between the base model that only considers HONO production from OH + NO and the measured HONO is shown below in figure 4.19. This clearly shows that the model is not able to replicate the measured HONO and other HONO sources need to be included in the model chemistry scheme.

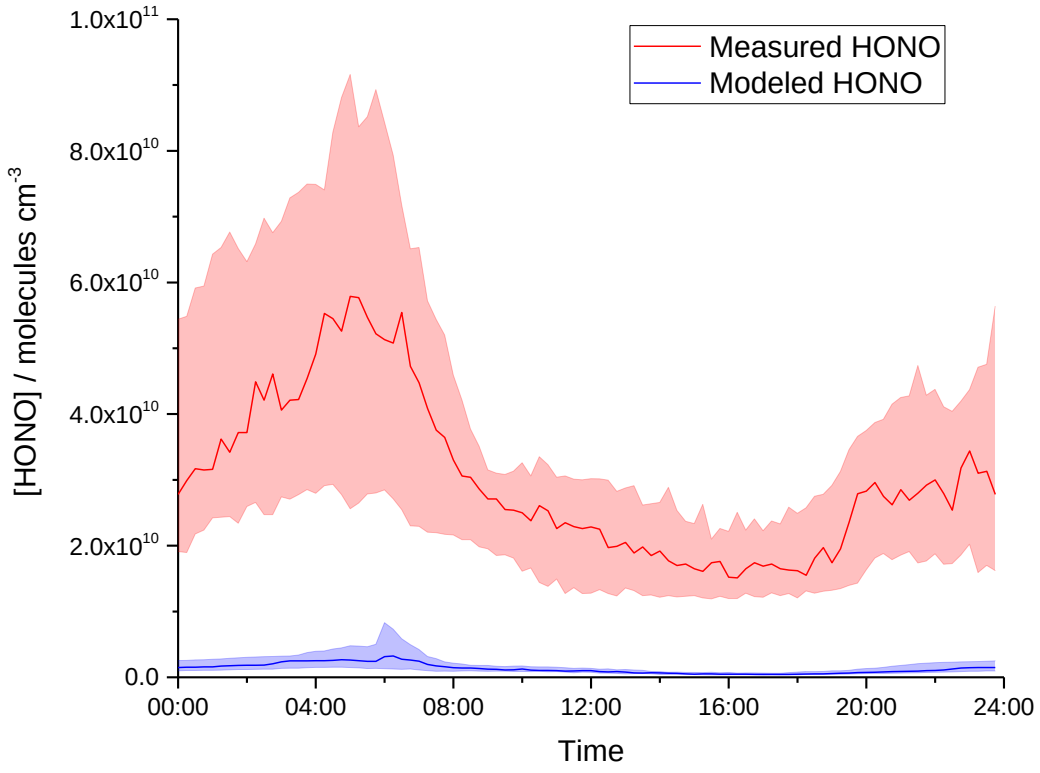

Figure 4.19. Diurnal plot showing the difference in concentration between the measured HONO and the HONO predicted by the model. The coloured sections show the 75 and 25 percentiles in the data.

This missing source of HONO is significant because in urban centres, such as Beijing, HONO is the dominant primary source of radicals during the day in both summer and winter.

Figure 4.20 below shows the model breakdown in the primary radical sources summer and winter. The yellow section of each plot represents the contribution from HONO. In winter it is the primary source while in the summer the number of sources are more varied but HONO is still a major contributor to the radical budget. The missing HONO would, therefore, be expected to have a significant impact on the model's ability to predict OH.

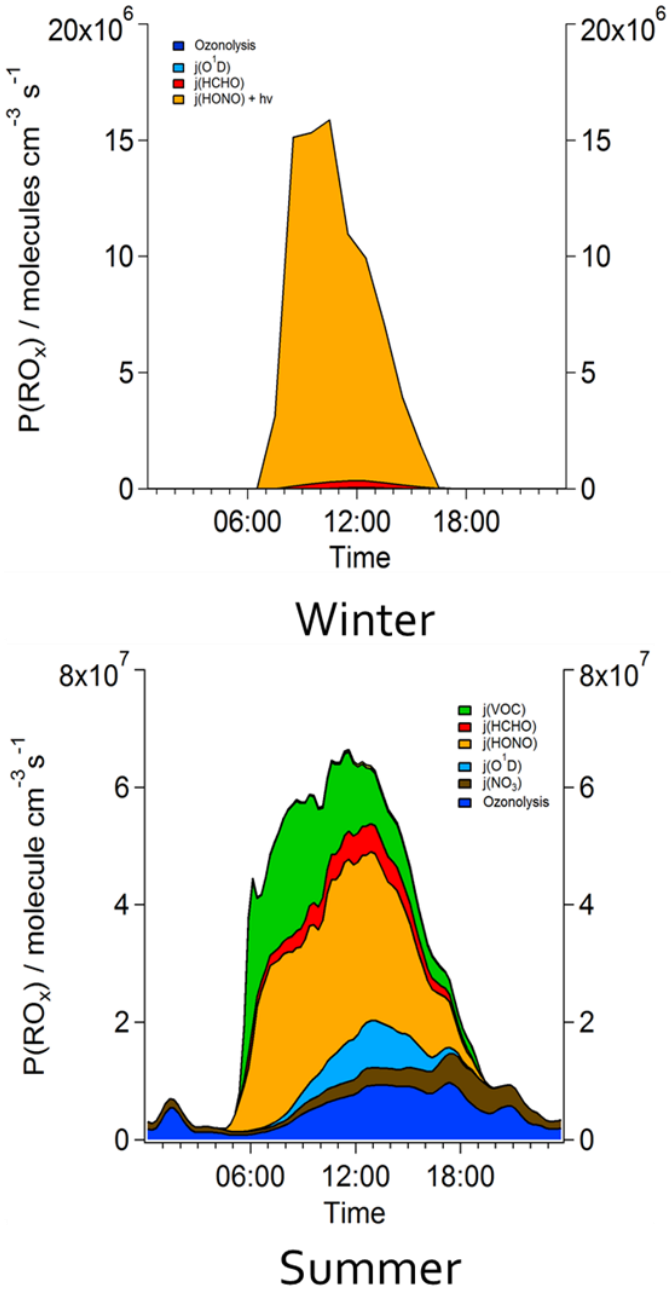

Figure 4.20. Diurnal plots showing the primary sources of radicals during both the 2016 winter (top) and 2017 summer (bottom) campaigns in Beijing. Radical propagation reactions are not included. Plots provided by Lisa Whalley.

4.3.1 Master Chemical Mechanism

The master chemical mechanism (http://mcm.leeds.ac.uk/MCM/home) is a zero-dimensional box model, which has a near-explicit chemical mechanism representing the degradation of methane and 142 primary emitted VOCs. The mechanism has a total of ~17,000 and ~6700 species. The model was run using a sub-set of the MCM that included 11500 reactions and ~3800 species. A full description of the kinetic and photochemical data used in the mechanism can be found on the MCM website (http://mcm.leeds.ac.uk/MCM/home). The model was constrained by measurements of NO, NO_2, O_3, CO, VOCs, CH_4, HCHO, HNO_3, HONO, water vapour, temperature and pressure. The VOCs species were measured by GC-FID and PTR-ToF-MS. The photolysis rates for $j(O^1D)$, $j(NO_2)$ and j(HONO), calculated from the measured actinic flux and published absorption cross sections and quantum yields, were included as model inputs. Other photolysis frequencies used in the model were calculated. For UV-active species, such as HCHO and CH_3CHO, photolysis rates were calculated by scaling to the ratio of clear-sky $j(O^1D)$ to observed $j(O^1D)$ to account for clouds. For species able to photolyse further into the visible the ratio of clear-sky $j(NO_2)$ to observed $j(NO_2)$ was used. Inputs into the model were updated every 15 minutes. The model was run both as a time-series for the whole campaign, but also as an average campaign day with mean concentrations from the whole campaign used as the model constraints; the latter model was run to quickly assess the impact of the different HONO sources considered.

4.3.2 Beijing Measurement Site

Results used in this model were collected during the APHH measurement campaign at the Institute of Atmospheric Physics in central Beijing. This site represented a residential area of Beijing with multiple roads located nearby. Details of the project are described in Shi. Z et. al.[122] along with the list of instruments used.

This modelling work will focus primarily on the summer Beijing measurements. Modelling studies from the winter project, highlighted that the observed HONO in the day could be described reasonably well when only the gas phase reaction between OH and NO was included in model simulations; as shown in figure 4.21. This finding is surprising considering the high aerosol loading where we may have expected heterogeneous sources to be important. In the wintertime, extremely high concentrations of NO were observed in Beijing and this leads to fast HONO production from OH+NO. Furthermore, radiation is reduced due to the severe haze events which inhibits light-induced processes.

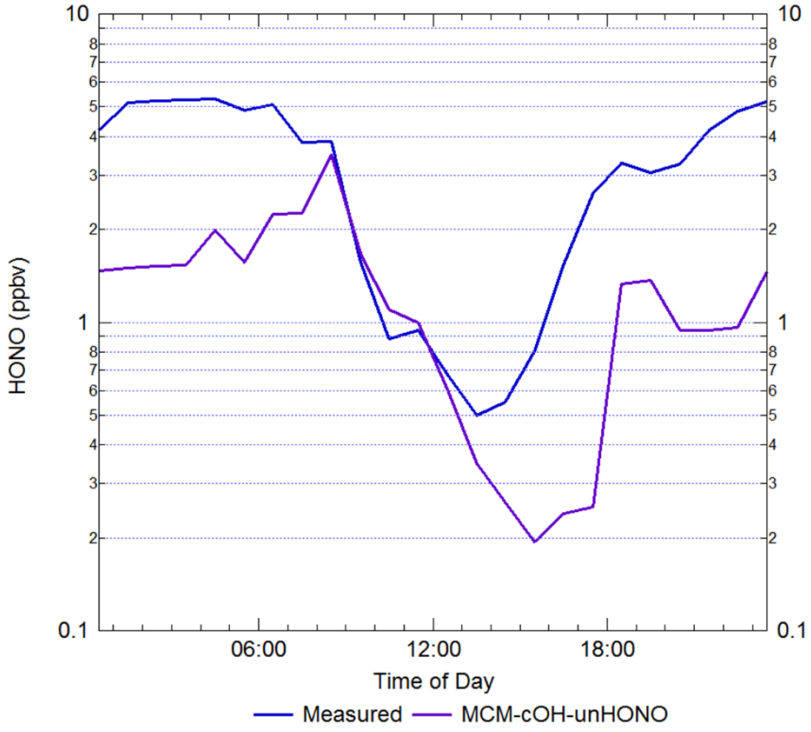

Figure 4.21. Comparison between the measured HONO (blue) and modelled HONO (purple) for the winter months during the APHH campaign. Graph provided by E. Slater from University of Leeds.

4.3.2.1 Data correlations

In order to identify potential sources of HONO, the missing production rate for HONO was correlated with other measured species from the campaign. The missing production rates were calculated using the concentration difference between measured HONO and modelled HONO where only the reaction between OH and NO forming HONO was considered.

$$[HONO] = k_{missing} + k_{(OH+NO)}[OH][NO] - k_{loss}[HONO] \qquad \text{R(48)}$$

The concentrations and rates were normalised to their highest measured value. In order to capture any synergistic links between species, the products of all species were also calculated and plotted against the missing HONO rate. The highest values are shown below in table 4.3.

Table 4.3. Highest correlation values from plots of the missing HONO production rate versus different measured species. A larger value indicates a better correlation indicating a potential link to the unknown HONO source.

Species	*R^2 of correlation*
$NO_2 \times J_{HONO}$	0.8034
$NO_2 \times J_{NO2}$	0.8034
J_{HONO}	0.7910
J_{NO2}	0.7889
$NO_2 \times J_{O1D}$	0.7339
J_{O1D}	0.7014
$O_3 \times NO \times T$	0.6803
$O_3 \times NO$	0.6780
$NO \times HO_2$	0.5148
$NO_2 \times HO_2$	0.2593
NO × HCHO	0.2580
NO × T	0.2471
NO	0.2438
HO_2	0.2373
$NO_2 \times HCHO$	0.1715
T	0.1658
HCHO	0.1538
NO_2	0.1089
Toluene	0.0251

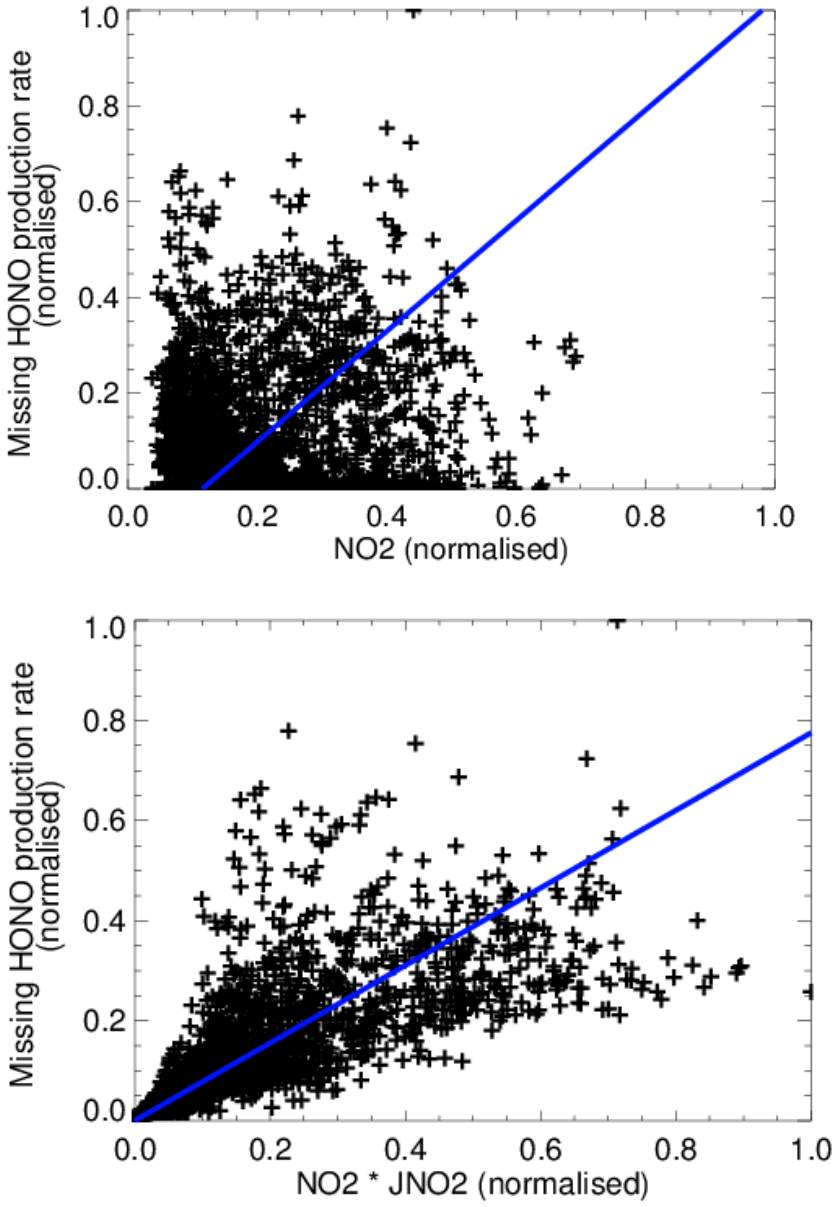

Figure 4.22. Correlation plots of the missing HONO production rate vs NO_2 and NO_2 * J_{NO2}. This shows how on its own NO_2 concentration do not correlate well with the missing HONO source however the product of NO_2 and various photolysis rate constants show very good correlation. Indicating the possibility of a daytime conversion of NO_2 to HONO.

Examples of two correlations plots are shown in figure 4.22 where the normalised missing production rate is plotted against the NO_2 concentration. On its own there is no significant correlation however, when plotting the product of NO_2 and J_{NO2} a very good correlation is produced with an R^2 value of 0.8. This shows that the missing HONO rate is highest when NO_2 concentration is high during the day which would fit with the suggested production route from illuminated surfaces.

4.3.3 Model Inputs

The following proposed sources for HONO were included in the MCM model for Beijing. Details of the individual reactions are discussed in the introduction in section 1.5. The reaction between OH and NO is the only source of HONO included in the base MCM model run, and uses the IUPAC recommended rate. The remaining reaction have been adapted from previous studies of proposed sources and the daytime aerosol production rate uses results from the TiO_2 experiments discussed previously in chapter 1. The direct emission of HONO was calculated as a fraction of the total NO_2. The fraction used was taken from Liu et al.[51] where they measured HONO emission ratios using a rolling road experiment under Beijing driving conditions. The dark conversion of NO_2 to HONO was set so that the HONO concentration at night was correct in the model using the assumption that HONO is produced at night via NO_2 reactions on humid surfaces. The nitrophenol reaction was taken from Benjan et. al.[46], where a HONO production rate of 100 pptv h^{-1} for 1 ppbv nitrophenol was determined under illuminated conditions equivalent to J_{NO2} equal to 10^{-2} s^{-1} . The rate constant used in the model was scaled to account for the differences in $J_{NO2.}$

The daytime aerosol NO_2 conversion rate is determined using the reactive uptake coefficient calculated in this work. Using the TiO_2 experiments discussed above scaled to account for the differences between the J_{NO2} in the experiment (determined in section 4.1.2) and observed J_{NO2}.a reactive uptake coefficient was calculated for each time step in the model using the measure aerosol SA. This model will assume that the measured aerosols are pure TiO_2.

Table 4.4. HONO production reactions used in the modified MCM box model for Beijing, showing the rate of production for each reaction.

Reaction	***Rate***	***Ref.***
OH + NO = HONO	$8.9\text{x}10^{-31} \times (T/298)^{-2.1} \times [M]$	MCM
Direct Emission	$[NO_2] \times 0.0042$	Liu et al.[51]
Aerosol NO_2 conversion *NO_2 = HONO*	$\frac{\gamma_r \times SA \times \omega}{4}$ $= 6.79\times10^{-6}$ s^{-1} for $J_{NO2} = 8.4\times10^{-3}$ s^{-1} And $[NO_2]$ = 13 ppb	This work
Dark NO_2 conversion *NO_2 = HONO*	0.5/(MH)	Matched to night time HONO
Day-time NO_2 conversion *NO_2 = HONO*	$(1/MH)\times J_{NO2}$*300 Set so average = 10^{-6} s^{-1}	Lee et. al.[102]
Nitro-phenol photolysis $HOC_6H_4NO_2$=HONO	$0.0028\times JNO_2$	Benjan et. al [46]

4.3.3.1 Night time HONO contribution

In order to ensure that the daytime HONO is simply not present due to the photolysis and recycling of night time HONO, a model was run where during the night the measured HONO concentration was input into the model while during the day the model was run unconstrained to the observed HONO. As shown in figure 4.23, these results demonstrate that despite the build-up of high concentrations of HONO overnight, this does not contribute to the HONO source in the daytime and the production rate is still not high enough to maintain the measured HONO concentration during the day.

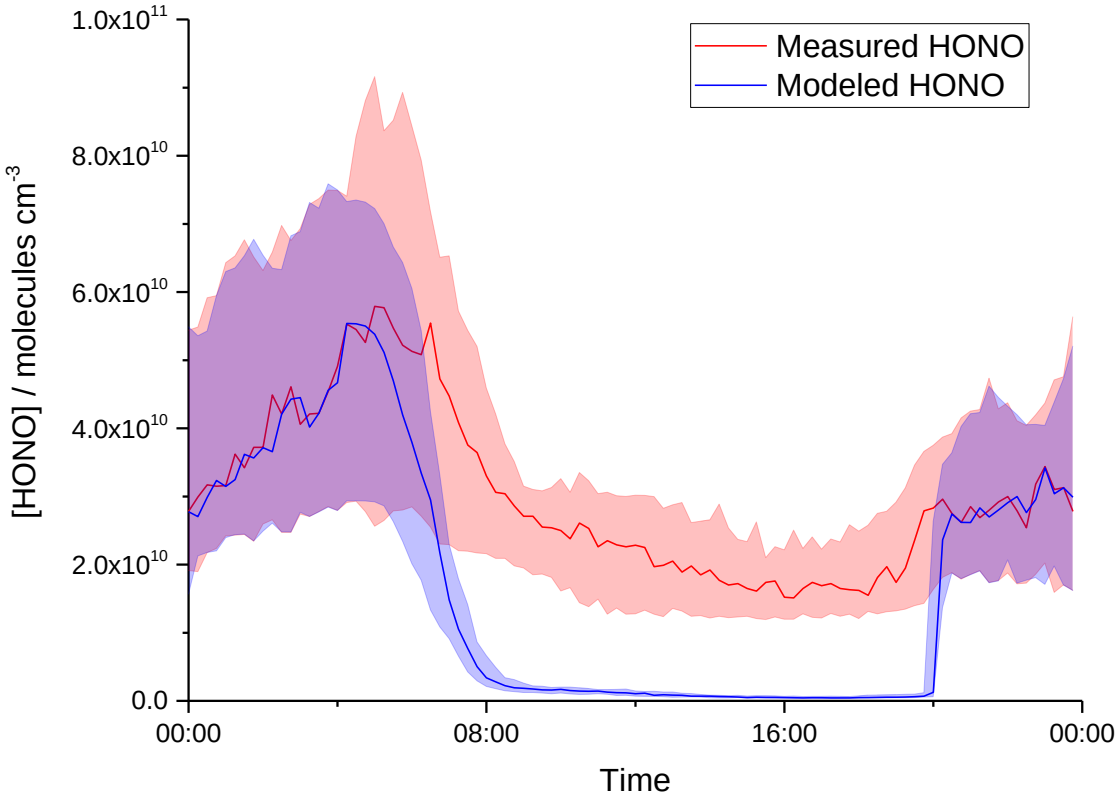

Figure 4.23. Diurnal plot showing measured (red) vs modelled (blue) HONO concentrations. HONO concentration at night in the model were fixed to the measured values.

4.3.4 Model Outputs

Figure 4.24 shows the output from the average model. The model is able to simulate the HONO concentration that was observed during the night-time and early morning, however, the daytime production is still too slow to simulate the observed HONO concentration during the day. The aerosol contribution to the modelled HONO production is small and peaks in the morning and then decreases later in the day. Figure 4.25 shows the production rates for HONO from various sources throughout the day.

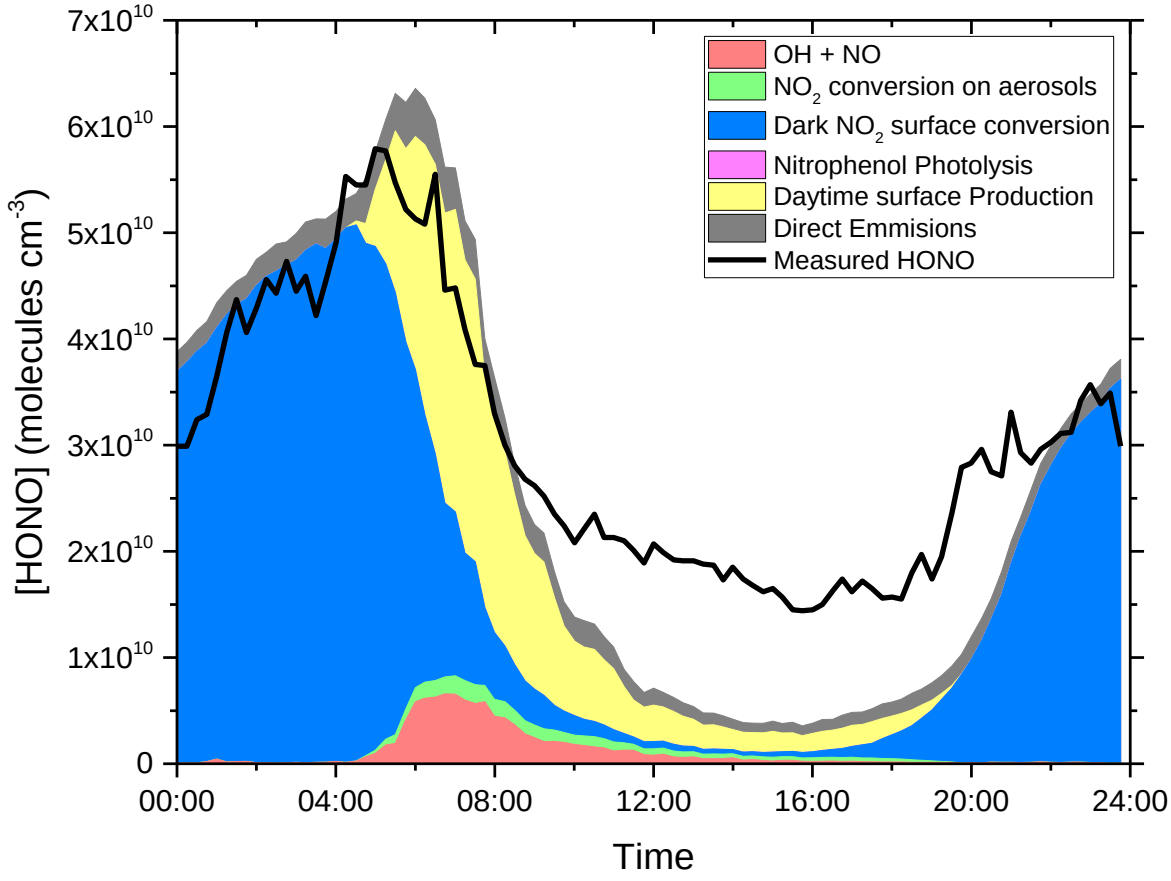

Figure 4.24. Diurnal plot showing measured HONO, black line, and modelled HONO, coloured sections, from the average MCM model. Each colour represents the fraction that is associated with each source that contributes to the total modelled HONO. Green section represent the fraction generated from aerosols using the calculated uptake coefficient from this work.

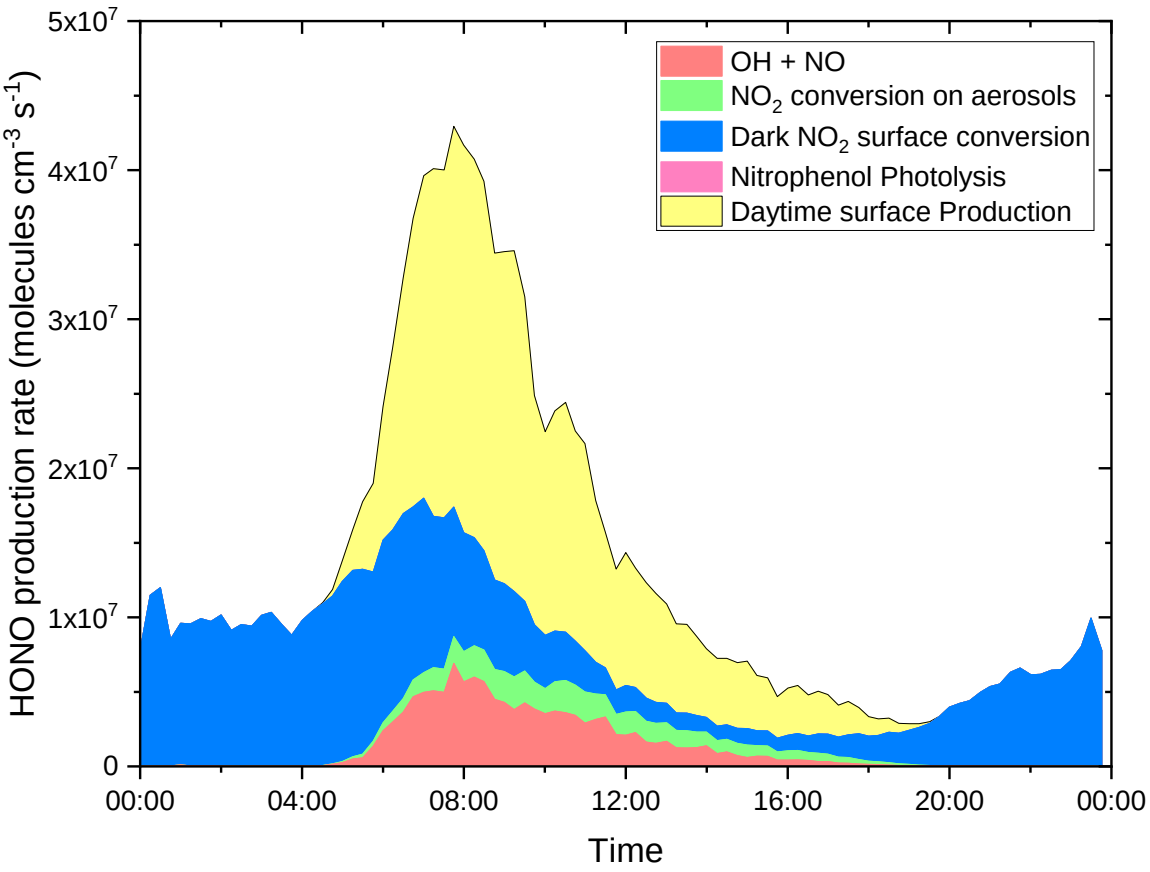

Figure 4.25. HONO production rates in the modified model showing the contribution from each HONO source.

As discussed in the introduction, HONO is important in the atmosphere because it is photolysed during the day to form the hydroxyl radical, OH. To demonstrate the importance of understanding HONO production pathways, figure 4.26 shows the modelled OH concentration from three model runs. The pink line is modelled OH, where the only HONO source included is from the OH + NO reaction. The blue line is average OH measured during the campaign and the black line is the modified model that includes the additional sources of HONO listed in Table 4. It can be seen that the base model (that only considers OH+NO as a source of HONO) under predicts the OH concentration throughout the daytime. While the modified model is over predicting in the morning but matching the measured data more closely at midday.

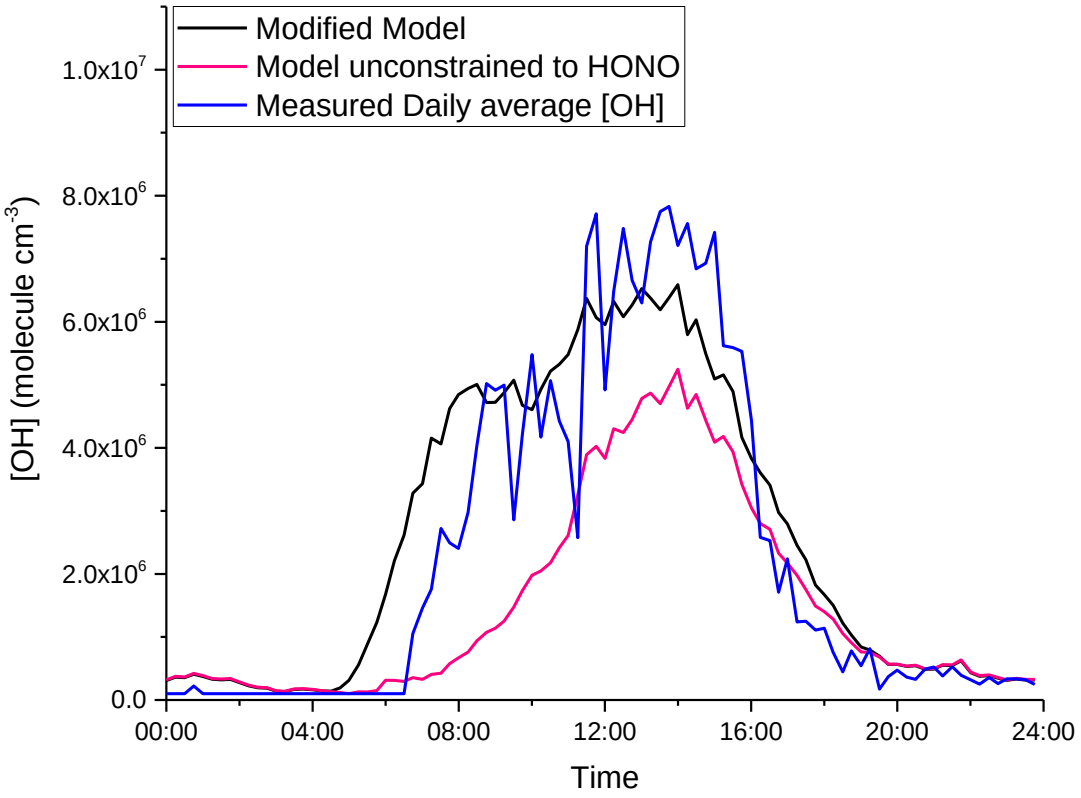

Figure 4.26. Diurnal plot showing [OH] during the day for different model runs. The model was either the base model unconstrained to HONO, pink, constrained to measured HONO, blue, or the modified model, black.

4.4 Conclusions and Future Work

Under illuminated conditions, TiO_2 aerosols have been shown to generate HONO when exposed to NO_2. The reactive uptake coefficient determined ranged from 0.1×10^{-4} and 2.5×10^{-4} for NO_2 concentrations in the range 25 ppb to 1000 ppb under UV radiation equivalent to $j_{no2} = 0.00133\ s^{-1}$. These uptake coefficients are lower than reported by Gustafsson et. al. where a value of 13×10^{-4} was calculated. The Gustafsson et. al. study does not report the lamp output and so it is difficult to compare the two studies directly. The measured reactive uptake coefficients follow the Lindemann-Hinshelwood mechanism, with the reactive uptake coefficient decreasing at high NO_2 concentrations, indicating a competition in binding on the surface between NO_2 and water. The aerosol reaction was found to be dependent on RH with the peak in HONO production being observed at ~20 % RH.

Using the TiO_2 experiment results from figure 4.15, reactive uptake coefficients for NO_2 on aerosol surfaces were calculated and used in a box model for Beijing. The model showed that the aerosol contribution peaks early in the morning. This simulation assumes that all the aerosols measured in Beijing contain TiO_2 at the surface while in reality they will be a mixture of both organic and inorganics.

This leads on to some potential future research changing from model aerosols in the lab to “real” aerosols found in the atmosphere that consist of a mix of compounds that may interact differently. In order to investigate this potential difference, aerosols collected in Beijing will be added to the flow tube and the production of HONO measured. Two methods will be used; extraction of the aerosols from the filter samples followed by re-atomisation, or investigation using the filter sample as a reactive surface. This will provide production rates for HONO that may be correlated to the different aerosol components which will also be measured during the collection of the initial samples.

Studies will also be done to investigate the effect of the wavelengths of light on production as the wavelengths in the solar spectrum change during the day with the short wavelengths primarily being present at midday while longer wavelengths persist into the early mornings and late afternoon. This will be important as UV light is higher in energy but at ground level the amount is low

when compared to the visible and infra-red wavelength. Therefore if the reactions are activate by these longer wavelengths the production of HONO will occur over a wider period during the day.

HONO production was not observed in the nitrate aerosol studies.. These experiments will be repeated in the future using a more optimal setup to maximise HONO production to a detectable level. This will be done using the most recent instrument design that is more sensitive to HONO and increasing the UV exposure in the tube using multiple lamps.

Results from these experiments will be important in future atmospheric models as heterogeneous chemistry is rarely considered in detail in chemistry models. This study has shown that the unknown source of HONO could be explained by a heterogeneous process. In areas where HONO is a primary hydroxal radical source it would be important to include these heterogeneous reaction when modelling future changes in air quality

Chapter 5 Atmospheric chemistry of Amines

In July and September 2016 a series of amine oxidation experiments were carried out at the EUPHORE chamber in Valencia, Spain. The compounds investigated were morpholine, piperadine, piperazine, ethylenediamine, diaminopropane, piperazine nitramine, nitrosopiperazine, imidazole and methylmethanimine. These species were investigated because of their potential role as solvents in carbon capture plants. The aims of these studies was to investigate the potential oxidation products if these amines were released into the atmosphere during the carbon capture process. This was a continuation of previous projects carried out by Nielsen et al. including studies at the EUPHORE chamber in 2015[123].

In this chapter a description of the chamber experiments will be given and the results derived from the OH and HO_2 data collected by the Leeds group, along with a comparison between the measured OH in the chamber and predicted concentrations using the decay of amines in the chamber. Only the experiments for morpholine, piperedine and piperazine, figure 5.1, will be covered due to a sparse OH and HO_2 data set from the September Campaign, when the remaining species were measured, due to instrumental problems.

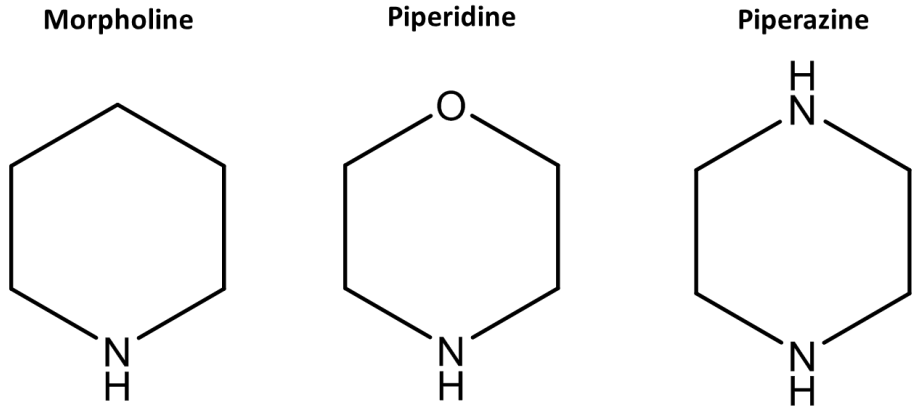

Figure 5.1. The 3 amines studied during the June 2016 campaign.

5.1 Carbon Capture

With CO_2 being the dominant anthropogenic greenhouse gas in the atmosphere[124], a primary goal of mitigating climate change is the prevention of further increases in CO_2 emissions and eventually reduction to a zero CO_2 emission rate. A major source of CO_2 in the atmosphere is the burning of fossil fuels for industry and electricity generation[125]. To minimise these emissions, various methods have been proposed that allow capture of the CO_2 produced, these include; pre-combustion capture, post-combustion capture and oxy-fuel combustion.

Pre-combustion capture involves the removal of all carbon content in the fuel before burning, this is done by converting the fuel to CO_2 and H_2 via gasification of coal or reforming natural gas with oxygen[126] where the CO_2 can be captured and the H_2 can be used in gas turbines or fuel cells[127].

In oxy-fuel combustion the fuel is burnt in a mixture of pure oxygen and recycled flue gas resulting in a cleaner burn so that the main products that form are CO_2 and H_2O vapour. This makes it easier for post-combustion carbon capture while also reducing other combustion products such as NO_x[128].

The post-combustion carbon capture technique is what most people are aware of when they think of carbon capture. It involves removal of the CO_2 from the flue gases generated by fossil fuel burning. Methods include chemical absorption, adsorption, membrane separation, Ca-Looping technology and cryogenic fractionation, with chemical absorption using amines being the most common[129].

Amine carbon capture, simplified in figure 5.2, involves scrubbing CO_2 from the flue gases using aqueous amine solutions. This process involves passing the flue gas through a scrubber containing the amine solution. This scrubber will normally contain a high surface to volume ratio to maximise the interaction between the gas and liquid. The process operates by converting the CO_2 to a carbamate or bicarbonate in the liquid phase. The solution is then sent to a stripper where it is heated using steam releasing the CO_2 from the solution. The CO_2 can then be compressed for transport to storage sites or to be utilised in different industrial processes[130].

The stripping process also regenerates the amine allowing reuse in the carbon capture process. To prevent the release of unreacted amines into the atmosphere the flue gas is passed through water which scrubs the amine from the gas.

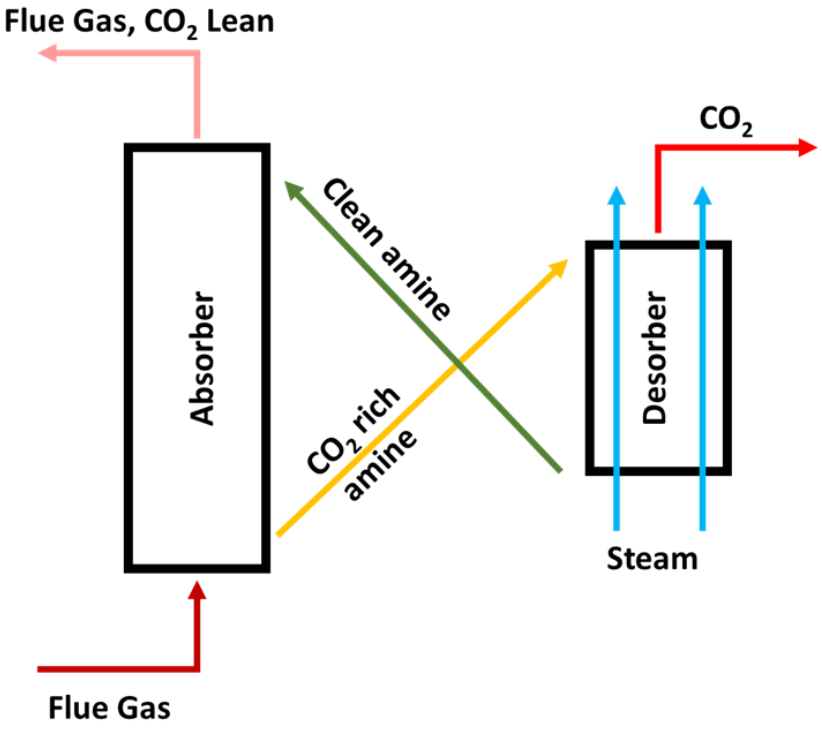

Figure 5.2. Simplified schematic showing the CO_2 capture process. Adapted from reference Dutcher et. al.[131].

The challenges with the amine based solvent is that they can be oxidatively and thermally degraded in the scrubber. However, the problem of interest for the Atmospheric Chemistry of Amines (ACA) project is the formation of nitrosamines and nitramines, with N-Nitrosomorpholine and N-Nitrosopiperidine both being classified as group 2a agents by the international agency for research on cancer; i.e. probably carcinogenic to humans, [132]. Nitrosamines and nitramines form when the amines react with NO_x in the carbon capture system or after the release of the amines into the atmosphere where they are oxidised by OH before reacting with NO_2[133, 134].

The ACA project aims to identify and quantify the gas phase photochemical degradation products of the possible amine emissions. The data will then be used to update current photo oxidation schemes for those amines[135].

5.2 The European Photoreactor

The EUPHORE chamber is located in Valencia, Spain and is operated by the Mediterranean Centre for Environmental Studies Foundation (CEAM)[136]. The research site has two half spherical atmospheric simulation chambers each with a volume of approximately 200 m^3.This large volume provides a low surface-to-volume ratio minimising losses and heterogeneous reactions on the chamber walls. The chamber domes, shown in figure 5.3, are made of 0.13 mm thick fluorine-ethene-propene (FEP), and allows transmission of more than 80 % of sunlight in the near UV and visible light range. The FEP surface is also chemically inert, further minimising the chance of heterogeneous processes. The chamber floors consist of aluminium panels covered in FPE with rubber cord being used to seal the chamber walls to the floor. The chamber floor is also cooled using a refrigeration system to compensate for the heating by solar radiation. Instruments are connect to the chambers via ports in the chamber floor. The chamber also has a steel canopy that can be opened and closed allowing shielding or exposure to sunlight.

Figure 5.3. The chamber used in the experiments described in this chapter. The inlet for the FAGE cell, not visible, was located on the opposite side of the chamber.

5.2.1 OH measurements

Measurements of OH and HO_2 were carried out using the FAGE technique described in chapter 2. The FAGE cell was located near the edge of the chamber, with the pinhole situated 10 cm above the base of the chamber floor. Figure 5.4 shows a cross section of the instrument. The setup to measure OH and HO_2 simultaneously with the two cells was not possible during the ACA campaign due to the poor performance of the detector on the second cell. Hence OH and HO_2 were measured sequentially in the first detection cell. During the measurements, the detector was cooled with chilled air in order to reduce the elevated background noise observed due to instrumental heating via thermal conduction from the chamber floor. A typical measurement day involved beginning measurements whilst the chamber was closed, continuing when the shields were opened and finishing after the chamber was closed once more and chamber flushing, with zero air, had begun. Throughout the campaign, calibrations were run once a week in order to track instrument sensitivity. To do this, the instrument was disconnected from the chamber and placed in a floor mount, then calibrated using the calibration wand method described in section 2.3. It was not possible to calibrate every day, which would be the ideal case, due to the start and end times of the experiments in relation to working hours at the EUPHORE chamber. It was also not possible to disconnect or reconnect to the chamber during an experiment due to the toxic nature of the species used. This meant that when calibrating it was not possible to measure with FAGE on that day, so where possible these calibrations were done on days when no measurements were taking place, primarily due to poor weather.

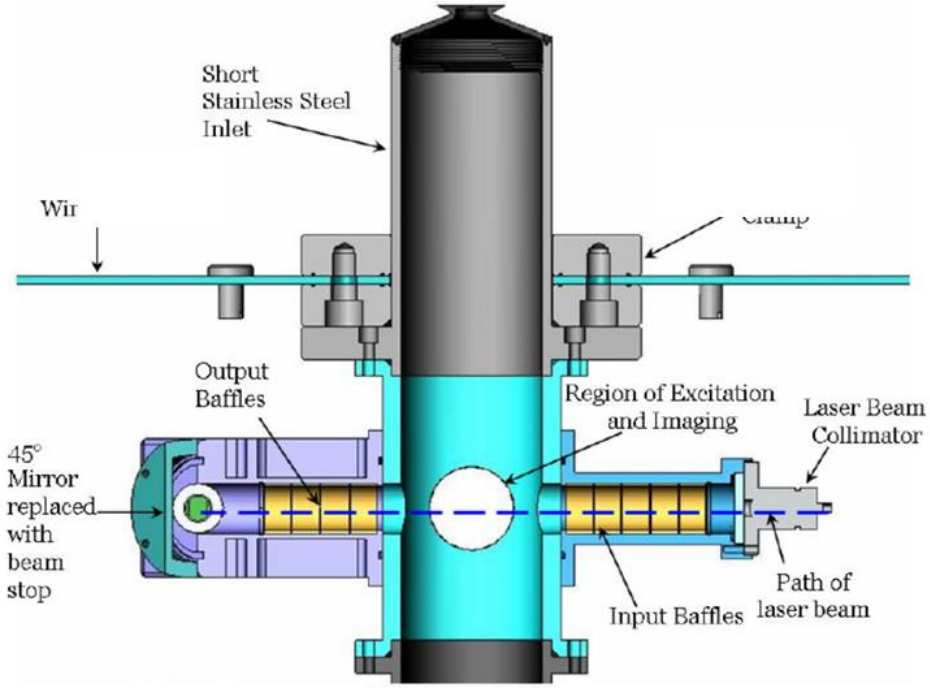

Figure 5.4. Schematic of the FAGE cell connected to the EUPHORE chamber. Image created by Trevor Ingham.

5.2.1.1 EUPHORE chamber instrumentation

As an international chamber, the EUPHORE chamber is equipped with a range of instrumentation that are permanently installed allowing monitoring of the chamber conditions. These instruments were operated by the staff at CEAM. Measurements of NO_x in the chamber were performed using a NO-NO_2 analyser (T200UP Teledyne API) and $j(NO_2)$ was monitored using a filter radiometer. HONO was measured using a LOPAP, see section 3.1.2. Ozone was monitored using a Serinus 10 ozone analyser (Ecotech). A SMPS and CPC were used to monitor the number concentration of particles formed in the chamber during measurements. A Nicolet FTIR spectrometer with a path length of 553 m between two mirrors in the chamber allowed in situ spectra to be measured every 10 min. The FTIR was used to measure the decay of SF_6 in the chamber, an inert tracer gas. The decay rate of SF_6 provides the dilution rate in the chamber due to the inflow of replacement air to compensate for the loss of gas in the chamber caused by instrument sampling and minor leaks. The chamber pressure, temperature and humidity were also monitored during each experiment.

5.2.1.2 ACA participant instrumentation

Other instrumentation used during the project by participants of the campaign were 4 mass spectrometers; an aerosol mass spectrometer (AMS)[137], a high-resolution proton transfer time of flight mass spectrometer (PTR-TOF-MS)[138], a high-temperature proton transfer mass spectrometer (HT-PTR-MS)[139] and a chemical analysis of aerosol online system coupled to a proton transfer time of flight mass spectrometer (CHARON-PTR-TOF-MS)[140]. Filter samples were also collected to allow offline analysis using 2D gas chromatography time of flight mass spectrometry (GC×GC-TOF-MS)[141].

5.2.2 Experimental summary

Before each experiment the chamber was flushed overnight with zero air removing any contaminants from previous experiments. During this period the steel canopy is closed. Instruments then begin sampling to provide a chamber background measurement. The required reagents are then added and time is given to allow for the chamber to become homogenously mixed. The canopy is then opened to sunlight to allow reactions to begin. Once the reaction was finished, the chamber was closed and the flushing process was started. During the campaign two types of studies were carried out these will be described here as the amine studies, were the reaction products of amine oxidation were studied, and the kinetic studies where the oxidation of the amine was measured alongside several tracer species.

5.2.2.1 Generation of OH radicals

The primary source of OH in the chamber was isopropyl nitrite, IPN, which was added to the chamber in the dark and when the chamber was opened to the sunlight was photolysed to form an alkoxy radical and NO. This radical can then go on to react with O_2 to form and HO_2 which can go on to react with NO forming OH[142]. This reaction scheme is shown in reactions 49 to 42.

$$iC_3H_7ONO\ (S_0) + hv\ (\lambda = 300 - 450\ nm) \rightarrow\ iC_3H_7ONO(S_1) \quad \text{R(49)}$$

$$iC_3H_7ONO(S_1)i \rightarrow\ iC_3H_7O + NO \quad \text{R(50)}$$

$$iC_3H_7O\ + O_2\ \rightarrow CH_3C(O)CH_3 + \mathrm{HO_2} \quad \text{R(51)}$$

$$\mathrm{HO_2} + NO\ \rightarrow OH + NO_2 \quad \text{R(52)}$$

Another source of OH in the chamber is photolysis of heterogeneously produced HONO, formed from NO_2 and H_2O in the dark on the chamber walls, see section 1.5.3, which photolyses to form OH when the chamber is opened. Minimal OH was seen via this pathway with the addition of IPN being the primary route for OH generation. However, it was possible to see the impact of OH from HONO production on one experimental day. Figure 5.5 shows a day where due to high wind the chamber was closed part way through the experiment when the chamber was reopened HO_x concentrations reached higher levels that before the closed period. It is assumed that this is due to HONO production during the dark period, however, it is not possible to validate this due to a fault with the LOPAP instrument which showed a level concentration of HONO across the experimental day which cannot be correct.

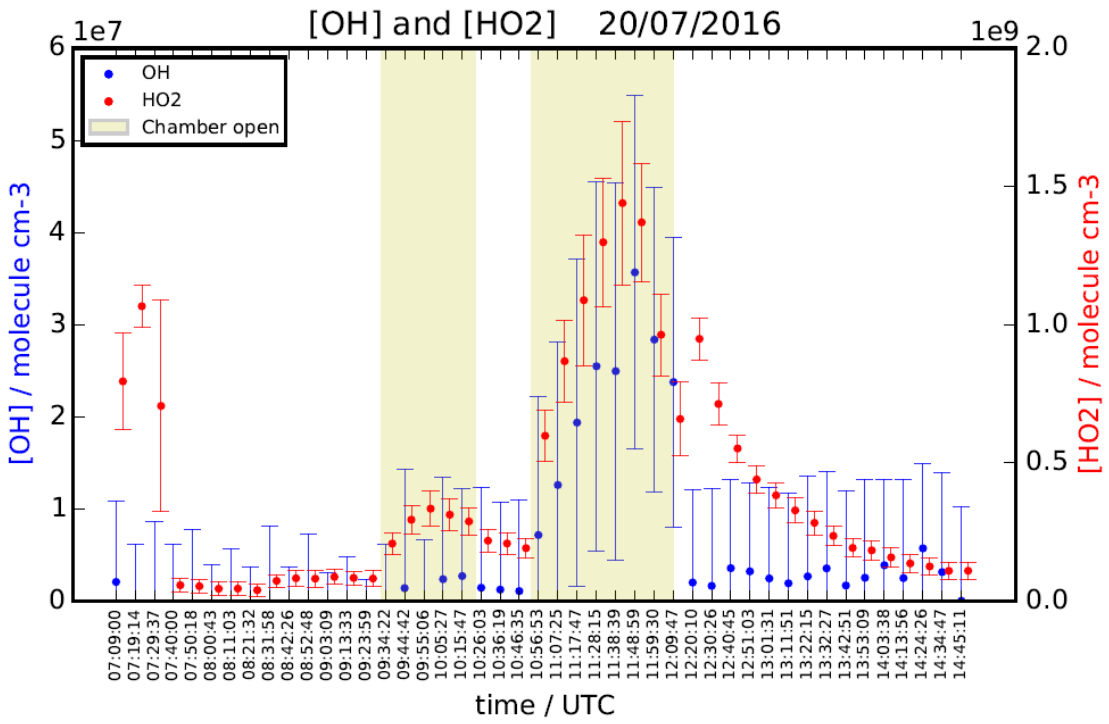

Figure 5.5. Experimental day that included a period where the chamber was closed to sunlight during the experimental run. The yellow section represent show when the chamber was opened, the red points are [HO_2] and blue is the [OH]. When the chamber has been reopened significantly more OH and HO_2 are seen, this is likely due to a build-up of HONO during the dark period.

5.3 Results

Due to the role Leeds played during the campaign, minimal analysis of the amine chemistry will be discussed here, with that aspect of the project being covered by the project leads at the University of Oslo in future papers. However, several topics covering the measured radical data will be discussed here. This includes HO_2 decays observed in the dark and comparisons between measured and calculated OH concentrations. Figure 5.6 shows a typical measurement of OH and HO_2 collected for one of the amine studies using piperadine, see figure 5.4. The same trend of increasing concentrations when the chamber was opened was seen for all days in the HO_2 signal. The OH signal was always much smaller with the major peaks above the background appearing on days when larger amounts of the OH precursor were added.

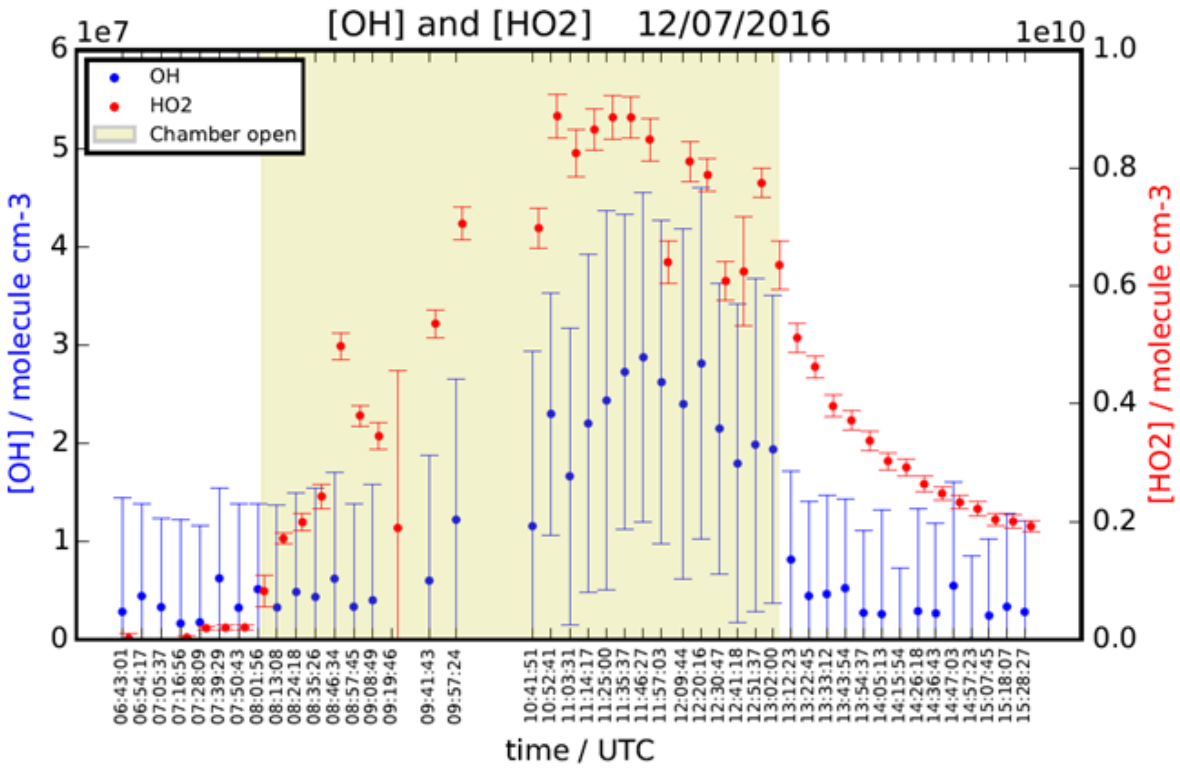

Figure 5.6. Example of a measurement taken during the ACA campaign. This experiment studied the oxidation of piperadine. The plot shows the changes in [OH], blue points, and [HO_2], red points. The errors on these plots come from the standard deviation of the signal in each run.

5.3.1 Calculated OH concentrations

The kinetic studies were run with the addition of multiple OH tracers (see table 5.1) to the chamber to allow the determination of the OH concentration in the chamber via a secondary method[143]. The rate coefficients of the tracer species with OH are well known, and by using their decay rates in the chamber it is possible to calculate the OH concentration present in the chamber. This calculated OH, assuming no other species removes the amine, can then be compared to the measured OH. Figure 5.7 shows the decay of two species in an experiment; Acetonitrile does not react with OH so its loss route is only through dilution and wall loss, and Isoprene that reacts with the OH present in the chamber.

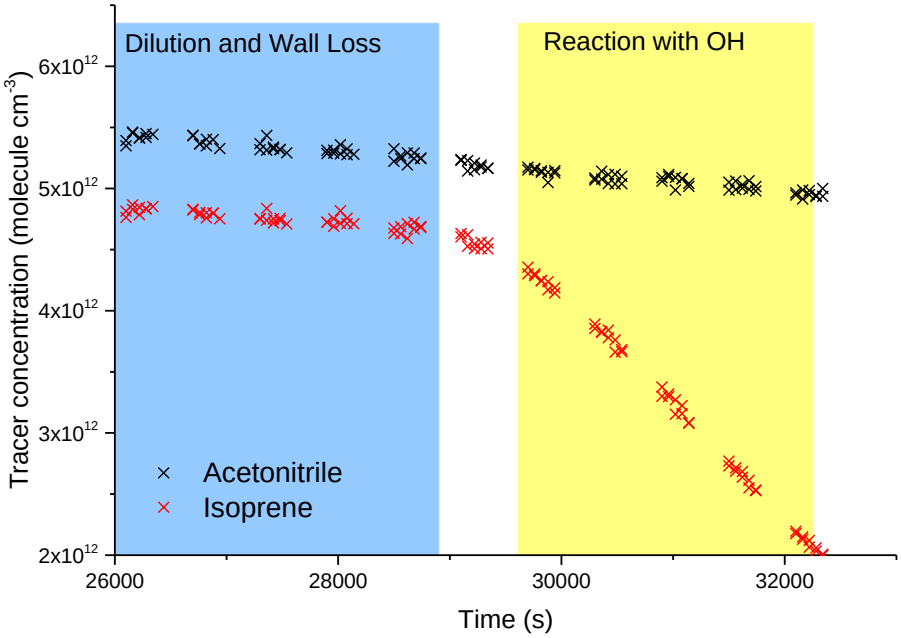

Figure 5.7. Concentration measurements of two tracers during a kinetic study. The blue section shows the period used to calculate the non-oxidative removal processes while the yellow section shows when the tracer is undergoing removal by OH. Acetonitrile shows a constant decay as it does not react with OH, while Isoprene will react with OH leading to the increased loss rate.

Using equation 37, using the decay of each species before the addition of OH to the chamber, the rate constant k_{loss} can be calculated. When OH is present the rate of loss is determined using equation 38 which can be rearranged to allow calculation of the OH concentration, equation 39. The values for k_{OH} for each species is shown in table 5.1.

The time period used for the loss rates was varied between experiments to ensure that the decay rate observed for all tracers at that time was linear.

$$\frac{d[T]}{dt} = -k_{loss}[T] \quad \text{Eq(37)}$$

$$\frac{d[T]}{dt} = -k_{OH}[OH][T] - k_{loss}[T] \quad \text{Eq(38)}$$

$$[OH] = -\frac{\frac{d[T]}{dt} - k_{loss}[T]}{k_{OH}[T]} \quad \text{Eq(39)}$$

The calculated OH from each kinetic study is shown in figures 5.8 to 5.11. For the first three plots the calculated OH showed good agreement from all tracers, because of this the averaged calculated OH is shown. For the final plot, figure 5.11, the 3 tracers showed very different shapes so the calculated OH has been shown for each individual tracer.

Table 5.1. Rate coefficients used to calculate the OH concentration in the chamber using the loss rate of each tracer.

Tracer	k_{OH} / cm³ molecule⁻¹ s⁻¹ ***T= 300 K***
Morpholine[144]	$9.5 \pm 0.95 \times 10^{-11}$
Piperidine[144]	$7.4 \pm 0.7 \times 10^{-11}$
Piperazine[145]	$23.8 \pm 0.28 \times 10^{-11}$
Isoprene (IUPAC)	8.96×10^{-11}
Styrene (IUPAC)	5.80×10^{-11}
Trimethyl benzene (IUPAC)	5.67×10^{-11}
Limonene (IUPAC)	1.63×10^{-10}
Pyrrole (IUPAC)	6.59×10^{-11}

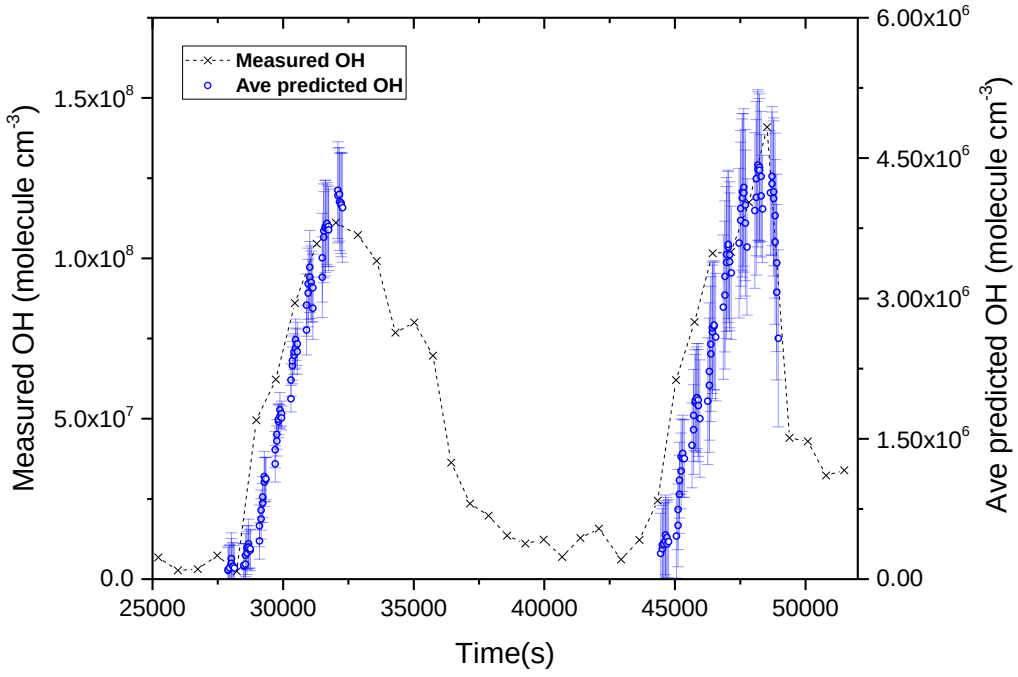

Figure 5.8. Comparison between the measured, black cross, and predicted OH, blue circles, for the morpholine kinetic study. Tracers; isoprene, styrene, trimethyl benzene, morpholine.

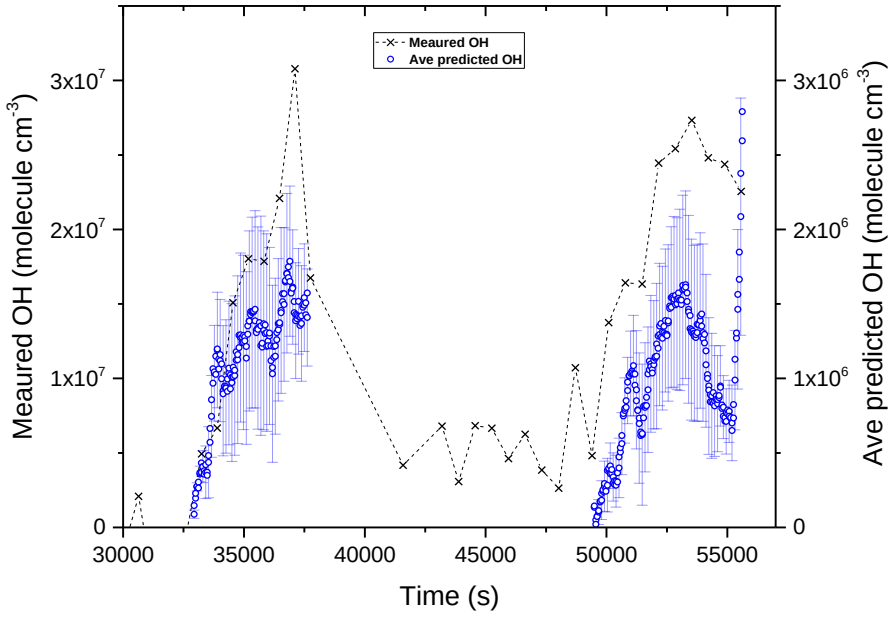

Figure 5.9. Comparison between the measured, black cross, and predicted OH, blue circles, for the piperidine kinetic study. Tracers; isoprene, styrene, trimethyl benzene, piperidine.

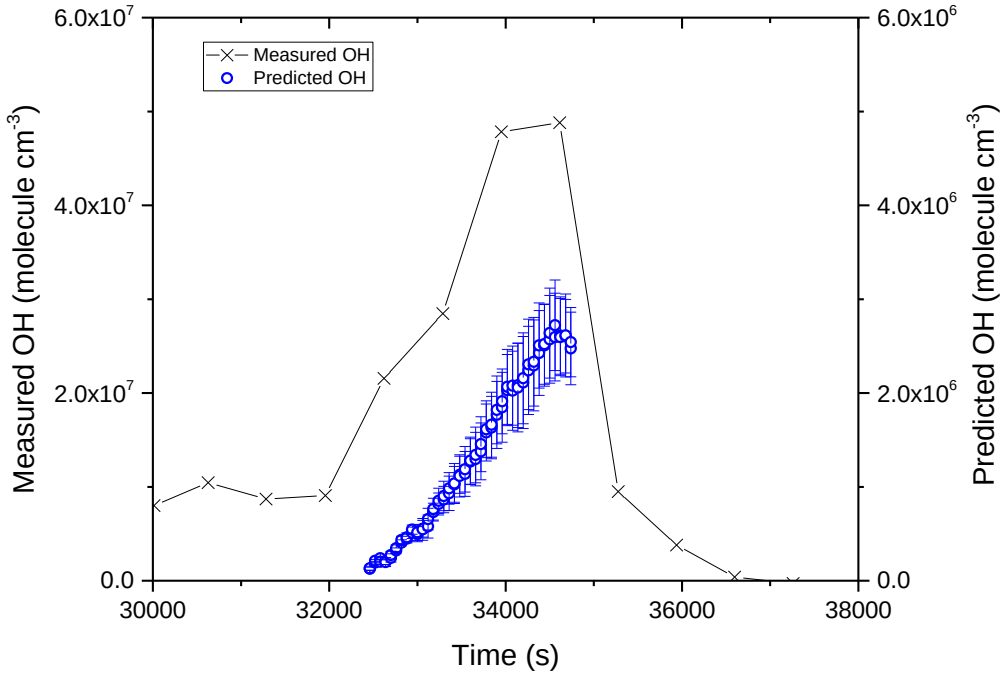

Figure 5.10. Comparison between the measured, black cross, and predicted OH, blue circles, for the piperazine kinetic study. Tracers; isoprene, limonene, trimethyl benzene, piperazine.

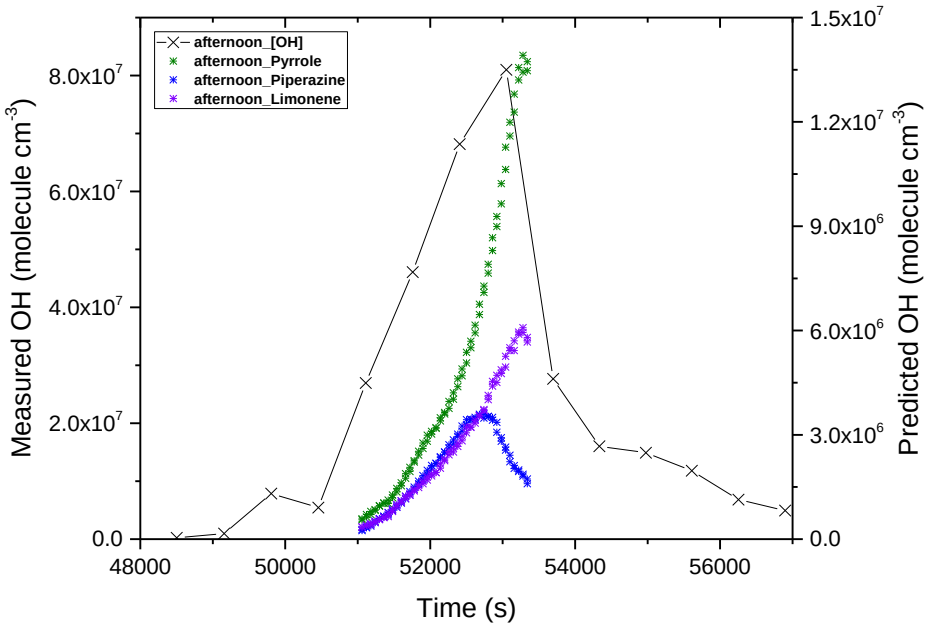

Figure 5.11. Comparison between the measured, black cross, and predicted OH, blue circles, for the piperazine kinetic study. Tracers; pyrrole, limonene, piperazine.

These plots show a clear difference in the measured concentrations, left axis, and calculated, right axis, with calculated OH being at least 10 times lower than the measured OH. This under prediction was also observed in the product studies where the removal of the initial amines was slower than would be expected for the measured OH. There are several possible explanations for this. The first is that the comparison assumes that the chamber is well mixed. However, because both instruments were sampling from different locations and both were sampling near the outer edges of the chamber there is the possibility of poor mixing resulting in an uneven distribution of both the OH and amine throughout the chamber. The second is that a possible interference in the FAGE cell caused by species in the chamber is contributing to the elevated OH signal. These are species that will generated OH in the detection cell when photolysed by the 308 nm laser light, or by decomposition when they are drawn into the low pressure cell[146]. No interference testing has been done for the Leeds aircraft cell in relation to this project so it is not possible to identify a specific compound. A final possibility is that an incorrect calibration factor for the FAGE instrument was applied.

As well as the weekly calibrations conducted during the campaign, the FAGE instrument was calibrated at Leeds before and after the ACA campaign for OH. These calibrations showed that when calibrated at Leeds the instrument was much more sensitive to OH than when calibrated at the EUPHORE chamber. When applying the Leeds calibration factors the measured OH concentrations decrease by a factor of 3. This decrease, shown in figure 5.12, does bring the measured values closer to the predicted values however there is still no agreement indicating that an unknown effect, such as inadequate chamber mixing, that is still contributing to the difference.

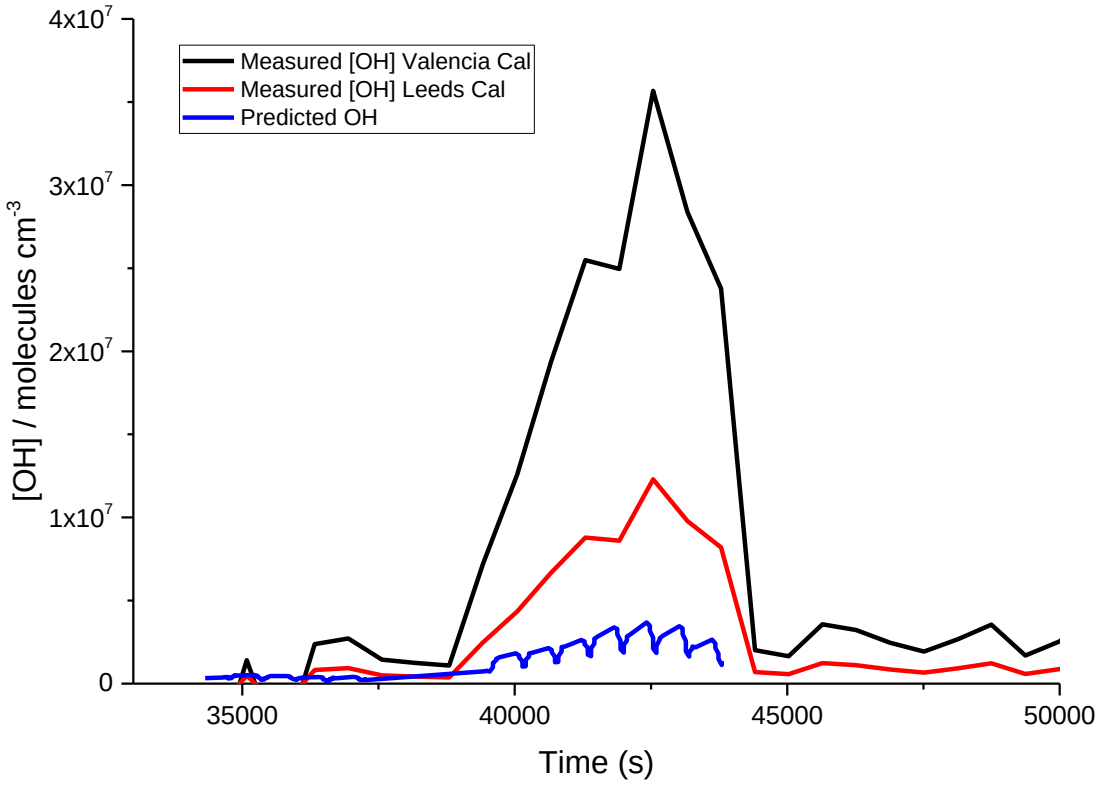

Figure 5.12. Comparison of the measured OH concentration, with both the Leeds, red line, and Valencia, black line, calibration factors applied, to the predicted OH, blue line for an amine study of Morpholine.

5.3.2 Decay of HO_2 in the dark

When the chamber was closed at the end of an experiment, elevated concentrations of HO_2 were still observed for up to 1.5 hours after. This observed decay was compared to a modelled decay of HO_2 Predicted using a model incorporating the mechanisms described by reactions 53 to 59 and utilising the Kintecus integrator[103]. For the reactions used to in the model, the rate constants have been calculated using the IUPAC recommended values[108] for the average chamber temperature during the HO_2 decay. The model inputs (HO_2, NO_2, NO, OH, O_3) were set to the concentration of each species 5 minutes after the chamber was closed.

$$HO_2 + HO_2 \xrightarrow{k=1.56E-12\ cm^3 molecule^{-1} s^{-1}} H_2O_2 + O_2 \quad \text{R(53)}$$

$$HO_2 + HO_2 + M \xrightarrow{k=1.10E-12\ cm^3 molecule^{-1} s^{-1}} H_2O_2 + O_2 + M \quad \text{R(54)}$$

$$HO_2 + NO \xrightarrow{k=8.54E-12\ cm^3 molecule^{-1} s^{-1}} NO_2 + OH \quad \text{R(55)}$$

$$HO_2 + O_3 \xrightarrow{k=2.14E-15\ cm^3 molecule^{-1} s^{-1}} OH + 2O_2 \quad \text{R(56)}$$

$$HO_2 + OH \xrightarrow{k=1.09E-10\ cm^3 molecule^{-1} s^{-1}} H_2O + O_2 \quad \text{R(57)}$$

$$HO_2 + NO_2 \xrightarrow{k=3.10E-12\ cm^3 molecule^{-1} s^{-1}} HO_2NO_2 \quad \text{R(58)}$$

$$HO_2NO_2 \xrightarrow{k=0.158\ s^{-1}} HO_2 + NO_2 \quad \text{R(59)}$$

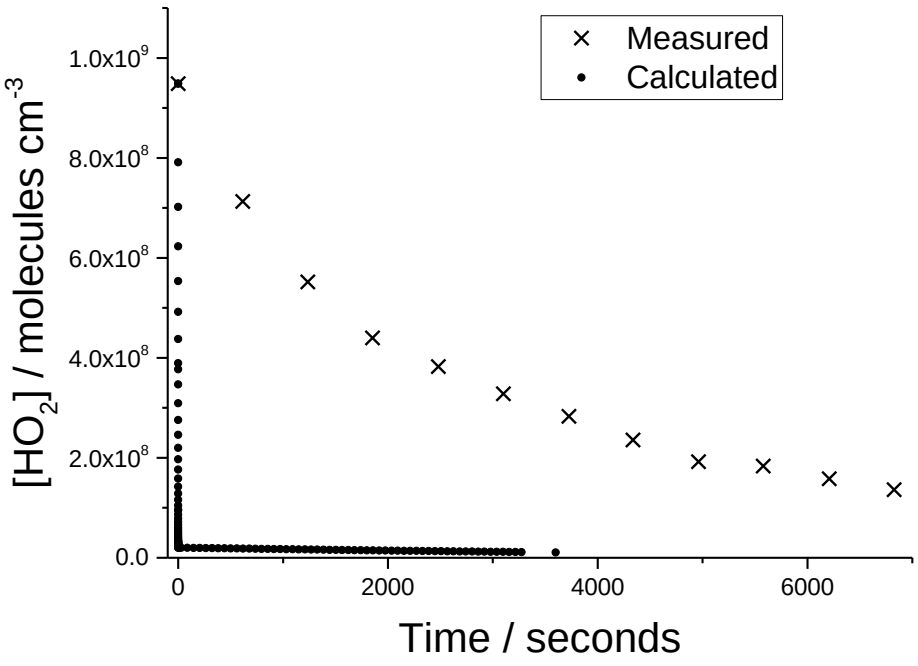

Figure 5.13. Comparison between measured HO_2, black crosses, and a calculated HO_2 decay, black circles. The decay of HO_2 occurs after the chamber has been closed at time zero. The full measurement day is shown in figure 6.6.

Figure 5.13 shows the comparison between the measured HO_2 and the model results. The model shows a considerably faster decay in HO_2 concentration than is seen in the chamber. This finding indicates that there is a source of HO_2 in the chamber in the dark. Possible sources of HO_2 in the dark include amine RO_2 species that can react with NO and O_2 to form HO_2 (R 60-64), or reactions between O_3 and species with double bonds generating Criegee intermediates that can break down to form HO_2[147].

$$RO_2 + NO \rightarrow RO \quad \text{R(60)}$$

$$RO_2 + NO_3 \rightarrow RO \quad \text{R(61)}$$

$$RO_2 + RO_2 \rightarrow RO \quad \text{R(62)}$$

$$RO_2 + HO_2 \rightarrow ROOH + O_2 \quad \text{R(63)}$$

$$RO + O_2 \rightarrow HO_2 \quad \text{R(64)}$$

This will be significant as in regions of high amines where this will be both a potential source during the day and will extend the production of HO_2 after sunset when the primary radical sources are normally reduced. This occurs because HO_2 can react with O_3 and NO_3 generating OH leading to removal of VOCs.

5.4 Chapter Summary

This chapter has described the use of the Leeds FAGE instrument during the atmospheric chemistry of amines project carried out at the EUPHORE chamber in June and August 2016. Results showed high concentrations of HO_2 on all days when the radical precursor, IPN, was added, while concentrations of OH were always close to the background signal. Challenges were discovered due to differences between measured OH and a calculated OH concentration, using the removal rates of different compounds in the chamber that indicated possible problems with uneven mixing in the chamber, possible FAGE interferences or uncertainties in OH calibration factors. Variation in the calibration coefficient due to the quality of gas used will be an important factor to consider when calibrating on field campaigns were the quality of the cylinder gas may vary depending on the manufacturing process. To account for this it will be important that calibrations are done using a trusted cylinder gas source before and after campaigns to ensure consistency of the calibration coefficient.

The Leeds aircraft FAGE cell needs to be tested for interferences from amines and their oxidation products to identify to what extent it is affected. These possible interferences from amine environments would need to be considered during future field measurements of OH. However recent developments of inlet pre injector devices (IPIs) that are used on field FAGE instruments are able to measure the OH interference. The device operates by removing ambient OH from the sample gas using a scavenger such as propane. By turning the flow of the scavenger on and off the instrument can measure ambient OH or the OH interference generated in the detection cell.

After the chamber was closed HO_2 was seen to remain for up to 2 hours. However, a modelled HO_2 decay was considerably faster indicating the presence of an HO_2 source in the dark potentially linked to amine RO_2's or the formation of Criegee radicals. It was not possible to expand of this observation further as there was limited data so dependence on variations of NO_x, O_3 or amine type could not be studied. Future studies could be include investigations into the night time sources of HO_x generated by amine based carbon capture plants, either via field studies or chamber measurements.

Bibliography

1. F.a.R.A. Department for Environment, *Clean Air Stratergy 2019*, 2019.
2. WHO, *WHO Air quality guidelines for particulate matter, ozone, nitrogen dioxide and sulfur dioxide* [online], [Accessed 20/09/2019]. Available from: https://apps.who.int/iris/bitstream/handle/10665/69477/WHO_SDE_PHE_OEH_06.02_eng.pdf;jsessionid=F2401C0EDB3BB31ACE56752C82F8D61A?sequence=1
3. DEFRA, *National air quality objectives* [online], [Accessed 20/09/2019]. Available from: https://uk-air.defra.gov.uk/assets/documents/Air_Quality_Objectives_Update.pdf
4. D.L. Jarvis, B.P. Leaderer, S. Chinn and P.G. Burney, 'Indoor nitrous acid and respiratory symptoms and lung function in adults', *Thorax*, 2005, 60, 474-479.
5. G. Topham, S. Clarke, C. Levett, P. Scruton and M. Fidler, *The Volkswagen emissions scandal explained* [online], 2015 [Accessed 20/09/2019]. Available from: https://www.theguardian.com/business/ng-interactive/2015/sep/23/volkswagen-emissions-scandal-explained-diesel-cars
6. Z.S. An, R.J. Huang, R.Y. Zhang, X.X. Tie, G.H. Li, J.J. Cao, W.J. Zhou, Z.G. Shi, Y.M. Han, Z.L. Gu and Y.M. Ji, 'Severe haze in northern China: A synergy of anthropogenic emissions and atmospheric processes', *Proceedings of the National Academy of Sciences of the United States of America*, 2019, 116, 8657-8666.
7. R.J. Huang, Y.L. Zhang, C. Bozzetti, K.F. Ho, J.J. Cao, Y.M. Han, K.R. Daellenbach, J.G. Slowik, S.M. Platt, F. Canonaco, P. Zotter, R. Wolf, S.M. Pieber, E.A. Bruns, M. Crippa, G. Ciarelli, A. Piazzalunga, M. Schwikowski, G. Abbaszade, J. Schnelle-Kreis, R. Zimmermann, Z.S. An, S. Szidat, U. Baltensperger, I. El Haddad and A.S.H. Prevot, 'High secondary aerosol contribution to particulate pollution during haze events in China', *Nature*, 2014, 514, 218-222.
8. Y. Wang, G.S. Zhuang, Y.L. Sun and Z.S. An, 'The variation of characteristics and formation mechanisms of aerosols in dust, haze, and clear days in Beijing', *Atmospheric Environment*, 2006, 40, 6579-6591.
9. J. Duan, R.J. Huang, C.S. Lin, W.T. Dai, M. Wang, Y.F. Gu, Y. Wang, H.B. Zhong, Y. Zheng, H.Y. Ni, U. Dusek, Y. Chen, Y.J. Li, Q. Chen, D.R. Worsnop, C.D. O'Dowd and J.J. Cao, 'Distinctions in source regions and formation mechanisms of secondary aerosol in Beijing from summer to winter', *Atmospheric Chemistry and Physics*, 2019, 19, 10319-10334.
10. S.C. S.C.Pryor, P. P.Crippa and R.C. Sullivan, 'Atmospheric Chemistry', *Reference Module in Earth Systems and Environmental Sciences*, 2015.
11. L.K. Whalley, D. Stone, I.J. George, S. Mertes, D. van Pinxteren, A. Tilgner, H. Herrmann, M.J. Evans and D.E. Heard, 'The influence of clouds on radical concentrations: observations and modelling studies of HOx during the Hill Cap Cloud Thuringia (HCCT) campaign in 2010', *Atmospheric Chemistry and Physics*, 2015, 15, 3289-3301.

12. J. Mao, S. Fan, D.J. Jacob and K.R. Travis, 'Radical loss in the atmosphere from Cu-Fe redox coupling in aerosols', *Atmospheric Chemistry and Physics*, 2013, 13, 509-519.
13. P.S.J. Matthews, M.T. Baeza-Romero, L.K. Whalley and D.E. Heard, 'Uptake of HO2 radicals onto Arizona test dust particles using an aerosol flow tube', *Atmospheric Chemistry and Physics*, 2014, 14, 7397-7408.
14. P.S.J. Matthews, 'Heterogenous uptake of HO2 radicals onto atmospheric aerosols', *PhD thesis, University of Leeds*, 2014.
15. I.J. George, P.S.J. Matthews, L.K. Whalley, B. Brooks, A. Goddard, M.T. Baeza-Romero and D.E. Heard, 'Measurements of uptake coefficients for heterogeneous loss of HO2 onto submicron inorganic salt aerosols', *Physical Chemistry Chemical Physics*, 2013, 15, 12829-12845.
16. D.R. Moon, G.S. Taverna, C. Anduix-Canto, T. Ingham, M.P. Chipperfield, P.W. Seakins, M.T. Baeza-Romero and D.E. Heard, 'Heterogeneous reaction of HO2 with airborne TiO2 particles and its implication for climate change mitigation strategies', *Atmospheric Chemistry and Physics*, 2018, 18, 327-338.
17. D.R. Moon, T. Ingham, L.K. Whalley, P.W. Seakins, M.T. Baeza-Romero and D.E. Heard, 'Production of HO2 and OH radicals from near-UV irradiated airborne TiO2 nanoparticles', *Physical Chemistry Chemical Physics*, 2019, 21, 2325-2336.
18. B.J. Finlayson-Pitts and J.N. Pitts,'Chemistry of the Upper and Lower Atmosphere: Theory, Experiments, and Applications', Academic Press, 2000, Chapter Particles in the Troposphere.
19. Y. Zhou and H. Savijarvi, 'The effect of aerosols on long wave radiation and global warming', *Atmospheric Research*, 2014, 135, 102-111.
20. A. Valenzuela, A. Arola, M. Anton, A. Quirantes and L. Alados-Arboledas, 'Black carbon radiative forcing derived from AERONET measurements and models over an urban location in the southeastern Iberian Peninsula', *Atmospheric Research*, 2017, 191, 44-56.
21. M.O. Andreae, 'Correlation between cloud condensation nuclei concentration and aerosol optical thickness in remote and polluted regions', *Atmospheric Chemistry and Physics*, 2009, 9, 543-556.
22. A.I. Calvo, C. Alves, A. Castro, V. Pont, A.M. Vicente and R. Fraile, 'Research on aerosol sources and chemical composition: Past, current and emerging issues', *Atmospheric Research*, 2013, 120, 1-28.
23. T. Ingham, A. Goddard, L.K. Whalley, K.L. Furneaux, P.M. Edwards, C.P. Seal, D.E. Self, G.P. Johnson, K.A. Read, J.D. Lee and D.E. Heard, 'A flow-tube based laser-induced fluorescence instrument to measure OH reactivity in the troposphere', *Atmospheric Measurement Techniques*, 2009, 2, 465-477.
24. K.D. Lu, F. Rohrer, F. Holland, H. Fuchs, B. Bohn, T. Brauers, C.C. Chang, R. Haseler, M. Hu, K. Kita, Y. Kondo, X. Li, S.R. Lou, S. Nehr, M. Shao, L.M. Zeng, A. Wahner, Y.H. Zhang and A. Hofzumahaus, 'Observation and modelling of OH and HO2 concentrations in the Pearl River Delta 2006: a missing OH source in a VOC rich atmosphere', *Atmospheric Chemistry and Physics*, 2012, 12, 1541-1569.
25. J.P. Abram, D.J. Creasey, D.E. Heard, J.D. Lee and M.J. Pilling, 'Hydroxyl radical and ozone measurements in England during the solar eclipse of 11 August 1999', *Geophysical Research Letters*, 2000, 27, 3437-3440.

26. D. Perner and U. Platt, 'Detection of Nitrous-Acid in the Atmosphere by Differential Optical-Absorption', *Geophysical Research Letters*, 1979, 6, 917-920.
27. J.Z. Ma, Y.C. Liu, C. Han, Q.X. Ma, C. Liu and H. He, 'Review of heterogeneous photochemical reactions of NOy on aerosol - A possible daytime source of nitrous acid (HONO) in the atmosphere', *Journal of Environmental Sciences-China*, 2013, 25, 326-334.
28. R.M. Harrison, J.D. Peak and G.M. Collins, 'Tropospheric cycle of nitrous acid', *Journal of Geophysical Research-Atmospheres*, 1996, 101, 14429-14439.
29. A.J. Colussi, S. Enami, A. Yabushita, M.R. Hoffmann, W.G. Liu, H. Mishra and W.A. Goddard, 'Tropospheric aerosol as a reactive intermediate', *Faraday Discussions*, 2013, 165, 407-420.
30. J.D. Lee, L.K. Whalley, D.E. Heard, D. Stone, R.E. Dunmore, J.F. Hamilton, D.E. Young, J.D. Allan, S. Laufs and J. Kleffmann, 'Detailed budget analysis of HONO in central London reveals a missing daytime source', *Atmospheric Chemistry and Physics*, 2016, 16, 2747-2764.
31. K. Acker, D. Moller, W. Wieprecht, F.X. Meixner, B. Bohn, S. Gilge, C. Plass-Dulmer and H. Berresheim, 'Strong daytime production of OH from HNO2 at a rural mountain site', *Geophysical Research Letters*, 2006, 33.
32. J. Kleffmann, 'Daytime sources of nitrous acid (HONO) in the atmospheric boundary layer', *Chemphyschem*, 2007, 8, 1137-1144.
33. X. Li, T. Brauers, R. Haseler, B. Bohn, H. Fuchs, A. Hofzumahaus, F. Holland, S. Lou, K.D. Lu, F. Rohrer, M. Hu, L.M. Zeng, Y.H. Zhang, R.M. Garland, H. Su, A. Nowak, A. Wiedensohler, N. Takegawa, M. Shao and A. Wahner, 'Exploring the atmospheric chemistry of nitrous acid (HONO) at a rural site in Southern China', *Atmospheric Chemistry and Physics*, 2012, 12, 1497-1513.
34. S. Kim, T.C. VandenBoer, C.J. Young, T.P. Riedel, J.A. Thornton, B. Swarthout, B. Sive, B. Lerner, J.B. Gilman, C. Warneke, J.M. Roberts, A. Guenther, N.L. Wagner, W.P. Dube, E. Williams and S.S. Brown, 'The primary and recycling sources of OH during the NACHTT-2011 campaign: HONO as an important OH primary source in the wintertime', *Journal of Geophysical Research-Atmospheres*, 2014, 119, 6886-6896.
35. B. Alicke, A. Geyer, A. Hofzumahaus, F. Holland, S. Konrad, H.W. Patz, J. Schafer, J. Stutz, A. Volz-Thomas and U. Platt, 'OH formation by HONO photolysis during the BERLIOZ experiment', *Journal of Geophysical Research-Atmospheres*, 2003, 108, article number 8247, 17.
36. Y.J. Leong, A.P. Rutter, H.Y. Wong, C.V. Gutierrez, M. Junaid, E. Scheuer, L. Gong, R. Lewicki, J.E. Dibb, F.K. Tittel and R.J. Griffin, 'Impact of environmental variables on the reduction of nitric acid by proxies for volatile organic compounds emitted by motor vehicles', *Atmospheric Pollution Research*, 2015.
37. C. Reed, M.J. Evans, L.R. Crilley, W.J. Bloss, T. Sherwen, K.A. Read, J.D. Lee and L.J. Carpenter, 'Evidence for renoxification in the tropical marine boundary layer', *Atmospheric Chemistry and Physics*, 2017, 17, 4081-4092.
38. R. Atkinson, 'Atmospheric chemistry of VOCs and NOx', *Atmospheric Environment*, 2000, 34, 2063-2101.

39. R. Vingarzan, 'A review of surface ozone background levels and trends', *Atmospheric Environment*, 2004, 38, 3431-3442.
40. R.J. Huang, L. Yang, J.J. Cao, Q.Y. Wang, X.X. Tie, K.F. Ho, Z.X. Shen, R.J. Zhang, G.H. Li, C.S. Zhu, N.N. Zhang, W.T. Dai, J.M. Zhou, S.X. Liu, Y. Chen, J. Chen and C.D. O'Dowd, 'Concentration and sources of atmospheric nitrous acid (HONO) at an urban site in Western China', *Science of the Total Environment*, 2017, 593, 165-172.
41. W.Q. Zhang, S.R. Tong, M.F. Ge, J.L. An, Z.B. Shi, S.Q. Hou, K.H. Xia, Y. Qu, H.X. Zhang, B.W. Chu, Y.L. Sun and H. He, 'Variations and sources of nitrous acid (HONO) during a severe pollution episode in Beijing in winter 2016', *Science of the Total Environment*, 2019, 648, 253-262.
42. J.D. Lee, L.K. Whalley, D.E. Heard, D. Stone, R.E. Dunmore, J.F. Hamilton, D.E. Young, J.D. Allan, S. Laufs and J. Kleffmann, 'Detailed budget analysis of HONO in central London reveals a missing daytime source', *Atmos. Chem. Phys. Discuss.*, 2015, 15, 22097-22139.
43. J. Kleffmann, T. Gavriloaiei, A. Hofzumahaus, F. Holland, R. Koppmann, L. Rupp, E. Schlosser, M. Siese and A. Wahner, 'Daytime formation of nitrous acid: A major source of OH radicals in a forest', *Geophysical Research Letters*, 2005, 32.
44. R. Forster, M. Frost, D. Fulle, H.F. Hamann, H. Hippler, A. Schlepegrell and J. Troe, 'High-Pressure Range of the Addition of Ho to Ho, No, No2, and Co .1. Saturated Laser-Induced Fluorescence Measurements at 298 K', *Journal of Chemical Physics*, 1995, 103, 2949-2958.
45. D. Stone, M.J. Evans, H. Walker, T. Ingham, S. Vaughan, B. Ouyang, O.J. Kennedy, M.W. McLeod, R.L. Jones, J. Hopkins, S. Punjabi, R. Lidster, J.F. Hamilton, J.D. Lee, A.C. Lewis, L.J. Carpenter, G. Forster, D.E. Oram, C.E. Reeves, S. Bauguitte, W. Morgan, H. Coe, E. Aruffo, C. Dari-Salisburgo, F. Giammaria, P. Di Carlo and D.E. Heard, 'Radical chemistry at night: comparisons between observed and modelled HOx, NO3 and N2O5 during the RONOCO project', *Atmospheric Chemistry and Physics*, 2014, 14, 1299-1321.
46. I. Bejan, Y. Abd El Aal, I. Barnes, T. Benter, B. Bohn, P. Wiesen and J. Kleffmann, 'The photolysis of ortho-nitrophenols: a new gas phase source of HONO', *Physical Chemistry Chemical Physics*, 2006, 8, 2028-2035.
47. X. Li, F. Rohrer, A. Hofzumahaus, T. Brauers, R. Haseler, B. Bohn, S. Broch, H. Fuchs, S. Gomm, F. Holland, J. Jager, J. Kaiser, F.N. Keutsch, I. Lohse, K.D. Lu, R. Tillmann, R. Wegener, G.M. Wolfe, T.F. Mentel, A. Kiendler-Scharr and A. Wahner, 'Missing Gas-Phase Source of HONO Inferred from Zeppelin Measurements in the Troposphere', *Science*, 2014, 344, 292-296.
48. R. Kurtenbach, K.H. Becker, J.A.G. Gomes, J. Kleffmann, J.C. Lorzer, M. Spittler, P. Wiesen, R. Ackermann, A. Geyer and U. Platt, 'Investigations of emissions and heterogeneous formation of HONO in a road traffic tunnel', *Atmospheric Environment*, 2001, 35, 3385-3394.
49. J.N. Pitts, H.W. Biermann, A.M. Winer and E.C. Tuazon, 'SPECTROSCOPIC IDENTIFICATION AND MEASUREMENT OF GASEOUS NITROUS-ACID IN DILUTE AUTO EXHAUST', *Atmospheric Environment*, 1984, 18, 847-854.

50. A.P. Rutter, Q.G.J. Malloy, Y.J. Leong, C.V. Gutierrez, M. Calzada, E. Scheuer, J.E. Dibb and R.J. Griffin, 'The reduction of HNO3 by volatile organic compounds emitted by motor vehicles', *Atmospheric Environment*, 2014, 87, 200-206.
51. Y.H. Liu, K.D. Lu, Y.F. Ma, X.P. Yang, W.B. Zhang, Y.S. Wu, J.F. Peng, S.J. Shuai, M. Hu and Y.H. Zhang, 'Direct emission of nitrous acid (HONO) from gasoline cars in China determined by vehicle chassis dynamometer experiments', *Atmospheric Environment*, 2017, 169, 89-96.
52. R.J. Gustafsson, A. Orlov, P.T. Griffiths, R.A. Cox and R.M. Lambert, 'Reduction of NO2 to nitrous acid on illuminated titanium dioxide aerosol surfaces: implications for photocatalysis and atmospheric chemistry', *Chemical Communications*, 2006, 3936-3938.
53. V. Michoud, J.F. Doussin, A. Colomb, C. Afif, A. Borbon, M. Camredon, B. Aumont, M. Legrand and M. Beekmann, 'Strong HONO formation in a suburban site during snowy days', *Atmospheric Environment*, 2015, 116, 155-158.
54. M. Kalberer, M. Ammann, F. Arens, H.W. Gaggeler and U. Baltensperger, 'Heterogeneous formation of nitrous acid (HONO) on soot aerosol particles', *Journal of Geophysical Research-Atmospheres*, 1999, 104, 13825-13832.
55. B. D'Anna, A. Jammoul, C. George, K. Stemmler, S. Fahrni, M. Ammann and A. Wisthaler, 'Light-induced ozone depletion by humic acid films and submicron aerosol particles', *Journal of Geophysical Research-Atmospheres*, 2009, 114, article number D12301, 12.
56. K. Stemmler, M. Ammann, C. Donders, J. Kleffmann and C. George, 'Photosensitized reduction of nitrogen dioxide on humic acid as a source of nitrous acid', *Nature*, 2006, 440, 195-198.
57. K. Stemmler, M. Ndour, Y. Elshorbany, J. Kleffmann, B. D'Anna, C. George, B. Bohn and M. Ammann, 'Light induced conversion of nitrogen dioxide into nitrous acid on submicron humic acid aerosol', *Atmospheric Chemistry and Physics*, 2007, 7, 4237-4248.
58. Y. Dupart, L. Fine, B. D'Anna and C. George, 'Heterogeneous uptake of NO2 on Arizona Test Dust under UV-A irradiation: An aerosol flow tube study', *Aeolian Research*, 2014, 15, 45-51.
59. S. Laufs, G. Burgeth, W. Duttlinger, R. Kurtenbach, M. Maban, C. Thomas, P. Wiesen and J. Kleffmann, 'Conversion of nitrogen oxides on commercial photocatalytic dispersion paints', *Atmospheric Environment*, 2010, 44, 2341-2349.
60. B. Alexander, M.G. Hastings, D.J. Allman, J. Dachs, J.A. Thornton and S.A. Kunasek, 'Quantifying atmospheric nitrate formation pathways based on a global model of the oxygen isotopic composition (delta O-17) of atmospheric nitrate', *Atmospheric Chemistry and Physics*, 2009, 9, 5043-5056.
61. W.L. Chang, P.V. Bhave, S.S. Brown, N. Riemer, J. Stutz and D. Dabdub, 'Heterogeneous Atmospheric Chemistry, Ambient Measurements, and Model Calculations of N2O5: A Review', *Aerosol Science and Technology*, 2011, 45, 665-695.
62. Y. Feng and J.E. Penner, 'Global modeling of nitrate and ammonium: Interaction of aerosols and tropospheric chemistry', *Journal of Geophysical Research-Atmospheres*, 2007, 112.

63. C.X. Ye, N. Zhang, H.L. Gao and X.L. Zhou, 'Photolysis of Particulate Nitrate as a Source of HONO and NOx', *Environmental Science & Technology*, 2017, 51, 6849-6856.
64. C.X. Ye, X.L. Zhou, D. Pu, J. Stutz, J. Festa, M. Spolaor, C. Tsai, C. Cantrell, R.L. Mauldin, T. Campos, A. Weinheimer, R.S. Hornbrook, E.C. Apel, A. Guenther, L. Kaser, B. Yuan, T. Karl, J. Haggerty, S. Hall, K. Ullmann, J.N. Smith, J. Ortega and C. Knote, 'Rapid cycling of reactive nitrogen in the marine boundary layer', *Nature*, 2016, 532, 489-491.
65. C.X. Ye, D.E. Heard and L.K. Whalley, 'Evaluation of Novel Routes for NOx Formation in Remote Regions', *Environmental Science & Technology*, 2017, 51, 7442-7449.
66. Y. Bedjanian and A. El Zein, 'Interaction of NO2 with TiO2 Surface Under UV Irradiation: Products Study', *Journal of Physical Chemistry A*, 2012, 116, 1758-1764.
67. P. Davidovits, C.E. Kolb, L.R. Williams, J.T. Jayne and D.R. Worsnop, 'Mass accommodation and chemical reactions at gas-liquid interfaces', *Chemical Reviews*, 2006, 106, 1323-1354.
68. B.J. Finlayson-Pitts, *Chemistry of the upper and lower atmosphere : theory, experiments, and applications / Barbara J. Finlayson-Pitts, James N. Pitts, Jr*, Academic, San Diego, Calif. ; London :, 2000.
69. R. Commane, C.F.A. Floquet, T. Ingham, D. Stone, M.J. Evans and D.E. Heard, 'Observations of OH and HO2 radicals over West Africa', *Atmospheric Chemistry and Physics*, 2010, 10, 8783-8801.
70. S. Gligorovski, R. Strekowski, S. Barbati and D. Vione, 'Environmental Implications of Hydroxyl Radicals (center dot OH)', *Chemical Reviews*, 2015, 115, 13051-13092.
71. A. Kukui, G. Ancellet and G. Le Bras, 'Chemical ionisation mass spectrometer for measurements of OH and Peroxy radical concentrations in moderately polluted atmospheres', *Journal of Atmospheric Chemistry*, 2008, 61, 133-154.
72. D. Poppe, T. Brauers, H.P. Dorn, M. Karl, T. Mentel, E. Schlosser, R. Tillmann, R. Wegener and A. Wahner, 'OH-initiated degradation of several hydrocarbons in the atmosphere simulation chamber SAPHIR', *Journal of Atmospheric Chemistry*, 2007, 57, 203-214.
73. H. Fuchs, H.P. Dorn, M. Bachner, B. Bohn, T. Brauers, S. Gomm, A. Hofzumahaus, F. Holland, S. Nehr, F. Rohrer, R. Tillmann and A. Wahner, 'Comparison of OH concentration measurements by DOAS and LIF during SAPHIR chamber experiments at high OH reactivity and low NO concentration', *Atmospheric Measurement Techniques*, 2012, 5, 1611-1626.
74. T. Brauers, M. Hausmann, A. Bister, A. Kraus and H.P. Dorn, 'OH radicals in the boundary layer of the Atlantic Ocean 1. Measurements by long-path laser absorption spectroscopy', *Journal of Geophysical Research-Atmospheres*, 2001, 106, 7399-7414.
75. D.E. Heard, 'Atmospheric field measurements of the hydroxylradical using laser-induced fluorescence spectroscopy', *Annual Review of Physical Chemistry*, 2006, 57, 191-216.
76. E.L. Baardsen and R.W. Terhune, 'Detection of Oh in Atmosphere Using a Dye Laser', *Applied Physics Letters*, 1972, 21, 209-&.
77. S. Dusanter, D. Vimal, P.S. Stevens, R. Volkamer and L.T. Molina, 'Measurements of OH and HO2 concentrations during the MCMA-2006

field campaign - Part 1: Deployment of the Indiana University laser-induced fluorescence instrument', *Atmospheric Chemistry and Physics*, 2009, 9, 1665-1685.

78. P.S. Stevens, J.H. Mather and W.H. Brune, 'Measurement of Tropospheric Oh and Ho2 by Laser-Induced Fluorescence at Low-Pressure', *Journal of Geophysical Research-Atmospheres*, 1994, 99, 3543-3557.
79. E.C. Wood and R.C. Cohen,'Fluorescence Methods', in *Analytical techniques for atmospheric measurements*, ed. D. Heard, Blackwell Publishing, 1st edition edition, 2006, Chapter Chapter 4, 190-194.
80. D.E. Heard,'Atmospheric field measurements of the hydroxylradical using laser-induced fluorescence spectroscopy', in *Annual Review of Physical Chemistry*, Annual Reviews, Palo Alto, 2006, vol. 57, 191-216.
81. D.J. Creasey, D.E. Heard, M.J. Pilling, B.J. Whitaker, M. Berzins and R. Fairlie, 'Visualisation of a supersonic free-jet expansion using laser-induced fluorescence spectroscopy: Application to the measurement of rate constants at ultralow temperatures', *Applied Physics B-Lasers and Optics*, 1997, 65, 375-391.
82. J.M.C. Plane and N. Smith,'Atmospheric Monitoring by Differential Optical Absorption Spectroscopy', in *Spectroscopy in Environmental Science*, eds. R.J.H. Clark and R.E. Hester, John Wiley & Sons, 1995, Chapter 5, 223-241.
83. D. Garcia-Nieto, N. Benavent and A. Saiz-Lopez, 'Measurements of atmospheric HONO vertical distribution and temporal evolution in Madrid (Spain) using the MAX-DOAS technique', *Science of the Total Environment*, 2018, 643, 957-966.
84. T. Wagner, O. Ibrahim, R. Shaiganfar and U. Platt, 'Mobile MAX-DOAS observations of tropospheric trace gases', *Atmospheric Measurement Techniques*, 2010, 3, 129-140.
85. J. Heland, J. Kleffmann, R. Kurtenbach and P. Wiesen, 'A new instrument to measure gaseous nitrous acid (HONO) in the atmosphere', *Environmental Science & Technology*, 2001, 35, 3207-3212.
86. J. Kleffmann, J.C. Lorzer, P. Wiesen, C. Kern, S. Trick, R. Volkamer, M. Rodenas and K. Wirtz, 'Intercomparison of the DOAS and LOPAP techniques for the detection of nitrous acid (HONO)', *Atmospheric Environment*, 2006, 40, 3640-3652.
87. C. Reed, C.A. Brumby, L.R. Crilley, L.J. Kramer, W.J. Bloss, P.W. Seakins, J.D. Lee and L.J. Carpenter, 'HONO measurement by differential photolysis', *Atmospheric Measurement Techniques*, 2016, 9, 2483-2495.
88. W. Liao, A. Hecobian, J. Mastromarino and D. Tan, 'Development of a photo-fragmentation/laser-induced fluorescence measurement of atmospheric nitrous acid', *Atmospheric Environment*, 2006, 40, 17-26.
89. Y.Q. Li, J.J. Schwab and K.L. Demerjian, 'Fast time response measurements of gaseous nitrous acid using a tunable diode laser absorption spectrometer: HONO emission source from vehicle exhausts', *Geophysical Research Letters*, 2008, 35, article number L04803, 5.
90. N. Takenaka, H. Terada, Y. Oro, M. Hiroi, H. Yoshikawa, K. Okitsu and H. Bandow, 'A new method for the measurement of trace amounts of HONO in the atmosphere using an air-dragged aqua-membrane-type denuder and fluorescence detection', *Analyst*, 2004, 129, 1130-1136.

91. K. Acker, D. Moller, R. Auel, W. Wieprecht and D. Kalass, 'Concentrations of nitrous acid, nitric acid, nitrite and nitrate in the gas and aerosol phase at a site in the emission zone during ESCOMPTE 2001 experiment', *Atmospheric Research*, 2005, 74, 507-524.
92. J.E. Dibb, L.G. Huey, D.L. Slusher and D.J. Tanner, 'Soluble reactive nitrogen oxides at South Pole during ISCAT 2000', *Atmospheric Environment*, 2004, 38, 5399-5409.
93. X.L. Zhou, H.C. Qiao, G.H. Deng and K. Civerolo, 'A method for the measurement of atmospheric HONO based on DNPH derivatization and HPLC analysis', *Environmental Science & Technology*, 1999, 33, 3672-3679.
94. *Wet chemical Techniques for the Detection of Nitrous Acid (HONO) in the Atmosphere* [online], [Accessed 02/02/2016]. Available from: http://www.eurochamp.org/datapool/page/58/Kleffmann.pdf
95. R. Oswald, M. Ermel, K. Hens, A. Novelli, H.G. Ouwersloot, P. Paasonen, T. Petaja, M. Sipila, P. Keronen, J. Back, R. Konigstedt, Z.H. Beygi, H. Fischer, B. Bohn, D. Kubistin, H. Harder, M. Martinez, J. Williams, T. Hoffmann, I. Trebs and M. Sorgel, 'A comparison of HONO budgets for two measurement heights at a field station within the boreal forest in Finland', *Atmospheric Chemistry and Physics*, 2015, 15, 799-813.
96. T. Gherman, D.S. Venables, S. Vaughan, J. Orphal and A.A. Ruth, 'Incoherent broadband cavity-enhanced absorption spectroscopy in the near-ultraviolet: Application to HONO and NO2', *Environmental Science & Technology*, 2008, 42, 890-895.
97. K.Y. Zheng, C.T. Zheng, Y. Zhang, Y.D. Wang and F.K. Tittel, 'Review of Incoherent Broadband Cavity-Enhanced Absorption Spectroscopy (IBBCEAS) for Gas Sensing', *Sensors*, 2018, 18.
98. R.A. Cox and R.G. Derwent, 'The ultra-violet absorption spectrum of gaseous nitrous acid', *Journal of Photochemistry*, 1976, 6, 23-34.
99. J.H. Shan, S.J. Wategaonkar and R. Vasudev, 'Vibrational-State Dependence of the a-State Lifetime of Hono', *Chemical Physics Letters*, 1989, 158, 317-320.
100. A.S. Brust, K.H. Becker, J. Kleffmann and P. Wiesen, 'UV absorption cross sections of nitrous acid', *Atmospheric Environment*, 2000, 34, 13-19.
101. L.K. Whalley, D. Stone, R. Dunmore, J. Hamilton, J.R. Hopkins, J.D. Lee, A.C. Lewis, P. Williams, J. Kleffmann, S. Laufs, R. Woodward-Massey and D.E. Heard, 'Understanding in situ ozone production in the summertime through radical observations and modelling studies during the Clean air for London project (ClearfLo)', *Atmospheric Chemistry and Physics*, 2018, 18, 2547-2571.
102. J.D. Lee, S.J. Moller, K.A. Read, A.C. Lewis, L. Mendes and L.J. Carpenter, 'Year-round measurements of nitrogen oxides and ozone in the tropical North Atlantic marine boundary layer', *Journal of Geophysical Research-Atmospheres*, 2009, 114.
103. J.C. Ianni, 'A comparison of the Bader-Deuflhard and the Cash-Karp Runge-Kutta integrators for the GRI-MECH 3.0 model based on the chemical kinetics code Kintecus', *Computational Fluid and Solid Mechanics 2003, Vols 1 and 2, Proceedings*, 2003, 1368-1372.

104. T. Lewis, D.E. Heard and M.A. Blitz, 'A novel multiplex absorption spectrometer for time-resolved studies', *Review of Scientific Instruments*, 2018, 89.
105. S.C. Smith, 'Atmospheric Measurements of OH and HO2 using the FAGE Technique: Instrument Development and Data Analysis', *PhD thesis, University of Leeds*, 2007.
106. R. Broske, J. Kleffmann and P. Wiesen, 'Heterogeneous conversion of NO2 on secondary organic aerosol surfaces: A possible source of nitrous acid (HONO) in the atmosphere?', *Atmospheric Chemistry and Physics*, 2003, 3, 469-474.
107. G.D. Edwards and P.S. Monks, 'Performance of a single-monochromator diode array spectroradiometer for the determination of actinic flux and atmospheric photolysis frequencies', *Journal of Geophysical Research-Atmospheres*, 2003, 108.
108. R. Atkinson, D.L. Baulch, R.A. Cox, J.N. Crowley, R.F. Hampson, R.G. Hynes, M.E. Jenkin, M.J. Rossi and J. Troe, 'Evaluated kinetic and photochemical data for atmospheric chemistry: Volume I - gas phase reactions of O-x, HOx, NOx and SOx species', *Atmospheric Chemistry and Physics*, 2004, 4, 1461-1738.
109. K. Bogumil, J. Orphal, T. Homann, S. Voigt, P. Spietz, O.C. Fleischmann, A. Vogel, M. Hartmann, H. Kromminga, H. Bovensmann, J. Frerick and J.P. Burrows, 'Measurements of molecular absorption spectra with the SCIAMACHY pre-flight model: instrument characterization and reference data for atmospheric remote-sensing in the 230-2380 nm region', *Journal of Photochemistry and Photobiology a-Chemistry*, 2003, 157, 167-184.
110. TSI, 'Model 3076 Constant Output Atomizer Instruction Manual', 2005.
111. B. Forsyth, B.Y.H. Liu and F.J. Romay, 'Particle charge distribution measurement for commonly generated laboratory aerosols', *Aerosol Science and Technology*, 1998, 28, 489-501.
112. TSI, 'Series 3080 Electrostatic Classifiers Operation an service manual', 2009.
113. TSI, 'Model 3775 Condensation Particle Counter, Operation and Service Manual', 2007.
114. E.I. Cedillo-Gonzalez, R. Ricco, M. Montorsi, M. Montorsi, P. Falcaro and C. Siligardi, 'Self-cleaning glass prepared from a commercial TiO2 nano-dispersion and its photocatalytic performance under common anthropogenic and atmospheric factors', *Building and Environment*, 2014, 71, 7-14.
115. F. Mothes, S. Ifang, M. Gallus, B. Golly, A. Boreave, R. Kurtenbach, J. Kleffmann, C. George and H. Herrmann, 'Bed flow photoreactor experiments to assess the photocatalytic nitrogen oxides abatement under simulated atmospheric conditions', *Applied Catalysis B-Environmental*, 2018, 231, 161-172.
116. N.K. Scharko, A.E. Berke and J.D. Raff, 'Release of Nitrous Acid and Nitrogen Dioxide from Nitrate Photolysis in Acidic Aqueous Solutions', *Environmental Science & Technology*, 2014, 48, 11991-12001.
117. C. Han, W.J. Yang, Q.Q. Wu, H. Yang and X.X. Xue, 'Heterogeneous Photochemical Conversion of NO2 to HONO on the Humic Acid Surface under Simulated Sunlight', *Environmental Science & Technology*, 2016, 50, 5017-5023.

118. M.R. Hoffmann, S.T. Martin, W.Y. Choi and D.W. Bahnemann, 'Environmental Applications of Semiconductor Photocatalysis', *Chemical Reviews*, 1995, 95, 69-96.
119. T. Berger, M. Sterrer, O. Diwald, E. Knozinger, D. Panayotov, T.L. Thompson and J.T. Yates, 'Light-induced charge separation in anatase TiO2 particles', *Journal of Physical Chemistry B*, 2005, 109, 6061-6068.
120. K. Nakata and A. Fujishima, 'TiO2 photocatalysis: Design and applications', *Journal of Photochemistry and Photobiology C-Photochemistry Reviews*, 2012, 13, 169-189.
121. J. Schneider, M. Matsuoka, M. Takeuchi, J.L. Zhang, Y. Horiuchi, M. Anpo and D.W. Bahnemann, 'Understanding TiO2 Photocatalysis: Mechanisms and Materials', *Chemical Reviews*, 2014, 114, 9919-9986.
122. Z.B. Shi, T. Vu, S. Kotthaus, R.M. Harrison, S. Grimmond, S. Yue, T. Zhu, J. Lee, Y. Han, M. Demuzere, R.E. Dunmore, L.J. Ren, D. Liu, Y.L. Wang, O. Wild, J. Allan, W.J. Acton, J. Barlow, B. Barratt, D. Beddows, W.J. Bloss, G. Calzolai, D. Carruthers, D.C. Carslaw, Q. Chan, L. Chatzidiakou, Y. Chen, L. Crilley, H. Coe, T. Dai, R. Doherty, F. Duan, P. Fu, B. Ge, M. Ge, D. Guan, J.F. Hamilton, K. He, M. Heal, D. Heard, C.N. Hewitt, M. Hollaway, M. Hu, D. Ji, X.J. Jiang, R. Jones, M. Kalberer, F.J. Kelly, L. Kramer, B. Langford, C. Lin, A.C. Lewis, J. Li, W. Li, H. Liu, J.F. Liu, M. Loh, K.D. Lu, F. Lucarelli, G. Mann, G. McFiggans, M.R. Miller, G. Mills, P. Monk, E. Nemitz, F. O'Connor, Bin O. u. y. a. n. g. , P.I. Palmer, C. Percival, O. Popoola, C. Reeves, A.R. Rickard, L.Y. Shao, G.Y. Shi, D. Spracklen, D. Stevenson, Y. Sun, Z.W. Sun, S. Tao, S.R. Tong, Q.Q. Wang, W.H. Wang, X.M. Wang, X.J. Wang, Z.F. Wang, L.F. Wei, L. Whalley, X.F. Wu, Z.J. Wu, P.H. Xie, F.M. Yang, Q. Zhang, Y.L. Zhang, Y.H. Zhang and M. Zheng, 'Introduction to the special issue "In-depth study of air pollution sources and processes within Beijing and its surrounding region (APHH-Beijing)"', *Atmospheric Chemistry and Physics*, 2019, 19, 7519-7546.
123. W. Tan, L. Zhu, T. Mikoviny, C.J. Nielsen, A. Wisthaler, P. Eichler, M. Muller, B. D'Anna, N.J. Farren, J.F. Hamilton, J.B.C. Pettersson, M. Hallquist, S. Antonsen and Y. Stenstrom, 'Theoretical and Experimental Study on the Reaction of tert-Butylamine with OH Radicals in the Atmosphere', *Journal of Physical Chemistry A*, 2018, 122, 4470-4480.
124. [online], [Accessed 19/08/2019]. Available from: https://www.epa.gov/ghgemissions/global-greenhouse-gas-emissions-data
125. *CO2 source* [online], [Accessed 19/08/2019]. Available from: https://www.epa.gov/ghgemissions/sources-greenhouse-gas-emissions
126. M. Kanniche, R. Gros-Bonnivard, P. Jaud, J. Valle-Marcos, J.M. Amann and C. Bouallou, 'Pre-combustion, post-combustion and oxy-combustion in thermal power plant for CO2 capture', *Applied Thermal Engineering*, 2010, 30, 53-62.
127. S.M. Kim, J.D. Lee, H.J. Lee, E.K. Lee and Y. Kim, 'Gas hydrate formation method to capture the carbon dioxide for pre-combustion process in IGCC plant', *International Journal of Hydrogen Energy*, 2011, 36, 1115-1121.
128. S.M. Carpenter and H.A. Long III,'Integration of carbon capture in IGCC systems', in *Integrated Gasification Combined Cycle (IGCC)*

Technologies, eds. T. Wang and G. Stiegel, Woodhead publishing, 2017, Chapter 13, 445-463.
129. Y. Wang, L. Zhao, A. Otto, M. Robinius and D. Stolten, 'A Review of Post-combustion CO2 Capture Technologies from Coal-fired Power Plants', *13th International Conference on Greenhouse Gas Control Technologies, Ghgt-13*, 2017, 114, 650-665.
130. E. Alper and O.Y. Orhan, 'CO2 utilization: Developments in conversion processes', *Petroleum*, 2017, 3, 109-126.
131. B. Dutcher, M.H. Fan and A.G. Russell, 'Amine-Based CO2 Capture Technology Development from the Beginning of 2013-A Review', *Acs Applied Materials & Interfaces*, 2015, 7, 2137-2148.
132. *IARC Classifications* [online], [Accessed 20/08/2019]. Available from: https://monographs.iarc.fr/agents-classified-by-the-iarc/
133. K. Yu, W.A. Mitch and N. Dai, 'Nitrosamines and Nitramines in Amine-Based Carbon Dioxide Capture Systems: Fundamentals, Engineering Implications, and Knowledge Gaps', *Environmental Science & Technology*, 2017, 51, 11522-11536.
134. M.M. Maguta, M. Aursnes, A.J.C. Bunkan, K. Edelen, T. Mikoviny, C.J. Nielsen, Y. Stenstrom, Y.Z. Tang and A. Wisthaler, 'Atmospheric Fate of Nitramines: An Experimental and Theoretical Study of the OH Reactions with CH3NHNO2 and (CH3)(2)NNO2', *Journal of Physical Chemistry A*, 2014, 118, 3450-3462.
135. *ACA project description* [online], [Accessed 20/08/2019]. Available from: https://www.mn.uio.no/kjemi/english/research/projects/aca/
136. *EUPHORE webpage* [online], [Accessed 20/08/2019]. Available from: http://www.ceam.es/WWWEUPHORE/home.htm
137. F. Drewnick, S.S. Hings, P. DeCarlo, J.T. Jayne, M. Gonin, K. Fuhrer, S. Weimer, J.L. Jimenez, K.L. Demerjian, S. Borrmann and D.R. Worsnop, 'A new time-of-flight aerosol mass spectrometer (TOF-AMS) - Instrument description and first field deployment', *Aerosol Science and Technology*, 2005, 39, 637-658.
138. A. Jordan, S. Haidacher, G. Hanel, E. Hartungen, L. Mark, H. Seehauser, R. Schottkowsky, P. Sulzer and T.D. Mark, 'A high resolution and high sensitivity proton-transfer-reaction time-of-flight mass spectrometer (PTR-TOF-MS)', *International Journal of Mass Spectrometry*, 2009, 286, 122-128.
139. T. Mikoviny, L. Kaser and A. Wisthaler, 'Development and characterization of a High-Temperature Proton-Transfer-Reaction Mass Spectrometer (HT-PTR-MS)', *Atmospheric Measurement Techniques*, 2010, 3, 537-544.
140. P. Eichler, M. Muller, B. D'Anna and A. Wisthaler, 'A novel inlet system for online chemical analysis of semi-volatile submicron particulate matter', *Atmospheric Measurement Techniques*, 2015, 8, 1353-1360.
141. N.J. Farren, 'Investigating the Formation of Organic Nitrogen Species during the Atmospheric Oxidation of Volatile Organic Compounds', *PhD thesis, University of York*, 2017.
142. J.D. Raff and B.J. Fnlayson-Pitts, 'Hydroxyl Radical Quantum Yields from Isopropyl Nitrite Photolysis in Air', *Environmental Science & Technology*, 2010, 44, 8150-8155.
143. C. Bloss, V. Wagner, M.E. Jenkin, R. Volkamer, W.J. Bloss, J.D. Lee, D.E. Heard, K. Wirtz, M. Martin-Reviejo, G. Rea, J.C. Wenger and M.J.

Pilling, 'Development of a detailed chemical mechanism (MCMv3.1) for the atmospheric oxidation of aromatic hydrocarbons', *Atmospheric Chemistry and Physics*, 2005, 5, 641-664.

144. C.J. Nielsen, B. D'Anna, R. Bossi, A.J.C. Bunkan, L. Dithmer, M. Glasius, M. Hallquist, A.M.K. Hansen, A. Lutz, K. Salo, M.M. Maguta, Q. Nguyen, T. Mikoviny, M. Müller, H. Skov, E. Sarrasin, Y. Stenstrøm, Y. Tang, J. Westerlund and A. Wisthaler, *Atmospheric Degradation of Amines (ADA): Summary report from atmospheric chemistry studies of amines, nitrosamines, nitramines and amides*, University of Oslo: Oslo, Norway, 2012.
145. L. Onel, M. Dryden, M.A. Blitz and P.W. Seakins, 'Atmospheric Oxidation of Piperazine by OH has a Low Potential To Form Carcinogenic Compounds', *Environmental Science & Technology Letters*, 2014, 1, 367-371.
146. J. Mao, X. Ren, L. Zhang, D.M. Van Duin, R.C. Cohen, J.H. Park, A.H. Goldstein, F. Paulot, M.R. Beaver, J.D. Crounse, P.O. Wennberg, J.P. DiGangi, S.B. Henry, F.N. Keutsch, C. Park, G.W. Schade, G.M. Wolfe, J.A. Thornton and W.H. Brune, 'Insights into hydroxyl measurements and atmospheric oxidation in a California forest', *Atmospheric Chemistry and Physics*, 2012, 12, 8009-8020.
147. H.M. Walker, D. Stone, T. Ingham, S. Vaughan, M. Cain, R.L. Jones, O.J. Kennedy, M. McLeod, B. Ouyang, J. Pyle, S. Bauguitte, B. Bandy, G. Forster, M.J. Evans, J.F. Hamilton, J.R. Hopkins, J.D. Lee, A.C. Lewis, R.T. Lidster, S. Punjabi, W.T. Morgan and D.E. Heard, 'Night-time measurements of HOx during the RONOCO project and analysis of the sources of HO2', *Atmospheric Chemistry and Physics*, 2015, 15, 8179-8200.

Appendix A

Actinometry formula Derivatization

The following equations are used to calculate the equation used to calculate the lamp flux in section 3.3.1.

The rate of production of O(1D) is;

$$\frac{d[O(\,^1D)]}{dt} = [N_2O]\,\sigma_{N2O}\,\emptyset_{NO}F$$

The rate of removal of O(1D) through reactions is given by;

$$\frac{-d[O(\,^1D)]}{dt} = k_1\,[O(\,^1D)][O_2] + k_2\,[O(\,^1D)][N_2] + ((k_3 + k_4)\,[O(\,^1D)][N_2O])$$

By assuming a steady state so that O(1D) photolysis and removal are equal;

$$[N_2O]\,\sigma_{N2O}\,\emptyset_{NO}F = k_1\,[O(\,^1D)][O_2] + k_2\,[O(\,^1D)][N_2] + (k_3 + k_4)\,[O(\,^1D)][N_2O]$$

The rate of formation of NO2 is given by;

$$\frac{d[NO]}{dt} = 2k_4[O(\,^1D)][N_2O]$$

This equation can then be integrated;

$$[NO]_t = 2k_4[O(\,^1D)][N_2O]t$$

$$[NO]_0 = 0$$

By rearranging in terms of O(1D) and substituting into the steady state equation gives the equation for calculating the lamp flux;

$$F\,t = \frac{[NO]\,(k_1\,[O_2] + k_2\,[N_2] + (k_3 + k_4)\,[N_2O])}{2k_4\,\sigma_{N2O}\,\emptyset_{NO}[N_2O]^2}$$